The Dissertation Committee for Allan Edward Jones Certifies that this is the approved version of the following dissertation:

Where the River Meets the Sea:
An Initial Investigation into the Riverine Tidal Freshwater Zone

Committee:

Meinhard Bayani Cardenas, Supervisor

Kevan B. Moffett, Co-Supervisor

Joel P. Johnson

Daniella M. Rempe

James W. McClelland

Ben R. Hodges

Where the River Meets the Sea:
An Initial Investigation into the Riverine Tidal Freshwater Zone

by

Allan Edward Jones

Dissertation

Presented to the Faculty of the Graduate School of

The University of Texas at Austin

in Partial Fulfillment

of the Requirements

for the Degree of

Doctor of Philosophy

The University of Texas at Austin

December 2017

Dedication

This work is dedicated to my wife, Meghan McKinney Jones. Without her love and support each and every day, I would have never made it this far. Thank you.

Acknowledgements

There are numerous individuals to whom I owe many thanks for this body of work. Unfortunately, because of space limitations (both on the page and in my memory), I will not be able to thank everyone who deserves recognition for assisting me these last 5 years. However, if I have forgotten you here, please know that I am still very thankful for your help and friendship.

First and foremost, I must acknowledge the extensive guidance and help provided by my adviser, Dr. Kevan B. Moffett. The fact that I retain a shred of sanity upon completion of this dissertation is in large part due to her superb abilities as a mentor. From day one, she focused on teaching tools for maintaining a health work/life balance without sacrificing productivity. Her unwavering calmness and support left me reassured after nearly every meeting with her. In those same meetings, her unceasing dry wit consistently provided a needed laugh and a safe haven for my own snarky-ness. Her joy for scientific discovery and investigation is infectious and often served to remind me that the hard work of research is also fun. She is a voracious editor and always emphasized the importance of succinctly yet clearly presenting your scientific work. One day, I hope to write with similar concise eloquence. Most importantly, she always kept her family as her first priority and made sure to support every member of her research group in doing the same. One day I want to grow up to be just like Kevan: making the people around me (both peers and mentees) better and more self-confident; producing fascinating insights about the world around us; and always remembering to keep family as my first priority.

Field work and observations composed much of the data on which this dissertation is built. That said, I owe many people thanks for offering their services as a field hand, including: Nick Reyna, Sarah Douglas, Wayne Hall, Kylie Holt, Lauren Rowsey, Adam Marsh, Hengchen Wei, Xin Xu, Muhammad Ashraf, Jackie Rambo, and Robert Christensen. Drs. Jim McClelland and Amber Hardison also deserve significant recognition for their help in coordinating field efforts, obtaining field observations, and overall guidance in the field. I would not be able to pilot a boat or drive a trailer semi-successfully were it not for the patient teaching and help of Mr. Frank Ernst (Dr. McClelland also deserves a little credit here). Through my many boating stumbles, issues, and requests for gas, I always appreciated his patience and ready smile. Without the boat, field work would have been much more difficult. I must also acknowledge the Edwards family and staff at the Welder Wildlife Foundation for allowing us access to their land for sample collection, including samples overnight. Finally, I owe a huge debt of gratitude to the arctic marathoner, Craig Connelly. Craig never hesitated to help in the field and was the best type of field hand, one who anticipated your next need and was unafraid to do the dirty work. Craig helped me so regularly that he probably completed at least 50% of my field work with me. More important than that, he became a great friend who helped make Port Aransas feel like home. Without the help of these individuals, I would have no data, and, thereby, no dissertation. Many, many thanks.

For my work behind the desk, I again owe several people thanks. Without the National Science Foundation (NSF) funding secured by Drs. Ben Hodges, Jim McClelland, Amber Hardison, and Kevan Moffett, I would not have been able to complete this work.

(Thank you to the NSF for providing the funding through research grant 1417433 for my dissertation research). In addition, each of these individuals provided substantial feedback on our first publication and helped to generate ideas to expand our discussion. Although the distance provided obstacles, each of them remained patient and flexible throughout my PhD process. Thank you for guidance and assistance, even from afar. Dr. Lindsay Scheef was extremely helpful when troubleshooting the data obtained by the tilt current meters. Her quick responses and insights into field installations and data cleaning were vital to obtaining useful data from the tilt current meters.

I am appreciative of the education and TA opportunities provided by the Jackson School of Geosciences (JSG) during my first two years of my PhD. Thank you, Dr. M. Bayani Cardenas, for filling in as my supervisor on paper, while allowing me to continue to work with Kevan remotely from Portland, OR. This arrangement absolutely ensured that I was able to finish my dissertation. To Drs. Joel Johnson and Daniella Rempe, thank you for joining my committee even though, again, my remote work location made communication difficult. I appreciate the insights and guidance you three have provided along the way. Additionally, a huge thank you to Philip Guerrero. Philip saved my skin and kept me calm through a few scheduling mishaps, and helped to ensure that I checked all the right boxes while completing this dissertation. Thank you, Philip, for helping me navigate the nebulous administrative landscape. If not for your guidance, I would most certainly still be lost in that abyss.

I also should probably acknowledge the Washington State University Vancouver (WSUV) community for accepting me into their fold. To the faculty, staff, and students there who have helped me along the way – thank you.

Without our family, we most certainly would be lost. Thank you, Jones, Loop, Christensen, Judkins, and McKinney clans, for your unending support and cheering. It is a great blessing to be a part of each of your lives, and I am very thankful for being welcomed into each of your families so lovingly. A special shout out to my brothers, John and Ryan. One constantly inspires me to do good in the world and improve who I am, and the other reminds me to never lose the child-like sense of wonder and amazement about the world around us. I will let them debate to whom I am referring.

An enormous thank you to my mother and father, Karen L. and William F. Jones. Without their first teachings of love, support, and discipline, I would certainly not be the person, nor the student, I am today. Thank you for always offering a listening ear and a place to stay as I made my way to and from the field. Thank you for never giving up on this grumpy, grouchy teenager/adult, but instead always teaching me. I should continue to heap thanks and recount stories, but again constraints prohibit me. Simply know that I will always be your son and for that blessing I am incredibly grateful.

Finally, on to you, Meghan. I could probably write an additional dissertation on my thanks for you. However, I shall save us all from that reality. Instead, I'll simply say:

I love you.

Thank you.

Where the River Meets the Sea:
An Initial Investigation into the Riverine Tidal Freshwater Zone

Allan Edward Jones, Ph.D.
The University of Texas at Austin, 2017

Supervisor: Meinhard Bayani Cardenas
Co-supervisor: Kevan B. Moffett

Abstract

Riverine tidal freshwater zones (RTFZs) are transitional environments between terrestrial and coastal waters that have freshwater chemistry and tidal physics, and are neither river nor estuary. The residence time dynamics of RTFZs have not yet been discussed in the literature, but may ultimately control the timing and magnitude of freshwater and nutrient coastal discharges. Furthermore, climate change threatens to alter the nexus between the terrestrial hydrologic cycle and the coastal tidal environment where the RTFZ resides. This dissertation provides the foundation for investigations into RTFZs and their subsequent residence times.

An initial residence time analysis of 15 tidal river reaches along the south Texas Gulf Coast introduces tidal river reaches into the *lentic*/*lotic* nomenclature. This residence time analysis also quantifies the vernacular of *lentic* (reservoir-like) and *lotic* (riverine) systems via the Freshwater Continuum Classification (FCC). The FCC framework also incorporates temporal hydrologic variability, which is typically absent from other *lentic*/*lotic* classifications.

Further analysis on one of these systems (Aransas River, TX, USA) revealed an RTFZ. The analysis empirically observed RTFZ responses to precipitation and tide, while providing the RTFZ definition. The RTFZ is defined by three longitudinal points of interest: λ_1 – upstream limit of brackish water, downstream limit of freshwater, and downstream boundary of RTFZ; λ_2 – upstream limit of bidirectional tidal velocities; λ_3 – upstream limit of tidal stage fluctuations and of the RTFZ. The RTFZ was typically (median) 59.9 km long and typically (median) began 11.84 km upstream (15.43 km/11.16 km, max/min) of the river mouth.

From field data collected during RTFZ isolation, a tidal rating curve was created to model tidal discharge. The tidal rating curve expanded on traditional non-tidal gauging methods by incorporating stage-rate-of-change observations into the typical stage to discharge relationship. The method was performed on several sites along the Mission and Aransas Rivers, TX, USA, and twelve USGS tidal gauging stations, and resulted in strong agreement between estimated and observed discharge (i.e., $r^2 > 0.70$). With the tidal discharge estimations and RTFZ observations, future investigations should focus on RTFZ residence times and their impacts on estuarine ecology.

Table of Contents

Abstract ix

List of Tables xvi

List of Figures xviii

Chapter 1: Introduction 1

1.1 Motivation 1

1.1.1 Global Context 1

1.1.2 Tidal freshwater environments 5

1.1.3 The riverine TFZ 6

1.2 Problem statement:
Investigating Transitional Riverine and Tidal Environments 9

1.3 Organization of Dissertation 11

1.4 References 16

Chapter 2: Residence-time-based classification of surface water systems 20

Abstract 20

2.1 Introduction 22

2.1.1 Importance of distinguishing lentic vs. lotic behavior 22

2.1.2 Present use of *lentic* and *lotic* in the literature 24

2.2 Methods 27

2.2.1 System integrated residence time (iT_R) 27

2.2.2 Determine lentic/lotic classification
after accounting for volume effects 33

2.2.2.1 Calculating the iT_R threshold
for all possible natural volumes 35

2.2.2.2 A caveat for iT_R time series
and threshold calculations 38

2.2.3 Determining oscillic nature
from system-specific iT_R thresholds 39

2.3 Application of framework to classifying Texas coastal rivers 40

2.3.1 Study region and selected systems 40

2.3.2 Texas river iT_R results....44
2.3.3 Texas river lentic/lotic and oscillic classifications....45
2.4 Discussion....48
2.4.1 Freshwater Continuum Classification assessment....48
2.4.2 Linked Hydrologic and Ecologic System Characterizations....54
2.4.3 The Time-dependency of Oscillic Systems....57
2.5 Conclusions....60
2.6 Acknowledgments....61
2.7 References....63
Chapter 3: Defining the Riverine Tidal Freshwater Zone and their Spatiotemporal Dynamics in Response to Tide and Precipitation....69
Abstract....69
3.1 Introduction....70
3.2 Riverine Tidal Freshwater Zone definition....73
3.3 RTFZ Identification and Analysis....74
3.3.1 Aransas River Field Area....75
3.3.1.1 Aransas River monitoring....77
3.3.1.2 Publicly available data....78
3.3.2 Empirical RTFZ Identification in space and time....78
3.3.2.1 Identifying the freshwater limit: λ_1....78
3.3.2.2 Identifying the limit of bidirectional tidal flow: λ_2....79
3.3.2.3 Identifying the limit of tidal river stage: λ_3....80
3.4 Results....86
3.4.1 Seasonal RTFZ reach length dynamics....86
3.4.2 Long-term rates of RTFZ length change....90
3.5 Discussion....93
3.5.1 Significance of the RTFZ and its definition....93
3.5.2 Controls on the downstream limit of the RTFZ, λ_1....94
3.5.3 Controls on the transition between uni- and bidirectional flow, λ_2....95

3.5.4 Controls on the upstream limit of the RTFZ, λ_3 97
3.5.5 Empirical RTFZ identification considerations.....99
3.5.6 Time scale responses of the RTFZ.....102
3.5.6.1 Event time scales.....102
3.5.6.2 Seasonal time scales.....103
3.5.6.3 Annual time scales 104
3.5.6.4 Time scales of global climate cycle 105
3.5.6.5 Time scales of global climate trends.....105
3.6 Summary and Conclusion 106
3.7 Acknowledgments.....108
3.8 References.....109

Chapter 4: Creation of a Tidal Rating Curve
by Expansion of Classic River Gauging Methods 113
Abstract 113
4.1 Introduction.....114
4.2 Methods.....117
4.2.1 Mission and Aransas River Field Area 117
4.2.2 Field Data.....119
4.2.2.1 Installed Instruments.....119
4.2.2.2 Acoustic Doppler Profiler (ADP) observations 121
4.2.3 TCM Calibration and data cleaning for tidal river applications122
4.2.4 Determination of Phase Offset (φ).....125
4.2.4.1 Standing vs. Mixed vs. Progressive Waves 126
4.2.5 Creation of the Tidal Rating Curve.....128
4.2.5.1 Relating Q observations to
Stage and Stage-rate-of-change 128
4.2.5.2 Discharge approximation during storm periods.....129
4.3 Results.....130
4.3.1 M-A and USGS baseflow characterization.....130
4.3.1.1 Baseflow phase offset (φ) comparison.....130

4.3.1.2 baseflow tidal rating curve....131
4.3.2 Mission and Aransas Rivers' discharge time series....132
4.4 Discussion....133
4.4.1 Model Caveats....133
4.4.1.1 Assumptions....133
4.4.1.2. Piecewise rating curve issues....139
4.4.2 Why not relate discharge to TCM velocity?....141
4.4.3 Model Insights....143
4.4.3.1 Phase offset insights....148
4.4.4 Tidal Rating Curve regression....152
4.4.4.1 Model Equations....152
4.4.4.2 Model coefficients (k_i) vs. waveform expectations....153
4.5 Summary and Conclusion....155
4.6 Acknowledgements....157
4.7 References....158

Chapter 5: Conclusion....163
5.1 Motivation....163
5.2 Summary of Chapter 2....165
5.3 Summary of Chapter 3....166
5.4 Summary of Chapter 4....168
5.5 Scientific and methodologic contributions....169
5.6 Future work....173
5.7 Acknowledgments....174
5.8 References....175

Appendix A: Description of lentic/lotic threshold calculations....177
A.1 Volume Approximations....177
A.2 Integrated residence time approximations....178

Appendix B: Quantitative classification framework guide....184
B.1 How to recreate Figure 2.1....184

B.1.1 Obtain the proper data 184
B.1.2 Approximating Volume if time series unavailable 187
B.1.3 Calculating integrated discharge 189
B.1.4 Re-creating Figure 2.1 191
B.2 Calculating iT_R for all time steps from discharge and volume time series 192
B.2.1 Adding the iT_R lines to Figure B.1 194
B.3 Classifying the example systems 195
B.3.1 Determine the iT_R thresholds across all possible natural volumes 195
B.3.2 Classify systems from unique iT_R thresholds 197
B.3.3 Plotting the classifications similar to Figure 2.3a and 2.3b 200
B.4 An additional note 202
Appendix C: Matlab *Main Script* 206
Appendix D: Storm λ_3 ID figure 221
Appendix E: Sinusoid derivation 223
Appendix F: Storm lag and spreading figure 225
Appendix G: TCM Coordinate rotation method and Matlab script 226
Appendix H: Individual phase offset analysis plots 253
Appendix J: M-A and USGS site regression plots 275
Appendix K: M-A discharge time series from tidal rating curve 297
Bibliography 307

List of Tables

Table 2.1: The 15 Texas Gulf Coast tidal river systems analyzed, (Rv – River, Ck – Creek, Bu – Bayou) and gauging stations used in applying the Freshwater Continuum Classification methodology. Data references are [*USGS*, 2015], [*NOAA Tides & Currents*, 2015]. The Texas Commission on Environmental Quality (TCEQ) Surface Water Quality Viewer (SWQV) provided the tidal reach length information [*TCEQ*, 2015]. 29

Table 2.2: Comparison of Freshwater Continuum Classification (FCC) designations to designations determined by other methods for the 15 analyzed Texas tidal river reaches. Most systems show an exact match between classification schemes. * Indicates a match in the river's oscillic classification only. ** Indicates no match. The Colorado, Brazos, and Neches Rivers do not match previous frameworks because of our introduction of the *intermediate* classification option. 52

Table 2.3: Lentic and lotic iT_R thresholds (in days), and FCC model designations, for the 15 Texas Coastal Plain tidal river reach systems analyzed. 55

Table 3.1: Description of four discrete river reaches that vary by degree of tidal and riverine dominance.....73

Table 3.2: Primary tidal constituents for the NOAA Copano Bay Fishing Pier tidal gauging station (Station ID: 8774513) [*NOAA* 2017c]. 81

Table 3.3: Location of each λ (km upstream from the river mouth) throughout the three time periods analyzed. 88

Table 4.1: List of USGS and Mission-Aransas tidal river sites analyzed, site numbers, figure labels, the calculated φ, and the assessed waveform. * - Phase offsets are likely of strongly standing character, even though slightly beyond ± 5 degree margin. ** - Insufficient TCM velocity data to accurately determine φ. 134

Table 4.2: Baseflow regression coefficient estimates (with standard error, t-statistic, and p value) and adjusted r^2 for each monitoring site on the Mission and Aransas Rivers and twelve USGS stations. * - No ADP transects were collected at site A5 due to safety concerns. ** - Insufficient data were collected at site M2, due to issues with the installed instrumentation.136

Table 4.3: Summary of the eight Mission-Aransas sites' discharge (m^3 s^{-1}) regime during identified baseflow and storm conditions, and over all conditions. * - No ADP transects were collected at site A5 due to safety concerns. ** - Insufficient data were collected at site M2, due to issues with the installed instrumentation. 137

List of Figures

Figure 2.1: Schematic of one integrated residence time (iT_R) calculation beginning from a given t_0 and based on simplistic discharge and volume time series. (a) Two conceptual discharge time series: uniform discharge (dashed line), or gradually increasing discharge (solid line). (b) Identifying t_n: calculate a cumulative discharge volume (V_C) starting from a given time step, t_0, by integrating through succeeding discharge conditions until such time that V_C equals the system volume (V_j, dotted line) of the water body of interest; this is time t_n. The subscript number on t_n refer to the discharge time series (1 or 2) associated with that t_n value. The integrated residence time calculated for t_0 is then: $iT_R = t_n - t_0$. Note that in a natural system, the discharge and volume time series would both be more variable and the calculation therefore less simplistic. 32

Figure 2.2: Conceptual iT_R distributions. There are six conceptual categories defining iT_R distributions within the overall continuum of possibilities. The narrow, less iT_R variable A-C distributions represent nonoscillic systems, while distributions D-F represent likely oscillic systems. Systems with larger iT_R and exhibiting distributions similar to F and C will be defined as lentic. Conversely, systems with distributions A and D are likely to be defined as lotic due to the shorter iT_R. The central B and E distributions will be classified as intermediate between lentic and lotic. 34

Figure 2.3: Schematic of FCC model determination of lentic/lotic and oscillic character. The process for quantitatively defining the system as lentic, intermediate, or lotic and as oscillic or nonoscillic begins with comparing the system's median iT_R to its median volume (a). For a given system volume, the threshold values of lentic and lotic residence time conditions (diagonal lines) are calculated from equations 2.3 and 2.4. The intersections of the median system volume with the lentic and lotic thresholds (gray dots) represents the minimum median iT_R for a system to be typically lentic, and the maximum median iT_R for it to be typically lotic. These thresholds can be compared to the more detailed iT_R time series (b) to determine if the system is oscillic over the analyzed time period; here, S2 is oscillic during the time period of interest, as it experiences iT_R conditions beyond both lentic and lotic thresholds, while S4 is nonoscillic during the time period of interest. Note that S1 and S3 are not included in (b) because they do not have the same median volume (and therefore do not have the same iT_R thresholds) as S2 and S4...37

Figure 2.4: Map of Texas coastal study region and tidal river reaches. Letter labels correspond to the rivers listed in Table 2.1. Highlighted (red) reaches represent each river's analyzed tidal reach. The inset depicts the state of Texas with the study region in the black box. 41

Figure 2.5: Texas rivers' tidal reaches' integrated residence time (iT_R) distributions. The iT_R distributions of the analyzed tidal river reaches cluster into the 'A'-, 'B'-, 'E'- and 'F'-type conceptual distributions from Figure 2.2. 46

Figure 2.6: Lentic/intermediate/lotic classification of 15 Texas rivers' tidal reaches according to the Freshwater Continuum Classification (FCC) approach. 47

Figure 2.7: Texas tidal river reaches' iT_R time series, with derived system-specific lentic/lotic thresholds indicated by horizontal lines. The lower shaded region of each subplot represents lotic conditions and the upper region lentic conditions, with an unshaded intermediate region (similar to Figure 2.3b). The subplots are organized geographically, south to north (also drier to wetter).....49

Figure 3.1: Spectrum of tidal freshwater zones, including the riverine tidal freshwater zone (RTFZ) in (b), with key locations λ_1, λ_2, and λ_3 all contained within the river banks. In contrast, a big-river estuary (a) may have λ_1 and λ_2 well downstream of the river mouth, while a classic estuary (c) with strong tidal forces may position λ_1, λ_2, and λ_3 atop one another and have virtually no TFZ. 71

Figure 3.2: Map of installed monitoring sites along the Aransas River of south Texas and USGS gauge 08189700 location [USGS 2017a]. Inset: Aransas watershed location within Texas, USA.....77

Figure 3.3: Methods for identification of λs during baseflow conditions. Conditions during and after a precipitation event between 13-28 Dec. 2015 are depicted at the USGS gauge (a) and in the stage (b) and velocity (c) time series of A1. The dashed line in (c) represents the 90th percentile threshold, to isolate storm conditions. The storm appearing at the USGS gauge was not strongly apparent far downstream at A1. For (d-n), rows correspond to identified λ location and columns represent the three highlighted time periods (i, ii, iii or "Recession", "Neap Tide", and "Spring Tide", respectively) in the time series (a-c). In (k-n) the 3 lines are 25th, 50th (median), and 75th percentiles of dSdt within a 24-hour moving window. 85

Figure 3.4: λ position along the length of the Aransas River. The median (star) and interquartile range (box) for each λ position are presented for (a) late summer (01 July through 01 September 2015), (b) late winter (01 December 2015 through 01 March 2016), and (c) one year (01 July 2015 through 01 July 2016). The position of λ_1 steadily intrudes throughout the year with salt transport upstream, λ_2 remains fairly constant, and λ_3 varies widely due to spring, neap, and secular tides.....87

Figure 3.5: Time series of USGS gauge discharge (a) and the length of the Aransas River RTFZ (b) from 01 July 2015 to 01 July 2016. The larger events, marked by the gray dashed arrows between (a) and (b), are associated with sudden lengthening of the RTFZ (b). Between those five major storms, the λs shift relative to one another and alter the proportion of the RTFZ with bidirectional versus unidirectional flow (c) and the RTFZ length shortens as a result of upstream saline intrusion (d-g). During the four periods of baseflow and saline intrusion, the RTFZ length shortens at a similar rate (0.15, 0.16, 0.40, and 0.31 km d^{-1}, respectively). 89

Figure 3.6: Temporal relations between spring and neap tide, and λ_3. During a period baseflow, as evidenced by the minimal discharge at the USGS gauge (a), the tidal stage at the most downstream site, A5, (b) displayed periods of strong neap and spring tidal conditions. Neap tides were related to λ_3 moving downstream and spring tides to λ_3 being positioned farther upstream (c). 91

Figure 3.7: The inversion of λ_2 and λ_1 relative positions during a storm event in the Aransas watershed in March 2016. Although the Aransas River USGS gauge did not record a dramatic peak in discharge on 11 March (a), a large amount of freshwater entered the system below the gauge. This runoff caused the TCM velocity at site A1 (b) to significantly exceed the annual 90^{th} velocity percentile (dashed line in (b)), classifying the event at A1 as a significant storm by our criteria. The position of each λ varied in response to the hydrograph peak, including a portion of time when λ_2 was pushed downstream of λ_1 (beginning approximately on 11 March 2016). The inversion of λ_2 and λ_1 was due to riverine discharge overwhelming tidal velocities and creating an entirely unidirectional velocity regime along the length of the river (λ_2 far downstream), while estuarine salt had yet to be extruded from the river (little movement in λ_1). 92

Figure 4.1: Mission and Aransas River watersheds, their topography (see colorbar), and monitoring locations (circles) including each river's USGS gauge (Station ID: 08189500 and 08189700, respectively) [USGS 2017]. Inset: Mission and Aransas watershed locations within Texas, USA.....120

Figure 4.2: Pitch, roll, and yaw corrections for TCM data and resulting corrected velocity time series. The data presented were observed at site A4 between 02 March and 30 April 2016. The pitch, roll, and yaw corrections align the potentially offset or rotated raw data with the proper downstream flow direction, which we oriented along the positive y-axis. The pitch and roll corrections align the observed, normalized TCM coordinate data (blue dots in (a)) to the ideal X-Y origin (black dots in (a)). The isolated storm data (cyan and yellow data in (b)) are used to determine the primary direction of downstream flow (red arrow in (b)). This downstream trend is yaw-rotated to align with the positive y-axis (c). From the cleaned, normalized, and properly oriented TCM coordinate observations (c), an empirical relationship between tilt (angle-from-vertical) and local velocity (d) create a final velocity time series (e). In (d), the orange and blue lines refer to the tilt-velocity relationship for the 'p50' and 'b15' SeaHorse TCMs, respectively. The red dashed lines in (e) outline the TCM detection limit of ± 2 cm s^{-1}. 124

Figure 4.3: Schematic of the relationships between stage and discharge (first row) and between stage-rate-of-change and discharge (second row) for progressive (a, d), mixed (b, e), and standing (c, f) waveforms. Each subfigure has two y-axes; the left axis is stage or its derivative, and the right axis is discharge, with the curves color-coded to match the associated axis. The absolute phase offset between stage and discharge is represented by ϕ. 127

Figure 4.4: Comparison of phase offset and FFT tidal signal magnitude for the Mission-Aransas and USGS sites. The labels and φ values for each site correspond to the "label" column in Table 4.1. 135

Figure 4.5: Linear model relating TCM velocity to ADP discharge observations at three sites along the Aransas River, Texas. TCM velocities for sites A1 (a), A3 (b), and A4 (c) increase in magnitude with increased distance downstream (toward A4). The regressions for the two downstream sites, A3 and A4, present much better coefficients of determination (r^2 = 0.73 and 0.48, respectively) than the upstream-most site, A1 (r^2 = 0.03). This is primarily due to the velocity observed at A1 often falling below the TCM sensitivity and, therefore, being unreliable in the model. 142

Figure 4.6: Scatter plots of five of the twelve analyzed USGS sites' discharge (observed by USGS), stage, and stage-rate-of-change. Two weeks of baseflow data are shown for each site. The left-hand column (a, c, e, g, and j) plot discharge against stage and are colored with respect to stage-rate-of-change conditions. The right-hand column (b, d, f, h, and k) compare discharge against stage-rate-of-change conditions and are colored by stage. Each row represents a different USGS site; the Shark River's conditions are depicted in (a) and (b), the Connecticut River's conditions are shown in (c) and (d), the Halls River's details are described in (e) and (f), the Crystal River's data are provided in (g) and (h), and the Plum Island River's data are illustrated in (j) and (k). The Shark, Halls, and Plum Island Rivers presented stage relative to a zero MSL datum (hence positive and negative stage). 147

Figure 4.7: Linear models relating the stage-rate-of-change to ADP discharge observations along the Aransas and Mission Rivers, Texas. Each linear model assumes the origin is the y-intercept. The Aransas River sites, A1-4, are depicted in the top row of subfigures (a-d), while the Mission River sites M1 and M3-5 are portrayed on the lower row (subfigures e-h), respectively. In general, each site shows a fair-to-strong relationship between discharge and stage-rate-of-change conditions, which reflects each site's φ values and strongly standing wave-like character; for an ideal standing wave we should expect a linear relationship. The data are colored in reference to their corresponding stage values.....150

Figure A.2: Summary of large-/small-volume, lentic/lotic coordinate calculation. Lentic and lotic velocities remain constant at both volumetric endmembers. The largest volume is approximated by the product of the length of the Nile River, the maximum width of the Amazon River, and the maximum depth of Congo River, while the smallest volume is 1 m^3. The area ratio at the large volume approximation is 60:1 while 1:1 at the smallest. From the volume traverse length, the lentic/lotic velocity and the area ratio, we estimate and pair the iT_R conditions at each endmember with the respective volume to form our spectrum endpoints.....181

Figure A.3: Comparison of calculated iT_R thresholds to literature observations. For the 15 rivers analyzed in this study, each river's calculated lentic/lotic iT_R thresholds (orange/blue dots, respectively) were compared against some threshold values between lentic and lotic behaviors from the literature: 30 days (dot-dashed line, from Hein et al., [2003] and Baranyi et al., [2002]), 15 days (solid line, from Rennella and Quirós [2006]) and 7 days (black dashed line, from Baranyi et al., [2003]). The letter labels along each plot's x-axis are associated with the tidal reaches of the rivers named in Table 2.1. This comparison shows that the derived power laws, which generated the orange and blue dots, divide systems into lentic/intermediate/lotic around the same iT_R values that prior (non-scalable) methods would have (although they lacked the intermediate class). 183

Figure B.1: Initial replication of conceptual Figure 2.1. For simplicity, the example analysis uses a constant (steady-state) and simple linearly increasing discharge time series (a); the same goes for the volume time series (b). 191

Figure B.2: Replication of Figure 2.1 including the iT_R calculation descriptions. The left-most vertical line, marking $t_{initial}$, is the first time step (a). Although the plots only display the iT_R calculations for the first time step, the vertical lines representing the placement of t_{final} cross the intersections between the steady-state and transient accumulated discharge and volume time series (b).....195

Figure B.3: The decision tree of the proposed classification framework. Beginning with a system's iT_R time series, there are two separate classifications to complete: lentic/lotic/intermediate and oscillic/nonoscillic. The former classification examines how the system's median, or typical, iT_R conditions relate to the system-specific lentic/lotic thresholds. The oscillic classification analyzes how the extremes of the time series relate to the iT_R thresholds. The left limb of the decision tree can be graphically represented as Figures 2.3a and 2.6, while the right limb is depicted in Figures 2.3b and 2.7. 199

Figure B.4: Example data plot replicating conceptual Figure 2.3. The orange line represents the lentic threshold conditions for all volumes in (a), while representing the system-specific lentic thresholds for the steady-state time series in (b), and the *Transient* time series in (c). Similarly, the blue line represents the spectrum (a) and system-specific ((b) and (c)) lotic threshold conditions. The purple lines (b) and (c) represent the iT_R time series for the steady-state and transient hydrologic conditions, respectively. 201

Figure B.5: Replication of Figure 2.1 using a faux-flashy discharge regime. Due to the "storm" peaks in (a) alter the "Accumulated Discharge 2" curve in (b), translating the intersection with the Transient volume time series to near Jan-10 as opposed to after Feb-05 for the initial analysis. 203

Figure B.6: Replication of Figure 2.1 with faux-flashy discharge regime and iT_R calculations lines. Although the "storm" peaks in (a) alter the "Accumulated Discharge 2" curve in (b), and translate the intersection with the Transient volume time series to earlier, the iT_R calculations still correctly identified t_{final} for the Transient data (intersection between solid blue and red lines in b).....204

Figure B.7: Faux-flashy discharge regime plotted with Figure 2.3 conceptual framework. Although the intermediate (a) and nonoscillic classifications ((b) and (c)) did not change, the Transient iT_R time series changed to accommodate the increased discharge dynamics (c). 205

Figure F.1: A storm pulse on the Aransas River in November 2015 that is lagged in transport downstream, decreases in velocity downstream, and is spread over a wider time window.....225

Figure H.1: The phase analysis for M-A site A1. The two subfigures (one atop the other) on the left-hand side of this figure show the FFT magnitudes of the stage (left-top) and discharge (left-bottom) for the identified semidiurnal and diurnal harmonics analyzed for phase offset. The right-hand figure shows the calculated phase offset for each harmonic and compares it to the predicted offsets for a standing, mixed and progressive wave. 253

Figure H.2: The phase analysis for M-A site A2. The two subfigures (one atop the other) on the left-hand side of this figure show the FFT magnitudes of the stage (left-top) and discharge (left-bottom) for the identified semidiurnal and diurnal harmonics analyzed for phase offset. The right-hand figure shows the calculated phase offset for each harmonic and compares it to the predicted offsets for a standing, mixed and progressive wave. 254

Figure H.3: The phase analysis for M-A site A3. The two subfigures (one atop the other) on the left-hand side of this figure show the FFT magnitudes of the stage (left-top) and discharge (left-bottom) for the identified semidiurnal and diurnal harmonics analyzed for phase offset. The right-hand figure shows the calculated phase offset for each harmonic and compares it to the predicted offsets for a standing, mixed and progressive wave. 255

Figure H.4: The phase analysis for M-A site A4. The two subfigures (one atop the other) on the left-hand side of this figure show the FFT magnitudes of the stage (left-top) and discharge (left-bottom) for the identified semidiurnal and diurnal harmonics analyzed for phase offset. The right-hand figure shows the calculated phase offset for each harmonic and compares it to the predicted offsets for a standing, mixed and progressive wave. 256

Figure H.5: The phase analysis for M-A site A5. The two subfigures (one atop the other) on the left-hand side of this figure show the FFT magnitudes of the stage (left-top) and discharge (left-bottom) for the identified semidiurnal and diurnal harmonics analyzed for phase offset. The right-hand figure shows the calculated phase offset for each harmonic and compares it to the predicted offsets for a standing, mixed and progressive wave. 257

Figure H.6: The phase analysis for M-A site M1. The two subfigures (one atop the other) on the left-hand side of this figure show the FFT magnitudes of the stage (left-top) and discharge (left-bottom) for the identified semidiurnal and diurnal harmonics analyzed for phase offset. The right-hand figure shows the calculated phase offset for each harmonic and compares it to the predicted offsets for a standing, mixed and progressive wave. 258

Figure H.7: The phase analysis for M-A site M2. The two subfigures (one atop the other) on the left-hand side of this figure show the FFT magnitudes of the stage (left-top) and discharge (left-bottom) for the identified semidiurnal and diurnal harmonics analyzed for phase offset. The right-hand figure shows the calculated phase offset for each harmonic and compares it to the predicted offsets for a standing, mixed and progressive wave. 259

Figure H.8: The phase analysis for M-A site M3. The two subfigures (one atop the other) on the left-hand side of this figure show the FFT magnitudes of the stage (left-top) and discharge (left-bottom) for the identified semidiurnal and diurnal harmonics analyzed for phase offset. The right-hand figure shows the calculated phase offset for each harmonic and compares it to the predicted offsets for a standing, mixed and progressive wave. 260

Figure H.9: The phase analysis for M-A site M4. The two subfigures (one atop the other) on the left-hand side of this figure show the FFT magnitudes of the stage (left-top) and discharge (left-bottom) for the identified semidiurnal and diurnal harmonics analyzed for phase offset. The right-hand figure shows the calculated phase offset for each harmonic and compares it to the predicted offsets for a standing, mixed and progressive wave. 261

Figure H.10: The phase analysis for M-A site M5. The two subfigures (one atop the other) on the left-hand side of this figure show the FFT magnitudes of the stage (left-top) and discharge (left-bottom) for the identified semidiurnal and diurnal harmonics analyzed for phase offset. The right-hand figure shows the calculated phase offset for each harmonic and compares it to the predicted offsets for a standing, mixed and progressive wave. 262

Figure H.11: The phase analysis for USGS site on the Connecticut River [site number: 01193050]. The two subfigures (one atop the other) on the left-hand side of this figure show the FFT magnitudes of the stage (left-top) and discharge (left-bottom) for the identified semidiurnal and diurnal harmonics analyzed for phase offset. The right-hand figure shows the calculated phase offset for each harmonic and compares it to the predicted offsets for a standing, mixed and progressive wave. 263

Figure H.12: The phase analysis for USGS site on the Murderkill River [site number: 01484085]. The two subfigures (one atop the other) on the left-hand side of this figure show the FFT magnitudes of the stage (left-top) and discharge (left-bottom) for the identified semidiurnal and diurnal harmonics analyzed for phase offset. The right-hand figure shows the calculated phase offset for each harmonic and compares it to the predicted offsets for a standing, mixed and progressive wave. 264

Figure H.13: The phase analysis for USGS site on the Middle River [site number: 02198950]. The two subfigures (one atop the other) on the left-hand side of this figure show the FFT magnitudes of the stage (left-top) and discharge (left-bottom) for the identified semidiurnal and diurnal harmonics analyzed for phase offset. The right-hand figure shows the calculated phase offset for each harmonic and compares it to the predicted offsets for a standing, mixed and progressive wave. 265

Figure H.14: The phase analysis for USGS site on the Savannah River [site number: 02198980]. The two subfigures (one atop the other) on the left-hand side of this figure show the FFT magnitudes of the stage (left-top) and discharge (left-bottom) for the identified semidiurnal and diurnal harmonics analyzed for phase offset. The right-hand figure shows the calculated phase offset for each harmonic and compares it to the predicted offsets for a standing, mixed and progressive wave. 266

Figure H.15: The phase analysis for USGS site on the Ogeechee River [site number: 02203536]. The two subfigures (one atop the other) on the left-hand side of this figure show the FFT magnitudes of the stage (left-top) and discharge (left-bottom) for the identified semidiurnal and diurnal harmonics analyzed for phase offset. The right-hand figure shows the calculated phase offset for each harmonic and compares it to the predicted offsets for a standing, mixed and progressive wave. 267

Figure H.16: The phase analysis for USGS site on the St. Mary's River [site number: 02231254]. The two subfigures (one atop the other) on the left-hand side of this figure show the FFT magnitudes of the stage (left-top) and discharge (left-bottom) for the identified semidiurnal and diurnal harmonics analyzed for phase offset. The right-hand figure shows the calculated phase offset for each harmonic and compares it to the predicted offsets for a standing, mixed and progressive wave. 268

Figure H.17: The phase analysis for USGS site on the Chassahowitzka River [site number: 02310663]. The two subfigures (one atop the other) on the left-hand side of this figure show the FFT magnitudes of the stage (left-top) and discharge (left-bottom) for the identified semidiurnal and diurnal harmonics analyzed for phase offset. The right-hand figure shows the calculated phase offset for each harmonic and compares it to the predicted offsets for a standing, mixed and progressive wave. 269

Figure H.18: The phase analysis for USGS site on the Halls River [site number: 02310689]. The two subfigures (one atop the other) on the left-hand side of this figure show the FFT magnitudes of the stage (left-top) and discharge (left-bottom) for the identified semidiurnal and diurnal harmonics analyzed for phase offset. The right-hand figure shows the calculated phase offset for each harmonic and compares it to the predicted offsets for a standing, mixed and progressive wave. 270

Figure H.19: The phase analysis for USGS site on the Crystal River [site number: 02310747]. The two subfigures (one atop the other) on the left-hand side of this figure show the FFT magnitudes of the stage (left-top) and discharge (left-bottom) for the identified semidiurnal and diurnal harmonics analyzed for phase offset. The right-hand figure shows the calculated phase offset for each harmonic and compares it to the predicted offsets for a standing, mixed and progressive wave. 271

Figure H.20: The phase analysis for USGS site on the Mobile River [site number: 02470629]. The two subfigures (one atop the other) on the left-hand side of this figure show the FFT magnitudes of the stage (left-top) and discharge (left-bottom) for the identified semidiurnal and diurnal harmonics analyzed for phase offset. The right-hand figure shows the calculated phase offset for each harmonic and compares it to the predicted offsets for a standing, mixed and progressive wave. 272

Figure H.21: The phase analysis for USGS site on the Shark River [site number: 252230081021300]. The two subfigures (one atop the other) on the left-hand side of this figure show the FFT magnitudes of the stage (left-top) and discharge (left-bottom) for the identified semidiurnal and diurnal harmonics analyzed for phase offset. The right-hand figure shows the calculated phase offset for each harmonic and compares it to the predicted offsets for a standing, mixed and progressive wave. 273

Figure H.22 The phase analysis for USGS site on the Plum Island River [site number: 424752070491701]. The two subfigures (one atop the other) on the left-hand side of this figure show the FFT magnitudes of the stage (left-top) and discharge (left-bottom) for the identified semidiurnal and diurnal harmonics analyzed for phase offset. The right-hand figure shows the calculated phase offset for each harmonic and compares it to the predicted offsets for a standing, mixed and progressive wave. 274

Figure J.1: The linear regression data for site A1.....276

Figure J.2: The linear regression data for site A2.....277

Figure J.3: The linear regression data for site A3.....278

Figure J.4: The linear regression data for site A4.....279

Figure J.6: The linear regression data for site M2. Because this linear regression produced an r^2 less than 0, these results were not included in Chapter 4. The poor nature of this fit is likely due to limited ADP observations and installation data. Evidence suggests that our installation was stolen.281

Figure J.7: The linear regression data for site M3. 282

Figure J.8: The linear regression data for site M4. 283

Figure J.9: The linear regression data for site M5. 284

Figure J.10: The linear regression data for USGS site on the Connecticut River [site number: 01193050]. 285

Figure J.11: The linear regression data for USGS site on the Murderkill River [site number: 01484085]. 286

Figure J.12: The linear regression data for USGS site on the Middle River [site number: 02198950]. 287

Figure J.13: The linear regression data for USGS site on the Savannah River [site number: 02198980]. 288

Figure J.14: The linear regression data for USGS site on the Ogeechee River [site number: 02203536]. 289

Figure J.15: The linear regression data for USGS site on the St. Mary's River [site number: 02231254]. 290

Figure J.16: The linear regression data for USGS site on the Chassahowitzka River [site number: 02310663]. 291

Figure J.17: The linear regression data for USGS site on the Halls River [site number: 02310689]. 292

Figure J.18: The linear regression data for USGS site on the Crystal River [site number: 02310747]. 293

Figure J.20: The linear regression data for USGS site on the Shark River [site number: 252230081021300]. 295

Figure J.21: The linear regression data for USGS site on the Shark River [site number: 424752070491701]. 296

Figure K.1: The calculated discharge time series for M-A site: A1. 297

Figure K.2: The calculated discharge time series for M-A site: A2. 298

Figure K.3: The calculated discharge time series for M-A site: A3. 299

Figure K.4: The calculated discharge time series for M-A site: A4. 300

Figure K.5: The calculated discharge time series for M-A site: A5. There are no baseflow discharge conditions calculated for this site, because no ADP transects were completed at this site due to safety concerns. All that is presented are predicted storm discharges. 301

Figure K.6: The calculated discharge time series for M-A site: M1. 302

Figure K.7: The calculated discharge time series for M-A site: M2. Baseflow discharge was not calculated for this sites due to multiple sensor malfunctions and insufficient ADP transects. The discharges presented are only predictions of storm discharge. 303

Figure K.8: The calculated discharge time series for M-A site: M3. The spike in upstream discharge near 16 May 2016 is related to the rising limb of storm dramatically altering the dS conditions before shifting the cross-sectional velocity towards storm conditions. This meant that the simplistic method for discerning storm v. baseflow periods calculated discharge with the baseflow equation (eq. 4.3) and coefficients producing a negative (i.e., upstream) discharge associated with sharp rise in stage (i.e., large magnitude positive dS). 304

Figure K.9: The calculated discharge time series for M-A site: M4. 305

Figure K.10: The calculated discharge time series for M-A site: M5. Unfortunately, throughout much of the study period, the TCM for this site was malfunctioning. Thus, this is a very incomplete record of discharge, one that may not have any actual storm periods.....306

Chapter 1: Introduction

1.1 MOTIVATION

1.1.1 Global Context

Climate change and global warming threaten to dramatically alter the global climate in numerous ways, including rising global temperatures and associated rising sea level. The forecasted increases in global temperature and sea level will impact many aspects of our world, including the hydrologic cycle and its interaction with the coastal environment. Thus, the impact of these two symptoms of global climate change will meet at the transition between terrestrial and estuarine waters. In other words, our planet's *tidal freshwater zones* (TFZs) sit at the nexus between these two climate change trends.

Tidal freshwater zones (TFZs) are the transition between the fully riverine and estuarine environments [*Knights et al*. 2017, *Ganju et al.* 2004, *Yankovsky et al.* 2012]. TFZs are portions of the river-estuary continuum that are entirely fresh in chemistry, yet tidal in physics. These environments experience both tidal surface level fluctuations and bidirectional velocity. Tidal surface level rises and falls in tandem with estuarine flood and ebb tide, while tidal bidirectional velocity switches orientation between upstream and downstream throughout the tidal cycle. These environments exist in coastal river reaches where tidal forces intrude 10-100+ km inland (e.g., the Hudson, Potomac, Scheldt, and Incomati Rivers [*Findlay et al.* 1991, *Cole et al.* 1992, *Lovley and Phillip*s 1986a, *Lovley and Phillip*s 1986b, *Arndt et al.* 2007, *Arndt et al.* 2011, *Savenije* 2005]). However, with the looming implications of climate change, global TFZs are in danger of being permanently altered, especially as they are caught between two of the primary expected

climatic shifts resulting from climate change: rising temperature impacting the hydrologic cycle and rising sea level.

Rising global surface temperatures will greatly impact the terrestrial hydrologic cycle, since the rising temperature alters the Earth's energy cycle, which drives many planetary processes. Increased global temperatures will correspond to increases in global precipitation, with currently wet areas receiving more rainfall and dry areas receiving less rainfall. Tropics and poles will experience increased precipitation, but the subtropical regions (e.g., Texas, USA) will likely experience a $\geq 30\%$ decrease in average precipitation by the end of the century (i.e., 2100). Increased temperatures in these subtropical regions will also likely increase annual evaporation rates. This will lead to increased aridity and the potential expansion of deserts within the subtropics [*Collins et al.* 2013]. In addition to the compounding precipitation effects, rainfall intensity is forecasted to increase due to the increased water vapor present in the atmosphere from elevated temperatures. However, these intense rainfalls will happen less frequently. These two factors in conjunction will lead to more deluges that promote flooding while separated by increasingly long dry periods that promote drought. Thus, future projections predict a hydrologic cycle increasingly dominated by hydrologic extremes: flooding and drought [*Collins et al.* 2013].

Global TFZs will suffer many changes due to these consequences of global warming. TFZs mark the interaction between tidal and riverine forces, and serve as the transition between terrestrial rivers and estuaries. The hydrologic extremes of flooding and drought, which are expected to occur more regularly throughout the upcoming century, have major implications on TFZs. Specifically, these changes to the hydrologic cycle alter the hydrodynamic regime of the upstream forcings on TFZs and reduce the spectrum of riverine discharge to a binary option of either flood or drought conditions. During flood conditions, fresh riverine discharge will likely overwhelm any evidence of tidal character,

either eliminating the TFZ or extruding it offshore. Drought conditions have the opposite effect. With riverine inflow at a minimum, tidal forces and saline encroachment dominate this transition and enable saline waters to intrude far upstream. If given a sufficiently long drought, saline waters may intrude far enough to eliminate the TFZ and reach the extent of tidal influence. Such salinization may potentially prove detrimental to coastal populations dependent upon fresh surface waters.

Rising sea level threatens to drastically alter and even inundate modern-day coastline. With a temperature rise of only 2°C, historic paleo sea level records indicate a potential sea level rise of 5 meters [*Church et al.* 2013]. This rise in sea level will be due to both thermal expansion of oceanic waters and the introduction of major volumes of cold freshwater from melting glacial and polar sheet ice [*Church et al.* 2013]. Such a marked sea level rise would not only flood many coastal environments and populations (e.g., much of the Gulf of Mexico coastline along the southern USA [*Scavia et al.* 2002, *Neumann et al.* 2015]), but also dramatically alter tidal freshwater environments. At minimum, these tidal freshwater environments would be shifted far inland from their present day locations. In some instances where tidal freshwaters exist in small coastal rivers, the dramatic rise in sea level may eliminate the freshwater environment altogether by entirely submerging these coastal ecosystems (e.g., Mission River of south Texas, USA).

While changes to the hydrologic cycle impact the upstream forcings experienced by the TFZ, rising sea level will impact the opposite end of the TFZ by increasing tidal influence. Increased tidal base level will enable tidal forcings to propagate farther upstream and increase the length of the river reach affected by tidal physics. Similarly, as tidal influence extends farther upstream, saline waters will encroach farther upstream and shift the downstream boundary of TFZs upstream. Thus, if the TFZ once straddled the river estuary continuum, under increased tidal influence and potentially paired with decreased

riverine inflow, the TFZ may now be solely contained within the reaches of the river (i.e., upstream of the river mouth). The increased saline intrusion may also serve to contaminate freshwater supplies upon which coastal populations may be dependent for either drinking water or food. The change in river salinity may dramatically alter the instream biota and remove the present economic benefit of these coastal ecosystems. The increased tidal influence, potentially minimal freshwater discharge, and increased evaporation rates may serve to create hypersaline estuarine environments where local salinity exceeds that of the global average (i.e., > 35 PSU). Although technically upstream, the balance of forcings creating the TFZ will cause the TFZ to retain any available freshwater for extended periods and potentially further contribute to salinization.

The climate change shifts in both sea level and hydrologic processes will certainly be accompanied by an anthropogenic response that will further impact the future climate. The future growth and redistribution of global populations, especially those along coastlines, will need to adapt to the new hydrologic and climatic norms by planning for extended droughts, sporadic periods of flooding, and oceanic encroachment from rising sea level [*Collins et al.* 2013, *Church et al.* 2013, *Neumann et al.* 2015]. Coastal populations reserving water for their own municipal use further reduce the volume of freshwater available for transport to estuarine environments, which potentially exacerbates the impacts of tidal forcing. Growing coastal populations will also exacerbate demands on coastal freshwaters and potentially increase pollution of coastal waters [*Destouni et al.* 2008, *Johnson* 2009, *Neumann et al.* 2015].

Anthropogenic response to climate change will impact TFZs. Increased demand on coastal freshwaters from coastal populations will increasingly diminish the supply of freshwater available for coastal environments. This potentially increases the effective influence of tide on TFZs. Construction of a dam or saltwater sill to conserve freshwater

for use by coastal populations may halt the upstream progression of the tide. Such anthropogenic structures may have a variety of impacts on TFZs. If sufficiently large and imposing (i.e., a dam), these anthropogenic structures may eliminate potential TFZs by creating an artificial boundary that divides riverine and estuarine character. Conversely, a salt sill may halt only saline intrusion while tidal influence continues farther upstream, which effectively creates a permanent TFZ. Thus, TFZs will be greatly impacted by both the anthropogenic responses to climate change and the direct effects of global temperature and sea level rise.

1.1.2 Tidal freshwater environments

While TFZs exist at the intersection of these two climate change symptoms, TFZs are also a unique environment where tidal and riverine forces coexist. TFZs have been identified in the literature, yet much of the research surrounding tidal freshwater ecosystems has focused on intertidal wetland environments [*Odum* 1988, *Day et al.* 2007, *Doyle et al.* 2007]. Tidal freshwater wetlands and swamps are inundated during the flood tide, drained during the ebb tide, and remain freshwater in chemistry. However, until recently, research into tidal freshwater has not focused on TFZs that exist within the channel confines of the river-estuary continuum. *Knights et al.* [2017] provided the most recent discussion on potential nutrient dynamics and impacts of tidal surface water stage fluctuations within the TFZ. However, *Knights et al.* [2017] focus heavily on nitrification and denitrification rates along the length of the TFZ and not on the residence time dynamics imposed by the tidal physics. *Yankovsky et al.* [2012] investigated a portion of the transitional TFZ in the Santee River of South Carolina, USA, and focused on the river reach that has “comparable tidal and fluvial velocities.” Ultimately, since nearly equal in magnitude, these opposing velocities caused this river reach’s overall regime to

periodically shift from "two-directional flow to unidirectional." However, this investigation into the fluvial/tidal transition did not address the potential subsequent impacts on residence time. Studies of tidal rivers have discussed the importance of tidal freshwater reaches in manipulating riverine nutrient and suspended particle dynamics [*Findlay et al.* 1991, *Cole et al.* 1992, *Lovley and Phillips* 1986a]. However, no studies yet link these tidal freshwater reaches to extended residence times and discuss the subsequent impact on nutrient dynamics.

While TFZ residence times have not been investigated, tidal estuarine residence times and their associated dynamics have been discussed in the literature [*Wang et al.* 2004, *Sheldon and Aber* 2002]. Freshwater inflow is often not included due to the negligible density of freshwater compared to saline estuarine waters. Incoming freshwaters are incorporated into investigations of estuarine residence time when focusing on "flushing time." *Flushing time* is defined as the "time required for freshwater inflow to equal the amount of freshwater originally present in the estuary," potentially representing the transit time through the entire river-estuary continuum [*Sheldon and Aber* 2004, *Shen and Haas* 2004]. However, these studies do not focus on the residence time of only the TFZ and the impacts of that residence time on the overall residence time of the river-estuary continuum.

1.1.3 The riverine TFZ

A unique tidal freshwater environment exists under the broader category of the TFZ, a *riverine tidal freshwater zone* (RTFZ). An RTFZ is a TFZ that exists entirely within the confines of the river channel and upstream of the river mouth. Thus, the RTFZ is a river reach that is upstream of the river mouth and contains freshwater chemistry and tidal physics. Technically, a TFZ may span from far upstream to out into an adjacent coastal embayment. Similar to TFZs' fate in literature, RTFZs have not been greatly discussed and

as such their residence time dynamics have not been explored. However, RTFZs provide a unique opportunity to explore the interaction of riverine discharge and tidal dynamics and their subsequent impacts on freshwater and nutrient residence times. RTFZs represent the upstream-most endmember of alluvial estuaries, where riverine and tidal forcings are similar in magnitude [*Yankovsky et al.* 2012]. They act as the "gatekeepers" of the estuary; thus, nutrient and freshwater residence times through these zones may be highly influential.

An RTFZ's location shifts and length fluctuates (i.e., grows and shrinks) with changes in the balance between riverine and estuarine forcings. Depending upon the magnitude of riverine discharge, different amounts of tidal physics (i.e., surface water oscillations and/or bidirectional velocity) may be present upstream. When baseflow riverine discharge is smaller relative to tidal discharge, tidal forces may intrude inland to create a tidal river reach. Simultaneously, tidal motion transports estuarine salt upstream, which actively shrinks the RTFZ and moves the downstream RTFZ boundary inland. However, during a period of high river stage and discharge, the tidal signal is overwritten, and the river reach that once contained an RTFZ may now be entirely riverine in character (i.e., unidirectional flow, with discharge increasing monotonically with increases in stage). Throughout this flood pulse, tidal stage, discharge, and salinity may be pushed downstream beyond the river mouth to create a TFZ somewhere off shore. Minimal fluctuations in the balance between riverine and tidal forces (i.e., not flooding, but also not baseflow) may result in either a shift in the location of the RTFZ and/or a change in the length of the RTFZ. For example, a small, steady, prolonged increase in riverine discharge may result in salt transport downstream that lengthens the RTFZ. The unique hydrodynamic conditions of an RTFZ create a similarly unique set of residence time conditions that may control the timing and magnitude of nutrients reaching the coastal environment. The tidal bidirectional discharge inherent within RTFZs promote the potential for exceptionally long

residence times, on the order of several months, before freshwater and nutrients can traverse these systems [*Mooney and McClelland* 2012, *Jones et al.* 2017]. For example, *Ensign et al.* [2013] investigated a tidal transitional river reach and determined an average longitudinal discharge trend that switched directions over the length of the transitional zone. River reaches upstream exhibited discharge oriented downstream, while sites farther downstream depicted upstream-oriented discharge [*Ensign et al.* 2013]. This longitudinal discharge trend describes a nutrient and/or freshwater sink (pseudo-lentic), where such important substances may reside for a long time. Additionally, minimal inflow conditions, such as those along the south Texas Gulf of Mexico coastline, only serve to elongate RTFZ residence time conditions [*Mooney and McClelland* 2012, *Jones et al.* 2017]. Thus, for systems with minimal riverine baseflow, flood conditions provide the majority of freshwater transport to downstream estuaries [*Bruesewitz et al.* 2013, *Mooney and McClelland* 2012, *Jones et al.* 2017]. These large, sporadic pulses of freshwater have major implications for the salinity and biota of downstream estuaries [*Pollack et al.* 2011, *Palmer et al.* 2011].

These TFZs and RTFZs provide a unique opportunity for investigation. Composed of freshwater chemistry yet tidal physics, these transitional environments may control the nutrient and freshwater transport from terrestrial sources to estuarine sinks. Although several studies have discussed TFZs and their impacts, no study has provided a definitive nomenclature and framework to formally define the TFZ or RTFZ, nor has any study isolated the residence time dynamics of the RTFZ and their impact on the downstream estuary. In addition, no study has yet described nor formally identified an RTFZ. Furthermore, the projected impacts of climate change will alter RTFZs and TFZs, which may impact our present riverine and estuarine resources. As such, certain present-day climates may allow for us to investigate the RTFZ and its responses to variations in the

balance between tidal and riverine forcings. For example, the minimal baseflow, regular summer drought, and potential for large flash floods (in response to tropical storms and hurricanes) may make south Texas, and other subtropical semiarid locales, ideal locations to investigate the RTFZ. RTFZs also may potentially provide an early case study for the forecasted effects of climate change, as they represent the nexus of rising sea level and an impacted hydrologic cycle.

1.2 PROBLEM STATEMENT: INVESTIGATING TRANSITIONAL RIVERINE AND TIDAL ENVIRONMENTS

Transitional TFZs that exist along the river-estuary continuum offer the potential to control the timing and magnitude of freshwater and nutrients entering the coastal bays. These environments have only recently been discussed within scientific literature. They were often overlooked due to their tidal physics, yet freshwater chemistry. However, the residence time conditions from the mixture of tidal and riverine discharge effectively create a nutrient and freshwater sink. This transitional environment may store, transform, and/or remove nutrients until a significant inflow pulse arrives to override tidal forcings and extrude any and all stored substances (from nutrients to detritus) downstream. The stored nutrients are rapidly transported to the estuary, potentially leading to detrimental pollution of the coastal environment [*Bruesewitz et al.* 2013, *Destouni et al.* 2008].

To improve our understanding of these tidal freshwater environments, an initial investigation is needed into the RTFZ and its residence time dynamics. First and foremost, the initial investigation must isolate and identify an RTFZ. The identification of an RTFZ will present a coherent framework and nomenclature describing the RTFZ that has thus far been lacking from the literature. This foundational framework will supply the basis for which future studies may improve and expand our understanding of RTFZs and TFZs.

Subsequent empirical observations of the RTFZ's temporal character will provide insight into the factors controlling the system's residence time dynamics.

Identifying an RTFZ for observation should consist of a two-part analysis to increase the likelihood of finding an RTFZ. The analysis should begin by analyzing the residence time conditions of several rivers within a particular region likely to contain an RTFZ. Rivers containing an RTFZ will likely experience long residence times beyond what is typically expected for a river of similar size. The Texas portion of the Gulf of Mexico coastline exhibits the tidal and discharge conditions we would expect to create an RTFZ [*Evans et al.* 2012]. Minimal discharge from extreme summer evaporation make these coastal river systems susceptible to control by tidal forcings and to the creation of an RTFZ [*Mooney and McClelland* 2012, *Bruesewitz et al.* 2013, *Evans et al.* 2012]. Periodic flooding events may serve to freshen the rivers and momentarily eliminate tidal influence and the associated RTFZ. However, with the return of post-flood baseflow conditions, we may monitor the reestablishment of the RTFZ. In addition, south Texas hydrology already appears to emulate the discrete future flood and drought conditions forecasted to result from climate change. Extreme summer drought, which often outpaces annual precipitation, coupled with the potential of deluge events, especially associated with the El Niño Southern Oscillation (ENSO), often leads to extreme flash floods [*Evans et al.* 2012, *Ropelewski and Halpert* 1986, *Wolter et al.* 1999]. For example, from 1998 to 2008 the Aransas River, a small 94.6 km river in south Texas, experienced an average discharge of 1.39 $m^3 s^{-1}$, peak flow of 829.68 $m^3 s^{-1}$, and minimum flow of 0.0065 $m^3 s^{-1}$ [*Evans et al.* 2012]. Thus, we chose to focus our investigation for an RTFZ on the south Texas coastal region.

The second part of identifying an RTFZ comes from an in-depth empirical analysis of field monitoring. The residence time conditions obtained from the preliminary regional

analysis should identify the tidal rivers that are likely to exhibit an RTFZ. For the given regional context (i.e., south Texas), tidal river systems acting as (pseudo-) lentic environments may exhibit an RTFZ. These selected (pseudo-) lentic systems are acting as a reservoir where nutrients and freshwater may pool and reside for long periods, similar to our expectations for an RTFZ. From a selection of these identified (pseudo-) lentic systems, a field monitoring campaign will empirically define the presence of an RTFZ.

These field observations will provide insight into the discharge dynamics present throughout the transition between riverine and tidal conditions. Determining the temporal and spatial character of discharge throughout the riverine-tidal transition will be the first step in characterizing the residence time dynamics of the RTFZ. Also, the longitudinal discharge trend may provide foresight into the future discharge conditions of many tidal river systems beyond the semiarid subtropics.

To further our understanding of RTFZs and transitional tidal river environments, a consistent and definitive framework for the RTFZ needs to be presented. The new consistent nomenclature and conceptual model must provide a solid foundation for future tidal freshwater studies. In addition, the conceptual model should be updated and informed by investigations into the discharge regime of these transitional environments. From this both fundamental and empirical foundation, future studies may analyze the impact of the freshwater transport on nutrient residence times and their combined influence on the downstream estuarine ecology.

1.3 Organization of Dissertation

The aim of the following research was to complete an initial investigation into the RTFZ and lay the foundation for future studies to diagnose the system's nutrient processes and residence time dynamics. The following chapters attempt to address the investigations

introduced in the previous section. Each chapter builds on the work of previous chapters to present insight into the character and dynamics of tidal freshwater systems, with a specific emphasis on the RTFZ.

Chapter 2: Perform a residence-time-based classification of Texas tidal river reaches as a precursor to characterization of RTFZs.

Chapter 2 presents the initial analysis that models the expected residence time through the tidal freshwater river reach for fifteen rivers along the Texas coastline. The analysis characterizes the systems' residence time conditions within the lentic (reservoir-like)/lotic (river-like) vernacular. By doing so, the analysis expands the discrete lentic/lotic metrics to incorporate a system's temporal variability and to introduce aspects of tidal systems into the lentic/lotic discussion. Such systems would exhibit exceptionally long residence times due to the interaction of minimal discharge and tidal dynamics.

This work presented in Chapter 2 has been published by the American Geophysical Union (AGU) in the *Water Resources Research* journal. Co-authors helped develop the idea of *oscillic* systems and assisted in crafting the final manuscript. Much of the analysis was performed by me, with significant aid from Dr. Kevan B. Moffett. Dr. Ben Hodges also helped with the initial conceptualization of the modeling methods. As per AGU's copyright permissions, this work may be reused by the author in a new publication (i.e., this dissertation) without prior permission. The published work is cited as follows:

Jones, A. E., B. R. Hodges, J. W. McClelland, A. K. Hardison, and K. B. Moffett (2017), *Residence-time-based classification of surface water systems*, Water Resour. Res., 53, 5567–5584, doi:10.1002/ 2016WR019928.

Chapter 3: Within the Aransas River of south Texas, isolate an RTFZ and observe its responses to precipitation pulses and tidal cycles.

Chapter 3 presents an analysis of an RTFZ's responses to precipitation and tidal stimuli. The study presented in Chapter 2 identified the Aransas River as exhibiting a unique residence time character, i.e., *lentic, oscillic*. Thus, for the south Texas region, this system presented residence time conditions conducive to the presence of an RTFZ. Field monitoring installations recorded the temporal character of the Aransas River RTFZ. The temporal analysis emphasized the RTFZ's response to precipitation, drought, and tide. A conceptual model, framework, and nomenclature are also presented to provide a foundation for future RTFZ investigations.

This analysis presented in Chapter 3 will be submitted for publication shortly. Dr. Jim McClelland helped with the installation of monitoring equipment, while Dr. Kevan B. Moffett assisted with the temporal, empirical analysis of the field data.

Chapter 4: Develop a tidal rating curve to quantify the longitudinal discharge trend of a tidal river.

To begin addressing higher-resolution, system-specific residence time dynamics, a tidal rating curve is necessary to provide estimates of volumetric discharge. Chapter 4 presents a method for creating a tidal rating curve and relates the rating curve to waveform theory, i.e., standing versus progressive waves. The rating curve relates site-specific acoustic doppler profiler (ADP) measurements of volumetric discharge to records of water stage and the stage-rate-of-change ($\frac{dS}{dt}$). The tidal rating curve provides an inexpensive, simple, and repeatable method for gauging tidal rivers and investigating residence time dynamics.

Chapter 4 will soon be submitted for publication. Drs. Jim McClelland and Amber Hardison assisted in recording discharge measurements and installing field monitoring equipment. Drs. Kevan B. Moffett and Ben R. Hodges provided input and feedback regarding the phase offset and regression analyses to create the tidal rating curve.

Chapter 5: Summary and concluding remarks

The final chapter (5) presents a summary of the preceding chapters, highlighting each chapter's scientific and methodologic contributions. For example, Chapter 2 presents a repeatable, quantitative framework for classifying hydrologic systems as *lentic*/*lotic*/*intermediate* or *oscillic*/*nonoscillic* based upon temporal residence time conditions. Chapter 3 identifies, observes, and conceptually discusses the RTFZ, specifically focusing on RTFZ responses to precipitation and tide. Chapter 4 provides an inexpensive (both computationally and monetarily) method for modeling tidal discharge using a tidal rating curve.

In addition, the concluding chapter attempts to weave the information presented in preceding chapters into a cohesive contribution and highlight the broader context and impacts of the work. For example, climate change's rising temperature, decreasing inflow, and rising sea level will impact RTFZs worldwide. Therefore, an understanding of the dynamics that create and stem from RTFZs is necessary to prepare for potential future climatic conditions. In addition, management practices, such as dam construction for municipal reservoirs, may impact the nature of our TFZs. If the balance between riverine and tidal forces are impacted too severely, more RTFZs may appear or even disappear as saline waters intrude throughout the entire tidal river reach. Management policies should also take into account a hydrologic system's *lentic*/*lotic*/*oscillic* character and ensure that system continues to exhibit that behavior post-management.

Finally, potential future work is also discussed in the concluding chapter. For example, modeled discharge data presented in Chapter 4 will be used to describe each system's empirical residence time conditions. These residence time results will be compared against each system's RTFZ location and temporal character.

1.4 REFERENCES

Arndt, S., Vanderborght, J.-P., & Regnier, P. (2007). Diatom growth response to physical forcing in a macrotidal estuary: Coupling hydrodynamics, sediment transport, and biogeochemistry. *Journal of Geophysical Research: Oceans*, *112*(C5), C05045. https://doi.org/10.1029/2006JC003581

Arndt, Sandra, Lacroix, G., Gypens, N., Regnier, P., & Lancelot, C. (2011). Nutrient dynamics and phytoplankton development along an estuary–coastal zone continuum: A model study. *Journal of Marine Systems*, *84*(3), 49–66. https://doi.org/10.1016/j.jmarsys.2010.08.005

Bruesewitz, D. A., Gardner, W. S., Mooney, R. F., Pollard, L., & Buskey, E. J. (2013). Estuarine ecosystem function response to flood and drought in a shallow, semiarid estuary: Nitrogen cycling and ecosystem metabolism. *Limnol. Oceanogr*, *58*(6), 2293–2309.

Cole, J. J., Caraco, N. F., & Peierls, B. L. (1992). Can Phytoplankton Maintain a Positive Carbon Balance in a Turbid, Freshwater, Tidal Estuary? *Limnology and Oceanography*, *37*(8), 1608–1617. https://doi.org/10.2307/2838056

Collins, M., R. Knutti, J. Arblaster, J.-L. Dufresne, T. Fichefet, P. Friedlingstein, X. Gao, W.J. Gutowski, T. Johns, G. Krinner, M. Shongwe, C. Tebaldi, A.J. Weaver and M. Wehner, (2013): Long-term Climate Change: Projections, Commitments and Irreversibility. In: *Climate Change 2013: The Physical Science Basis. Contribution of Working Group I to the Fifth Assessment Report of the Intergovernmental Panel on Climate Change* [Stocker, T.F., D. Qin, G.-K. Plattner, M. Tignor, S.K. Allen, J. Boschung, A. Nauels, Y. Xia, V. Bex and P.M. Midgley (eds.)]. Cambridge University Press, Cambridge, United Kingdom and New York, NY, USA.

Church, J.A., P.U. Clark, A. Cazenave, J.M. Gregory, S. Jevrejeva, A. Levermann, M.A. Merrifield, G.A. Milne, R.S. Nerem, P.D. Nunn, A.J. Payne, W.T. Pfeffer, D. Stammer and A.S. Unnikrishnan, (2013): Sea Level Change. In: *Climate Change 2013: The Physical Science Basis. Contribution of Working Group I to the Fifth Assessment Report of the Intergovernmental Panel on Climate Change* [Stocker, T.F., D. Qin, G.-K. Plattner, M. Tignor, S.K. Allen, J. Boschung, A. Nauels, Y. Xia, V. Bex and P.M. Midgley (eds.)]. Cambridge University Press, Cambridge, United Kingdom and New York, NY, USA.

Day, R. H., Williams, T. M., & Swarzenski, C. M. (2007). Hydrology of Tidal Freshwater Forested Wetlands of the Southeastern United States. In *Ecology of Tidal Freshwater Forested Wetlands of the Southeastern United States* (pp. 29–63). Springer Netherlands.

Destouni, G., Hannerz, F., Prieto, C., Jarsjö, J., & Shibuo, Y. (2008). Small unmonitored near-coastal catchment areas yielding large mass loading to the sea. *Global Biogeochemical Cycles*, *22*(4), n/a-n/a. https://doi.org/10.1029/2008GB003287

Doyle, T. W., O'Neil, C. P., Melder, M. P. V., From, A. S., & Palta, M. M. (2007). Tidal Freshwater Swamps of the Southeastern United States: Effects of Land Use, Hurricanes, Sea-level Rise, and Climate Change. In *Ecology of Tidal Freshwater Forested Wetlands of the Southeastern United States* (pp. 1–28). Springer Netherlands. Retrieved from http://link.springer.com/chapter/10.1007/978-1-4020-5095-4_1

Ensign, S. H., Doyle, M. W., & Piehler, M. F. (2013). The effect of tide on the hydrology and morphology of a freshwater river: TIDAL RIVER HYDROLOGY AND MORPHOLOGY. *Earth Surface Processes and Landforms*, *38*(6), 655–660. https://doi.org/10.1002/esp.3392

Evans, A., Madden, K., & Morehead Palmer, S. (2012). *The Ecology and Sociology of the Mission-Aransas Estuary: an estuarine and watershed profile*. Port Aransas, TX: Mission-Aransas National Estuarine Research Reserve. Retrieved from http://www.missionaransas.org/pdf/Mission-Aransas_NERR_Site_Profile_11062012_web.pdf

Findlay, S., Pace, M., & Lints, D. (1991). Variability and transport of suspended sediment, particulate and dissolved organic carbon in the tidal freshwater Hudson River. *Biogeochemistry*, *12*(3), 149–169. https://doi.org/10.1007/BF00002605

Ganju, N. K., Schoellhamer, D. H., Warner, J. C., Barad, M. F., & Schladow, S. G. (2004). Tidal oscillation of sediment between a river and a bay: a conceptual model. *Estuarine, Coastal and Shelf Science*, *60*(1), 81–90. https://doi.org/10.1016/j.ecss.2003.11.020

Johnson, S. L. (2009). *A general method for modeling coastal water pollutant loadings* (Ph.D.). The University of Texas at Austin, United States -- Texas. Retrieved from http://search.proquest.com/docview/856598483/abstract?accountid=7118

Jones, A. E., Hodges, B. R., McClelland, J. W., Hardison, A. K., & Moffett, K. B. (2017). Residence-time-based classification of surface water systems. *Water Resources Research*. https://doi.org/10.1002/2016WR019928

Knights, D., Sawyer, A. H., Barnes, R. T., Musial, C. T., & Bray, S. (2017). Tidal controls on riverbed denitrification along a tidal freshwater zone: Tides on Riverbed Denitrification. *Water Resources Research*, *53*(1), 799–816. https://doi.org/10.1002/2016WR019405

Lovley, D. R., & Phillips, E. J. P. (1986a). Availability of Ferric Iron for Microbial Reduction in Bottom Sediments of the Freshwater Tidal Potomac River. *Applied and Environmental Microbiology*, *52*(4), 751–757. Retrieved from http://aem.asm.org/content/52/4/751

Lovley, D. R., & Phillips, E. J. P. (1986b). Organic Matter Mineralization with Reduction of Ferric Iron in Anaerobic Sediments. *Applied and Environmental Microbiology*, *51*(4), 683–689.

Mooney, R. F., & McClelland, J. W. (2012). Watershed Export Events and Ecosystem Responses in the Mission–Aransas National Estuarine Research Reserve, South Texas. *Estuaries and Coasts*, *35*(6), 1468–1485. https://doi.org/10.1007/s12237-012-9537-4

Neumann, B., Vafeidis, A. T., Zimmermann, J., & Nicholls, R. J. (2015). Future Coastal Population Growth and Exposure to Sea-Level Rise and Coastal Flooding - A Global Assessment. *PLOS ONE*, *10*(3), e0118571. https://doi.org/10.1371/journal.pone.0118571

Odum, W. E. (1988). Comparative Ecology of Tidal Freshwater and Salt Marshes. *Annual Review of Ecology and Systematics*, *19*, 147–176. https://doi.org/10.2307/2097151

Palmer, T. A., Montagna, P. A., Pollack, J. B., Kalke, R. D., & DeYoe, H. R. (2011). The role of freshwater inflow in lagoons, rivers, and bays. *Hydrobiologia*, *667*(1), 49–67. https://doi.org/10.1007/s10750-011-0637-0

Pollack, J., Kim, H.-C., Morgan, E., & Montagna, P. (2011). Role of Flood Disturbance in Natural Oyster (Crassostrea virginica) Population Maintenance in an Estuary in South Texas, USA. *Estuaries and Coasts*, *34*(1), 187–197. https://doi.org/10.1007/s12237-010-9338-6

Ropelewski, C. F., & Halpert, M. S. (1986). North American Precipitation and Temperature Patterns Associated with the El Niño/Southern Oscillation (ENSO). *Monthly Weather Review*, *114*(12), 2352–2362. https://doi.org/10.1175/1520-0493(1986)114<2352:NAPATP>2.0.CO;2

Savenije, H. H. G. (2005). *Salinity and tides in alluvial estuaries* (1st ed). Amsterdam ; Boston: Elsevier.

Scavia, D., Field, J. C., Boesch, D. F., Buddemeier, R. W., Burkett, V., Cayan, D. R., … Titus, J. G. (2002). Climate Change Impacts on U. S. Coastal and Marine Ecosystems. *Estuaries*, *25*(2), 149–164. Retrieved from http://www.jstor.org/stable/1353306

Sheldon, J. E., & Alber, M. (2002). A comparison of residence time calculations using simple compartment models of the Altamaha River estuary, Georgia. *Estuaries*, *25*(6), 1304–1317. https://doi.org/10.1007/BF02692226

Shen, J., & Haas, L. (2004). Calculating age and residence time in the tidal York River using three-dimensional model experiments. *Estuarine, Coastal and Shelf Science*, *61*(3), 449–461. https://doi.org/10.1016/j.ecss.2004.06.010

Wang, C.-F., Hsu, M.-H., & Kuo, A. Y. (2004). Residence time of the Danshuei River estuary, Taiwan. *Estuarine, Coastal and Shelf Science*, *60*(3), 381–393. https://doi.org/10.1016/j.ecss.2004.01.013

Wolter, K., Dole, R. M., & Smith, C. A. (1999). Short-term climate extremes over the continental United States and ENSO. Part I: Seasonal temperatures. *Journal of Climate; Boston*, *12*(11), 3255–3272. Retrieved from https://search-proquest-com.ezproxy.lib.utexas.edu/docview/222898488?pq-origsite=summon

Yankovsky, A. E., Torres, R., Torres-Garcia, L. M., & Jeon, K. (2012). Interaction of Tidal and Fluvial Processes in the Transition Zone of the Santee River, SC, USA. *Estuaries and Coasts*, *35*(6), 1500–1509. https://doi.org/10.1007/s12237-012-9535-6

Chapter 2*:
Residence-time-based classification of surface water systems

ABSTRACT

Defining surface water systems as lentic or lotic is an important first step in linking hydrology and ecology. Existing approaches for classifying surface water as lentic (reservoir-like) or lotic (river-like) use qualitative observations, solitary snapshot measurements in time and space, or ecologic metrics that are not broadly repeatable. This study introduces the Freshwater Continuum Classification (FCC), a quantitative method to consistently and objectively classify lentic/lotic systems based on integrated residence time (iT_R), the time incoming water would take to exit the system given observed temporal variations in the system's discharge and volume. Lentic/lotic classification is determined from comparison of median iT_R with critical flow thresholds related to key timescales such as zooplankton generation. Some systems switch between lentic and lotic behaviors over time, which are additionally defined in the FCC as *oscillic*. Pilot application of the FCC to 15 tidally influenced river segments along the Texas Gulf Coast produced good agreement with previous methods of determining lentic/lotic character. The FCC defined 8 of 15 tidal reaches as primarily lentic, 6 as intermediate, and 1 as lotic between October 2007 and March 2015. Of the 15 reaches, 9 were also oscillic, characterized in this climate by short-lived lotic character during flash floods. The FCC provides a broadly applicable, repeatable, quantitative method to classify surface water bodies as lentic/intermediate/lotic

* As stated in Chapter 1, the work presented in Chapter 2 has been published by the American Geophysical Union (AGU) in the Water Resources Research journal. I worked with collaborators to develop the *oscillic* terminology. I also performed much of the analysis and writing with assistance from Dr. Kevan B. Moffett.

Jones, A. E., B. R. Hodges, J. W. McClelland, A. K. Hardison, and K. B. Moffett (2017), *Residence-time-based classification of surface water systems*, Water Resour. Res., 53, 5567–5584, doi:10.1002/ 2016WR019928.

and oscillic/nonoscillic regardless of size or nature (e.g., river or reservoir) based on system volume and flow characteristics.

2.1 INTRODUCTION

2.1.1 Importance of distinguishing lentic vs. lotic behavior

In aquatic ecology, terrestrial surface waters are generally classified in a Boolean manner, as either *lentic* or *lotic* [*Adebisi*, 1981; *Pellett et al*., 1983; *Soballe and Kimmel*, 1987; *Baranyi et al*., 2002; *Hein et al*., 2003]. *Lentic* surface water bodies are effectively reservoir-like and exhibit minimal advective transport. *Lotic* surface water bodies act riverine and are typically dominated by advective transport. Although the *lentic* and *lotic* descriptors do not account for salinity, the terms have been primarily applied to fresh surface waters, but may be applicable to terrestrial surface waters with a variety of salinity conditions (e.g., an inland saline lake). However, for simplicity, we will primarily discuss the application of *lentic* and *lotic* to freshwaters. The lentic/lotic classification organizes aquatic systems by flow characteristics that are of ecologic relevance. However, droughts, flash flooding, and tidal interactions in lowland systems, or non-temperate or non-humid climates, can create behaviors that fall between the lentic/lotic divide and include temporal dependence. Additionally, humans are increasingly impacting waterways through reservoir construction, wastewater treatment plant (WWTP) discharges, increased diversions, and managed hydrology, which alter the discharge regime of freshwaters and ultimately disrupt these systems' biota [*Stanley et al*., 1990; *Mooney and McClelland*, 2012].

Classifying flowing freshwater systems (e.g., rivers, lakes, and reservoirs) by their physical dynamics helps to generalize how these dynamics influence biogeochemical cycling, species assemblages and interspecific interactions within the aquatic environment [*Soballe and Kimmel*, 1987; *Baranyi et al*., 2002; *Hein et al*., 2003; *Monsen et al*., 2002]. Hydrologic conditions exert significant influence on aquatic ecosystem species composition (e.g., *Basu and Pick* [1996], *Baranyi et al.* [2002], *Rennella and Quirós* [2006]). Biogeochemical rates are often compared against hydrologic conditions,

specifically water retention times, to predict ecologic population dynamics [*Monsen et al*., 2002]. The first step to comprehensively understanding the biogeochemistry and ecology of freshwater systems is to characterize their relevant hydrologic properties (i.e., whether lentic or lotic based upon discharge regime, which relates to advective transport) [*Benke et al*., 2000].

To accurately and consistently classify fresh surface water systems, improvements are needed to the current two-endmember framework of wholly lentic or wholly lotic assignments. In any given system, the variability of water flow, whether via natural or anthropogenic flow controls, may cause the system to switch between lentic and lotic conditions at different times [*Rennella and Quirós*, 2006; *Adebisi*, 1981; and *Vegas-Vilarrúbia and Herrera*, 1993]. This observation has been made before, e.g., Soballe and Kimmel [1987] proposed shifting the classification scheme from discrete observational definitions toward a continuum. However, prior works have not developed quantitative methodologies accounting for temporal flow variability, which is a necessary first step toward a hydrologic classification continuum. This study derives a quantitative framework for classifying freshwaters as primarily lentic, intermediate, or lotic based on integrated residence time (iT_R), a metric that incorporates transient system discharge and volume to quantify the impact of temporal hydrologic variability on water transport. The framework also explicitly represents the range of system variability, defining that a system is *oscillic*, regardless of its typical lentic/lotic classification, if it achieves both lentic and lotic endmembers, e.g., as caused by flood or drought, for at least some time during the study interval of interest, e.g., a week, a month, a season, or a year. We call this new quantitative classification model the Freshwater Continuum Classification (FCC).

2.1.2 Present use of *lentic* and *lotic* in the literature

Several studies distinguish lentic and lotic freshwater bodies via a flow rate threshold. Pellett et al. [1983] defined the boundary between lentic and lotic conditions as 0.10 m s^{-1}, with velocity less than this threshold representing lentic systems. Andersen and Shafroth [2010] approximated the threshold velocity as 0.20 m s^{-1}, because it is the minimum velocity at which a sand particle resting on the streambed will move. Baranyi et al. [2002] discussed the velocity of 0.40 m s^{-1} as a possible ecologically significant threshold, initially proposed by Rzoska [1978], as the velocity above which zooplankton reproduction is not supported. Buffagni et al. [2009] created the Lentic-lotic River Descriptor (LRD) model, which uses laminar flows as a key factor to indicate lentic systems and turbulent flows to suggest lotic behavior. More qualitatively, Adebisi [1981] studied seasonal oscillations of water depth in the upper Ogun River in Nigeria, associating lotic conditions with greater water depths and their faster flow rates. The lack of consistency regarding the designation of lentic and lotic environments signifies the need for a broadly applicable, objective, and repeatable classification framework.

Water residence time has been used as an ecologically significant index of a water body's function [*Soballe and Kimmel*, 1987]. A river's residence time has greater control on zooplankton biomass than the availability of resources; in contrast, a lake's longer residence time promotes biomass control by resource availability [*Basu and Pick*, 1996; *Pace et al*., 1992]. High flushing rate, or low residence time, has been proposed as a major factor governing the species composition of phytoplankton communities [*Dickman*, 1969]. These ideas were supported by Soballe and Kimmel [1987], who found that water residence time in 345 US water bodies acts as a significant indicator of the influence of hydrodynamics on a system's biota. Flow regime and downstream transport, encompassed in residence time measurements, exert a significant control over downstream ecology

[*Soballe and Kimmel*, 1987; *Thorp et al.*, 2006; *Humphries et al.*, 2014; *Adebisi*, 1981] and floodplain aquatic biomass [*Baranyi et al.*, 2002].

Relatively short residence times have been previously proposed as a threshold indicator for distinguishing lentic and lotic behavior. For example, Rennella and Quirós [2006] used a residence time threshold of 15 days in the Carpincho and Gomez lakes of the Pampa Plain, Argentina. Unfortunately, such simple residence time thresholds appear to be either system- or species-specific, as Bledzki and Ellison [2000] found that a 6-day residence time was appropriate for discriminating between lentic and lotic zooplankton biomass behaviors for the Wloclawek Dam Reservoir (Poland) and the Upper Lake (South Hadley, Massachusetts, USA) systems. At the extreme end of the lentic/lotic continuum, residence time in years for lakes has been noted as a key lentic feature [*Krawczyk et al*., 2013, by *Rasmussen et al*., 1989].

As a further complication, water residence time is also affected by hydrologic network connectivity and may have a temporal character. For example, Hein et al. [2003] calculated velocities of less than 0.01 m s^{-1} and a water age of more than 6 days during time periods of hydrologically disconnected lentic behavior on the Regelsbrunn floodplain in Austria. Similarly, Baranyi et al. [2002] determined that lentic and lotic conditions on the Regelsbrunn floodplain were separated by water residence times of 7 days, although the maximum water residence time observed was 39 days. Although it is clear that residence time encapsulates the relationship between hydrologic dynamics and ecologic effects, the previously reported residence time thresholds are site- and time-specific and cannot be used for broader understanding of the lentic/lotic classifications.

As an alternative to residence time, ecologic productivity and species composition have been used to discriminate between lentic and lotic systems. In general, high freshwater zooplankton biomass is related to lentic, or lake-like environments, while low biomass is

indicative of lotic, or riverine environments [*Basu and Pick,* 1996]. Benke et al. [2000] referred to the invertebrate assemblage of a river changing from “lentic taxa” to “lotic taxa” as discharge increases. Basu and Pick [1996] observed rotifers to be more populous in lake environments, and Benenati et al. [2000] expected declines in *Cladocera* with increased lotic velocity. Hoffsten and Malmqvist [2000] used predetermined lentic and lotic taxa assemblages to predict the sources of species measured in a glaciofluvial spring. Unfortunately, similar to prior work with residence time thresholds, the taxonomic associations are necessarily site- or time-specific and have not yet been developed into broadly applicable system classification methods.

It is clear that several issues exist with the present usage of lentic/lotic terminology, most prominently that quantitative definitions based on threshold velocities are inconsistent across systems and do not seem to be reconcilable. In addition, those same threshold velocity definitions fail to incorporate long-term hydrologic variation in to their determination of lentic/lotic character. Regular oscillations in physical conditions can have important impacts on adaptations and life history of in-stream biota [*Thorp et al*., 2006; *Humphries et al*., 2014]. For example, a rapid decrease in residence time may promote the advective loss of species biomass [*Basu and Pick,* 1996; *Pace et al.*, 1992].

In addition to inconsistent definitions and velocity thresholds, many studies report systems that oscillate between apparent lentic and lotic character depending upon recent hydrologic conditions [*Rennella and Quirós*, 2006; *Vegas-Vilarrúbia and Herrera*, 1993; *Adebisi*, 1981; *Hein et al*., 2003; *Ward et al*., 2002; and *Baranyi et al*., 2002]. These oscillations may be either related to regular and predictable seasonal shifts in hydrologic regime, or to sporadic, rapid responses to specific hydrologic events. Adebisi [1981] identified seasonally oscillating lentic and lotic nature along the Ogun River in Nigeria and reported similar results in two other Nigerian rivers. Rennella and Quirós [2006] observed

oscillations from lentic to lotic conditions annually as the climate shifted from a dry to a wet year in Argentina. Hein et al. [2003] and Baranyi et al. [2002] observed lotic conditions after summer flooding events in Austria. Soballe and Kimmel [1987] discussed the need for a new way to characterize "transitional lentic systems," i.e., systems that act primarily lentic, yet experience regular flushing (lotic) conditions, within a "continuum [of] water residence time" values. Ward et al. [2002] describe "semi-lotic" geomorphologic features that "frequently alternat[e] between lentic and lotic conditions." However, a new characterization that consistently encompasses these interesting temporally variable conditions has yet to materialize in the literature. Benenati et al. [2000] also called for increased study of lentic/lotic interactions, specifically where the two systems meet, e.g., a river flowing into a reservoir (or other base-level water body such as the ocean), or a river leaving a reservoir or lake.

Understanding the interaction between lentic and lotic states, both temporally and spatially, will improve our understanding of hydrologic-ecologic links in freshwater systems. The quantitative FCC provides a foundation for establishing this link.

2.2 METHODS

2.2.1 System integrated residence time (iT_R)

Herein we develop and demonstrate a quantitative lentic/lotic classification framework based on a metric of the system's empirical discharge magnitude and variability. The new metric is the *integrated residence time* (iT_R). The iT_R metric captures aspects of the relationship between the cumulative discharge of a system and its time-varying volume, and the iT_R time series reflects temporal variability in modeled kinematic water transit time (average volume flushing time). Once calculated, the iT_R time series can be analyzed for improved characterization of a system's lentic/lotic behavior. To do so, we

propose the Freshwater Continuum Classification (FCC) approach, which compares the median iT_R for the time period of interest to critical lentic/lotic threshold values derived from the literature. These values are chosen to span the range of relevant ecologic (e.g., zooplankton reproduction), geomorphological, and hydrologic (e.g., minimum system connectivity) concerns and reflect the typical range of research interests related to lentic/lotic behavior.

It is worth emphasizing that the iT_R metric is fundamentally different from residence time (T_R) sometimes used in classifying a system's lentic/lotic nature (e.g., *Rennella and Quirós*, [2006]). T_R is often calculated by dividing the average system volume (V) by either the volumetric discharge at one point in time (Q_i) or the velocity at one point in time (q_i) through a given system cross-sectional area (A), i.e., $T_R = V/Q_i = V/(q_i A)$. This T_R value might then be considered representative for that point in time and space. A time series of T_R could be produced using concurrent time series of volume and discharge data. However, calculating T_R in this way can produce highly unrealistic "residence time" values. For example, the approximate median volume of the lower 30 km of the Cedar Bayou in semiarid south Texas, USA, is 1.15×10^7 m^3 (Table 2.1), and its median baseflow was 0.0935 $m^3 s^{-1}$ between October 2007 – March 2015. These minimal baseflow conditions would generate the implausible T_R value of 1423.55 days, or about 3.89 years. In reality, the residence time of surface water in the Cedar Bayou is governed by seasonal precipitation that peaks in May-June and September-October. Additionally, the system experiences increased annual rainfall (often as summer deluges) during the El Niño phase of the Southern Oscillation (ENSO) [*Fulbright et al.* 1990; *Ropelewski and Halpert*, 1986]. These precipitation peaks rapidly flush the river systems in this region and effectively reset the clock on the water residence time [*Mooney and McClelland*, 2012; *Johnson*, 2009]. This phenomenon, wherein a T_R calculation based on present discharge

	River names	Dates (MM/YYYY) of Available Data	Tidal Reach Length [km]	Median Discharge [$m^3 s^{-1}$]	Median Volume [m^3]	Median River Stage [m]	MSL Datum [m]	NOAA/TCOON Tidal Gauge ID	USGS NWIS Gauge ID
a	Nueces Rv	10/2009 to 03/2015	20.21	3.68E-01	1.24E+07	1.34	7.53	185 Nueces Bay	8211500
b	Aransas Rv	10/2007 to 03/2015	45.56	1.13E-01	3.40E+06	0.23	1.66	036 Copano Bay	8189700
c	Mission Rv	10/2007 to 03/2015	25.62	4.53E-02	1.31E+06	0.63	1.66	036 Copano Bay	8189500
d	Guadalupe Rv	10/2011 to 03/2015	16.39	1.08E+01	3.02E+06	3.04	3.62	057 Port O'Connor	8177520
e	Garcitas Ck	10/2007 to 03/2015	23.22	3.96E-02	3.16E+06	1.40	1.08	033 Port Lavaca	8164600
f	Lavaca Rv	10/2007 to 03/2015	36.99	3.96E-01	8.09E+06	1.56	1.08	033 Port Lavaca	8164000
g	Tres Palacios Rv	10/2007 to 03/2015	15.53	4.53E-01	1.19E+07	1.03	3.62	057 Port O'Connor	8162600
h	Colorado Rv	10/2007 to 03/2015	40.62	2.40E+01	3.06E+07	1.15	3.62	057 Port O'Connor	8162500
i	San Bernard Rv	10/2007 to 03/2015	54.21	1.02E+00	5.55E+07	0.98	8.60	152 USCG Freeport	8117500
j	Brazos Rv	10/2007 to 03/2015	38.86	5.13E+01	5.82E+07	1.95	8.60	152 USCG Freeport	8116650
k	Chocolate Bu	10/2007 to 03/2015	25.12	3.12E-01	8.69E+06	3.10	1.51	526 San Luis Pass	8078000
m	Cedar Bu	10/2007 to 03/2015	30.65	9.35E-02	1.15E+07	11.14	1.80	503 Morgan's Point	8067500
n	Trinity Rv	12/2007 to 02/2015	57.09	5.27E+02	1.84E+07	6.30	1.46	507 Eagle Point	8067000
o	Neches Rv	10/2007 to 03/2015	49.13	6.37E+01	2.77E+07	1.99	1.36	504 Rainbow Bridge	8041000
p	Sabine Rv	10/2007 to 03/2015	30.01	6.68E+01	2.46E+07	5.27	1.36	504 Rainbow Bridge	8030500

Table 2.1: The 15 Texas Gulf Coast tidal river systems analyzed, (Rv – River, Ck – Creek, Bu – Bayou) and gauging stations used in applying the Freshwater Continuum Classification methodology. Data references are [*USGS*, 2015], [*NOAA Tides & Currents*, 2015]. The Texas Commission on Environmental Quality (TCEQ) Surface Water Quality Viewer (SWQV) provided the tidal reach length information [*TCEQ*, 2015].

and system volume conditions may not reflect the system's actual hydrologic function, is not unique to south Texas or semiarid rivers. For this reason, it is necessary to have a residence time metric that encapsulates a longer period of climatic and hydrologic variation within each value of its time series, up to the point that the system volume might reasonably be expected to have been fully flushed; this is our *integrated residence time*, iT_R.

To calculate iT_R, the user must first choose their system of interest and time period of interest. For example, this could be a river reach (of defined length and known depth) or lake volume. The user must then obtain observations of both volume and discharge over the chosen time period. Typically the discharge time series may be obtained from a gauging station or continuous flow measurements at the upstream end of the volume of interest. The volume time series might be estimated in multiple ways. For example, in the simplest approach for a river reach, the channel cross-sectional shape could be approximated rectangularly at the upstream and downstream ends of the reach, stage monitored continuously at the upstream and downstream ends, and system volume approximated by linearly interpolating between the upstream and downstream reach cross-sectional areas (see example application in Section 3). If river reach bathymetry data are available, a much more detailed integration of reach volume could be calculated. For a lacustrine system, volume or bathymetry data may already be available. It is incumbent upon the users' discretion to define or obtain the system volume time series in a manner appropriate to their application. Since the FCC method flexibly accounts for imperfect characterization of the system volume (explained in Section 2.2.2), the volume need not be calculated to extremely high precision for the FCC categorization to be informative.

Figure 2.1 provides a simplified conceptual schematic of the iT_R calculation when applied to a steady-state volumetric time series ("Steady-State System Volume Time series" in Figure 2.1b) and a corresponding steady-state discharge time series ("Discharge

1" in Figure 2.1a). For a real segment, volume and discharge would almost certainly be time-varying not steady-state, but the figure is illustrative.

To calculate iT_R using discharge data from the upstream end of the segment, we first calculate the cumulative volume of discharge, V_{C0}, by integrating from a given point in time, t_0, through the succeeding discharge conditions from the discharge time series Q_j (i.e., forward-in-time integration of discharge). Conceptually, V_{C0} is like the total discharge that would come behind a parcel of water released from the upstream gauge point at time t_0. The iT_R metric, conceptually, is like the mean travel time of that parcel to reach the other end of the segment of interest; it is therefore calculated from the condition when V_{C0} equals the system volume V_j. The system volume, however, may change in time, so V_j is a time series; therefore, the condition is only met when, at some time t_n, the forward-in-time integration of Q_j *(for j=0 to n)* has accumulated exactly the volume V_{C0} (equal to $V_{j=n}$) such that:

$$V_{C0} = \int_{t_0}^{t_n} Q_j \, \partial t = V_{j=n} \quad (1)$$

The iT_{R0} related to discharge integration beginning at t_0 is then calculated as the difference between the integration bounds (Figure 2.1b).

$$iT_{R0} = t_n - t_0 \quad (2)$$

This process is repeated for each timestamp within the discharge time series to produce an iT_R time series. Essentially, the iT_R metric represents the theoretical mean time necessary to flush a parcel of water released from the upstream end of the segment through the entire system volume, given the succeeding volume and discharge conditions of the segment. Periods of increased discharge will shorten the calculated iT_R, and droughts lengthen it. This approach is arguably the simplest analytical framework that captures the time-varying system conditions without requiring numerical flow modeling.

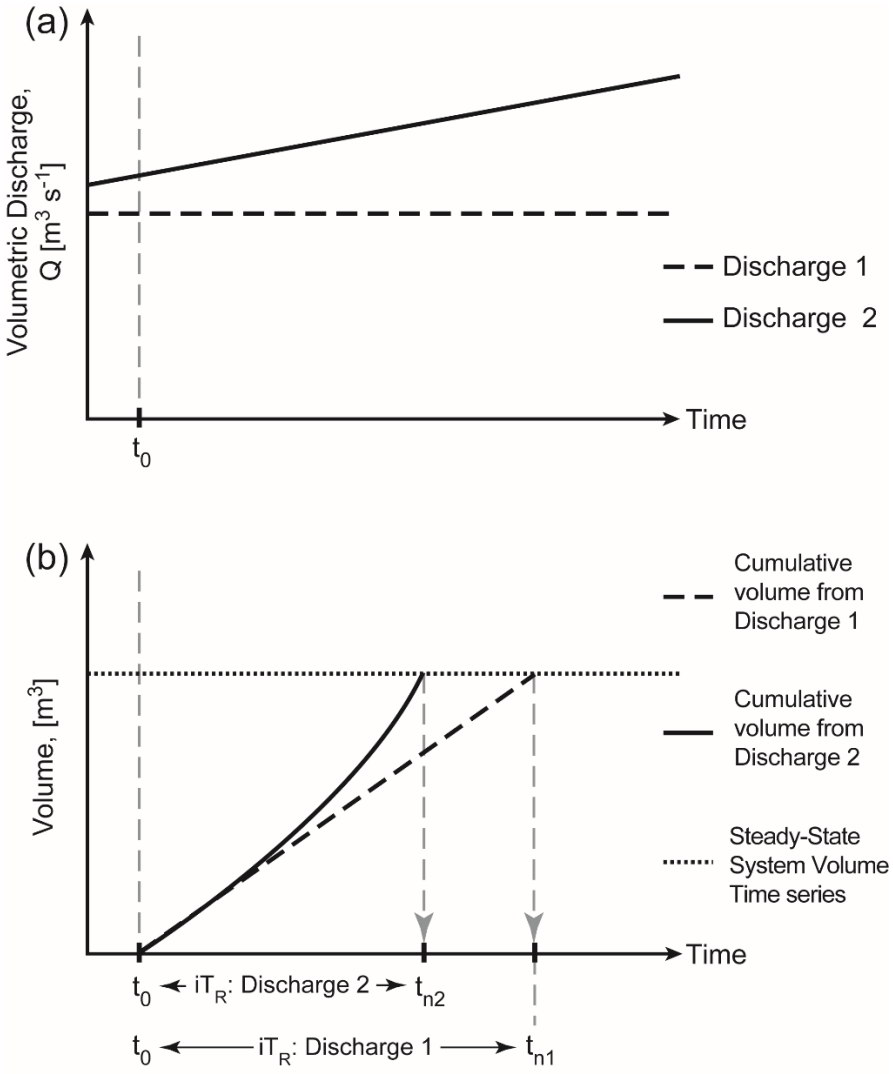

Figure 2.1: Schematic of one integrated residence time (iT_R) calculation beginning from a given t_0 and based on simplistic discharge and volume time series. (a) Two conceptual discharge time series: uniform discharge (dashed line), or gradually increasing discharge (solid line). (b) Identifying t_n: calculate a cumulative discharge volume (V_C) starting from a given time step, t_0, by integrating through succeeding discharge conditions until such time that V_C equals the system volume (V_j, dotted line) of the water body of interest; this is time t_n. The subscript number on t_n refer to the discharge time series (1 or 2) associated with that t_n value. The integrated residence time calculated for t_0 is then: $iT_R = t_n - t_0$. Note that in a natural system, the discharge and volume time series would both be more variable and the calculation therefore less simplistic.

Statistical descriptors obtained from the probability distribution of the iT_R time series can provide initial, qualitative insight into the lentic/lotic nature of the system. The median iT_R suggests the system's typical lentic/lotic conditions. The variability and potential oscillic nature of a system's hydrologic conditions are depicted by the width of the iT_R histogram. Conceptually, there are six general categories of possible iT_R distributions (Figure 2.2) within the overall continuum of possibilities. River systems with narrow iT_R distributions (A-C in Figure 2.2) should represent nonoscillic systems, while wide distributions D-F are likely to be oscillic. Systems exhibiting A and D distributions would likely be classified as lotic due to short median iT_R and the C and F distributions as lentic, with long median iT_R. Quantitatively and objectively determining a system's lentic/lotic and oscillic natures requires more detailed analyses of iT_R distribution statistics, as discussed below.

2.2.2 Determine lentic/lotic classification after accounting for volume effects

Because a larger system volume of interest (e.g., longer arbitrary reach length) will automatically produce a larger iT_R value, all else being equal, the interpretation of the iT_R metric must carefully account for the chosen total system volume. Many residence time studies define the study volume of interest via natural geographic or anthropogenic constraints, such as a lake or a dammed-reservoir [*Benenati et al*., 2000; *Krawczyk et al*., 2013; *Rennella and Quirós*, 2006], or a specified river reach [*Hein et al*., 2003; *Baranyi et al*., 2002; *Adebisi*, 1981]. If an analysis does not properly account for the dependence of iT_R on the bulk system volume, the analysis might provide unrealistic characterizations. For example, if a riverine study doubled the reach length of interest but maintained the same study location and with the same discharge, the study might observe a switch in system character from lotic to lentic, simply because it takes water longer to traverse a

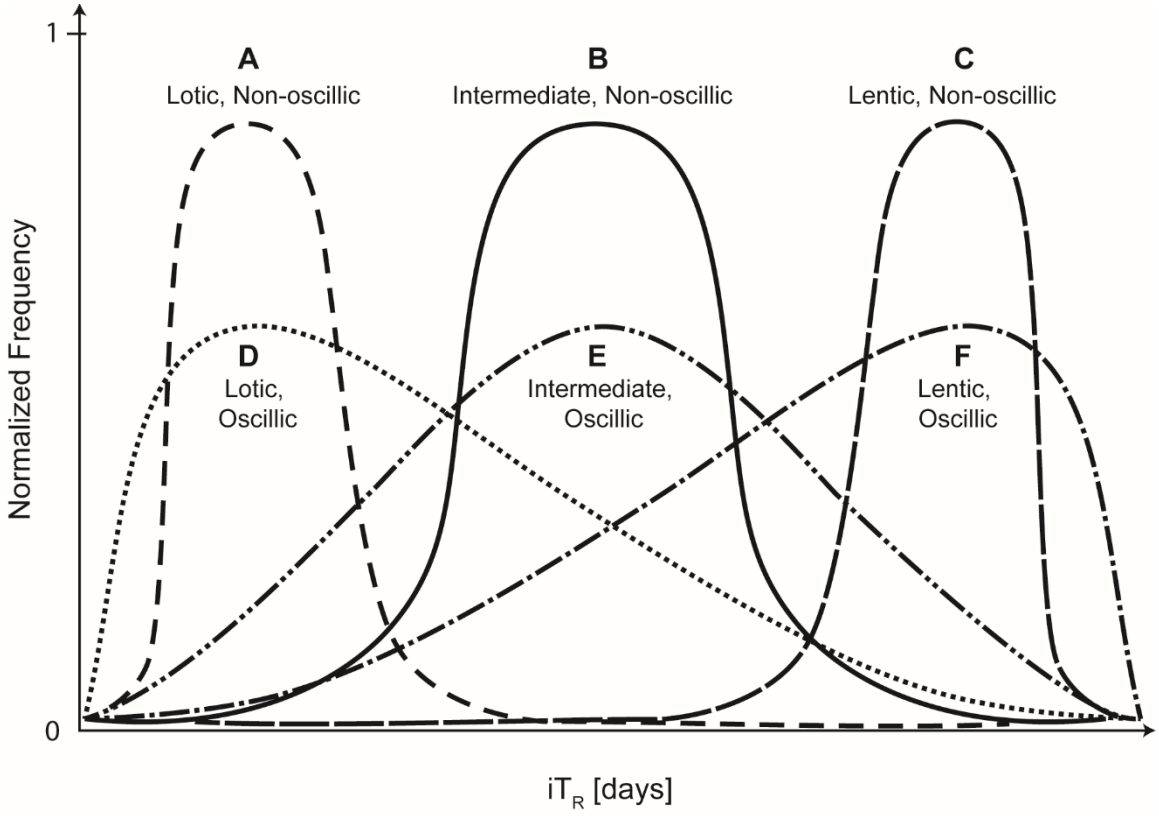

Figure 2.2: Conceptual iT_R distributions. There are six conceptual categories defining iT_R distributions within the overall continuum of possibilities. The narrow, less iT_R variable A-C distributions represent nonoscillic systems, while distributions D-F represent likely oscillic systems. Systems with larger iT_R and exhibiting distributions similar to F and C will be defined as lentic. Conversely, systems with distributions A and D are likely to be defined as lotic due to the shorter iT_R. The central B and E distributions will be classified as intermediate between lentic and lotic.

longer reach. The FCC's iT_R:volume scaling analysis solves this problem, maintaining system classifications essentially by considering the ratio of iT_R to volume, not just iT_R alone. In the FCC, a system's median iT_R is plotted against its median volume; then both metrics are analyzed with respect to iT_R:volume thresholds representing the broad range of limits of lentic/lotic character extrapolated from the literature for all possible water body volume conditions. This comparison orients the chosen system's typical conditions within the continuum of possible volumes and flow regimes in the natural world and avoids introducing bias into the classification from either the potential choice of a larger or smaller system volume or minor inaccuracies in the volume time series.

2.2.2.1 Calculating the iT_R threshold for all possible natural volumes

The FCC model requires specification of iT_R threshold values that discriminate between system types and apply across a natural range of system volumes. To respect prior definitions of lentic and lotic that depend upon observations of flow rate and ecologic indicators, we adopt a lotic threshold velocity of 0.40 m s^{-1} [Baranyi et al., 2002], representing a proposed upper limit for zooplankton reproduction. We adopt a lentic threshold of 0.01 m s^{-1} [Hein et al., 2003], a measured velocity within the lentic Regelsbrunn floodplain when hydrologically disconnected (i.e., no water-driven exchange of energy and matter between adjacent riverine corridors [Tockner et al., 2000]) from the lotic, primary Danube River. We categorize any flow velocity between these two limits as *intermediate*. These threshold velocities could be updated, if appropriate given future research, without altering the substance or method of the FCC method.

To overcome the potential volume bias, we extrapolated from these threshold velocities to calculate time-scale (iT_R) threshold values for systems spanning spatial scales from the largest to smallest riverine systems. A large volume endmember system was based

on the world's largest rivers (7.2×10^{12} m^3, from the Nile length ~6853 km, Amazon width ~4800 m, and Congo depth ~220 m), and a small volume endmember was set at 1 m^3. Lentic and lotic threshold velocities were converted into threshold volumetric flow rates using a system area ratio (which contrasts the average cross-sectional area to the cross-sectional area at the inflow, A_{avg}:A_{in}, respectively) of 60 and 1 for the large and small volume endmembers, respectively [*Trigg et al.*, 2009; *Sullivan*, 2013]. By assuming steady-state threshold volumetric discharge conditions, we calculated the lentic and lotic iT_R thresholds associated with each volume endmember. We interpolated each iT_R threshold's values between the two volume endmembers using a power law, yielding equations predicting the iT_R thresholds separating lentic and lotic system behaviors for any system size in the natural world (equations 2.3 and 2.4, respectively). (See Appendix A for further detail.) The power laws for the lentic and lotic iT_R thresholds, respectively, where $\tilde{V}$ represents the median system volume, are:

$$iT_{R,\ \text{Lentic threshold}} = 1.157 \times 10^{-3}\ (\tilde{V}^{\ 0.6699}) \tag{2.3}$$

$$iT_{R,\ \text{Lotic threshold}} = 2.894 \times 10^{-5}\ (\tilde{V}^{0.6699}) \tag{2.4}$$

These equations denote the lentic (orange diagonal line) and lotic (blue diagonal line) thresholds through iT_R vs. volume space shown in Figure 2.3a. It is critical to note that each system volume will have a unique pair of iT_R threshold values: substituting a system's median volume into equations 2.3 and 2.4 will yield that system's particular lentic and lotic iT_R thresholds, and thus enable the classification of the system.

Figure 2.3a conceptually depicts the placement of four systems' median iT_R and volume values with respect to the lentic and lotic iT_R thresholds. Systems S1, S2, and S3 have substantially different median volume, and fall into different regions in the lentic/intermediate/lotic classification space despite exhibiting similar iT_R values. However, if a system's volume is increased slightly (e.g., due to extending the designated

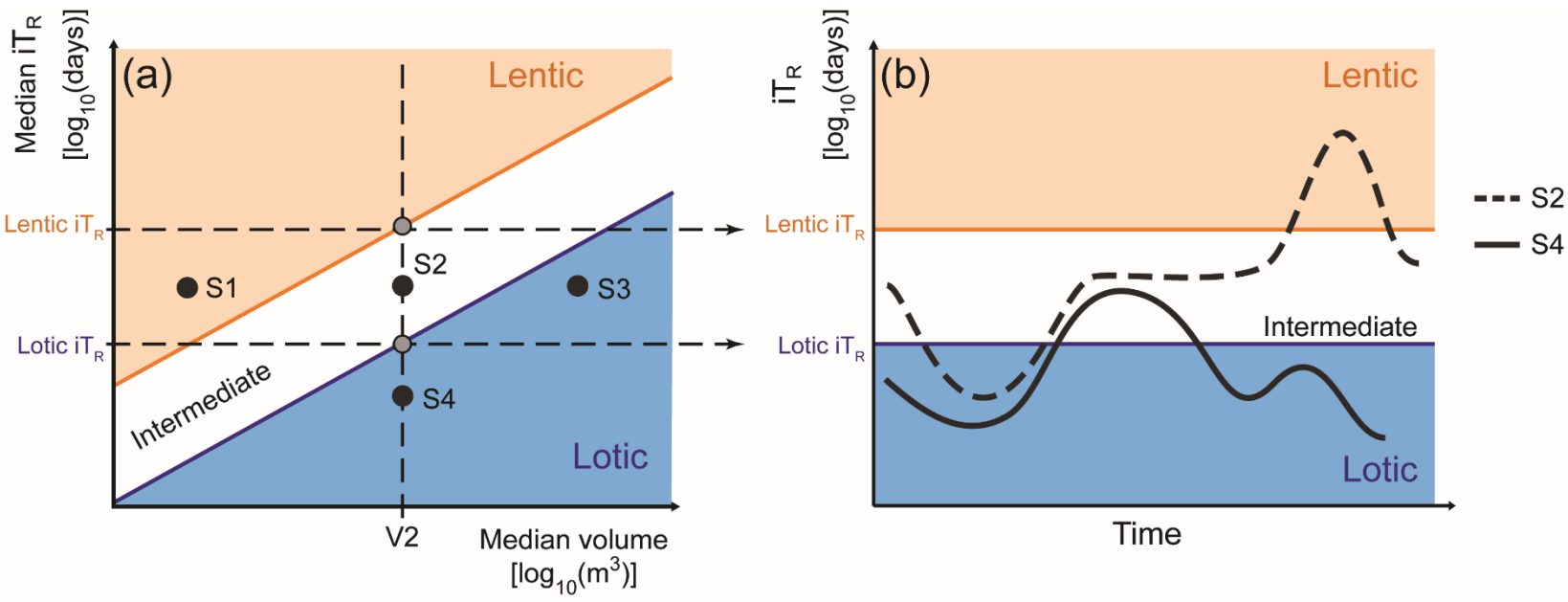

Figure 2.3: Schematic of FCC model determination of lentic/lotic and oscillic character. The process for quantitatively defining the system as lentic, intermediate, or lotic and as oscillic or nonoscillic begins with comparing the system's median iT_R to its median volume (a). For a given system volume, the threshold values of lentic and lotic residence time conditions (diagonal lines) are calculated from equations 2.3 and 2.4. The intersections of the median system volume with the lentic and lotic thresholds (gray dots) represents the minimum median iT_R for a system to be typically lentic, and the maximum median iT_R for it to be typically lotic. These thresholds can be compared to the more detailed iT_R time series (b) to determine if the system is oscillic over the analyzed time period; here, S2 is oscillic during the time period of interest, as it experiences iT_R conditions beyond both lentic and lotic thresholds, while S4 is nonoscillic during the time period of interest. Note that S1 and S3 are not included in (b) because they do not have the same median volume (and therefore do not have the same iT_R thresholds) as S2 and S4.

study reach a bit further downstream), the expected consequent increase in iT_R will shift the system up and to the right in Figure 2.3a, and not allow the volume change to significantly alter the "typical" classification of the system's character, unless the discharge regime is also altered. System S4 exhibits the same median volume (V2) as S2, but a substantially smaller median iT_R, resulting in the different lotic and intermediate classifications, respectively. However, because S2 and S4 exhibit the same median volume, these systems also share the same iT_R thresholds (gray dots in Figure 2.3a).

2.2.2.2 A caveat for iT_R time series and threshold calculations

For simplicity, the FCC uses only upstream discharge as an input, and the system model assumes volumetric discharge remains uniform throughout the system length; therefore, if the downstream cross-sectional area increases (typical of natural systems), the local flow velocity will be diminished. As the proposed approach does not include lateral inflows over the system length, the downstream velocity will generally be less than that observed at the upstream inflow. For lentic upstream conditions, a slower downstream velocity would not alter the water body's velocity-derived classification. However, a lotic inflow might transition to lentic downstream conditions, which makes the classification inconclusive. Users of the FCC are advised to check for this phenomenon in lotic systems and, if present, select a shorter reach or smaller system volume as the basic unit of study. In such a case, this insight into the appropriate discretization scale for study could be useful in itself. The FCC model can be modified to incorporate additional system information as shown in Appendix B.

In addition, although we believe the power-law thresholds (eqs. 3 and 4) are a robust starting point for classifying lentic/lotic behavior, we recognize that this initial framework may not immediately accurately reflect the lentic/lotic threshold conditions for

every natural system. However, because the volume-scaling approach to defining the thresholds does allow for the application of the FCC to all conceivable natural systems, we hope that continued use and updating of the FCC will iteratively improve the thresholds' accuracy.

2.2.3 Determining oscillic nature from system-specific iT_R thresholds

The classification framework based on median conditions (Figure 2.3a**)** identifies a typical system state, but does not describe possible temporal variability in that state. By comparing the system's iT_R time series with its iT_R thresholds (as determined specifically for its median volume from equations 2.3 and 2.4) any variable character of the system can be identified. If the system's iT_R time series crosses over both lentic and lotic thresholds within the time period chosen for the analysis (e.g., one year of discharge and volume data) then the system is defined as *oscillic* during that period.

For example, for the system S2 in Figure 2.3b, the iT_R threshold values are determined by projecting a vertical line through the median volume, V2, that intersects the lentic (orange) and lotic (blue/darker) threshold lines (or solving equations 2.3 and 2.4). The lentic and lotic iT_R thresholds values for system S2 (gray dots) can be translated to an iT_R time series plot (Figure 2.3b). Because the time series of iT_R conditions for S2 crosses both thresholds, the system is classified as *oscillic*. Because for S2 the median iT_R is between the lentic and lotic thresholds (Figure 2.3a), while the temporal variability of iT_R exceeds both thresholds (Figure 2.3b), a complete FCC model designation is *intermediate, oscillic*. In contrast, because S4 in Figure 2.3b does not cross both thresholds and has a median below the lotic iT_R threshold, it is classified as *lotic, nonoscillic*. Through the combination of the oscillic/nonoscillic and the lentic/intermediate/lotic nomenclature, a full classification is provided.

2.3 APPLICATION OF FRAMEWORK TO CLASSIFYING TEXAS COASTAL RIVERS

The following section describes the application of the FCC to 15 Texas coastal rivers. The objective of the FCC case study are threefold: (1) to compare the results of the FCC against those of other classification methods; (2) to identify oscillic nature in the Mission and Aransas Rivers (Buesewitz et al. [2013] and Mooney and McClelland [2012] observed potential oscillic indicators in these systems), as well as other Texas coastal rivers experiencing similar physiographic setting; and, (3) to determine which coastal rivers (typically thought to be lotic) may be impeded sufficiently by the tide and low baseflow discharges to typically exhibit lentic conditions. Additionally, these initial classifications inform preliminary predictions about potential ecologic factors present in these systems.

2.3.1 Study region and selected systems

The Texas coastal plain is situated along the western portion of the Gulf of Mexico. The coastline stretches from the border between the United States and Mexico in the southwest to the border between Texas and Louisiana in the northeast (Figure 2.4). The rivers discharging through the nearly flat Texas coastal plain experience a variety of climatic conditions [*Fulbright et al.*, 1990]. The region's subhumid to semiarid-subtropical climate presents extreme variability in precipitation (tropical storms, hurricanes, and drought) and strong seasonal oscillations in wind and temperature [*Evans et al.*, 2012; *Fulbright et al.*, 1990]. A North-South temperature gradient exists along the coastal plain. The southern region is characterized by high summer temperatures (33.3-35.6 ˚C) and mild winter temperatures (8.3-8.9 ˚C) [*Evans et al.*, 2012]. Perpendicular to the temperature gradient, an East-West precipitation gradient exists within the Texas Gulf Coastal Plain. Greater annual precipitation is observed in the east (142 cm yr^{-1}) than along the Mexican border (69 cm yr^{-1}) in the west [*Evans et al.*, 2012]. In the southwest of the coastal plain, where annual temperatures are the highest and precipitation is the lowest, extreme summer

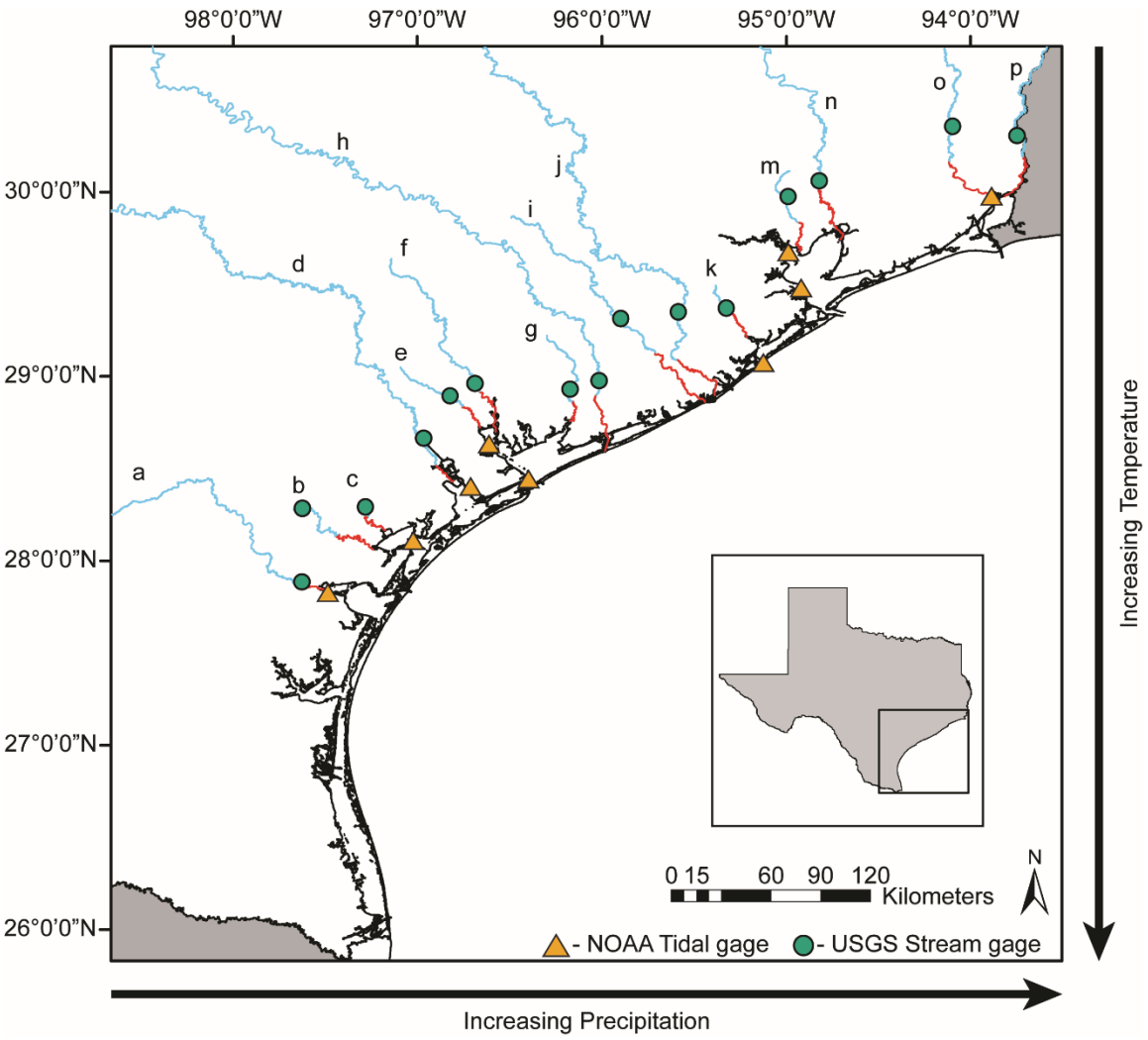

Figure 2.4: Map of Texas coastal study region and tidal river reaches. Letter labels correspond to the rivers listed in Table 2.1. Highlighted (red) reaches represent each river's analyzed tidal reach. The inset depicts the state of Texas with the study region in the black box.

evaporation may exceed local annual precipitation [*Evans et al*., 2012; *Ward*, 1997]. Several years of summer evaporation combined with poor rainfall will lead to drought conditions, decreased freshwater inflows, and potentially hypersaline estuaries. Drought conditions are a regular occurrence throughout much of the Texas Gulf of Mexico coastline [*Evans et al*., 2012; *Ward*, 1997]. However, the warm waters of the Gulf of Mexico in the summer bring the potential for large, sporadic rains associated with thunder storms, tropical storms and hurricanes. These events often promote flash flooding in the region and freshets into many of the coastal bays [*Mooney and McClelland*, 2012; *Bruesewitz et al*., 2013; *Pollack et al*., 2011].

The interaction of hydrologic dynamics and tides in the lower Coastal Plain river reaches is thought to play a role in the timing and magnitude of nutrient fluxes to the coastal ecosystems, and hence coastal productivity [*Mooney and McClelland*, 2012; *Arndt et al*., 2011; *Bruesewitz et al*., 2013; *Palmer et al*., 2011; *Pollack et al*., 2011]. The tidal river reaches along the Texas Coastal Plain represent a variety of discharge, volume, and tidal conditions [*Bruesewitz et al*., 2013; *Mooney and McClelland*, 2012; *Pollack et al*., 2011]. Texas's typical low-baseflow conditions and low-relief coastal plain are thought to allow for tidal forces to impede discharge and create more lentic conditions; however, extreme rainstorm events overcome the tidal forces and establish periods of net riverine nutrient export [*Bruesewitz et al*., 2013; *Mooney and McClelland*, 2012]. The wide array of climate, discharge, and complicating tidal conditions make this set of river reaches useful for testing the FCC method. A better understanding of the residence time regimes and system classifications of these river reaches is also needed to inform understanding of the coupled controls hydrology and riverine aquatic ecology exert on nutrient transport into the bays and estuaries.

The minimum data required to apply the FCC model to each river's tidally influenced segment were: tidal-influenced reach length, upstream stage, and downstream tidal stage (to approximate the volume time series of each river), and upstream discharge data (for calculating iT_R). The tidal reach length, median discharge, and volume data for the 15 river reaches analyzed are presented in Table 2.1. Tidal reach length data were obtained from the online Surface Water Quality Viewer module presented by the Texas Commission on Environmental Quality (TCEQ) [*TCEQ*, 2015]. Discharge and stage time series were obtained from United States Geological Survey (USGS) through their National Water Information System (NWIS) for each river's farthest downstream, non-tidal gauging station [*USGS*, 2015]. Most of the rivers' USGS data (discharge and river stage) spanned from October 2007 to March 2015 (Table 2.1). Harmonic tidal water level data were obtained from the Texas Coastal Ocean Observation Network (TCOON) network [*TCOON*, 2015], now available from the National Oceanic and Atmospheric Administration's (NOAA) Tides and Currents monitoring network [*NOAA Tides & Currents*, 2015].

In the absence of comprehensive bathymetric survey data, the tidally varying volumes of each river had to be estimated. We assumed the cross-sectional areas of the river reaches could be approximated as rectangular. While simplifying our calculations, the assumption of a rectangular cross-section may slightly overestimate the volume of each tidal river reach, which may mildly inflate the iT_R calculations toward more lentic conditions. We assumed the width of the river varied linearly from the upstream USGS gauging station to the river mouth. To estimate the water column depth along the river over time, we linearly interpolated between synchronous observations of stage at the USGS gauge and the river mouth. To simplify our calculations, we assumed the river mouth stage would reproduce the harmonic time series of the nearest NOAA tidal gauging station. From

the resultant volume time series spanning from gauge to mouth, we isolated the tidal segment of each river (as published by TCEQ) to use as the study reach volume time series. Table 2.1 summarizes the analyzed portions of the 15 Texas rivers. Figure 2.4 displays a map of the Texas coastline with the tidal river reaches of interest highlighted (red).

We used the discharge and volume time series to calculate iT_R (as in equations 2.1 and 2.2), and created iT_R histograms to compare against the theorized distributions from Figure 2.2. In creating the histograms, the iT_R results were binned into time-periods that reflected thresholds used in the literature and separated by logically spaced intervals. The bins were defined as follows: less than 1 hour, 1 - 6 hours, 6 - 12 hours, 12 hours - 1 day [*Basu and Pick*, 1996; *Rennella and Quirós*, 2006], 1 day - 1 week (7 days) [*Baranyi et al*., 2002; *Hein et al*., 2003; *Rennella and Quirós*, 2006; *Bledzki and Ellison*, 2000], 1 week - 1 month (30 days) [*Baranyi et al*., 2002; *Hein et al*., 2003], 1 - 3 months, 3 - 6 months [*Mooney and McClelland*, 2012], 6 months - 1 year (365.25 days) [*Rennella and Quirós*, 2006], 1 - 2 years, 2 - 5 years, 5 - 10 years [*Krawczyk et al.*, 2013], and greater than 10 years.

We calculated volume and iT_R medians for each Texas river and used each system's median volume, in equations 2.3 and 2.4 (section 2.2.1) to determine each river's lentic/lotic iT_R thresholds. We plotted these data as in Figure 2.3a and 3b to permit visual comparison among rivers and identify each river's lentic/intermediate/lotic and oscillic/nonoscillic nature (Figures 2.6 and 2.7, respectively).

2.3.2 Texas river iT_R results

A qualitative assessment of the iT_R time series from the 15 analyzed tidal reaches revealed that several systems appeared to exhibit highly variable residence time behavior (the Nueces, Aransas, Mission, Garcitas, Lavaca, Tres Palacios, San Bernard, Chocolate,

and Cedar systems), while a select few showed notably less variability (the Guadalupe, Trinity, Neches, and Sabine Rivers).

The systems' iT_R distributions (Figure 2.5) suggested that the 15 Texas tidal river reaches encompassed four of the six theoretical distributions from Figure 2.2. The Trinity River's tidal reach exhibited an 'A'-type distribution of relatively short iT_R conditions (6-12 hours) and little variability over the analyzed period of record (see Table 2.1). The narrow distributions of the tidal reaches of the Guadalupe, Neches and Sabine Rivers were indicative of the 'B'-distribution. These systems portrayed little variability and had somewhat longer iT_R times than the Trinity, on the order of days-to-a-week. The Colorado and Brazos Rivers' tidal reaches were perhaps characterized by the 'E'-distribution; however, visual inspection was insufficient for discrimination between oscillic/nonoscillic behavior for these rivers, instead requiring quantitative analysis of iT_R variability. The nine 'F'-distributions exhibited much longer iT_R medians, on the order of a few months, but also all exhibited greater variability and so wider distributions than the tidal reaches with shorter residence times.

2.3.3 Texas river lentic/lotic and oscillic classifications

We used the FCC model to quantitatively assess the median iT_R conditions and median volume for each of the 15 river systems relative to the critical lentic/lotic thresholds (Figure 2.6). We classified eight lentic systems (Nueces, Aransas, Mission, Garcitas, Lavaca, Tres Palacios, Chocolate, and Cedar), six intermediate systems (Guadalupe, Colorado, San Bernard, Brazos, Neches, and Sabine) and one lotic system (Trinity). These classifications describe each system's typical conditions during the ~3.5-7.5 years of records analyzed.

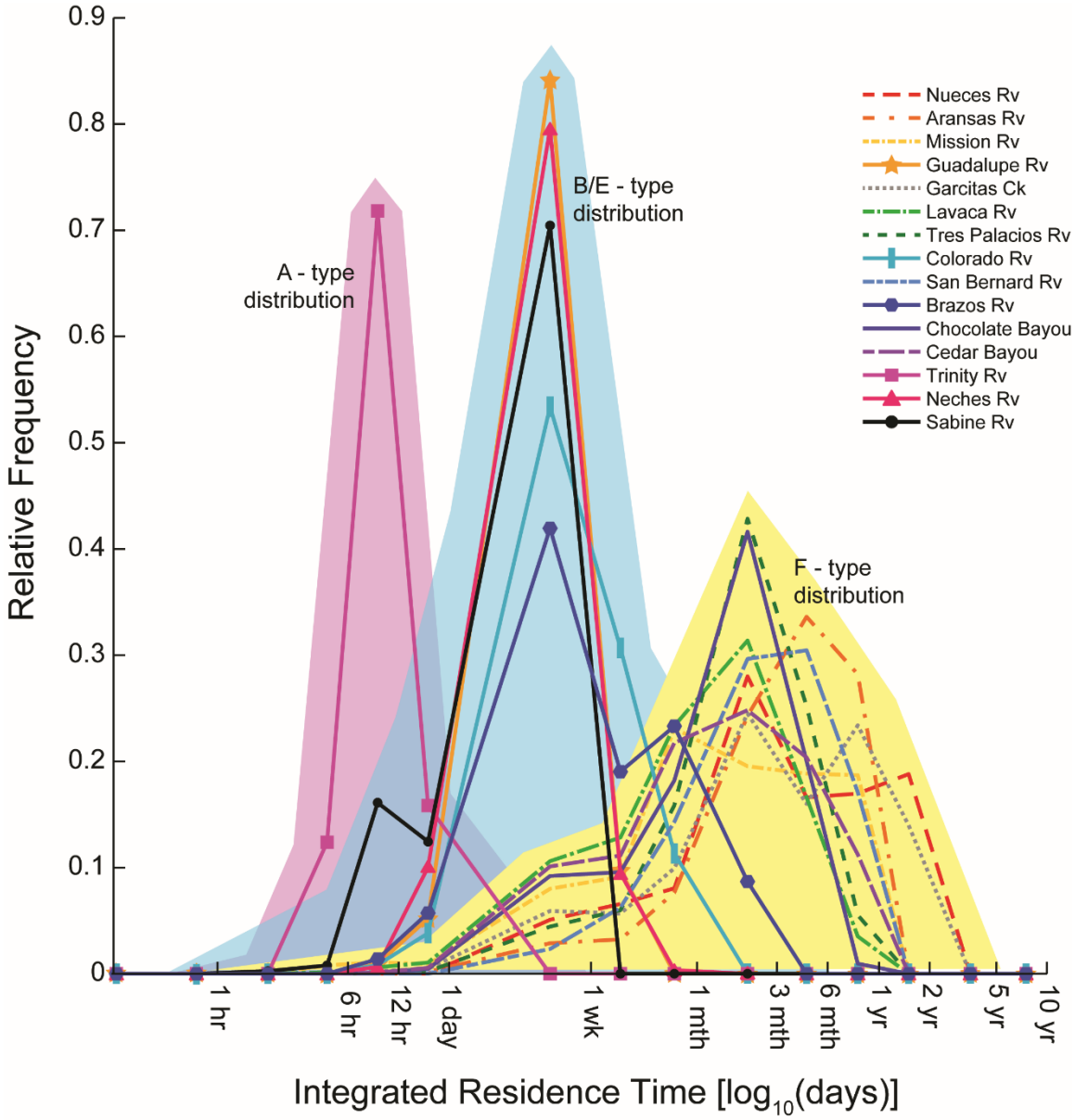

Figure 2.5: Texas rivers' tidal reaches' integrated residence time (iT_R) distributions. The iT_R distributions of the analyzed tidal river reaches cluster into the 'A'-, 'B'-, 'E'- and 'F'-type conceptual distributions from Figure 2.2.

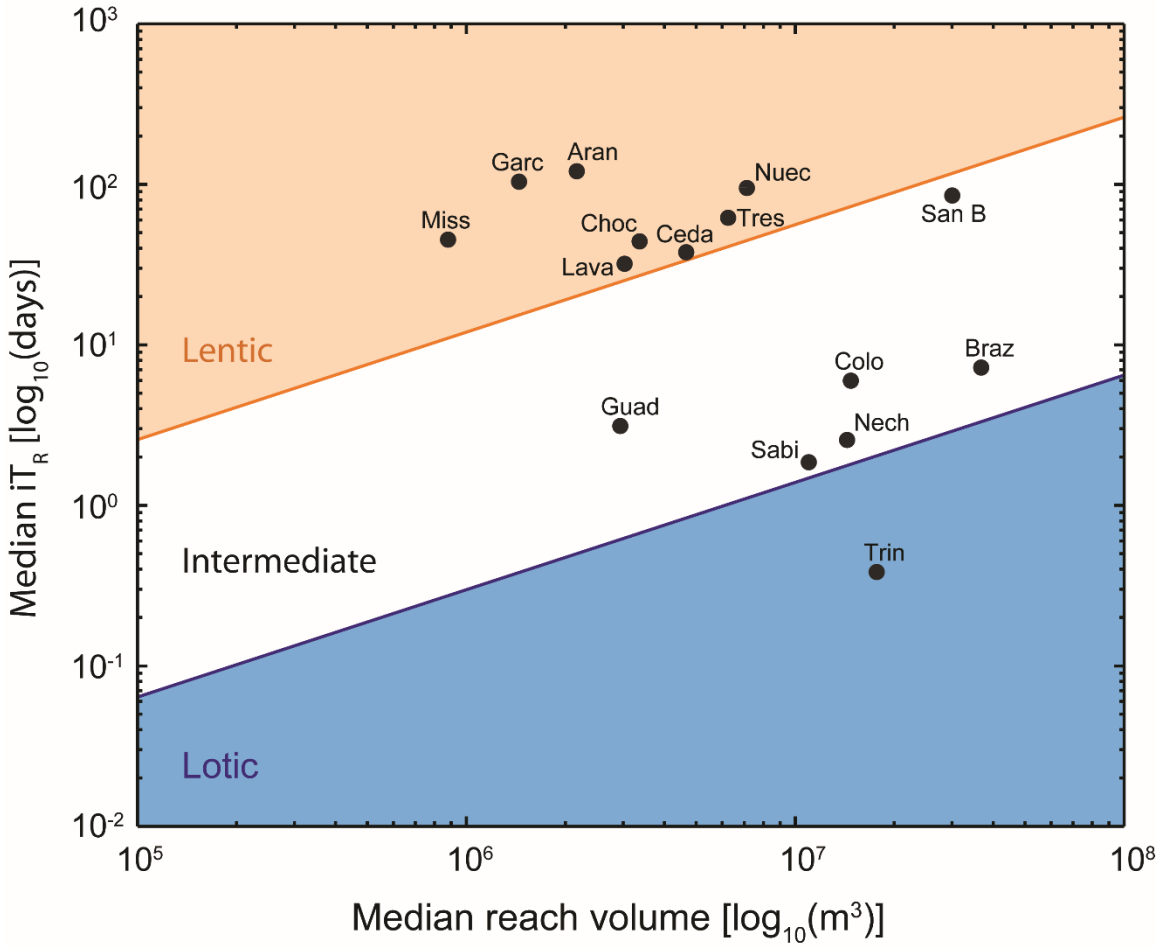

Figure 2.6: Lentic/intermediate/lotic classification of 15 Texas rivers' tidal reaches according to the Freshwater Continuum Classification (FCC) approach.

All of the lentic systems and one intermediate system (from group 'F' in Figure 2.5) exhibited high variability in hydrologic conditions, sufficient to have a maximum iT_R longer than the lentic threshold and a minimum iT_R shorter than the lotic thresholds during the time period of interest, as illustrated in Figure 2.7. These systems (Nueces, Aransas, Mission, Garcitas, Lavaca, Tres Palacios, San Bernard, Chocolate, and Cedar) were therefore classified as *oscillic* over their analyzed time period of record.

The remaining five intermediate systems (Guadalupe, Colorado, Brazos, Neches and Sabine Rivers, associated with 'B'- and 'E'- type distributions in Figures 2.2 and 2.5) were quantitatively determined to be nonoscillic during the period analyzed (Figure 2.7). The iT_R of these systems showed little variability and fluctuated only between lotic and intermediate conditions. The one lotic river reach (the Trinity) was also nonoscillic.

2.4 DISCUSSION

2.4.1 Freshwater Continuum Classification assessment

To be of greatest and broadest use, a method for linking hydrology and aquatic ecology system characterizations should be broadly applicable, quantitative, and repeatable and should define a system's lentic/lotic behavior based on objective physical parameters and relevant ecologic indicators, while incorporating the time variable aspect of surface water bodies. Through the use of the iT_R, the FCC meets these criteria and should be applicable to all freshwater environments, including rivers of any size and natural or man-made flow-through impoundments such as lakes and reservoirs. The FCC framework is created so the ecologically relevant lentic and lotic thresholds are quantitatively scaled to account for the effects of different systems' volumes in a logical manner. Also, these thresholds may be easily modified to reflect new or different ecologically or biogeochemically relevant velocities (e.g., solute velocities) if future research supports

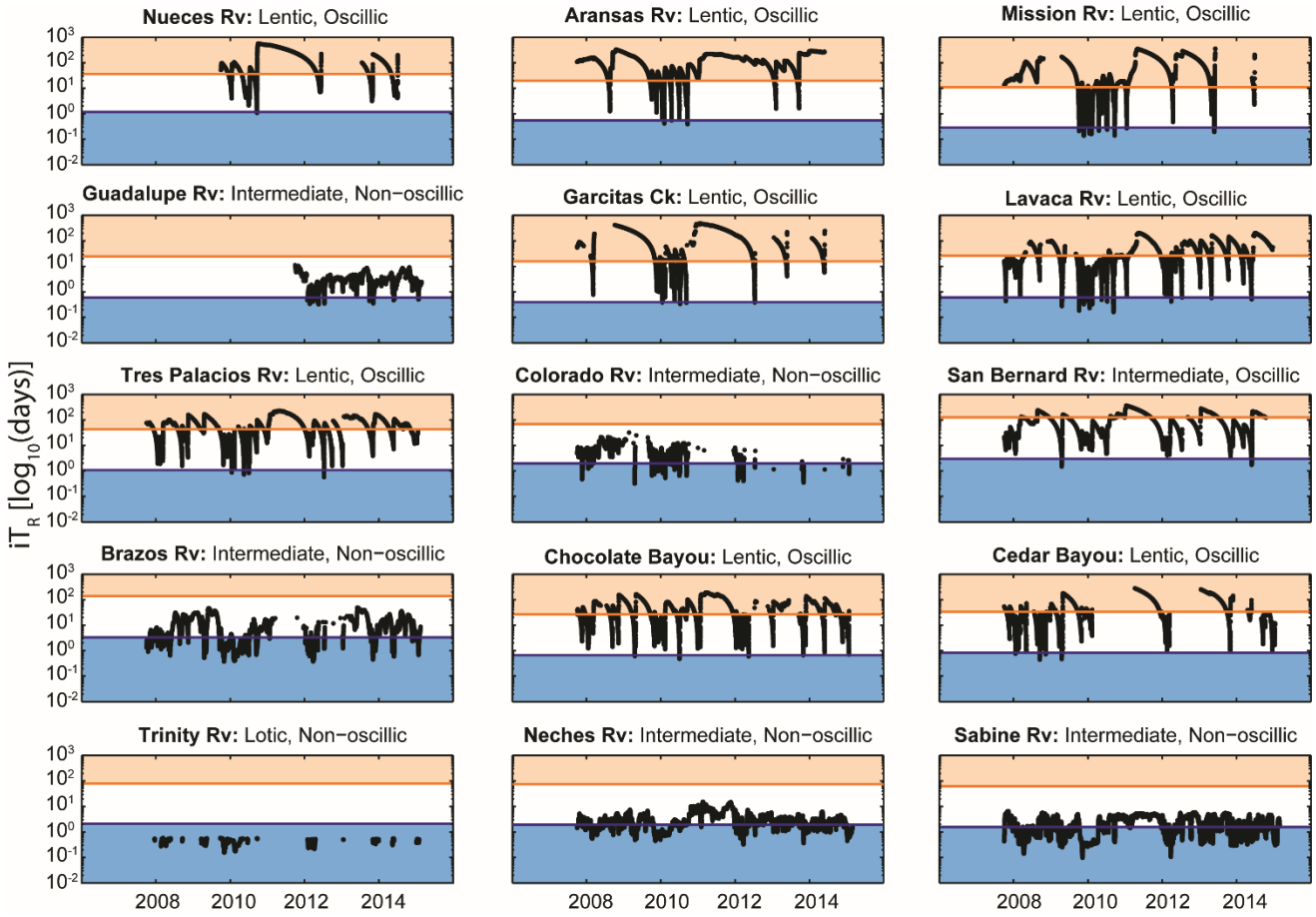

Figure 2.7: Texas tidal river reaches' iT_R time series, with derived system-specific lentic/lotic thresholds indicated by horizontal lines. The lower shaded region of each subplot represents lotic conditions and the upper region lentic conditions, with an unshaded intermediate region (similar to Figure 2.3b). The subplots are organized geographically, south to north (also drier to wetter).

such changes, by re-deriving the threshold equations (see the Appendices A, B, and C). Another key innovation of the FCC is the use of the class *intermediate* to denote systems that fall between traditional lentic and lotic endmember behaviors, which have been variously noted in publications as transitional or using other vocabulary [*Ward et al*., 2002; *Rennella and Quirós*, 2006; and *Buffagni et al*., 2009], but not previously collected into a well-defined system category.

The FCC model also proposes the first use of the term *oscillic* to describe systems that episodically switch between lentic and lotic conditions over a time period of interest. The oscillic nomenclature is critical for identifying systems which may have ecologic adaptations that promote survival under that highly variable hydrology. This new terminology, using both new *intermediate* and *oscillic* terms, bridges the previous lentic/lotic dichotomy and also more accurately represents the continuum of hydrologic variability in the natural world. Yet, the proposed FCC model respects the basic perception of a lentic versus a lotic system and indeed remains highly consistent with prior usages of the terms. Instead, the FCC aims to expand the conceptual utility of such classifications by providing a standardized basis and also incorporating a system's temporal hydrologic variability.

Although typically the terms *lentic* and *lotic* are used to describe freshwater ecosystems, the FCC could classify the transient hydrology of any terrestrial surface water, regardless of salinity, where *lentic* and *lotic* concepts may be applicable. For example, this work demonstrates the FCC's applicability to tidal river systems, which may become brackish. However, when applying the FCC to a non-freshwater system, the iT_R thresholds used in the model should be adjusted to suit the new application's hydrological and ecological conditions and functional constraints.

As a demonstration of the FCC model, we conducted an initial analysis of 15 tidal river reaches on the Texas Gulf Coastal Plain. Due to their temporally varying system volumes and flow directions, freshwater tidal reaches are notoriously difficult to classify in a manner both semantically meaningful and also consistent with existing freshwater system terminology. Table 2.2 compares the FCC labeling of the 15 Texas systems to classifications using the approaches of Pellet et al. [1983], Andersen and Shafroth [2010], Hein et al. [2003], and Rennella and Quirós [2006]. The comparisons to the methods of Pellet et al. [1983] and Andersen and Shafroth [2010] are based on comparing a computed velocity time series for each study reach to the prior authors' dichotomous lentic/lotic velocity thresholds (0.1 m s^{-1} and 0.2 m s^{-1}, respectively; no intermediate class). The comparisons to the methods of Hein et al [2003] and Rennella and Quirós [2006] are based on our median iT_R and the prior authors' residence time thresholds (7 and 15 days, respectively). In addition, we incorporated the oscillic definition into each analysis; for example, when using the framework of Rennella and Quirós [2006], if the system experienced iT_R conditions greater than and less than those authors' 15 day threshold, the system was defined as oscillic. Similarly, for the analyses that compared the systems' velocities (e.g., Pellet et al., 1983), if the system experienced velocities greater than and less than the threshold velocity (e.g., 0.1 m s^{-1}), the system was defined as oscillic.

Of the 15 systems, nine showed complete agreement in both lentic/intermediate/lotic and oscillic classifications among all five analysis frameworks (Table 2.2). Three systems showed partial agreement: the oscillic classification of the Guadalupe River showed agreement with the framework of Rennella and Quirós [2006], the oscillic classification of the Sabine River showed agreement with the frameworks of both Rennella and Quirós [2006] and Hein et al. [2003], and the oscillic designation of the San Bernard River agreed with all previous classification schema. The remaining three

River names	Current analysis System-specific iT_R thresholds	Pellet et al., [1983] q = 0.1 m/s	Anderson and Shafroth, [2010] q = 0.2 m/s	Hein et al., [2003] TR = 7 days	Rennella and Quirós, [2006] TR = 15 days
Nueces Rv	**Lentic, Oscillic**	**Lentic, Oscillic**	**Lentic, Oscillic**	**Lentic, Oscillic**	**Lentic, Oscillic**
Aransas Rv	**Lentic, Oscillic**	**Lentic, Oscillic**	**Lentic, Oscillic**	**Lentic, Oscillic**	**Lentic, Oscillic**
Mission Rv	**Lentic, Oscillic**	**Lentic, Oscillic**	**Lentic, Oscillic**	**Lentic, Oscillic**	**Lentic, Oscillic**
Guadalupe Rv	***Int., Nonoscillic****	Lentic, Oscillic**	Lentic, Oscillic**	Lotic, Oscillic**	***Lotic, Nonoscillic****
Garcitas Ck	**Lentic, Oscillic**	**Lentic, Oscillic**	**Lentic, Oscillic**	**Lentic, Oscillic**	**Lentic, Oscillic**
Lavaca Rv	**Lentic, Oscillic**	**Lentic, Oscillic**	**Lentic, Oscillic**	**Lentic, Oscillic**	**Lentic, Oscillic**
Tres Palacios Rv	**Lentic, Oscillic**	**Lentic, Oscillic**	**Lentic, Oscillic**	**Lentic, Oscillic**	**Lentic, Oscillic**
Colorado Rv	Int., Nonoscillic**	Lotic, Oscillic**	Lotic, Oscillic**	Lotic, Oscillic**	Lotic, Oscillic**
San Bernard Rv	***Int., Oscillic****	***Lentic, Oscillic****	***Lentic, Oscillic****	***Lentic, Oscillic****	***Lentic, Oscillic****
Brazos Rv	Int., Nonoscillic**	Lotic, Oscillic**	Lotic, Oscillic**	Lentic, Oscillic**	Lotic, Oscillic**
Chocolate Bayou	**Lentic, Oscillic**	**Lentic, Oscillic**	**Lentic, Oscillic**	**Lentic, Oscillic**	**Lentic, Oscillic**
Cedar Bayou	**Lentic, Oscillic**	**Lentic, Oscillic**	**Lentic, Oscillic**	**Lentic, Oscillic**	**Lentic, Oscillic**
Trinity Rv	**Lotic, Nonoscillic**	**Lotic, Nonoscillic**	**Lotic, Nonoscillic**	**Lotic, Nonoscillic**	**Lotic, Nonoscillic**
Neches Rv	Int., Nonoscillic**	Lotic, Oscillic**	Lotic, Oscillic**	Lotic, Oscillic**	Lotic, Oscillic**
Sabine Rv	***Int., Nonoscillic****	Lotic, Oscillic**	Lotic, Oscillic**	***Lotic, Nonoscillic****	***Lotic, Nonoscillic****

Table 2.2: Comparison of Freshwater Continuum Classification (FCC) designations to designations determined by other methods for the 15 analyzed Texas tidal river reaches. Most systems show an exact match between classification schemes. * Indicates a match in the river's oscillic classification only. ** Indicates no match. The Colorado, Brazos, and Neches Rivers do not match previous frameworks because of our introduction of the *intermediate* classification option.

rivers (the Colorado, Brazos and Neches rivers) did not show agreement with any of the previous classification schemes due to our use of the *intermediate* classification that does not have a parallel in any other scheme. Ultimately, our classification showed at least partial agreement with another classification scheme in 80% of the classified Texas tidal river reaches.

Although this comparison of methods shows the FCC model is broadly consistent with prior methods, its key improvement lies in its quantitative, scalable, methodology applicable to systems ranging from rivers to lakes to reservoirs and from smallest to largest surface water hydrology scales. The analysis defined eight lentic systems, six intermediate systems, and one lotic system among fifteen Texas coastal rivers of similar physiographic setting but somewhat different hydraulic geometry and climate. Classifying the majority of the analyzed reaches as lentic is not unreasonable for the semiarid Texas coastal plain. Annual and summer evaporation often exceed precipitation resulting in low-baseflow conditions and a functionally 'reservoir-like' river system with relatively stagnant waters [*Ward*, 1997; *Evans et al*., 2012; *Fulbright et al*., 1990; *Mooney and McClelland*, 2012; *Bruesewitz et al.*, 2013]. The low-baseflow conditions are evident in Table 2.1 where the median discharges for the eight lentic systems were all less than 1.0 $m^3 s^{-1}$. Also, for the ~3.5-7.5 year time period analyzed, nine of the fifteen tidal reaches presented oscillic conditions. Again, this classification is reasonable given the region's climate. Long summer droughts and extensive evaporation promote lentic conditions, while regular deluge events, associated with summer thunderstorms, hurricanes, and tropical storms from the Gulf of Mexico, may flood the system and induce temporary lotic conditions [*Ward*, 1997; *Evans et al*., 2012; *Fulbright et al*., 1990; *Mooney and McClelland*, 2012; *Bruesewitz et al*., 2013].

2.4.2 Linked Hydrologic and Ecologic System Characterizations

The application of the FCC to the Texas Gulf coast tidal river reaches demonstrated the FCC's broad applicability by providing lentic/lotic thresholds and classifications to fifteen systems of differing hydrologic norms and variability. In addition, the case study provided new insight into potential linked hydrologic and ecologic functions of the Texas tidal river reaches.

For example, for nine of the fifteen analyzed Texas tidal river reaches, the FCC model was able to connect the ecologic significance of non-lotic velocities (i.e., < 0.40 m s^{-1}, the proposed velocity threshold where zooplankton reproduction ceases [*Rzoska*, 1978; *Baranyi et al*., 2002]) to correspondingly ecologically significant predicted integrated residence times (i.e., zooplankton regeneration times of days to months [*Allan and Goulden*, 1980]). These nine systems were the Nueces, Tres Palacios, Colorado, San Bernard, Brazos, Cedar, Trinity, Neches and Sabine. More specifically, our analysis suggested that, given their system volumes, these nine rivers' tidal reaches have lotic iT_R thresholds near the low end of the zooplankton regeneration times (from ~1 – 3 days). In contrast, all fifteen tidal systems have lentic iT_R thresholds spanning the range of zooplankton regeneration times (from ~1.5 weeks – 4.5 months) (Table 2.3). Thus, we learn that, for the Texas Gulf Coast tidal river reaches over the analyzed time period, lotic conditions are likely associated with low zooplankton biomass generation, while lentic conditions provide ample hydrologic conditions to support the establishment of zooplankton communities not limited by advective transport.

In addition, most of the Texas systems' iT_R thresholds (23 of 30 thresholds) relate to pelagic and benthic regeneration time scales. Elser et al. [2007] reviewed 653 freshwater experiments and related the study durations to the generation time and size of dominant autotrophs. Elser et al. [2007] determined the average experimental durations for pelagic

studies was 7 days and for lake benthos was 40 days. In the FCC model, all of the Texas systems' lotic iT_R thresholds were shorter than 7 days. Thus, the pelagic ecology of any system classified as lotic would be predominantly controlled by advective transport and few species would regenerate in that environment. Also, eight of our systems' lentic iT_R thresholds reflect at least the 40 day average study length of lake benthos. Those systems are the Nueces, Tres Palacios, Colorado, San Bernard, Brazos, Trinity, Neches, and Sabine. The classification of any of these systems as lentic during any sustained time period (e.g., Nueces, Tres Palacios) might suggest the presence of significant benthic communities.

River Name	Lentic Threshold (days)	Lotic Threshold (days)	Median iT_R (days)	Freshwater Continuum Classification (FCC)
Nueces Rv	45.09	1.13	94.86	Lentic, Oscillic
Aransas Rv	20.30	0.51	120.73	Lentic, Oscillic
Mission Rv	11.10	0.28	45.24	Lentic, Oscillic
Guadalupe Rv	24.91	0.62	3.12	Intermediate, Nonoscillic
Garcitas Ck	15.49	0.39	103.73	Lentic, Oscillic
Lavaca Rv	25.40	0.64	32.01	Lentic, Oscillic
Tres Palacios Rv	41.29	1.03	61.83	Lentic, Oscillic
Colorado Rv	73.41	1.84	5.97	Intermediate, Nonoscillic
San Bernard Rv	118.14	2.95	85.17	Intermediate, Oscillic
Brazos Rv	135.35	3.38	7.21	Intermediate, Nonoscillic
Chocolate Bayou	27.27	0.68	44.11	Lentic, Oscillic
Cedar Bayou	33.93	0.85	37.71	Lentic, Oscillic
Trinity Rv	82.91	2.07	0.38	Lotic, Nonoscillic
Neches Rv	72.15	1.80	2.56	Intermediate, Nonoscillic
Sabine Rv	60.26	1.51	1.85	Intermediate, Nonoscillic

Table 2.3: Lentic and lotic iT_R thresholds (in days), and FCC model designations, for the 15 Texas Coastal Plain tidal river reach systems analyzed.

The eight Texas systems classified as lentic exhibit median discharges (Table 2.1) similar to the 23 lake average discharges (0.7 m^3 s^{-1}) reported by Saunders and Kalff

[2001]. These lentic-classified tidal river systems, effectively acting like lake environments with regards to discharge and residence time, may experience nitrogen (N) retention of up to the 34% of the total nitrogen (TN) loading through processes like remineralization and sedimentation [*Saunders and Kalff*, 2001, *Svendson and Kronvang*, 1993]. The retained N may become a source of nutrient transport later, especially during increased discharge events [*Svendsen and Kronvang*, 1993, *Mooney and McClelland*, 2012]. Furthermore, the biogeochemistry of these lentic systems will be dependent on autochthonous carbon and nutrient sources. In contrast, the biogeochemistry of the lotic tidal system (Trinity), acting effectively riverine, will be reliant on allochthonous inputs of nutrients and carbon [*Manzoni and Porporato*, 2011, *Simmons and Wallschläger*, 2005].

Most of the Texas systems were oscillic over the analyzed time period (~3.5-7.5 years depending on the river), which suggests that these aquatic ecosystems either need to be able to resist short-term lotic perturbations, or recover repeatedly from such perturbations. For example, Bruesewitz et al. [2013] monitored the biogeochemical impacts of a major storm (occurring from 20-24 September 2010) on the Mission and Aransas Rivers. During this storm period, both the Mission and Aransas Rivers exported a substantial portion of their annual (August 2010 – August 2011) NH_4^+, NO_3^-, and DON loads (69%, 69%, and 75%, respectively, for the Mission River and 55%, 24%, 51%, respectively, for the Aransas River) [*Bruesewitz et al.*, 2013]. Thus, during and immediately following the storm, advective transport dominated the hydrology of these systems, which reflects lotic conditions. However, upon returning to baseflow conditions following the storm (6 months, February – August 2011), each system supplied a markedly smaller portion of their N export load to offshore (22%, 8%, and 11%, respectively, for the Aransas River and ~2% each for the Mission River) [*Bruesewitz et al.*, 2013]. Hence, during the much longer period of baseflow conditions, retention exceeded transport

processes in these rivers, demonstrating lentic conditions. This same storm and subsequent baseflow period are present within our Mission and Aransas River datasets. During the storm period, the FCC analysis described a shift in the hydrologic character of these systems, as the increased discharge from the storm induced an oscillic transition from lentic to lotic conditions. The observed oscillic transition accurately reflects the export observations of the storm period from Bruesewitz et al. [2013]. In addition, the FCC analysis described extended lentic conditions following the storm event (Feb 2011 – August 2011), again coinciding with the observations of Bruesewitz et al. [2013]. Thus, the FCC's analysis provided further insight into the impact of the storm, by describing the shift in hydrologic nature that occurred in response to the storm's elevated discharge, and potentially making it easier to apply the detailed biogeochemical responses measured for one storm to other storms exhibiting similar oscillic-transition character.

2.4.3 The Time-dependency of Oscillic Systems

An important feature of the FCC model is that the system boundaries and the time period to be analyzed must be defined a priori although this does not differ from other such analyses. The FCC model is designed to be robust in the face of a slight increase or decrease of system volume, e.g., by slightly lengthening or contracting the river reach of interest, due to its volume-scaled iT_R thresholds. In application of the FCC model, however, it is quite possible that choosing a different time period to analyze might yield different classifications of lentic/lotic and oscillic character. This would occur if, for example, the magnitude of flood required to tip a system into oscillic behavior only happens every few years, such that analysis at shorter timescales would designate the system nonoscillic; still, it may be relevant to the ecosystem that strong lotic conditions recur every few years. Many of the oscillations in the Texas systems we analyzed are associated with major precipitation

events that result in rapid transitions to lotic conditions, sometimes within hours, and which recur multiple times in a season (Figure 2.7), after which they return to baseflow, lentic conditions. These rapid oscillations in system behavior might be described as a "flashy discharge" regime. However, not all oscillic systems will be characterized as "flashy". Systems experiencing large seasonal flow oscillations [*Adebisi*, 1981] or annual oscillations [*Rennella and Quirós*, 2006] would also be considered oscillic by the FCC model if longer time periods capturing these system behaviors were analyzed.

The time-scale dependence of the oscillic classification does not trivialize the FCC framework and can even be seen as a strength; it may enhance the ability to consider carefully how hydrologic dynamics, event recurrence frequencies, and the stability of aquatic ecologic systems are linked over time. To fully understand how systems respond to climatic influences, it may be necessary to apply the FCC model to a range of time scales. In theory, these timescales of interest could range from days to decades.

Daily timescales of oscillic system behavior would reflect short-lived perturbations to system discharge or volume, such as flash-flooding events, diurnal dam releases, daily cycles of phreatophyte water usage, or tides. Similarly, a system could be oscillic at the daily scale if it were a lotic coastal river, but with tidal forcing such that the net movement of water is negligible (effectively lentic) over one tidal cycle.

Seasonal timescales would instead show a system's typical hydrologic response to seasonal climatic shifts. Adebisi [1981] observed seasonal oscillations in lentic/lotic character with lotic behavior occurring throughout August to December and lentic conditions returning in February through May in the upper Ogun River in Nigeria. If a river reach oscillated seasonally between drought-induced lentic conditions and monsoon-induced lotic conditions, but was monitored throughout only the dry summer season, the analysis would likely classify the reach as *lentic, nonoscillic* for the summer season of

interest. However, if the same river reach were observed over an annual timescale, the seasonal oscillations in lentic/lotic character would be detected and likely define the river reach as *intermediate, oscillic* on average. This is not to say that either designation would be more or less correct; as with any model, the utility of the FCC model's result will depend on the research question to which it is applied. Continuing from the previous example, for a study of an aquatic species with a summer-only life cycle, the designation of *lentic, nonoscillic* would be the most useful to describe the hydrologic conditions that may potentially impact this species. In contrast, for longer-lived fauna or perennial aquatic flora, the annual *intermediate, oscillic* designation may be the relevant classification. Over even longer timescales, as climate modes shift perhaps decadally, a different designation may be relevant to more catastrophic system shifts driven by those influences.

In general, an annual scale incorporates a region's typical atmospheric and climatic cycles, to produce a system classification that is likely applicable in future years. These larger atmospheric and climatic cycles, in conjunction with the magnitude of the annual peak (or minimum) discharge event will determine whether a typically lentic (or lotic) system, such as many along the Texas gulf coast, is also oscillic. Although the annual classification may be fairly stable over multiple years of similar weather, no classification is permanent; it bears to remember that a system's *typical* designation may not be the *present* classification.

In addition, the FCC model analysis might be performed on longer timescales for those interested in longer-period cycles. For example, at a decadal timescale, continental waters respond to major climatic modes, such as the El Niño-Southern Oscillation (ENSO) [IPCC 2013]. Many of these Texas coastal rivers and much of the Gulf of Mexico coastline typically experience increased precipitation and flooding during 'El Niño' warm years [*Ropelewski and Halpert,* 1986], which may generate lotic conditions. In addition, over a

decadal time scale or longer, geomorphologic phenomena [*Ward et al*., 2002], such as channel migration and avulsion, and longer climate trends, such as the warming of global temperatures or sea level rise [*IPCC*, 2013] may impact a system's hydrologic regime and lentic/lotic or oscillic classifications.

Regardless of the length of the time period analyzed, a single shift between lentic/lotic endmembers over a studied time scale is sufficient to define the system as oscillic according to the FCC model. This is by design, as even a single short hydrologic state shift will tend to be critically relevant for aquatic ecosystems and biogeochemical processes [*Mooney and McClelland*, 2012]. In general, following a transition in hydrologic character one is likely to witness a state reversal, returning the system to its previous state, as observations continue. On the other hand, if a return event is never observed, a solitary transition may represent a permanent state-shift in lentic/lotic character. For example, dam removal could promote a single endmember-shift from lentic to lotic and there would be no expected state reversal. Since an alteration in hydrologic character immediately impacts the instream biota, any number of endmember transitions over the time period of interest should warrant the classification of oscillic.

2.5 CONCLUSIONS

The Freshwater Continuum Classification model developed and presented in this study was successful in discriminating between lentic, intermediate, and lotic system behaviors based on the metric of median integrated residence time, as well as quantitatively defining oscillic vs. nonoscillic systems based on the variability of system discharge. The approach is also highly flexible across the whole range of system volumes expected in terrestrial hydrology. The FCC model is designed such that any system defined by the FCC (e.g., lotic, nonoscillic) should have similar physical dynamics (e.g., discharge regime) to

another system with the same FCC designation, regardless of climate, size (i.e., volume), or geographic setting (i.e., coastal plain versus headwaters). This consistent, quantitative methodology may therefore benefit future intercomparison or meta-analysis studies as well as site-specific hydrology/aquatic ecology studies. Using the FCC model as a planning tool might also aid management decisions. For example, given a system defined as *lentic*, *oscillic* for the past several decades, if a reservoir were to be constructed upstream, preliminary management planning could use the FCC model to help seek to mimic the oscillic nature of the system via dam releases.

Classifying the flow and residence time attributes of terrestrial surface waters is a traditional step for providing insight into the expected interactions between hydrology, biogeochemistry, and ecology. From the residence time results of our FCC model, we expect that the ecology of a lotic system to be dominated by advective transport, depend on allochthonous carbon and nutrient sources, and contain minimal zooplankton population. This differs from the lentic systems, which will likely contain observable zooplankton populations due to sufficient water residence times enabling zooplankton regeneration. In addition, these lentic conditions provide ample time to create a biogeochemical environment that is reliant on autochthonous carbon and nutrient sources [*Saunders and Kalff*, 2001, *Seitzinger et al*., 2010, *Manzoni and Porporato*, 2011, *Simmons and Wallschläger*, 2005].

2.6 Acknowledgments

This material is based upon work supported by the National Science Foundation under Grant No. 1417433. Any opinions, findings, and conclusions or recommendations expressed in this material are those of the authors and do not necessarily reflect the views of the National Science Foundation.

The data and parameters used in this study are listed in the chapter, Appendices A and B, or available from the cited public sources. Appendices A and B additionally provide an instructional guide for applying the FCC model to any surface water system.

2.7 REFERENCES

Adebisi, A. A. (1981). The physico-chemical hydrology of a tropical seasonal river-upper Ogun river. *Hydrobiologia*, *79*(2), 157–165. Retrieved from http://link.springer.com/article/10.1007/BF00006123

Alexander, D., & Fairbridge, R. W. (Eds.). (1999). *Encyclopedia of environmental science*. Dordrecht ; Boston: Kluwer Academic Publishers.

Allan, J. D., & Goulden, C. E. (1980). Some aspects of reproductive variation among freshwater zooplankton. *Evolution and Ecology of Zooplankton Communities. University Press of New England*, 388–410.

Andersen, D. C., & Shafroth, P. B. (2010). Beaver dams, hydrological thresholds, and controlled floods as a management tool in a desert riverine ecosystem, Bill Williams River, Arizona. *Ecohydrology*, *3*(3), 325–338. https://doi.org/10.1002/eco.113

Arndt, S., Lacroix, G., Gypens, N., Regnier, P., & Lancelot, C. (2011). Nutrient dynamics and phytoplankton development along an estuary–coastal zone continuum: A model study. *Journal of Marine Systems*, *84*(3), 49–66. https://doi.org/10.1016/j.jmarsys.2010.08.005

Baranyi, C., Hein, T., Holarek, C., Keckeis, S., & Schiemer, F. (2002). Zooplankton biomass and community structure in a Danube River floodplain system: effects of hydrology. *Freshwater Biology*, *47*(3), 473–482. Retrieved from http://onlinelibrary.wiley.com/doi/10.1046/j.1365-2427.2002.00822.x/full

Basu, B. K., & Pick, F. R. (1996). Factors regulating phytoplankton and zooplankton biomass in temperate rivers. *Limnology and Oceanography*, *41*(7), 1572–1577. https://doi.org/10.4319/lo.1996.41.7.1572

Benenati, E. P., Shannon, J. P., Blinn, W., Wilson, K. P., & Hueftle, S. J. (2000). Reservoir-River Linkages: Lake Powell and the Colorado River, Arizona. *Journal of the North American Benthological Society*, *19*(4), 742. https://doi.org/10.2307/1468131

Benke, A. C., Chaubey, I., Ward, G. M., & Dunn, E. L. (2000). Flood pulse dynamics of an unregulated river floodplain in the southeastern US coastal plain. *Ecology*, *81*(10), 2730–2741. Retrieved from http://www.esajournals.org/doi/abs/10.1890/0012-9658(2000)081%5B2730:FPDOAU%5D2.0.CO%3B2

Błędzki, L. A., & Ellison, A. M. (2001). Effects of water retention time on zooplankton of shallow rheolimnic reservoirs. *Internationale Vereinigung Fur Theoretische Und*

Angewandte Limnologie Verhandlungen, *27*(5), 2865–2869. Retrieved from http://home.mtholyoke.edu/~lbledzki/Les_Publications/BE2000efects.PDF

Bruesewitz, D. A., Gardner, W. S., Mooney, R. F., Pollard, L., & Buskey, E. J. (2013). Estuarine ecosystem function response to flood and drought in a shallow, semiarid estuary: Nitrogen cycling and ecosystem metabolism. *Limnol. Oceanogr*, *58*(6), 2293–2309. Retrieved from http://www.researchgate.net/publication/258440362_Estuarine_ecosystem_function_response_to_flood_and_drought_in_a_shallow_semiarid_estuary_Nitrogen_cycling_and_ecosystem_metabolism/file/3deec5283d62f52ef0.pdf

Buffagni, A., Armanini, D. G., & Stefania, E. (2009). Does the lentic-lotic character of rivers affect invertebrate metrics used in the assessment of ecological quality? *Journal of Limnology*, *68*(1), 92–105. Retrieved from http://www.jlimnol.it/index.php/jlimnol/article/view/161

Dickman, M. (1969). Some Effects of Lake Renewal on Phytoplankton Productivity and Species Composition. *Limnology and Oceanography*, *14*(5), 660–666. Retrieved from http://www.jstor.org/stable/2834058

Elser, J. J., Bracken, M. E. S., Cleland, E. E., Gruner, D. S., Harpole, W. S., Hillebrand, H., … Smith, J. E. (2007). Global analysis of nitrogen and phosphorus limitation of primary producers in freshwater, marine and terrestrial ecosystems. *Ecology Letters*, *10*(12), 1135–1142. https://doi.org/10.1111/j.1461-0248.2007.01113.x

Evans, A., Madden, K., & Palmer, S. M. (Eds.). (2012). *The Ecology and Sociology of the Mission-Aransas Estuary* (1st ed.). Port Aransas, Texas: Mission-Aransas National Estuarine Research Reserve.

Fulbright, T. E., Diamond, D. D., Rappole, J., & Norwine, J. (1990). The coastal sand plain of southern Texas. *Rangelands*, 337–340. Retrieved from http://www.jstor.org/stable/4000522

Hein, T., Baranyi, C., Steel, A., & Schiemer, F. (2003). The importance of autochthonous particulate organic matter in large floodplain rivers: evidence of restoring hydrological connectivity. In *EGS-AGU-EUG Joint Assembly* (Vol. 1, p. 621). Retrieved from http://adsabs.harvard.edu/abs/2003EAEJA.....621H

Hoffsten, P.-O., & Malmqvist, B. (2000). The macroinvertebrate fauna and hydrogeology of springs in central Sweden. *Hydrobiologia*, *436*(1–3), 91–104. Retrieved from http://link.springer.com/article/10.1023/A:1026550207764

Humphries, P., Keckeis, H., & Finlayson, B. (2014). The River Wave Concept: Integrating River Ecosystem Models. *BioScience*, *64*(10), 870–882. https://doi.org/10.1093/biosci/biu130

Intergovernmental Panel on Climate Change (IPCC) (2013), Climate change 2013: The physical science basis, in *Contribution of Working Group I to the Fifth Assessment Report of the Intergovernmental Panel on Climate Change*, edited by T. F. Stocker, 1535 pp., Cambridge Univ. Press, Cambridge, U. K.

Krawczyk, A. C. de D. B., Baldan, L. T., Aranha, J. M. R., Menezes, M. S. de, & Almeida, C. V. (2013). The invertebrate's community in adjacent Alto Iguaçu's anthropic lakes of different environmental factors. *Biota Neotropica*, *13*(1), 47–60.

Manzoni, S., & Porporato, A. (2011). Common hydrologic and biogeochemical controls along the soil-stream continuum. *Hydrological Processes*, *25*(8), 1355–1360. https://doi.org/10.1002/hyp.7938

Monsen, N. E., Cloern, J. E., Lucas, L. V., & Monismith, S. G. (2002). A comment on the use of flushing time, residence time, and age as transport time scales. *Limnology and Oceanography*, *47*(5), 1545–1553. Retrieved from http://onlinelibrary.wiley.com/doi/10.4319/lo.2002.47.5.1545/full

Mooney, R. F., & McClelland, J. W. (2012). Watershed Export Events and Ecosystem Responses in the Mission–Aransas National Estuarine Research Reserve, South Texas. *Estuaries and Coasts*, *35*(6), 1468–1485. https://doi.org/10.1007/s12237-012-9537-4

NOAA Tides & Currents (2015), Station Selection—NOAA Tides & Currents NOAA Tides & Currents—Station Selection, National Oceanic and Atmospheric Administration, Washington, D. C.
[Available at https://tidesandcurrents.noaa.gov/stations.html?type5Water1Levels#Texas, accessed Oct. 2015.]

Pace, M. L., Findlay, S. E., & Lints, D. (1992). Zooplankton in advective environments: the Hudson River community and a comparative analysis. *Canadian Journal of Fisheries and Aquatic Sciences*, *49*(5), 1060–1069. Retrieved from http://www.nrcresearchpress.com/doi/abs/10.1139/f92-117

Palmer, T. A., Montagna, P. A., Pollack, J. B., Kalke, R. D., & DeYoe, H. R. (2011). The role of freshwater inflow in lagoons, rivers, and bays. *Hydrobiologia*, *667*(1), 49–67. https://doi.org/10.1007/s10750-011-0637-0

Pellett, S., Bigley, D. V., & Grimes, D. J. (1983). Distribution of Pseudomonas aeruginosa in a riverine ecosystem. *Applied and Environmental Microbiology*, *45*(1), 328–332. Retrieved from http://aem.asm.org/content/45/1/328.short

Pollack, J. B., Kim, H.-C., Morgan, E. K., & Montagna, P. A. (2011). Role of Flood Disturbance in Natural Oyster (Crassostrea virginica) Population Maintenance in an Estuary in South Texas, USA. *Estuaries and Coasts*, *34*(1), 187–197. https://doi.org/10.1007/s12237-010-9338-6

Rasmussen, J. B., Godbout, L., & Schallenberg, M. (1989). The humic content of lake water and its relationship to watershed and lake morphometry. *Limnology and Oceanography*, *34*(7), 1336–1343. Retrieved from http://onlinelibrary.wiley.com/doi/10.4319/lo.1989.34.7.1336/full

Rennella, A. M., & Quirós, R. (2006). The Effects of Hydrology on Plankton Biomass in Shallow Lakes of the Pampa Plain. *Hydrobiologia*, *556*(1), 181–191. https://doi.org/10.1007/s10750-005-0318-y

Ropelewski, C. F., & Halpert, M. S. (1986). North American Precipitation and Temperature Patterns Associated with the El Niño/Southern Oscillation (ENSO). *Monthly Weather Review*, *114*(12), 2352–2362. https://doi.org/10.1175/1520-0493(1986)114<2352:NAPATP>2.0.CO;2

Rzóska, J. (1978). *On the nature of rivers: with case stories of Nile, Zaire, and Amazon: essay*. The Hague ; Boston: Dr. W. Junk.

Saunders, D. L., & Kalff, J. (2001). Nitrogen retention in wetlands, lakes and rivers. *Hydrobiologia*, *443*(1–3), 205–212. Retrieved from http://link.springer.com/article/10.1023/A:1017506914063

Scavia, D., Field, J. C., Boesch, D. F., Buddemeier, R. W., Burkett, V., Cayan, D. R., Fogarty, M., Harwell, M. A., Howarth, R. W., Mason, C., Reed D. J., Royer, T.C., Sallenger, A. H., and Titus, J. G. (2002). Climate Change Impacts on U. S. Coastal and Marine Ecosystems. *Estuaries*, *25*(2), 149–164. Retrieved from http://www.jstor.org/stable/1353306

Seitzinger, S. P., Mayorga, E., Bouwman, A. F., Kroeze, C., Beusen, A. H. W., Billen, G., … Harrison, J. A. (2010). Global river nutrient export: A scenario analysis of past and future trends: GLOBAL RIVER EXPORT SCENARIOS. *Global Biogeochemical Cycles*, *24*(4), n/a-n/a. https://doi.org/10.1029/2009GB003587

Simmons, D. B. D., and D. Wallschlager (2005), A critical review of the biogeochemistry and ecotoxicology of selenium in lotic and lentic environments, *Environ. Toxicol. Chem.*, 24(6), 1331−1343.

Soballe, D. M., & Kimmel, B. L. (1987). A Large-Scale Comparison of Factors Influencing Phytoplankton Abundance in Rivers, Lakes, and Impoundments. *Ecology*, *68*(6), 1943. https://doi.org/10.2307/1939885

Stanley, E. H., Short, R. A., Harrison, J. W., Hall, R., & Wiedenfeld, R. C. (1990). Variation in nutrient limitation of lotic and lentic algal communities in a Texas (USA) river. *Hydrobiologia*, *206*(1), 61–71. Retrieved from http://link.springer.com/article/10.1007/BF00018970

Sullivan, S. M. (2013), Surveying amazon river tributaries for tug and barge navigation, Sea Surveyor, Inc., Benicia, Calif. [Available at http://www.seasurveyor.com/wp-content/uploads/2013/01/Surveying-Amazon-River-Tributaries-for-Tug-and-Barge-Navigation.pdf, accessed Oct. 2016.]

Svendsen, L. M., & Kronvang, B. (1993). Retention of nitrogen and phosphorus in a Danish lowland river system: implications for the export from the watershed. *Hydrobiologia*, *251*, 123–135. Retrieved from http://link.springer.com/chapter/10.1007/978-94-011-1602-2_15

Texas Coastal Ocean Observation Network (TCOON) (2015), CBI, Texas A&M University Corpus Christi, Corpus Christi, Tex. [Available at http://www.cbi.tamucc.edu/TCOON/, accessed Nov. 2015.]

Texas Commission on Environmental Quality (TCEQ) (2015), Surface Water Quality Viewer TCEQ Surface Water Quality Viewer, Texas Commission on Environmental Quality, Austin, Tex. [Available at https://gisweb.tceq.texas.gov/segments/default.htm, accessed Oct. 2015.]

Thorp, J. H., Thoms, M. C., & Delong, M. D. (2006). The riverine ecosystem synthesis: biocomplexity in river networks across space and time. *River Research and Applications*, *22*(2), 123–147. https://doi.org/10.1002/rra.901

Tockner, K., Malard, F., & Ward, J. V. (2000). An extension of the flood pulse concept. *Hydrological Processes*, *14*(16–17), 2861–2883. https://doi.org/10.1002/1099-1085(200011/12)14:16/17<2861::AID-HYP124>3.0.CO;2-F

Trigg, M. A., Wilson, M. D., Bates, P. D., Horritt, M. S., Alsdorf, D. E., Forsberg, B. R., & Vega, M. C. (2009). Amazon flood wave hydraulics. *Journal of Hydrology*, *374*(1–2), 92–105. https://doi.org/10.1016/j.jhydrol.2009.06.004

United States Geological Survey (USGS) (2015), USGS Current Water Data for Texas, USGS NWIS United States Geological Survey, Reston, Va. [Available at http://waterdata.usgs.gov/tx/nwis/rt, accessed Oct. 2015.]

Vannote, R. L., Minshall, G. W., Cummins, K. W., Sedell, J. R., & Cushing, C. E. (1980). The River Continuum Concept. *Canadian Journal of Fisheries and Aquatic Sciences*, *37*(1), 130–137. https://doi.org/10.1139/f80-017

Vegas-Vilarrúbia, T., & Herrera, R. (1993). Seasonal alternation of lentic/lotic conditions in the Mapire system, a tropical floodplain lake in Venezuela. *Hydrobiologia*, *262*(1), 43–55.

Ward, G. H. (1997). Process and Trends of Circulation Within the Corpus Christi Bay National Estuary Program Study Area. *Corpus Christi Bay National Estuary Program, CCBNEP-21*.

Ward, J. V., Tockner, K., Arscott, D. B., & Claret, C. (2002). Riverine landscape diversity. *Freshwater Biology*, *47*(4), 517–539. https://doi.org/10.1046/j.1365-2427.2002.00893.x

Chapter 3:
Defining the Riverine Tidal Freshwater Zone and their Spatiotemporal Dynamics in Response to Tide and Precipitation

ABSTRACT

Riverine tidal freshwater zones (RTFZs) are transitional environments between terrestrial and coastal waters that have freshwater chemistry and tidal physics, and are neither river nor estuary. RTFZs have appeared on occasion in the literature but lack a systematic definition and consistent framework for study. This work defines the RTFZ based on its basic characteristics of freshwater salinity, tidal flow, and tidal water surface oscillation through three longitudinal points of interest: λ_1 – upstream limit of brackish water, downstream limit of freshwater, and downstream boundary of RTFZ; λ_2 – upstream limit of bidirectional tidal velocities; λ_3 – upstream limit of tidal stage fluctuations and of the RTFZ. Each λ, and so the size and position of the RTFZ, is transient and depends on the balance of tidal and riverine forces. An RTFZ was isolated in the Aransas River of south Texas between July 2015 - July 2016. The median RTFZ length was 59.90 km, with a late summer maximum of 66.02 km and a winter minimum of 53.58 km. From the river mouth, the RTFZ typically (median) began 11.84 km upstream (15.43 km/11.16 km, max/min) and ended 71.74 km upstream (77.18 km/69.01 km). Climate-driven minimal baseflow in the Aransas River promoted gradual salt encroachment upstream and the shortening of the RTFZ. However, sporadic large rainfall/runoff events rapidly enlarged the RTFZ. Although previously not formally defined nor their dynamics explored, RTFZs are the nexus of hydrology, tides, and climate. The definition and framework presented provide a foundation and nomenclature for future investigations into RTFZs.

3.1 INTRODUCTION

Riverine freshwater discharge to the coast is critically important in estuarine and coastal ecology. In low relief costal river reaches, transitional environments along the river-estuary continuum experience the interaction of hydrologic dynamics and tides. These transitional environments are thought to play a role in the timing and magnitude of nutrient and freshwater fluxes to the coastal ecosystems, and hence coastal productivity. [*Mooney and McClelland* 2012, *Arndt et al*. 2011, *Bruesewitz et al*. 2013, *Palmer et al*. 2011, *Pollack et al*. 2011, *Knights et al.* 2017 *Dyer* 1997, *Savenije* 2005, *Brock* 2001, *Palmer et al.* 2002]. These transitional environments, here termed tidal freshwater zones (TFZs), are rarely monitored for river discharge or nitrogen (N) load due to their complex hydrodynamics [*Knights et al.* 2017, *Destouni et al.* 2008]. Empirically, *Mooney and McClelland* [2012] report the possibility of exceedingly long nutrient residence times (i.e., on the order of several months) within such tidal river reaches. In addition, these TFZ environments may exert controls on N-cycling along the length of the river [*Knights et al.* 2017]. An understanding of water residence times in these transitional environments [*Jones et al.* 2017] will improve and objectively inform policy decisions regarding coastal environmental flows and maximum daily loads (MDLs) [*Johnson*, 2009]. TFZs need to be recognized, defined using a consistent framework, and investigated much more thoroughly as they provide the potential for large pollution loads to the coastal environment, especially in conjunction with an increasingly large coastal population [*Johnson* 2009, *Destouni et al.* 2008, *Odum* 1988, *Neumann et al.* 2015].

A TFZ can exist in a variety of settings depending upon the balance of tidal and riverine forces interacting within a river-estuary continuum (Figure 3.1). Although in some settings a TFZ may include portions of the river mouth, near-shore zone, or riparian

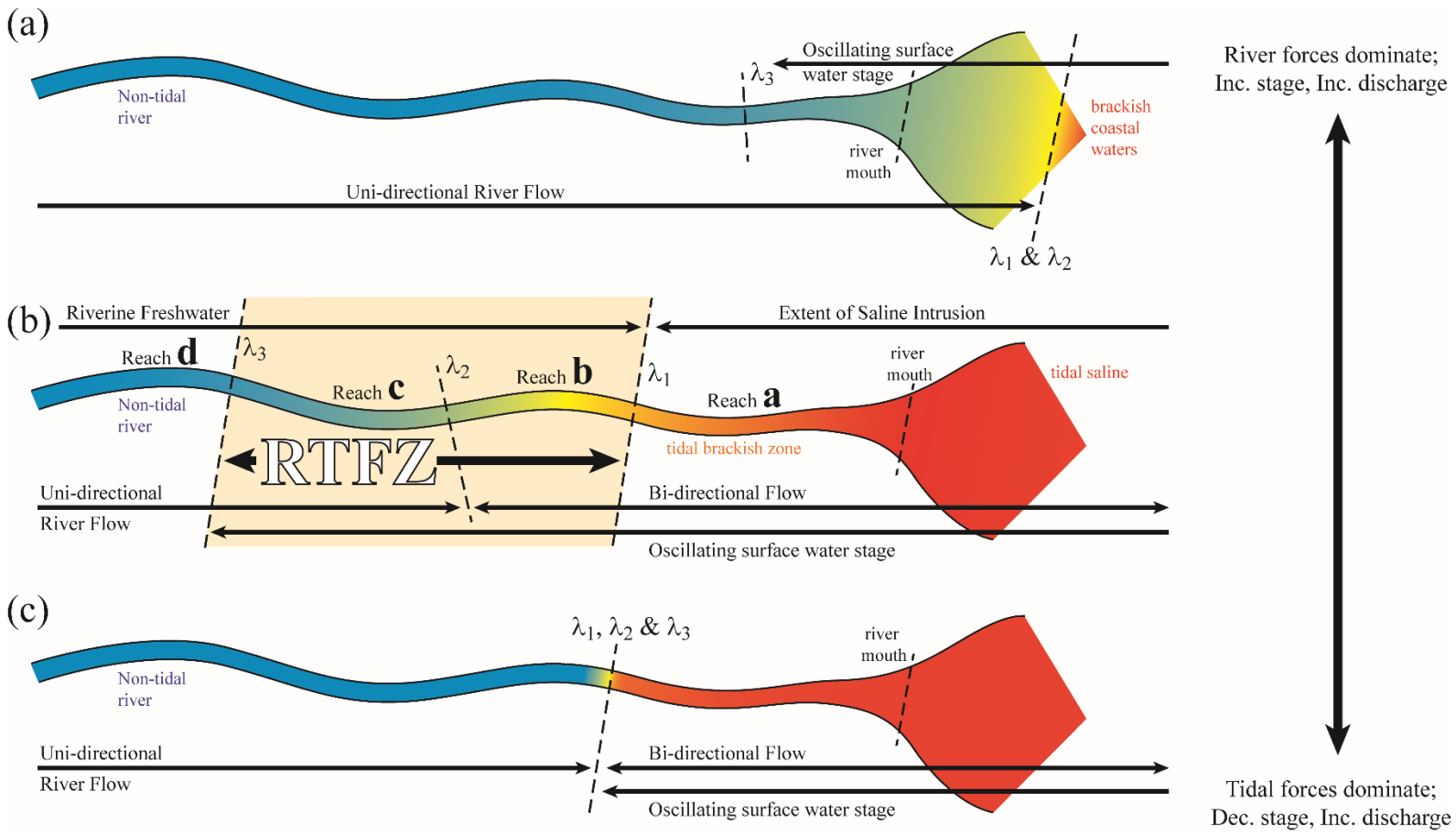

Figure 3.1: Spectrum of tidal freshwater zones, including the riverine tidal freshwater zone (RTFZ) in (b), with key locations λ_1, λ_2, and λ_3 all contained within the river banks. In contrast, a big-river estuary (a) may have λ_1 and λ_2 well downstream of the river mouth, while a classic estuary (c) with strong tidal forces may position λ_1, λ_2, and λ_3 atop one another and have virtually no TFZ.

wetlands (e.g., *Knights et al.* [2017], *Yankovsky et al.* [2012], *Odum* [1988]), this chapter focuses on TFZs contained entirely within the river banks and upstream of the river mouth (Figure 3.1b). Stated explicitly, this chapter discusses a *river reach composed of freshwater chemistry yet tidal physics (i.e., bidirectional velocity and/or surface water oscillations) that is bounded upstream by unidirectional fresh riverine discharge and downstream by a tidal estuarine brackish water column, all of which is upstream of the river mouth*. We term this reach the *riverine tidal freshwater zone* (RTFZ).

The presence of an RTFZ breaks the river-estuary continuum into three distinct units – the river, RTFZ, and estuary – each with its own physical dynamics, potentially with its own ecology and biogeochemistry. Each distinct segment may also, in turn, influence the ecology and biogeochemistry of the downstream environments. RTFZs, although not often defined as such, exist in numerous systems worldwide. For example, many rivers exhibit tidal water level oscillations 10-100+ km inland (e.g., the Hudson, Potomac, Scheldt, and Incomati Rivers [*Findlay et al.* 1991, *Cole et al.* 1992, *Lovley and Phillip*s 1986a, *Lovley and Phillip*s 1986b, *Arndt et al.* 2007, *Arndt et al.* 2011, *Savenije* 2005]). Although not termed or described as an RTFZ, *Lovley and Phillips* [1986a, 1986b] describe a "tidal river zone" just downstream of Washington, D.C. in the Potomac River, which flows into a "transition zone" and then into an "estuarine zone", which connects to Chesapeake Bay, with consequences for the benthic geochemistry of its waters. Similarly, *Ganju et al.* [2004] describe a conceptual "transitional regime" bordered upstream by a "river regime" and truncated downstream by a "bay regime". Within the Santee River, SC, USA, characteristics of the tidal signal and its mechanical dissipation have been measured at two points within its "freshwater transition zone" [*Yankovsky et al.* 2012]. Recently, the RTFZ has become appreciated for its potential control over the timing and magnitude of nutrient loads discharging to our estuarine systems [*Yankovsky et al.* 2012, *Knights et al.*

2017], but we lack a clear definition or consistent framework for recognizing and naming such zones.

This study introduces theory, nomenclature, and a classification scheme to define, describe, and empirically identify RTFZs. The classification scheme is then applied to document the existence of an RTFZ and its responses to a year of runoff events and tides in the Aransas River of south Texas, USA.

3.2 RIVERINE TIDAL FRESHWATER ZONE DEFINITION

A riverine tidal freshwater zone (RTFZ) is a *river reach composed of freshwater chemistry yet tidal physics (i.e., bidirectional velocity and/or surface water oscillations) that is bounded upstream by unidirectional fresh riverine discharge and downstream by a tidal estuarine brackish water column, all of which is upstream of the river mouth*. Using a conceptual one dimensional model of a river, we segment the system into four discrete sections based upon varying degrees of tidal and riverine dominance (Figure 3.1b, Table 3.1). Within Table 3.1, the "brackish or saline" water column chemistry must be estuarine-sourced. Also, the "bidirectional" discharge refers to tidal discharges that change direction throughout the tidal cycle. Similarly, "tidal" surface water stage describes tidally impacted stage that rises and falls throughout the tidal cycle (i.e., flood and ebb tide, respectively). Reaches a-d correspond to the labeled river reaches in Figure 3.1b.

Reach	Water Column Chemistry	Discharge	Surface Water Stage	Dominant controls	System
a	Brackish or saline	Bidirectional	Tidal	Tide >> River	Estuary
b	Fresh	Bidirectional	Tidal	Tide > River	RTFZ
c	Fresh	Unidirectional	Tidal	Tide < River	RTFZ
d	Fresh	Unidirectional	Riverine	Tide << River	River

Table 3.1: Description of four discrete river reaches that vary by degree of tidal and riverine dominance.

The transitions between these reaches we denote as:

λ_1 – downstream limit of depth- and horizontally-averaged *fresh* water column
λ_2 – upstream limit of functionally *bidirectional* (up- and downstream oriented) discharge
λ_3 – upstream limit of *tidal surface water stage* fluctuations

The TFZ is located between λ_3 and λ_1, and when contained entirely within the banks of the river it is an RTFZ (Figure 3.1b). To integrate this nomenclature into estuarine frameworks (e.g., 1-D formulations of vertically well-mixed estuaries), λ_0 may be incorporated to denote the location of a depth- and horizontally- averaged saline (estuarine/oceanic) water column.

Identifying the locations and movements of the λs within the river-estuary continuum reveals when an RTFZ exists, its length, and its response to perturbations (e.g., increased discharge due to precipitation events). Note that λ locations, and so the length and location of the RTFZ (or TFZ), are not stationary in space or time. The location of the λs depends upon the balance of riverine and estuarine forces. The relative positions of the λs may vary from the λs and TFZ straddling the river-estuary continuum (Figure 3.1a) to all three λs being spread along the river length creating an RTFZ (Figure 3.1b) to all λs being stacked atop one another (Figure 3.1c). Determination of λ locations at one point in time may not be valid over longer seasonal or tidal cycles.

3.3 RTFZ IDENTIFICATION AND ANALYSIS

To demonstrate empirical identification of an RTFZ and analysis of its spatiotemporal responses to external drivers, we provide an example analysis of the Aransas River, Texas, USA, monitored between July 2015 and July 2016. Over this period, the Aransas River RTFZ responded to numerous external stimuli such as large rainfall-runoff events, prolonged periods of baseflow and evaporation, and semi-diurnal to semi-annual tidal harmonics.

3.3.1 Aransas River Field Area

The Mission-Aransas (M-A) estuary, along the central Texas Gulf Coast, represents the western gulf biogeographic subregion as a part of the National Estuary Research Reserve (NERR) system [*Evans et al.* 2012]. The Aransas River is a primary source of freshwater input for Coapano Bay within the M-A bay system, which consists of three primary bays (Mesquite, Redfish, and Aransas bays) and three secondary bays (Copano, Port, and St. Charles bays) [*Evans et al.* 2012]. Although typically a diurnal, microtidal system, the interconnected bay system creates a highly convoluted tidal signal that reaches the Aransas River [*Evans et al.* 2012, *Bianchi et al.* 1999, *Bruesewitz et al.* 2013, *Mooney and McClelland* 2012].

The region's sub-humid to semiarid-subtropical climate generates extreme variability in precipitation (tropical storms, hurricanes, and drought) and strong seasonal oscillations in wind and temperature [*Evans et al.* 2012, *Fulbright et al.* 1990]. The Aransas River is situated in the southwestern portion of the Texas coastal plain, which is characterized by high summer temperatures (33.3 - 35.6°C), mild winter temperatures (8.3 - 8.9°C), and minimal annual precipitation (69 cm yr^{-1}). The high summer temperatures often result in annual evaporation exceeding local annual precipitation [*Mooney and McClelland* 2012, Evans *et al.* 2012, *Ward* 1997]. Several years of high evaporation combined with low rainfall will lead to drought conditions, decreased freshwater inflows, and potentially hypersaline estuaries, which are a regular occurrence throughout much of the Texas Gulf of Mexico coastline [*Evans et al.* 2012, *Ward* 1997, *Mooney and McClelland* 2012, *Bruesewitz et al.* 2013]. However, the warm summer waters of the Gulf of Mexico and the impacts of El Niño Southern Oscillation (ENSO) events supply the potential for large, sporadic rains associated with convective thunderstorms, tropical storms and hurricanes [*Evans et al.* 2012, *Ropelewski and Halpert* 1986, *Wolter et al.*

1999]. These events often promote flash flooding in the region and freshets into many of the coastal bays [*Mooney and McClelland* 2012, *Bruesewitz et al.* 2013, *Pollack et al.* 2011]. For example, from 1998 to 2008, the Aransas River experienced an average discharge of 1.39 $m^3 s^{-1}$, peak flow of 829.68 $m^3 s^{-1}$, and minimum flow of 0.0065 $m^3 s^{-1}$ [*Evans et al.* 2012].

The Aransas watershed covers approximately 2,146 km^2 of primarily cropland west of Copano Bay [*Mooney and McClelland* 2012]. Ten waste water treatment plants (WWTPs) contribute 14.4 million liters per day (mld) to the minimal inflow of the Aransas River upstream of the United States Geological Survey (USGS) sampling gauge near Skidmore, Texas [*Mooney and McClelland* 2012, *Johnson* 2009]. The Aransas River watershed rests within the Texas Gulf Coastal Plain and has very little relief, rising from near sea level at the river mouth to 22.06 m above sea level at the USGS gauge [08189700] that is 94.6 km upstream from the river mouth [*Evans et al.* 2012] (Figure 3.2).

The shallow bed slope, minimal riverine discharge during baseflow, and tidal forcing combine to create the potential for an RTFZ with long water residence times (e.g., on the order of months) within the Aransas River between storm events [*Mooney and McClelland* 2012]. During intervals of high riverine discharge the residence time is much shorter (e.g., on the order of days to hours) [*Evans et al.*, 2012, *Johnson* 2009, *Mooney and McClelland*, 2012, *Jones et al* 2017]. The interaction of hydrological dynamics and tides within these low-relief coastal river reaches (such as those found along the Texas Coastal Plain) impacts the timing, magnitude, and composition of nutrient fluxes to, and hence the biological productivity of, downstream estuarine environments [*Mooney and McClelland* 2012, *Arndt et al.* 2011, *Bruesewitz et al.* 2013, *Palmer et al.* 2011, *Pollack et al.* 2011].

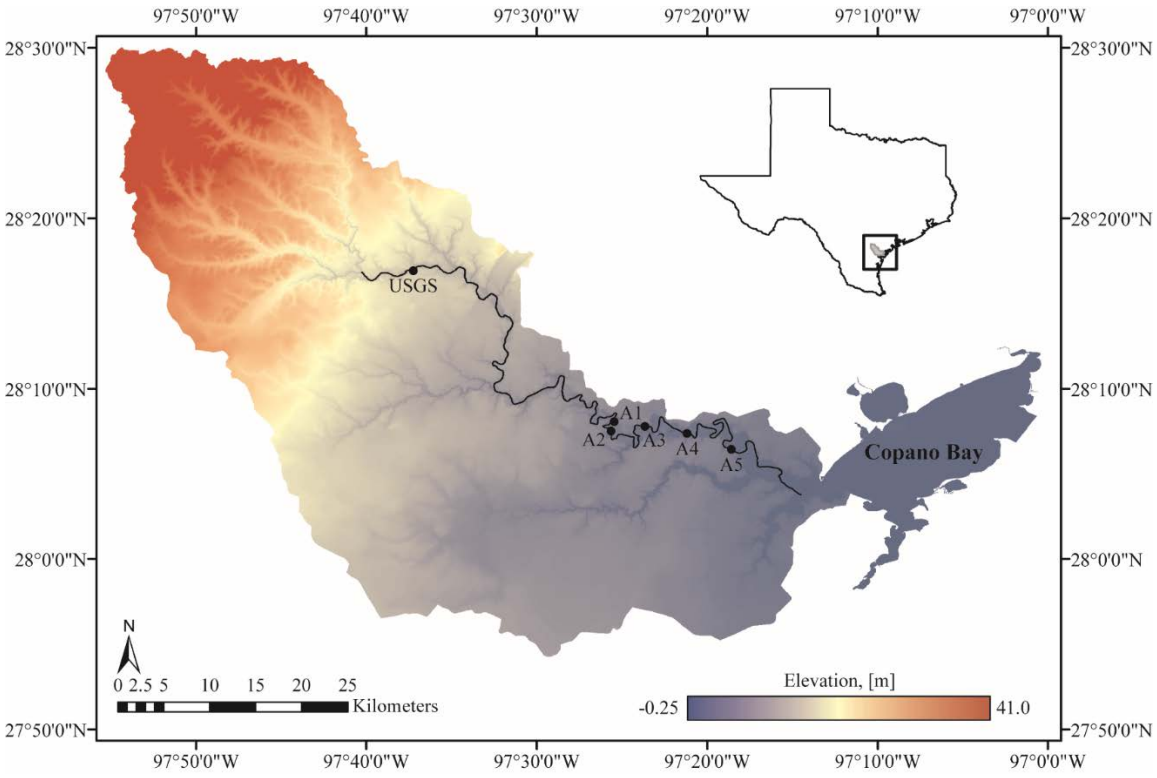

Figure 3.2: Map of installed monitoring sites along the Aransas River of south Texas and USGS gauge 08189700 location [USGS 2017a]. Inset: Aransas watershed location within Texas, USA.

3.3.1.1 Aransas River monitoring

Five monitoring locations along the Aransas River (sites A1-A5, Figure 3.2) recorded thalweg velocity, stage, and conductivity. At each site a SeaHorse tilt current meter (TCM) was anchored to the riverbed along the thalweg to record the magnitude and direction of flow. TCMs have been useful to investigate bottom circulation and sediment dynamics in the Gulf of Maine [*Aretxabaleta et al.* 2013, *Maio et al.* 2016], and the current dynamics in Mesquite, Aransas, and Copano Bays [*NERR* 2015] but not previously tested in rivers. Collocated with the TCMs at each site, a riverbed sonde recorded the conductivity and water depth. Monitoring data were smoothed using a 6-hour moving average to remove noise (e.g., from wind action), but preserve the active tidal/riverine signals.

3.3.1.2 Publicly available data

Discharge and stage time series were obtained from United States Geological Survey (USGS) through their National Water Information System (NWIS) for the Aransas River's farthest downstream gauging station (site number: 08189700) [USGS 2017a]. This gauge is 96.4 km upstream from the river mouth in a non-tidal, freshwater portion of the river. From the summer of 2015 through the summer of 2016, the Aransas River experienced a relatively wet year including several large storms. The gauging station recorded a discharge minimum of 0.10 $m^3 s^{-1}$, median of 0.17 $m^3 s^{-1}$, mean of 0.35 $m^3 s^{-1}$, and maximum 35.96 $m^3 s^{-1}$ over the study period (01 July 2015 through 01 July 2016).

3.3.2 Empirical RTFZ Identification in space and time

To determine the RTFZ location and temporal response to tides and storms, we identified the locations of λ_1, λ_2, and λ_3 using the longitudinally interpolated time series of salinity, stage, and velocity data collected at the six monitoring sites. The λ location was defined as where the interpolated conditions matched the λ definition. The definitions devised are provided in the subsequent subsections: 3.3.2.1, 3.3.2.2, 3.3.2.3. To obtain a time series of locations for each λ, this interpolation and comparison was completed using a 24-hour moving window centered around each timestamp. From the temporal character of the λ locations, we investigated the RTFZ response (e.g., contraction, expansion, and destruction) to environmental stimuli (e.g., saline encroachment versus increased freshwater inflow from precipitation events).

3.3.2.1 Identifying the freshwater limit: λ_1

To identify the most downstream extent of a freshwater column and so the RTFZ, we linearly interpolated the median PSU conditions across the river's monitoring stations and defined λ_1 where the interpolated salinity was 2.0 PSU. For the purposes of

interpolation, we assumed that the Gulf of Mexico, 59.26 km downstream of the river mouth, acted as the downstream endpoint with a constant salinity of 35.0 PSU. (The salinity of the intervening bays is often similar to the salinities of the rivers following rain events [*Bruesewitz et al.* 2013], so the proximal bays were not useful endmembers.) The freshwater threshold of 2.0 PSU was chosen to ensure that λ_1 estimated the limit of estuarine saline intrusion and not input from evaporation-concentrated terrestrial waters. Due to the region's semiarid subtropical climate, evaporation can produce increased salinities in otherwise fresh inland waters [*Evans et al.* 2012, *Mooney and McClelland* 2012]. For example, the nearby non-tidal USGS station on the Nueces River at Bluntzer, TX (station ID: 08211200) recorded specific conductance with a mean of 732.4, median of 680.0, and maximum of 1250.0 $\mu S\ cm^{-1}$ (corresponding to approximately 0.44, 0.41 and 0.75 PSU, respectively), between July 2015 – July 2016 [*USGS* 2017b]. Thus, defining the salinity threshold for freshwater at λ_1 at either 0.5 or 1.0 PSU may be insufficient to definitively determine the source of the observed salinity as estuarine.

3.3.2.2 Identifying the limit of bidirectional tidal flow: λ_2

To identify the location of the most upstream extent of tidal bidirectional velocities (synonymous with the most downstream extent of unidirectional river velocity), we defined unidirectional flow as occurring at a location for which 90% or more of times within the 24-hour moving window exhibited downstream velocity. Conversely, bidirectional tidal flow was described as occurring where more than 10% of times showed upstream river flow. To extrapolate between monitoring points, we linearly interpolated the 10^{th} percentile of the velocity data across the river length and defined λ_2 at the zero. Thus, at λ_2, 90% of the data (i.e., more than 21 hours of each 24-hour period analyzed) contained velocities oriented downstream and represented a non-tidal, unidirectional discharge regime. The

remaining 10% of the data often exhibited negligible (i.e., near-zero) discharge conditions. To approximate λ_2 through extreme precipitation events (i.e., flash floods) where λ_2 was pushed downstream of the river mouth, we linearly extrapolated the velocity conditions beyond the river mouth to the assumed constantly tidal Gulf of Mexico.

3.3.2.3 Identifying the limit of tidal river stage: λ_3

To identify the upstream limit of tidal surface water level oscillations, or λ_3, we had to first divide the data into storm vs. baseflow periods to avoid, e.g., the rising limb of a small storm mistakenly being identified as a rising tide. We defined a storm period as when the velocity at a given site exceeded that site's 90th percentile of measured TCM velocities.

During storm periods, we compared each site's tidal predictions against observations of stage to determine its position relative to λ_3. Sites that remained synchronized with predictions of high and low tide were determined to be downstream of λ_3, while sites that did not exhibit the periodic tidal signal were upstream of λ_3. To generate each monitoring site's tidal stage predictions, we performed a Real Fast Fourier Transform (RFFT), a frequency filter, and an inverse RFFT on the recorded stage data via Python's *numpy.fft* package. The RFFT and frequency filter isolated the five most significant (highest amplitude) harmonics in the recorded river stage data. We then used these five harmonics as input to an inverse RFFT to generate predicted tidal oscillations for that riverine monitoring location in the absence of any storm effects. For all our Aransas River monitoring stations, the five isolated harmonics matched the five primary harmonics reported for Copano Bay by the National Oceanic and Atmospheric Administration (NOAA) Tides and Currents prediction center (Table 3.2) [*NOAA* 2017c].

Harmonic	NOAA Amplitude [m]	Period	Description
SSA	0.098	182.62 days	Solar semiannual
SA	0.060	365.24 days	Solar annual
O1	0.032	25.8 hours	Lunar diurnal
K1	0.030	23.9 hours	Lunar diurnal
M2	0.007	12.42 hours	Principal lunar semidiurnal

Table 3.2: Primary tidal constituents for the NOAA Copano Bay Fishing Pier tidal gauging station (Station ID: 8774513) [*NOAA* 2017c].

We next sought to identify the predicted times of high and low river stage (S) for each monitoring location. High and low tide within S(t) will correspond to zeros in the $\frac{\mathrm{dS}}{\mathrm{dt}}$, so we converted both the predicted and observed stage time series into $\frac{\mathrm{dS}}{\mathrm{dt}}$ time series using eq. (3.1) and a *dt* of fifteen minutes between time$_n$ and time$_{n+1}$ (the field sampling interval).

$$\frac{dS_n}{dt} = \frac{Stage_{n+1} - Stage_n}{time_{n+1} - time_n} \tag{3.1}$$

For a 24-hour moving window associated with a given storm timestamp, we compare the timing of the predicted and observed $\frac{\mathrm{dS}}{\mathrm{dt}}$ roots to determine whether the site is upstream or downstream of λ_3. If a majority of observed roots do not occur concurrently (within ± 3 hours) with the predicted tidal $\frac{\mathrm{dS}}{\mathrm{dt}}$ roots, the site is defined as non-tidal and upstream of λ_3 at this timestamp. Otherwise, the site is tidal and downstream of λ_3. (A figure depicting the method for identifying the relative location of λ_3 during storm conditions can be found in Appendix D.) This time matching analysis of $\frac{\mathrm{dS}}{\mathrm{dt}}$ roots required an error window of ± 3 hours because noise inherent in the stage data (even after cleaning with 6-hour moving average) caused small, unpredictable offsets from the harmonic predictions. The rationale for a ± 3-hour error window for determining "concurrent" roots is that a 6-hour window over a 24-hour tidal cycle is a phase lag of $\frac{\pi}{2}$ (i.e., the phase offset between a sine and cosine curve). Thus, if the observed roots occur more than ± 3 hours

away from the predicted, the site's observed stage is significantly out of phase with the tidal predictions and is not tidal.

After determining each site's relative location (i.e., upstream or downstream of λ_3), we linearly interpolated between the two sites immediately surrounding λ_3 the predicted and observed stage and $\frac{dS}{dt}$ conditions. The analysis matching predicted and observed timings of $\frac{dS}{dt} = 0$, or high and low tides, was repeated along every meter of the interpolated conditions. The location of λ_3 was estimated as where the majority of $\frac{dS}{dt}$ roots transitioned from being tidally synchronous to asynchronous. If our most downstream monitoring location (A5) was non-tidal, we approximated the stage and $\frac{dS}{dt}$ for the Gulf of Mexico, 59.26 km downstream of mouth, using the five identified tidal harmonics, as the tidal end-point for the purposes of interpolation.

During baseflow conditions, we defined a location as tidal if it exhibited sustained periods of strong rising and falling stage throughout a 24-hour period. We used interpolated $\frac{dS}{dt}$ statistics (i.e., interquartile range and median) to identify these cycles of rising and falling stage, and determine the baseflow location of λ_3. The location of λ_3 occurs at the most downstream location where either: (1) the longitudinally interpolated interquartile range of $\frac{dS}{dt}$, with an interpolated median near zero, is less than a specific diurnal (0.31 m d^{-1}) or semidiurnal (0.62 m d^{-1}) threshold (see the Appendix E for the sinusoid derivation); or (2) the longitudinally interpolated 25^{th} or 75^{th} percentile of $\frac{dS}{dt}$ crosses zero (Figure 3.3k).

For condition (1), a significantly wide $\frac{dS}{dt}$ interquartile range with a median near zero, describes a site where significant rising and falling stage occurred in the 24-hour moving window around the time point analyzed. Each part of this condition (i.e., range and median) ensure that the observed stage is tidal (e.g., rather than a hydrograph's falling limb, or stagnant baseflow). The median near zero ensures that the window contains high and/or

low tidal stages and the width of the $\frac{dS}{dt}$ interquartile range ensures both significant rising and falling behavior.

We choose to locate λ_3 where the tidal surface water oscillation range was ≤ 5 cm. We calculated the expected range of $\frac{dS}{dt}$ for a tidal range of 5 cm (diurnal and semidiurnal, respectively). If the observed $\frac{dS}{dt}$ interquartile range is wider than the resulting thresholds, then the site exhibits significant positive and negative $\frac{dS}{dt}$ related to a tidal range of more than 5 cm. However, at the first location where the $\frac{dS}{dt}$ range no longer exceeds the threshold, the observed tidal range no longer experiences significant (i.e., $\geq$ 5cm range) tidal surface fluctuations and thus denotes the location of λ_3 (Figure 3.3).

Also for condition (1), to determine which $\frac{dS}{dt}$ interquartile range threshold (i.e., semidiurnal or diurnal) to use, we isolated the dominant tidal period for each analyzed 24-hour window. To determine the dominant tidal period, we performed an RFFT on each moving window of stage data, compared the magnitudes of the 12- and 24-hour period signals, and identified the signal with the stronger magnitude as the dominant period. Determination of the dominant tidal period was necessary because the tidal stage on the Aransas River acts differently during spring and neap tide (i.e., strongly diurnal and mixed-semidiurnal, respectively [*Evans et al.* 2012, *Mooney and McClelland* 2012]).

For condition (2), the USGS gauge is far upstream of the monitoring sites and can act disconnected from the lower reaches of the river. For example, a small hydrograph peak at the gauge may only be an isolated occurrence and not impact the sites downstream. However, this small hydrograph peak will alter the gauge's stage away from typical stagnant baseflow (i.e., a very narrow $\frac{dS}{dt}$ distribution near zero) and disrupt the longitudinal interpolation of $\frac{dS}{dt}$ interquartile range for estimating λ_3 under condition (1). For example, during the recession limb of a small hydrograph at the USGS gauge (highlighted period *(i)* in Figure 3.3a), the negative $\frac{dS}{dt}$ values at the gauge skew the interpolated median $\frac{dS}{dt}$ away

from zero, which fails condition (1) (Figure 3.3k). However, we can confidently say that tidal conditions are present where the river experiences a significant amount of rising stage (i.e., positive $\frac{dS}{dt}$). Where the river's interpolated 75th percentile transitions through zero, rising stage conditions persist for at least one-quarter (i.e., 6 hours) of the time period analyzed and indicates the presence of tidal conditions. For such instances when the USGS gauge contains wholly positive or negative $\frac{dS}{dt}$ values, λ_3 is defined where the 25th or 75th percentile, respectively, crosses zero and indicates significant tidal surface oscillations (Figure 3.3k).

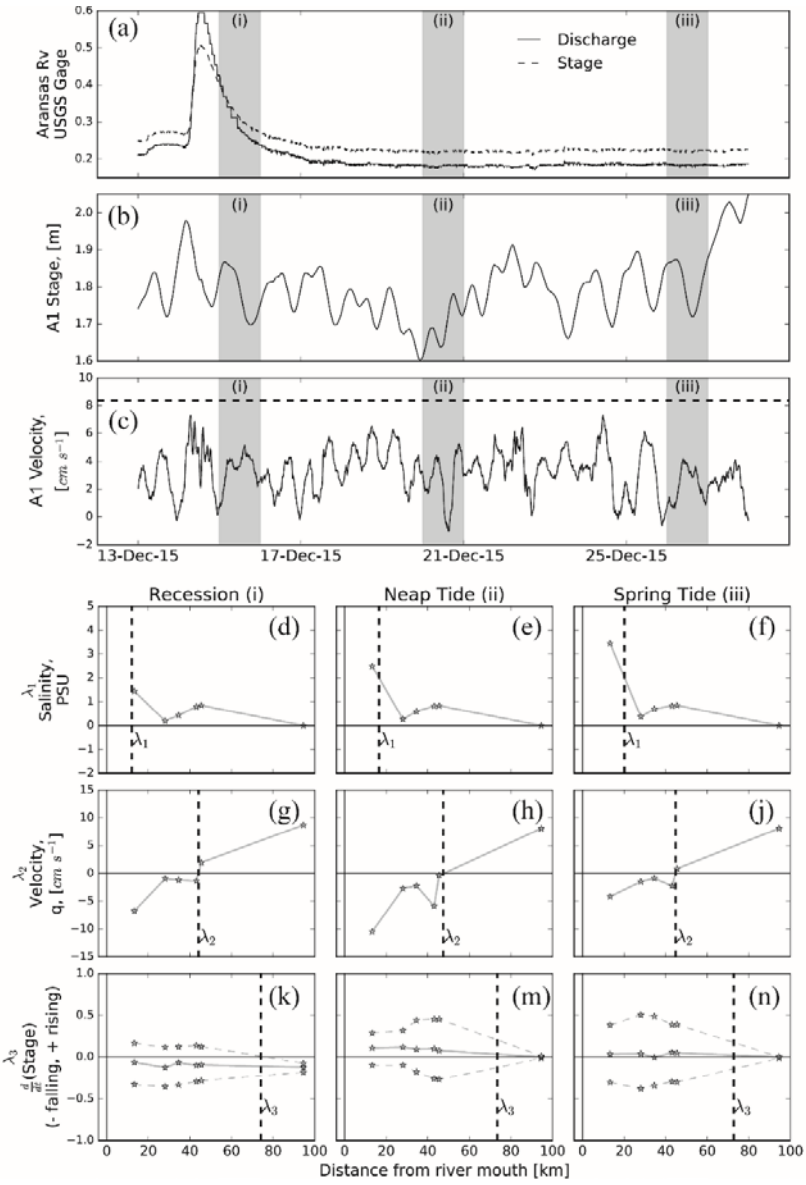

Figure 3.3: Methods for identification of λs during baseflow conditions. Conditions during and after a precipitation event between 13-28 Dec. 2015 are depicted at the USGS gauge (a) and in the stage (b) and velocity (c) time series of A1. The dashed line in (c) represents the 90th percentile threshold, to isolate storm conditions. The storm appearing at the USGS gauge was not strongly apparent far downstream at A1. For (d-n), rows correspond to identified λ location and columns represent the three highlighted time periods (i, ii, iii or "Recession", "Neap Tide", and "Spring Tide", respectively) in the time series (a-c). In (k-n) the 3 lines are 25th, 50th (median), and 75th percentiles of $\frac{dS}{dt}$ within a 24-hour moving window.

3.4 RESULTS

3.4.1 Seasonal RTFZ reach length dynamics

The RTFZ location and size in the Aransas River estuary was identified over three periods: late summer (01 July - 01 September 2015), late winter (01 December 2015 – 01 March 2016), and a full year (01 Jul 2015 – 01 July 2016). The typical (median) length of the RTFZ may be reported in two different ways, depending upon the order of operations.

1. Calculating the RTFZ length ($\lambda_{3,n}$-$\lambda_{1,n}$) for every time step, *n*, where λ_1 is upstream of the river mouth, then calculating the median
2. Calculating the median λ locations for all time steps, then subtracting the medians ($\tilde{\lambda}_3$-$\tilde{\lambda}_1$) to determine the overall RTFZ length (presented in Table 3.3)

Both median RTFZ length calculations produce similar results (Figure 3.4). In the late summer the median of each time step's RTFZ length was 66.32 km (calculation 1), while the overall RTFZ length was 66.02 km (calculation 2). The late winter months exhibited shortened RTFZ lengths, with a median RTFZ length for each time step of 51.94 km and an overall RTFZ length of 53.58 km. Throughout the entire year analyzed, the median RTFZ length for each time step was 56.25 km for each time step and 59.90 km from overall measurements (Table 3.3, Figure 3.4). The longer RTFZ length during the late summer months was likely due to a precipitation event, and subsequent increased discharge, from the early summer months (May–July) of 2015, as evidenced in the hydrograph peaks of the Aransas River USGS gauge (Figure 3.5a). This event extruded estuarine-derived saline waters downstream, pushing the lower end of the RTFZ (i.e., λ_1) toward the river mouth, which lengthened the RTFZ. The following months' baseflow balanced against tidal fluctuations to maintain an expanded RTFZ that was gradually eroded and shortened over time.

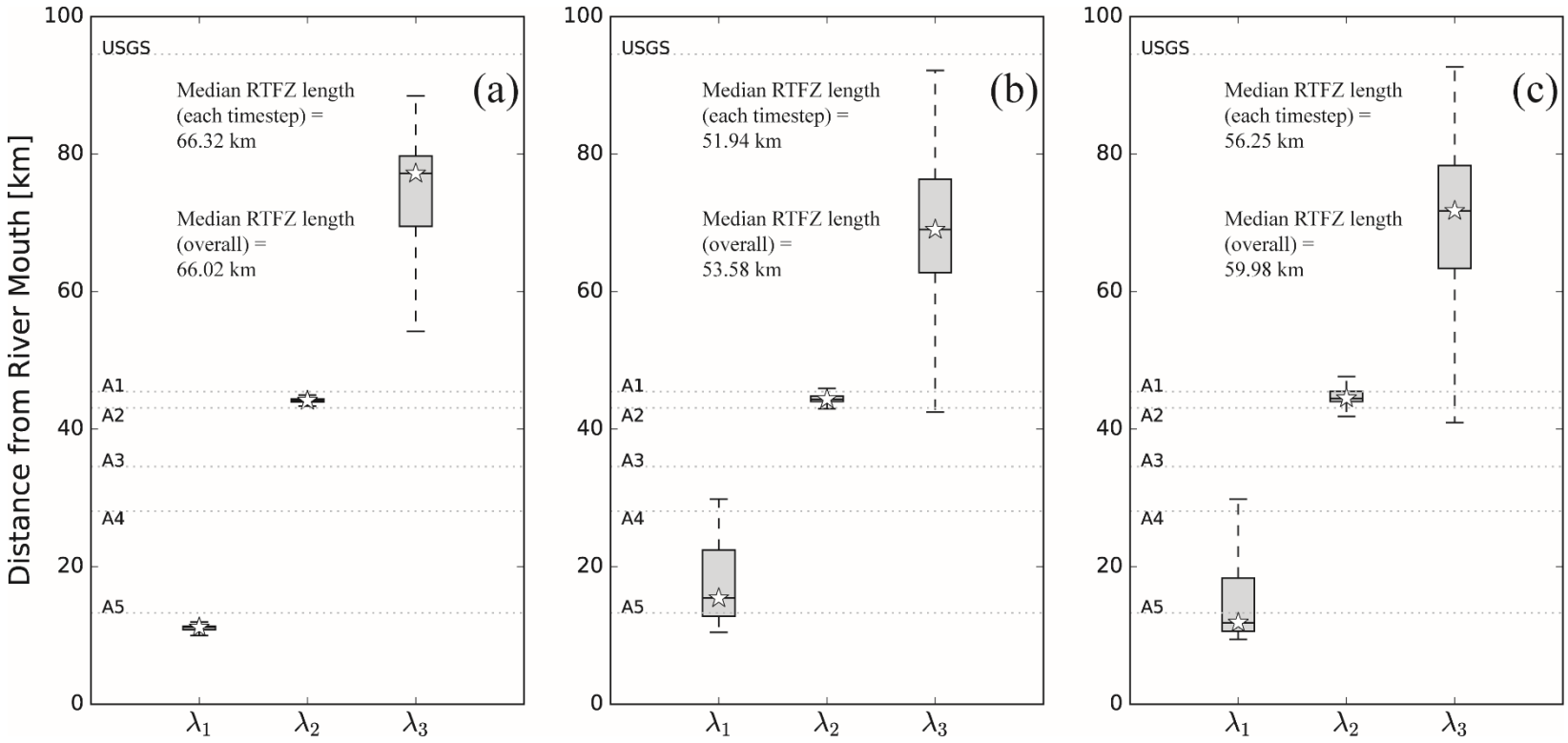

Figure 3.4: λ position along the length of the Aransas River. The median (star) and interquartile range (box) for each λ position are presented for (a) late summer (01 July through 01 September 2015), (b) late winter (01 December 2015 through 01 March 2016), and (c) one year (01 July 2015 through 01 July 2016). The position of λ_1 steadily intrudes throughout the year with salt transport upstream, λ_2 remains fairly constant, and λ_3 varies widely due to spring, neap, and secular tides.

	λ_1	λ_2	λ_3	**RTFZ Length: (λ_3-λ_1)**
Summer Median, [km]	11.16	44.14	77.18	66.02
Summer Mean, [km]	11.03	43.84	73.32	62.29
Summer Std. Deviation, [km]	0.57	3.56	11.30	-
Winter Median, [km]	15.43	44.36	69.01	53.58
Winter Mean, [km]	17.40	43.28	68.65	51.25
Winter Std. Deviation, [km]	5.21	5.78	10.56	-
Annual Median, [km]	11.84	44.48	71.74	59.90
Annual Mean, [km]	14.58	44.26	69.51	54.93
Annual Std. Deviation, [km]	5.389	9.76	11.62	-

Table 3.3: Location of each λ (km upstream from the river mouth) throughout the three time periods analyzed.

The upstream encroachment of saline waters was evident in the upstream movement of the overall median position of λ_1 between the summer and winter time periods (11.16 km and 15.43 km, respectively, Table 3.3). Additionally, the location of λ_3 moved downstream between the summer and winter time periods, from 77.18 km to 69.01 km (Table 3.3). Although, the positions of λ_1 and λ_3 shift during the three time periods analyzed, the median position of overall λ_2 observations changed little (44.14, 44.36., and 44.48 km, respectively, Table 3.3, Figure 3.4).

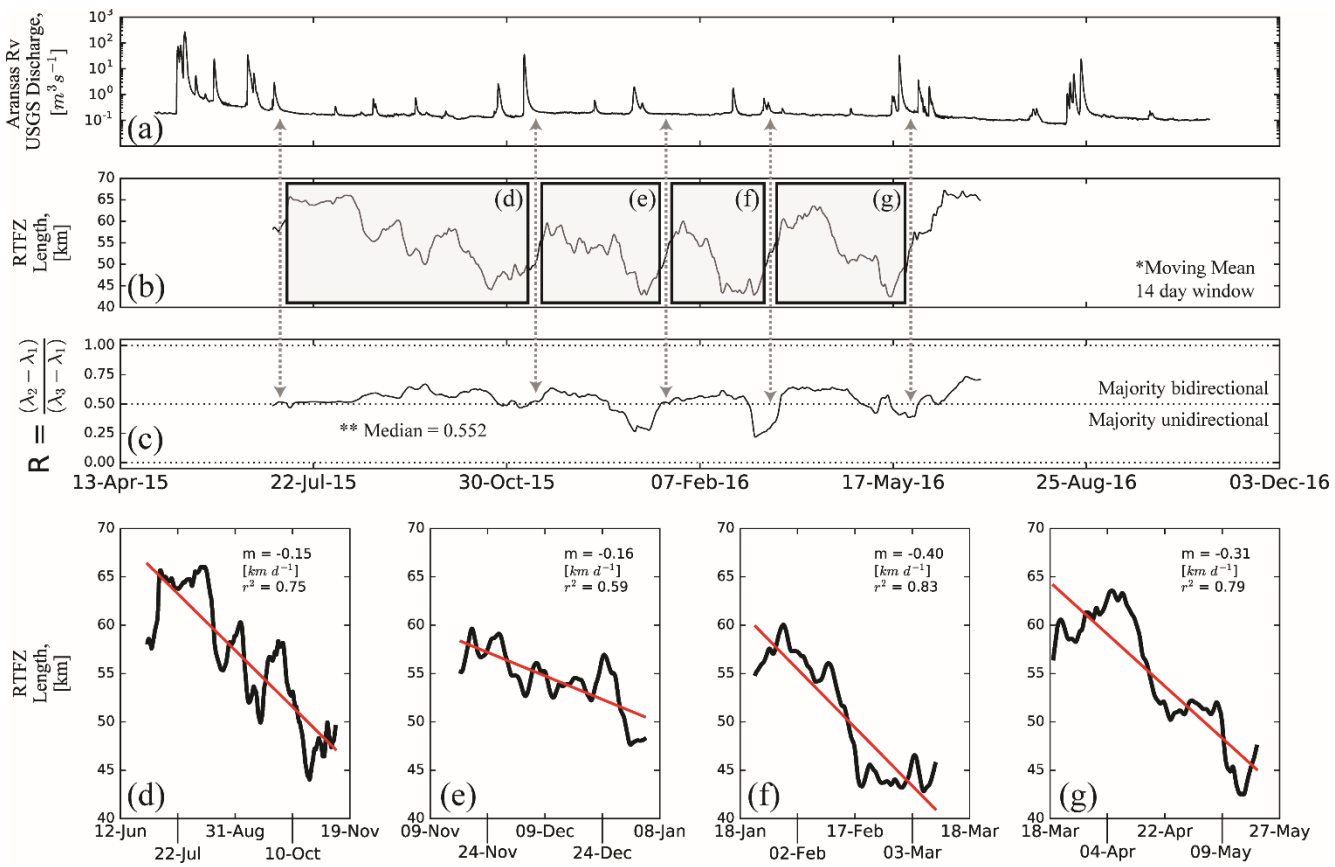

Figure 3.5: Time series of USGS gauge discharge (a) and the length of the Aransas River RTFZ (b) from 01 July 2015 to 01 July 2016. The larger events, marked by the gray dashed arrows between (a) and (b), are associated with sudden lengthening of the RTFZ (b). Between those five major storms, the λs shift relative to one another and alter the proportion of the RTFZ with bidirectional versus unidirectional flow (c) and the RTFZ length shortens as a result of upstream saline intrusion (d-g). During the four periods of baseflow and saline intrusion, the RTFZ length shortens at a similar rate (0.15, 0.16, 0.40, and 0.31 km d^{-1}, respectively).

3.4.2 Long-term rates of RTFZ length change

For the Aransas River, the RTFZ shortening rate may be observed from the RTFZ length time series, presented as a 14-day moving average in Figure 3.5b. There were 5 primary precipitation influxes that served to substantially lengthen the RTFZ (marked by the gray arrows between Figure 3.5a and 3.5b). However, in the intervening time between each of these storms, the length of the RTFZ decreased at a relatively consistent rate of upstream salt encroachment, moving λ_1. The four inter-storm time periods had RTFZ shortening rates of 0.15, 0.16, 0.40, and 0.31 km d^{-1}, respectively (Figure 3.5d-g).

During a runoff event, sufficient riverine discharge may cause the discharge regime of much or all of the RTFZ to become unidirectional before beginning to transport salt downstream. In other words, storms may collocate or even invert λ_1 and λ_2, expelling λ_2 downstream of λ_1 for the duration of the flood pulse (Figure 3.7). Also, after the storm event, the tidal discharge regime (i.e., λ_2) returns more quickly to its pre-storm location than the brackish water front (i.e., λ_1) (Figure 3.7).

Over short-term time scales (daily to weekly), spring and neap tidal conditions control λ_3, the upstream limit of the RTFZ, and thereby the RTFZ length (Figure 3.6). During a storm period, however, the flood pulse may override the tidal stage fluctuations and push λ_3 downstream from its typical baseflow location upstream of A1 (Figure 3.7).

We may characterize the RTFZ using the ratio of the bidirectional reach length compared to the length of the entire RTFZ:

$$R = \frac{(\lambda_2 - \lambda_1)}{(\lambda_3 - \lambda_1)} \tag{3.2}$$

This ratio describes how the location of the lambdas relate to one another along the length of the river, and also helps us to determine whether the RTFZ is primarily uni- or bidirectional (Figure 3.5c). For the three time periods analyzed (summer, winter, and the

July 2015-2016 year), the Aransas River exhibited median RTFZ ratios of 0.518, 0.545, and 0.552, respectively, indicating a slight majority of its length with bidirectional flow, overall (Figure 3.5c).

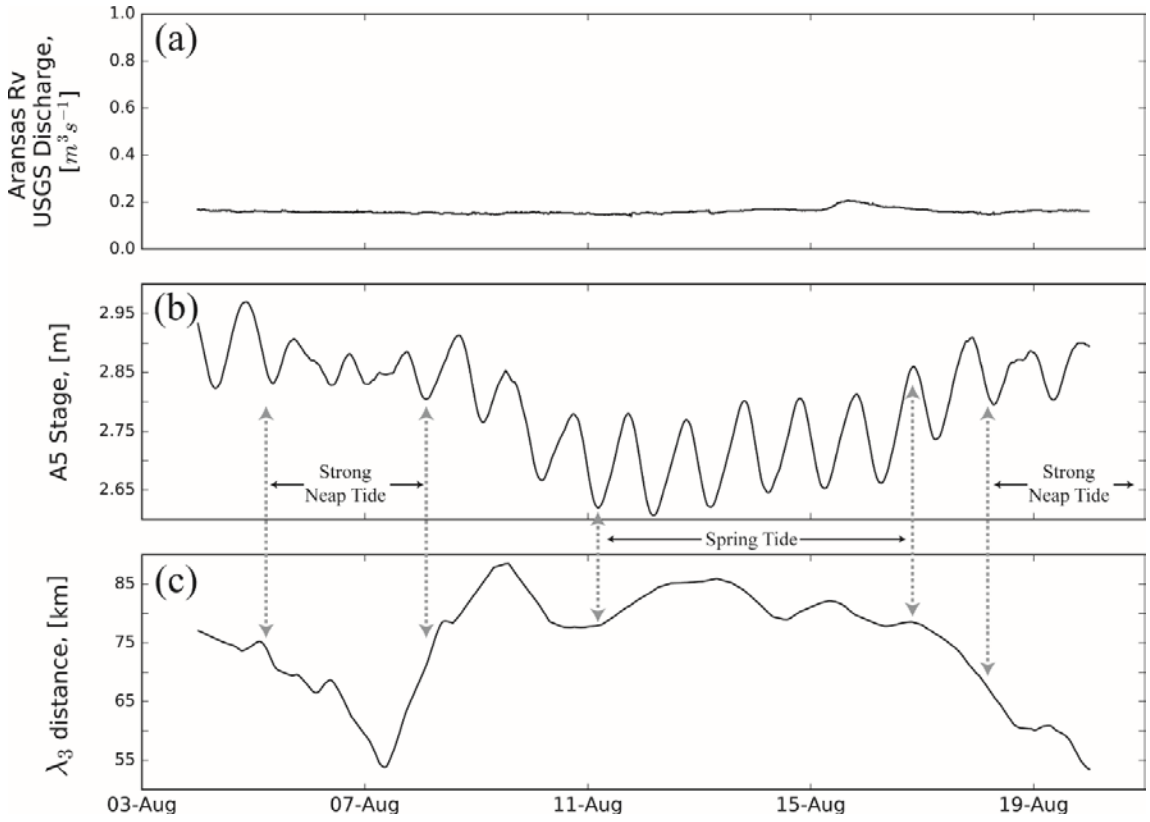

Figure 3.6: Temporal relations between spring and neap tide, and λ_3. During a period baseflow, as evidenced by the minimal discharge at the USGS gauge (a), the tidal stage at the most downstream site, A5, (b) displayed periods of strong neap and spring tidal conditions. Neap tides were related to λ_3 moving downstream and spring tides to λ_3 being positioned farther upstream (c).

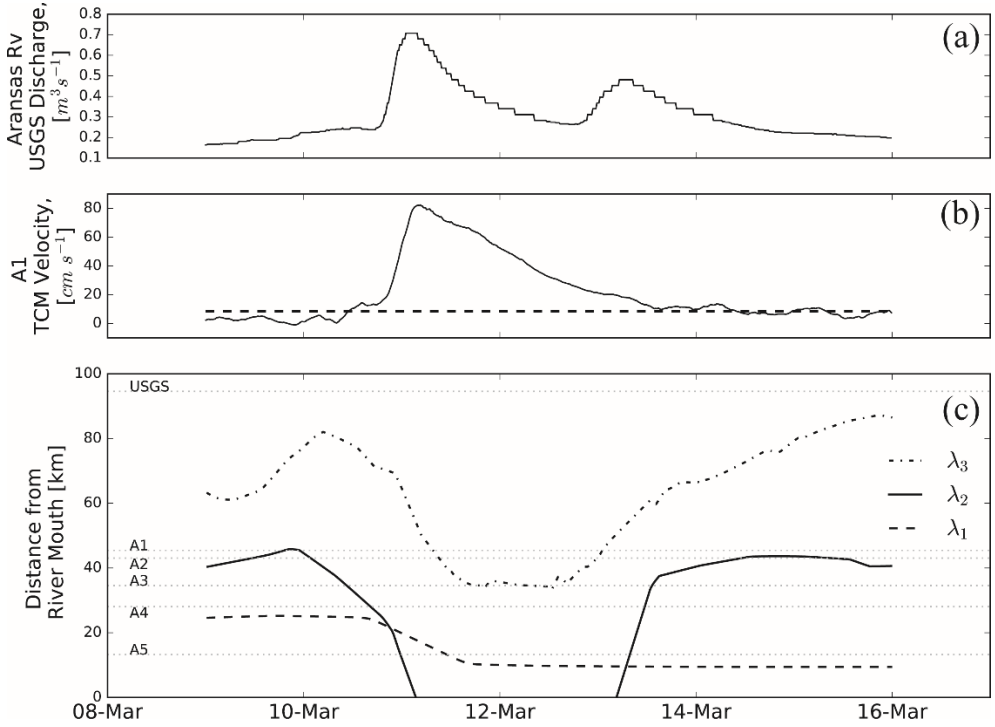

Figure 3.7: The inversion of λ_2 and λ_1 relative positions during a storm event in the Aransas watershed in March 2016. Although the Aransas River USGS gauge did not record a dramatic peak in discharge on 11 March (a), a large amount of freshwater entered the system below the gauge. This runoff caused the TCM velocity at site A1 (b) to significantly exceed the annual 90th velocity percentile (dashed line in (b)), classifying the event at A1 as a significant storm by our criteria. The position of each λ varied in response to the hydrograph peak, including a portion of time when λ_2 was pushed downstream of λ_1 (beginning approximately on 11 March 2016). The inversion of λ_2 and λ_1 was due to riverine discharge overwhelming tidal velocities and creating an entirely unidirectional velocity regime along the length of the river (λ_2 far downstream), while estuarine salt had yet to be extruded from the river (little movement in λ_1).

3.5 DISCUSSION

The goals of this study were threefold: (1) to systematically define the RTFZ and associated nomenclature for the literature; (2) to develop methods to empirically identify an RTFZ in the field; and, (3) to observe temporal dynamics of an RTFZ and its λs as they respond to changes in precipitation, inflow, and tide.

3.5.1 Significance of the RTFZ and its definition

While the RTFZ as a whole marks the transition between riverine and estuarine environments, the RTFZ and each λ represent unique transitional features of ecological and biogeochemical importance along the riverine-estuarine continuum. The tidal and riverine interactions within the RTFZ can create unique residence time conditions that significantly control the timing, magnitude, and composition of terrestrial nutrients discharging to the coastal systems. For example, *Knights et al*. [2017] modeled the change in denitrification rates over a theoretical longitudinal TFZ length. Denitrification rates decreased while nitrification rates increased headed downstream over the length of the TFZ. Thus, potentially over the length of the TFZ, we may see increases in nitrate (NO_3^-) content from riverine conditions. This may mean that TFZs increase the amount of nitrate entering the estuarine environment by nitrifying riverine inputs of ammonia or ammonium. *Knights* et *al.* [2017] proposes that TFZs, as the most downstream endmember of river networks, may have a reduced capacity to remove river-borne N, even though the tidal surface wave fluctuations increase the amount of hyporheic exchange. These transitional environments between the river and estuary are also important metabolically. *Ensign et al.* [2013] described tidal river reaches as "a critical zone affecting the transport of carbon and other biologically relevant elements from watersheds to estuaries." The interaction between riverine and tidal hydrology present within the RTFZ may also have implications for the geomorphology of a coastal river. *Ensign et al.* [2013] investigated the interaction between riverine and tidal hydrology, specifically with regard to channel morphology and energy dynamics, and determined that tidal energy and motion increased the bankfull channel cross-sectional area by a factor of three. RTFZs that exist

within small near-coastal unmonitored watersheds may be associated with substantial pollutant loads, especially if these systems are surrounded by a large population [*Destouni et al.* 2008, *Knights et al.* 2017].

The temporally variable RTFZ length provides a glimpse into the range of residence times experienced within the RTFZ. *Jones et al.* [2017] address and discuss the relationship between residence time and system volume, where increases in system volume relate to elongated residence times. Similarly for RTFZs, observations of kinematic residence times are related at least in part to the volume of the system. Thus, we might expect increased freshwater and nutrient residence times with elongated RTFZ lengths, e.g., post-storm conditions. Although a storm pulse may momentarily push all λs downstream, λ_3 and λ_2 will quickly return to pre-storm locations while λ_1 is slower to return to pre-storm conditions and remains downstream. Thus, for similar pre- and post-storm baseflow discharge, this post-storm, elongated RTFZ likely experiences longer residence times than the pre-storm, shorter RTFZ. These shifts in RTFZ length and residence time may cause the RTFZ to exhibit oscillating residence time character, potentially being described as *oscillic* [*Jones et al.* 2017].

3.5.2 Controls on the downstream limit of the RTFZ, λ_1

While central to the RTFZ definition, each λ also delineates an important feature within the tidal continuum. The downstream extent of the RTFZ is marked by λ_1, which tracks the extent of estuarine saline intrusion. Over extensive periods of baseflow (e.g., monthly to annual time scales), the length of the RTFZ is determined by the rate of upstream estuarine salt transport and so the upstream propagation of λ_1, which shortens the RTFZ over time. Salt transport upstream is generally described as dependent upon the balance between outgoing riverine discharge, residual tidal currents (gravitational circulation) from the upstream-oriented salinity gradient, and other tidal dispersion forces (wind, shear) [*Lerczak et al.* 2006, *Bowen et al.* 2003, *Fischer et al.* 1976]. The rate at which the RTFZ shortens is directly related to the rate of upstream salt transport. As such, the shorter RTFZ during the winter months was strongly related to longer winter periods of

minimal terrestrial freshwater inflow that allowed continued, relatively unimpeded saline intrusion. Specifically, saline encroachment shortens the RTFZ reach that is fresh with tidal bidirectional velocity (i.e., the river reach between λ_2 and λ_1), but does not affect the subsection from λ_2 to λ_3.

Changes in the salinity along the length of the river-estuary continuum, marked by the position of λ_1, can cause substantial shifts in the ecology of the affected reaches. For example, *Palmer et al.* [2011] discussed the importance of freshwater inflow into Texas estuaries, that "inflow hydrology [including water quality] drives estuarine condition and estuarine condition drives biological resource response" with salinity often being the main water quality factor. Similarly, *Pollack et al.* [2011] discussed how extreme freshwater inputs (i.e., flood discharges) and the associated decreases in estuarine salinity reduced estuarine oyster abundance, spat settlement, and filtration rates. Also, *Pollack et al.* [2011] found that "live oyster and dead shell abundance were significantly correlated with salinity." Thus, the location of λ_1 defines the divide between, and the extent of, habitats for species adapted to brackish/saline or fresh waters.

3.5.3 Controls on the transition between uni- and bidirectional flow, λ_2

While λ_1 tracks estuarine intrusion, λ_2 denotes the location within the RTFZ where there is a significant change in discharge character. The position of λ_2 divides the RTFZ into a unidirectional discharge regime upstream and a bidirectional discharge regime downstream. The extent of the bidirectional discharge regime not only characterizes the maximum upstream extent of fine marine sediment deposition, but also increases residence times of water traversing the RTFZ [*Savenije* 2005, *Jones et al.* 2017].

Although tidal energy exerted on the riverine system may slow unidirectional waters upstream of λ_2, reaches downstream of λ_2 experience small net transport over the tidal cycle due to relative flood/ebb tidal symmetry [*Savenije* 2005]. This negligible net transport severely impacts water residence times downstream of λ_2. For example, *Ensign et al.* [2013] analyzed three portions of an RTFZ in the Newport River, NC, USA, all downstream of λ_2, during a week in June 2008.

During the ebb tide, all three tidal reaches on average contained downstream velocities (0.10, 0.19, and 0.29 m s^{-1}), whereas on the flood tide each reach on average exhibited upstream-oriented velocities (-0.07, -0.19, and -0.32 m s^{-1}). Net transport throughout an entire tidal cycle for each site's average conditions was 0.03 m s^{-1} downstream at the most upstream reach, zero movement at the middle reach, and -0.03 m s^{-1} upstream at the most downstream reach. Effectively, the velocity conditions observed downstream of λ_2 indicate potentially long kinematic and solute residence times, which may alter the local benthic biota and sediments between λ_1 and λ_2, compared to upstream of λ_2 [*Ganju et al.* 2004]. The extent of tidal bidirectional discharge may alter biogeochemical processes as well, since bidirectional water transport may potentially increase the amount of hyporheic exchange possible [*Knights et al.* 2017, *Bianchin et al.* 2010]. Thus, the longer the RTFZ's bidirectional reach from λ_1 to λ_2, the greater the opportunity for biogeochemical processes and loads to be altered before discharging into the downstream estuary.

In some systems, λ_3 and λ_2 overlap, creating an RTFZ that has entirely bidirectional flow [*Ensign et al.* 2013, *Knights et al.* 2017]. In such systems, the impacts of both λ_2 and λ_3 create a "non-linear trend in energy dissipation along a tidal gradient" [*Ensign et al.* 2013]. Other systems, such as the Aransas River, exhibit a substantial spatial separation between λ_3 and λ_2, and the RTFZ is composed of two distinct discharge regimes. The ratio presented in eq. (3.2) in section 3.4.2 quantified the portion of the RTFZ that experiences tidal bidirectional flow (Figure 3.5c). Conceptually, a ratio of 0.5 describes an RTFZ that contains equal lengths bi- and unidirectional velocity regimes, whereas a ratio of < 0.5 experiences majority unidirectional velocity, while > 0.5 is majority bidirectional (Figure 3.5c). As the ratio approaches 1.0, the separation between λ_3 and λ_2 becomes negligible. Conversely, when the ratio approaches 0.0, saline encroachment (λ_1) has reached λ_2. These conditions may occur if large riverine freshwater discharge forces λ_2 downstream to reside near λ_1 (riverine dominated endmember in Figure 3.1a), or if prolonged low baseflow conditions have allowed estuarine saline waters to encroach upstream to λ_2. An "infinite" or "undefined" value of the ratio corresponds to all three lambdas existing at the same location (i.e., $\lambda_1 = \lambda_2 = \lambda_3$), describing the tidal dominated endmember in Figure 3.1c. A negative ratio

value is indicative of λ_2 being downstream of λ_1, which may happen briefly during storm pulses (Figure 3.7). (Mathematically, a negative ratio may be obtained if λ_3 were downstream of λ_1; however, this situation may only apply in theory, without extreme evaporation rates altering the water body's salinity.)

The location of λ_2 describes the balance between tidal and riverine forces as well as their interactions with the channel geometry. The position of λ_2 may be estimated where the freshwater and tidal momentums are equivalent during the flood tide. This is largely dependent upon the tidal prism, the volume of water entering the estuary between high and low water slack (HWS, LWS), and how that tidal volume discharges upstream [*Savenije* 2005]. Along the length of the river-estuary continuum, changes in channel geometry will alter the velocity, and thereby the momentum, of both the incoming fresh and estuarine waters [*Savenije* 2005]. For example, for the same discharge magnitude, the increased cross-sectional area near the mouth would theoretically cause velocities to decrease compared to narrower upstream cross-sections. In addition, geometric variations (e.g., channel shape or roughness) will impact the frictional forces that modify the river-estuary continuum's velocity and momentum regimes. Thus, the extent of λ_2, and its separation from λ_3, are greatly dependent upon the channel geometry and the geometric interactions with the tidal discharge regime (e.g., frictional impacts on tidal velocity and the damping/amplification of surface waves) [*Savenije* 2005].

3.5.4 Controls on the upstream limit of the RTFZ, λ_3

Although there is a fair amount of overlap between the importance of λ_2 and λ_3, each λ denotes unique impacts to the estuarine and RTFZ systems. While λ_2 marks the upstream extent of tidal bidirectional discharge, λ_3 denotes the upstream extent of all tidal influence, as evidenced by the extent of tidal surface water stage fluctuations.

The upstream extent of all tidal influence is a consequence of the interaction between riverine discharge, tidal base level, tidal amplitude, and channel geometry and bed slope (i.e., controlling tidal wave amplification or damping) [*Savenije* 2005]. The convergence rate of the

channel's geometry strongly controls whether the tidal surface wave amplifies or dampens along the length of the estuary and RTFZ [*Savenije* 2005]. The magnitude of surface water wave amplification or dampening along the RTFZ length determines the magnitude of the associated tidal pumping (i.e., the tidally induced infiltration and exfiltration of groundwater) [*Knights et al.* 2017]. Tidal pumping may increase the volume of surface water-groundwater exchange that occurs in the RTFZ as compared to reaches upstream. This may also alter the fates of dissolved oxygen (DO) and N [*Knights et al.* 2017]. For tidal systems where the surface waves are damped along the length of the estuary, N removal rates, specifically denitrification rates, may decrease longitudinally from λ_3 upstream to points farther downstream [*Knights et al.* 2017]. Finally, the river state transition at λ_3 corresponds with "lower energy dissipation, reduced sediment transport capacity, and a tendency for channel bed aggradation and resultant channel width expansion" according to *Ensign et al.* [2013].

It was strongly apparent that the lowest portion of the semiannual tide within the Aransas River region of the Gulf of Mexico hindered the upstream reach of tidal stage fluctuations and so the position of λ_3 in the example of the Aransas River [*Ward* 1997]. During the winter months (December – February), this secular tide decreased the base level of the estuary, which may have impeded the upstream extent of the tidal influence. Upon decreasing the tidal base level, channel bed slope may hinder the upstream movement of the tidal wave, either via now overwhelming frictional forces or a newly significant topographic feature that acts as a dam during exceptionally low stage conditions.

Although λ_1 and the associated saline encroachment dictates the length of the RTFZ at long time scales, over daily to weekly time scales λ_3 controls the more rapid length variations of the RTFZ. This is due to the fact that during neap tide the tidal range of the Aransas River system decreases substantially. Thus, the location where the tidal range is approximately 0.05 m, will shift along the river length, depending upon whether the tide is acting as neap or spring tide, or transitioning between the two (Figure 3.6). In fact, a Fourier Transform on the λ_3 location data

defines the strongest control on λ_3 as having period of approximately 13.56 days, similar to fortnightly spring/neap tidal cycles.

3.5.5 Empirical RTFZ identification considerations

The five stage, salinity, and tilt current meter monitoring sites installed along the Aransas River enabled the identification of the local RTFZ, associated λs, and the temporal nature of each. However, some considerations are necessary in order to identify the λs. For instance, thalweg TCM velocity measurements are not fully representative of the spatial variability present in cross-sectional discharge. Heterogeneous vertical and lateral velocity profiles are possible throughout a tidal cross-section from gravitational or residual circulation [*Fischer* 1976, *Savenije* 2005]. However, the thalweg velocities are indicative of the overall cross-sectional behavior, especially with regards to directionality and timing. It is the overall upstream or downstream orientation of discharge and when the transitions occur that are vital to the proper identification of λ_2, and so thalweg velocity was sufficient for this purpose.

The presented methodology is also based on near-bed thalweg salinity, likely the farthest upstream extent of observed isohalines, as gravitational circulation will preferentially transport salt upstream along the bed [*Fischer* 1976, *Savenije* 2005]. Thus, although λ_1 is supposed to represent average cross-sectional conditions, the calculated location of λ_1 may potentially be biased slightly upstream of the actual location, leading to RTFZ lengths generated by this approach to be conservative estimates.

In addition to the above considerations, alternate thresholds for λ identification could have been used. For example, when locating λ_2, we defined a unidirectional discharge regime to be present when 90% of the velocity observations over a tidal cycle were oriented downstream. In other words, λ_2 was identified where the longitudinally interpolated 10^{th} percentile of velocity observations equaled zero (Figure 3.3g-j). Why not determine the upstream extent of bidirectional flow, with the 0^{th} percentile? Or in other words, why not identify λ_2 at the location where no bidirectional flow is recorded? The definition of λ_2 aims to account for what portion of a

bidirectional velocity scheme is functionally relevant to the hydro-ecological river system and its analysis. For our study, identifying λ_2 using the 10th percentile was sufficient to adequately represent a location where discharge is transitioning from uni- to bidirectional and for which the small downstream duration of flow ($\leq$ 10% of 24 hours) was likely not ecologically or biogeochemical significant. Future studies might adapt to suit the goals, interests, and requirements of their study, so long as it remains consistent with the fundamental principle of λ_2: that it represents the transition point between unidirectional (riverine) and bidirectional (tidal) discharge.

Similarly, an alternate threshold could have been used to identify λ_3. Conceptually, at the location where there is no evidence of tidal surface waves, the $\frac{dS}{dt}$ interquartile range threshold of λ_3 should be zero. However, such a threshold is not a plausible empirical definition. In many tidal systems (e.g., the Hudson, Potomac, Scheldt, and Incomati Rivers) tidal influence extends hundreds of kilometers inland unless there is a dam impeding the transport of wave energy upstream [*Findlay et al.* 1991, *Cole et al.* 1992, *Lovley and Phillip*s 1986a, *Lovley and Phillip*s 1986b, *Arndt et al.* 2007, *Arndt et al.* 2011, *Savenije* 2005]. *Savenije* [2005] proposes that in a theoretically "ideal estuary" tidal surface waves may travel an infinite distance inland. The 5 cm minimum interquartile range of surface water level oscillations chosen in this study is a functionally significant threshold. This threshold range provides a conservative estimate for the extent of tidal fluctuations. For example, *Knights et al.* [2017] examined tidal freshwater nitrification and denitrification rates down to a tidal range of 20 cm. *Robbins et al.* [2015] produced a model to identify potential sites for the installation of "tidal-stream energy converters (TECs)" that convert tidal motion and energy into electricity with RMSE of 15 and 5 cm for the amplitudes of the lunar (M_2) and solar (S_2) semi-diurnal tidal constituents. Thus, our threshold range is similar to the small achievable uncertainty of a tidal resource management model. However, future studies may prefer a different threshold; for example, a study on groundwater discharge or hyporheic processes might define λ_3 by a stage range that has negligible effects on tidal pumping.

An additional consideration for identifying λ_3 was our simple method for identifying storm and baseflow periods. For our study, a single velocity threshold, the 90th percentile of all 15-minute

velocity samples in a year, isolated storm periods from baseflow periods. This criterion was sufficient due to the Aransas River's lack of an annual hydrograph, with most peaks are in response to precipitation pulses [*Bruesewitz et al.* 2013, *Mooney and McClelland* 2012]. However, for systems containing a cyclic annual hydrograph a more complex system for defining storm and baseflow periods will be necessary (e.g., using an FFT to predict the annual discharge cycle, then normalize, to determine the timing of elevated non-tidal stages).

In this initial RTFZ identification analysis, we analyzed λ locations using a 24-hour moving window around each timestamp. However, analyses of RTFZ and thus λ identification in other systems may not need a moving window 24 hours long. The Aransas River experiences strong diurnal tide during spring tide, yet mixed-to-semidiurnal tide during neap. Thus, the moving window was set to 24 hours to represent the longest regularly repeating tidal period present within our dataset [*Evans et al.*, 2012; *Mooney and McClelland* 2012]. For a different system, (e.g., solely dominated by semidiurnal tide) a moving window of a different length (e.g., 12 hours) may be adequate. However, the length of the moving window has implications for the resolution of the physical properties described by the analysis. Any movement of λ_2 and λ_3 that occurs on a timescale shorter than half of the longest tidal period (i.e., < 12 hours for the Aransas River) cannot be resolved. For a shift in conditions (e.g., from tidal to riverine) to be robustly observable, the majority of time stamps analyzed must exhibit the new hydrologic conditions. Thus, in the Aransas River, a storm of significant intensity must exceed at least 12 hours in duration for the analysis to properly resolve whether the hydrologic character shifted from tidal baseflow conditions to riverine.

For the empirical λ identification along the Aransas River, the spacing and number of the long-term monitoring stations limited the resolution (and thereby the accuracy) of determining the λ locations. Increasing the number of stations would have improved the identification of the λs, although at monetary cost. For example, a monitoring location at the river mouth would have more accurately allowed us to identify the location of λ_1 without using the Gulf of Mexico as an assumed interpolation end-point. An additional monitoring location between A1 and the USGS gauge,

upstream of tidal stage fluctuations, would have increased that accuracy of the λ_3 locations. However, a monitoring location could not be installed at either of these locations due to limited access to upstream river reaches (private land and unnavigable depths) and safety concerns near the mouth of the river.

On the other hand, although possibly lacking high resolution, rough λ locations might be estimated in systems using solely public resources, e.g., a coastal river monitored by USGS gauges at a tidal and non-tidal locations and by a nearby NOAA-sponsored tidal mooring with all three sites recording discharge (or velocity), water depth, and salinity. In such a situation, where a system is monitored at only three points, the resolution of interpolated λ locations will be lower but could provide a useful screening tool for the presence and nature of RTFZs.

3.5.6 Time scale responses of the RTFZ

The RTFZ responds at tidal, event, seasonal, and annual time scales, as well as time scales of larger global climate cycles (e.g., El Niño Southern Oscillation, or ENSO) and trends (e.g., global warming). Effects at the tidal time scales were thoroughly discussed in sections 3.5.2 – 3.5.4. This following section describes the potential and observed responses of RTFZs to other external stimuli across these varying time scales.

3.5.6.1 Event time scales

Rainfall-runoff events typically occur over time scales of hours to days. In the Aransas River example, the shortest event hydrograph during the monitored year, as measured at the upstream USGS gauge, was 1.25 hours and the longest lasted 11.0 days. As expected, the arrival of the storm peaks to the more downstream monitoring stations (A1-A5) was progressively lagged and spread over a wider time window with greater distances downstream from the gauge. (See Appendix F.) However, in some instances the gauge did not register an increase in discharge, even though the downstream monitoring sites reacted to influx of water (Figure 3.7a and 3.7b). The Aransas River USGS gauge is very far upstream and represents a small portion of the overall watershed. The potential exists for a storm to bypass the portion of the watershed feeding the gauge

and still provide a substantial amount of water to the river and monitoring sites (A1-A5) downstream.

Large influxes of terrestrial freshwater alter the system's stage, velocity, and salinity, although not equally. During a sufficiently large storm, the increased riverine forces may expel λ_2 from the river creating an entirely unidirectional discharge regime (Figure 3.7). Such a large storm would also likely push λ_3 and λ_1 downstream (Figure 3.7). However, the response of λ_1 occurs after, and much more slowly, than the downstream translation of λ_2 and λ_3 (Figure 3.7c). For the storm conditions depicted in Figure 3.7, after the storm pulse has passed λ_2 and λ_3 quickly return to their pre-storm positions while λ_1 needed until May 2016 (almost 2 months later) to return to pre-storm positions. The slower rate of recovery for λ_1 determines the long-term impact of a storm on the length of the RTFZ. If the storm is large enough to push λ_1 downstream, then the RTFZ is effectively lengthened post-storm. However, if the storm is not large enough to impact the location of λ_1, the storm may introduce enough riverine energy to push λ_3 and/or λ_2 downstream. If so the RTFZ will be shortened but only for the storm duration.

3.5.6.2 Seasonal time scales

Seasonal cycles strongly influence the length and position of the RTFZ and associated λs. For example, summer drought and minimal inflow conditions, often observed in a semiarid climate like that of south Texas, allow estuarine salt to intrude far upstream, shortening the length of the RTFZ. The extensive saline intrusion potentially experienced during drought conditions also creates conditions that more readily facilitate an inversion of λ_1 and λ_2 (i.e., where λ_1 is upstream of λ_2). As discussed in the section 3.4.2 and 3.5.6.1, large storm events promote the inversion of λ_1 and λ_2 due to energy transport being more rapid than mass transport. Given long enough minimal baseflow conditions, estuarine salt will intrude significantly upstream (i.e., $\lambda_1 = \lambda_2$) and a much smaller storm will be necessary to create an inversion of λ_1 and λ_2. These smaller storms may not extrude λ_1 significantly and so may result in λ_1-λ_2 inversions occurring more frequently. Conversely, if an RTFZ experiences a significant rainy season, that rainy season may serve to

elongate the RTFZ by pushing λ_1 (i.e., estuarine salinity) downstream or even "eliminate" the RTFZ by expelling λ_1 beyond the river mouth, which removes the river bank constraints on the system and changes it to a more general TFZ. Thus, a significantly strong rainy season may constrain the RTFZ to only exist during the dry season, which may make the RTFZ a seasonal rather than perennial occurrence.

3.5.6.3 Annual time scales

For systems experiencing more substantial variation within their annual hydrograph, the location and length of the RTFZ may also experience an annual cycle in response. For example, peak discharge for a snow-driven hydrograph would occur during the late spring to early summer months, during which time the RTFZ may be translated downstream to be closer to the mouth. When river discharge decreases during the autumn and winter months, the RTFZ may then shift upstream. Also, the length of the RTFZ may change with the annual hydrograph, lengthening during the months of increased riverine discharge, and shortening during the months of diminished inflow. Alternatively, the annual hydrograph's increase in discharge may cause the λ_1 to be extruded beyond the river mouth and eliminate the RTFZ. In such a system, the return of diminished discharge conditions may coincide with the return of the seasonal RTFZ.

Some estuarine systems also exhibit annual cycles, such as due to the semiannual secular tide of the northwest Gulf of Mexico [*Ward* 1997]. These annual tidal trends may also impact the location and size of the RTFZ. The semiannual low tides may move λ_3 downstream of its typical position as tidal base level drops and tidal forces cannot as effectively overcome the river's energy gradient. Conversely, the semiannual high tide may push λ_3, and potentially λ_1, upstream due to the higher tidal base level overcoming more of the river's energy gradient. For otherwise similar estuarine saline encroachment (i.e., λ_1 position) over the year, the RTFZ may thus lengthen and shorten in synchronization with the semiannual high and low tides. Potentially, these semiannual high and low tides may also extend and shorten the extent of bidirectional flow, or λ_2. During observation of the Aransas River's RTFZ, the median position of λ_3 was farther upstream during

the summer months of 2015 (i.e., secular high-low tide) than during the 2015-2016 winter (i.e., secular low-low tide) (Figure 3.4a and 3.4b).

3.5.6.4 Time scales of global climate cycle

Global climate cycles influence regional precipitation and evaporation conditions, which in turn will impact the position and length of an RTFZ. For example, in south Texas, the El Niño Southern Oscillation (ENSO), which has a recurrence every 2-7 years and will last from 9 to 12 months [*NOAA* 2017b], is typically associated with increased precipitation, increased discharge, cooler temperatures, and decreased evaporation rates [*Wolter et al.* 1999, *Ropelewski and Halpert*, 1986]. The year of our Aransas RTFZ observations was associated with strong El Niño conditions. During the monitoring period the Oceanic Niño Index (ONI) of the Pacific Ocean's Niño 3.4 region remained well above 0.5 for 11 months, exhibiting indications of a "strong El Niño event" [*NOAA* 2017a]. The increased discharge, especially the large storms in May and June 2015 that preceded the study period, pushed much of the estuarine salt downstream of our sampling locations. In addition, throughout the study period, the regular precipitation inputs and associated increased discharge events continued to hold λ_1 downstream of our most downstream monitoring site (A5). Although each precipitation event would also cause λ_2 and λ_3 to temporarily shift downstream, the recovery interval (i.e., the amount of time needed for a given λ to return to its previous location) for λ_1 was much longer (controlled by the rate of salt transport upstream) than that of λ_2 and λ_3 (controlled by the rate of energy transport). Thus, results of shifting λ_1 downstream had longer lasting effects, past the duration of the single event, effectively re-lengthening the RTFZ.

3.5.6.5 Time scales of global climate trends

Longer-term climate trends such as global warming and rising sea levels are associated with even longer decadal or centennial time scales and may have dramatic impacts on RTFZ placement and location in the future. Rising sea level and the associated rise in tidal base level will move tidal influence farther upstream where able, meaning that λ_3, λ_2, and λ_1 will be pushed farther inland. However, if the extent of tidal influence is impeded, whether artificially (e.g., a dam) or

naturally (e.g., topographic jump), rising sea level will shorten the RTFZ via increased saline intrusion. In such a scenario, sufficient climate-change-derived saline intrusion will collocate the λs and eliminate the RTFZ. In conjunction with possible warming and increased evaporation, rising base level might make the average annual RTFZ condition observed in south Texas more like that observed in the present-day summer, when the high secular (semi-annual) tide provides a simulacrum of a higher base level, and potential evaporation is also seasonally high. In addition, rising sea level may increase the amount of saline intrusion upstream. Thus, over time, all RTFZs, globally, may shift upstream with rising sea level except in unique cases where inland precipitation increases enough to offset sea level rise and climate warming effects.

On the same time scale as these larger global climate trends, geomorphological processes such as channel avulsion and migration may further alter the interaction of riverine discharge and tide [*Ward et al.,* 2002]. Over these decadal to centennial time scales, the morphologically altered riverine-tidal interactions may impact the location and length of an RTFZ [*Ward et al.,* 2002].

3.6 Summary and Conclusion

This study sought to (1) introduce and formally define the RTFZ and its important transition points (i.e., λs), (2) provide a methodology for empirically denoting and recording the location of an RTFZ and an example application to the Aransas River in south Texas, and (3) investigate the response of an RTFZ to variations in precipitation and tide over the course of a year.

The study defined the RTFZ as a river reach composed of freshwater chemistry yet tidal physics that is bounded upstream by unidirectional fresh riverine discharge and downstream by a tidal estuarine brackish water column, all of which is upstream of the river mouth. The upstream limit of the RTFZ, or location at which the daily interquartile range of surface water stage became less than 5cm, was denoted λ_3. The downstream limit of the RTFZ, or location at which bed salinity became greater than 2.0 PSU, was denoted λ_1. An RTFZ requires that λ_1 (and λ_3) be located within the river banks. The intermediate critical point of the RTFZ, where unidirectional riverine flow

transitioned to bidirectional tidal flow, was denoted λ_2. A ratio R, of the bidirectional RTFZ reach length over the total RTFZ reach length was also defined to summarize the dominant longitudinal flow character of the RTFZ. These definitions provide a standardized framework for drawing together the as yet dispersed and somewhat informal discussions and anecdotal observations of TFZ conditions in river systems around the world (e.g., *Findlay et al.* [1991], *Cole et al.* [1992], *Lovley and Phillip*s [1986a], *Lovley and Phillip*s [1986b], *Arndt et al.* [2007], *Arndt et al.* [2011], *Savenije* [2005]).

In the example given, the median and mean RTFZ length observed in the Aransas River during 01 July 2015 to 01 July 2016 was 59.90 and 54.93 km, respectively. The length of the RTFZ shrank at a fairly consistent rate, related to upstream salt flux, during extended periods of baseflow, while lengthening rapidly in response to deluges typical of ENSO conditions in south Texas [*Ropelewski and Halpert* 1986, *Wolter et al.* 1999]. The upper limit of the RTFZ (λ_3) responded as expected to external stimuli: λ_3 was pushed downstream during large storm events only to return upstream as the hydrograph peak receded, shifted longitudinally in response to rising and falling base level with the annual secular tide, and translated upstream and downstream during the spring and neap tidal cycles during baseflow. Interestingly, the upstream extent of bidirectional (i.e., tidal) discharge (λ_2) was quite stationary over the monitored year, at approximately 44 km upstream of the river mouth. While, λ_3 served as the short-term control on the RTFZ length (i.e., up to weekly time scales), λ_1 regulated the long-term length of the RTFZ, as extended periods of baseflow allowed estuarine saline waters to encroach upstream at an average rate of 0.26 km d^{-1} (Figure 3.5d-g).

Using the proposed systematic methods and nomenclature for identifying RTFZs, future studies may seek to determine how prevalent these transitional environments are along global coastlines, especially as rising sea level will likely increase the extent of tidal influence upstream. Also, investigations into the residence time of the RTFZ [*Jones et al.* 2017] and its impacts on the timing and magnitude of nutrients being transported to coastal environments [*Mooney and McClelland* 2012] are needed. A greater understanding of the RTFZ, which was, until recently, an

undiscussed portion of the river-estuarine continuum, is needed to inform our policy decisions about environmental flows and MDLs reaching our coastal environs. This need is especially great as coastal populations continue to increase and pose a greater threat to the pollution of coastal waterways [*Neumann et al.* 2015, *Destouni et al.* 2008, *Johnson* 2009].

3.7 ACKNOWLEDGMENTS

This material is based upon work supported by the National Science Foundation under Grant No. 1417433. Any opinions, findings, and conclusions or recommendations expressed in this material are those of the authors and do not necessarily reflect the views of the National Science Foundation.

3.8 REFERENCES

Aretxabaleta, A. L. *et al.* Near-bottom circulation and dispersion of sediment containing Alexandrium fundyense cysts in the Gulf of Maine during 2010–2011. *Deep Sea Research Part II: Topical Studies in Oceanography* **103,** 96–111 (2014).

Arndt, S., Vanderborght, J.-P. & Regnier, P. Diatom growth response to physical forcing in a macrotidal estuary: Coupling hydrodynamics, sediment transport, and biogeochemistry. *Journal of Geophysical Research: Oceans* **112,** C05045 (2007).

Arndt, S., Lacroix, G., Gypens, N., Regnier, P. & Lancelot, C. Nutrient dynamics and phytoplankton development along an estuary–coastal zone continuum: A model study. *Journal of Marine Systems* **84,** 49–66 (2011).

Bianchi, T., Pennock, J., and Twilley, R. *Biogeochemistry of Gulf of Mexico estuaries*. (John Wiley, 1999).

Bianchin, M., Smith, L., & Beckie, R. (2010). Quantifying hyporheic exchange in a tidal river using temperature time series. *Water Resources Research*, *46*(7), W07507. https://doi.org/10.1029/2009WR008365

Brock, D. A. Nitrogen Budget for Low and High Freshwater Inflows, Nueces Estuary, Texas. *Estuaries* **24,** 509–521 (2001).

Bruesewitz, D. A., Gardner, W. S., Mooney, R. F., Pollard, L. & Buskey, E. J. Estuarine ecosystem function response to flood and drought in a shallow, semiarid estuary: Nitrogen cycling and ecosystem metabolism. *Limnol. Oceanogr* **58,** 2293–2309 (2013).

Cole, J. J., Caraco, N. F. & Peierls, B. L. Can Phytoplankton Maintain a Positive Carbon Balance in a Turbid, Freshwater, Tidal Estuary? *Limnology and Oceanography* **37,** 1608–1617 (1992).

Destouni, G., Hannerz, F., Prieto, C., Jarsjö, J. & Shibuo, Y. Small unmonitored near-coastal catchment areas yielding large mass loading to the sea. *Global Biogeochemical Cycles* **22,** n/a-n/a (2008).

Dyer, K. R. *Estuaries: a physical introduction*. (John Wiley, 1997).

Ensign, S. H., Doyle, M. W. & Piehler, M. F. The effect of tide on the hydrology and morphology of a freshwater river: TIDAL RIVER HYDROLOGY AND MORPHOLOGY. *Earth Surface Processes and Landforms* **38,** 655–660 (2013).

Evans, A., K. Madden, and S. M. Palmer (Eds.) (2012), *The Ecology and Sociology of the Mission-Aransas Estuary,* Mission-Aransas Natl. Estuarine Res. Reserve, 200 pp., Port Aransas, Tex.

Findlay, S., Pace, M. & Lints, D. Variability and transport of suspended sediment, particulate and dissolved organic carbon in the tidal freshwater Hudson River. *Biogeochemistry* **12,** 149–169 (1991).

Fulbright, T. E., Diamond, D. D., Rappole, J. & Norwine, J. The coastal sand plain of southern Texas. *Rangelands* 337–340 (1990).

Ganju, N. K., Schoellhamer, D. H., Warner, J. C., Barad, M. F., & Schladow, S. G. (2004). Tidal oscillation of sediment between a river and a bay: a conceptual model. *Estuarine, Coastal and Shelf Science, 60*(1), 81–90. https://doi.org/10.1016/j.ecss.2003.11.020

Intergovernmental Panel on Climate Change (IPCC) (2013), Climate change 2013: The physical science basis, in *Contribution of Working Group I to the Fifth Assessment Report of the Intergovernmental Panel on Climate Change*, edited by T. F. Stocker, 1535 pp., Cambridge Univ. Press, Cambridge, U. K.

Johnson, S. L. A general method for modeling coastal water pollutant loadings. (The University of Texas at Austin, 2009).

Jones, A. E., Hodges, B. R., McClelland, J. W., Hardison, A. K. & Moffett, K. B. Residence-time-based classification of surface water systems. *Water Resources Research* (2017). doi:10.1002/2016WR019928

Knights, D., Sawyer, A. H., Barnes, R. T., Musial, C. T. & Bray, S. Tidal controls on riverbed denitrification along a tidal freshwater zone: Tides on Riverbed Denitrification. *Water Resources Research* **53,** 799–816 (2017).

Lovley, D. R. & Phillips, E. J. P. Organic Matter Mineralization with Reduction of Ferric Iron in Anaerobic Sediments. *Appl Environ Microbiol* **51,** 683–689 (1986).

Lovley, D. R. & Phillips, E. J. P. Availability of Ferric Iron for Microbial Reduction in Bottom Sediments of the Freshwater Tidal Potomac River. *Appl. Environ. Microbiol.* **52,** 751–757 (1986).

Maio, C. V. *et al.* Sediment dynamics and hydrographic conditions during storm passage, Waquoit Bay, Massachusetts. *Marine Geology* **381,** 67–86 (2016).

Mooney, R. F. & McClelland, J. W. Watershed Export Events and Ecosystem Responses in the Mission–Aransas National Estuarine Research Reserve, South Texas. *Estuaries and Coasts* **35,** 1468–1485 (2012).

National Estuarine Research Reserve (NERR) (2015). Tunnell, J., Buskey, E. J. & Peterson, T. (Eds.) *Freshwater Inflows: Determining Flow Regimes in the Face of Land Use Change, Climate Change, and Other Unknowns*. 47 (National Estuarine Research Reserve, 2015).

National Oceanic and Atmospheric Administration (NOAA) (2017a). Climate Prediction Center - Monitoring & Data: ENSO Impacts on the U.S. - Previous Events. *National Weather Service - Climate Prediction Center* (2015). Available at: http://www.cpc.ncep.noaa.gov/products/analysis_monitoring/ensostuff/ensoyears.shtml. (Accessed: 19th July 2017)

National Oceanic and Atmospheric Administration (NOAA) (2017b). El Niño Southern Oscillation (ENSO). *Earth System Research Laboratory: Physical Sciences Division* (2017). Available at: https://www.esrl.noaa.gov/psd/enso/enso_101.html. (Accessed: 19th July 2017)

National Oceanic and Atmospheric Administration (NOAA) Tides & Currents (2017c), Station Selection—NOAA Tides & Currents NOAA Tides & Currents—Station Selection, National Oceanic and Atmospheric Administration, Washington, D. C. [Available at https://tidesandcurrents.noaa.gov/stations.html?type5Water1Levels#Texas, accessed 19th July 2017.]

Neumann, B., Vafeidis, A. T., Zimmermann, J. & Nicholls, R. J. Future Coastal Population Growth and Exposure to Sea-Level Rise and Coastal Flooding - A Global Assessment. *PLOS ONE* **10,** e0118571 (2015).

Odum, W. E. Comparative Ecology of Tidal Freshwater and Salt Marshes. *Annual Review of Ecology and Systematics* **19,** 147–176 (1988).

Palmer, T. A., Montagna, P. A., Pollack, J. B., Kalke, R. D. & DeYoe, H. R. The role of freshwater inflow in lagoons, rivers, and bays. *Hydrobiologia* **667,** 49–67 (2011).

Pollack, J. B., Kim, H.-C., Morgan, E. K. & Montagna, P. A. Role of Flood Disturbance in Natural Oyster (Crassostrea virginica) Population Maintenance in an Estuary in South Texas, USA. *Estuaries and Coasts* **34,** 187–197 (2011).

Ropelewski, C. F. & Halpert, M. S. North American Precipitation and Temperature Patterns Associated with the El Niño/Southern Oscillation (ENSO). *Mon. Wea. Rev.* **114,** 2352–2362 (1986).

Russell, M. J., Montagna, P. A. & Kalke, R. D. The effect of freshwater inflow on net ecosystem metabolism in Lavaca Bay, Texas. *Estuarine, Coastal and Shelf Science* **68,** 231–244 (2006).

Savenije, H. H. G. *Salinity and tides in alluvial estuaries*. (Elsevier, 2005).

United States Geological Survey (USGS) (2017a), USGS Current Conditions for USGS 08189700 Aransas Rv nr Skidmore, TX, USGS NWIS United States Geological Survey, Reston, Va. [Available at https://waterdata.usgs.gov/tx/nwis/uv/?site_no=08189700, accessed May 2017]

United States geological Survey (USGS) (2017b), USGS Current Conditions for USGS 08211200 Nueces Rv at Bluntzer, TX, USGS NWIS United States Geological Survey, Reston, Va. [Available at https://waterdata.usgs.gov/tx/nwis/uv/?site_no=08211200, accessed May 2017]

Ward, G. H. (1997). Process and Trends of Circulation Within the Corpus Christi Bay National Estuary Program Study Area. *Corpus Christi Bay National Estuary Program, CCBNEP-21*.

Ward, J. V., Tockner, K., Arscott, D. B., & Claret, C. (2002). Riverine landscape diversity. *Freshwater Biology*, *47*(4), 517–539. https://doi.org/10.1046/j.1365-2427.2002.00893.x

Wolter, K., Dole, R. M. & Smith, C. A (1999). Short-term climate extremes over the continental United States and ENSO. Part I: Seasonal temperatures. *Journal of Climate; Boston* **12,** 3255–3272.

Yankovsky, A. E., Torres, R., Torres-Garcia, L. M. & Jeon, K. Interaction of Tidal and Fluvial Processes in the Transition Zone of the Santee River, SC, USA. *Estuaries and Coasts* **35,** 1500–1509 (2012).

Chapter 4:
Creation of a Tidal Rating Curve by Expansion of Classic River Gauging Methods

ABSTRACT

Although river discharge to the ocean is one of the most fundamental processes of earth, quantifying tidally influenced discharge is often laborious and expensive. This study provides an expansion of classical river gauging methods to gauge the bidirectional discharge of tidal rivers. The tidal rating curve model incorporates the stage-rate-of-change into the classic model relating discharge to stage. A method using inexpensive tilt current meters is also developed for monitoring tidal flow without requiring expensive acoustic doppler instrumentation or computationally expensive modeling. The tidal rating curve model relating discharge, stage-rate-of-change, and stage was applied to eight monitoring stations along the Mission and Aransas Rivers of south Texas, USA, and to 12 tidal United States Geological Survey (USGS) gauging sites. Phase offset (offset between tidal stage and velocity observations) for the Mission and Aransas Rivers indicated that each river was strongly influenced by standing wave effects and that stage-rate-of-change is a useful variable for approximating discharge. The resulting tidal rating curve models explained the majority of the variation between estimated and observed baseflow discharges, especially the 12 USGS site models, which exhibited r^2 values greater than 0.60 and as high as 0.97. The Mission and Aransas models showed that storm periods contribute the majority of discharge, even though baseflow conditions dominate the time series. The Mission and Aransas models' baseflow discharge reflect the negligible flow observed at each system's upstream non-tidal USGS gauge. The typical negligible baseflow discharge likely promotes extended residence times throughout the rivers' tidal freshwater zones.

4.1 INTRODUCTION

Long-term records of volumetric discharge describe riverine flow and transport conditions and enable the investigation of nutrient and freshwater residence times. These residence times have implications for instream and downstream aquatic biota [*Soballe and Kimmel* 1987, *Humphries et al.* 2014]. Obtaining accurate discharge observations may involve time-consuming field work [*Huhta* 2002, *Dingman* 2008] or permanent installations of expensive acoustic doppler instrumentation (e.g., *Levesque* [2004], *Hittle et al.* [2004]). However, accurate estimates of discharge may be acquired through the use of a discharge rating curve, where riverine discharge measurements are modeled from records of stage based on model calibration from paired discharge and stage data [*Dingman* 2008, *Dottori et al.* 2009]. The modeled relationship encompasses the effects of numerous factors influencing the site's discharge, including cross-sectional area, roughness, and bedslope [*Dingman* 2008]. These rating curves allow for the estimation of discharge magnitude from observations of stage without requiring expensive installations for discharge measurements.

Discharge and residence time within tidal systems also play a vital role in determining the composition of instream and downstream estuarine biota [*Palmer et al.* 2011, *Pollack et al.* 2011, *Jones et al.* 2017]. Due to the importance of freshwater discharge into coastal environments, *Moftakhari et al.* [2013] called for more discharge gauging stations to be installed closer to the coast, rather than well upstream of tidal influence (i.e., 100+ km inland) as is often intentionally the case. However, logistical difficulties have thus far prevented the creation of a rating curve for modeling discharge in tidal systems. The primary issue with the creation of a tidal rating curve is that a given value of stage is non-unique with respect to discharge observations. In other words, as tidal stage cycles and repeats the same stage values during flood and ebb tides, the observed discharge will be different.

To address this issue of non-unique stage, the United States Geological Survey (USGS) presently employs the Index-Velocity Method for gauging tidal rivers [*Ruhl and Simpson* 2005, *Levesque and Oberg* 2012]. The Index-Velocity method uses permanently installed acoustic

doppler velocity meters (ADVMs) to obtain velocity measurements (i.e., the "index velocity") that are then scaled up to estimates of mean channel velocity. This mean velocity is applied across the gauging site's cross-sectional area to model volumetric discharge. A series of detailed topographic cross-sectional surveys allow the USGS to estimate cross-sectional area accurately from a given measurement of stage. For greater detail, refer to the work of *Ruhl and Simpson* [2005] and *Levesque and Oberg* [2012]. The Index-Velocity Method does not directly relate stage to discharge and, thus, circumvents the non-unique stage issue inherent to tidal systems. However, the method does require the permanent installation and maintenance of an ADVM to obtain index velocity measurements.

Since river discharge to the coastal environment plays a major role in the global water budget and sediment supply to the ocean, studies have worked to improve calculations of freshwater tidal discharge. For example, *Moftakhari et al.* [2013] modeled tidal discharge estimates (TDEs) from historical records of tidal statistics. These TDEs were then compared against monthly averaged river flow conditions with a particular emphasis on elevated flood discharge conditions. However, *Moftakhari et al.* [2013] did not emphasize calculations or comparison of instantaneous tidal discharge under baseflow conditions.

Due to the vertical and horizontal stratification inherent in tidal systems, some studies (e.g., [*Shen and Haas* 2004]) gauge tidal river reaches using complex three-dimensional (3D) computer models that, while informative, do not provide real-time estimations of discharge. These models may provide insight into the cross-sectional heterogeneity of tidal freshwater discharge, but cannot provide real-time (i.e., occurring at present) estimates of discharge. For example, *Shen and Haas* [2004] investigated the water age and residence time of freshwater within the tidal York River. From their three-dimensional modeling study, *Shen and Haas* [2004] determined that water age distribution (both longitudinally and vertically) resembles the typical estuarine salinity distribution. They attribute this pattern to the control gravitational circulation exerts over the majority of mass transport within the estuary. However, the computationally expensive 3D model

could not produce discharge estimates nor residence times for present conditions along the river length.

Modeling studies, in fact, are working on methods for decreasing the computational expense of modeling tidal river discharge. For example, *Heniche et al.* [2000] presented a two-dimensional finite element model to estimate velocity fields within a tidal system that attempted to improve on classical modeling methods by simplifying their approach. However, the "speed of run" was still primarily dependent on the "solver to be used" [*Heniche et al.* 2000]. This implies that without the proper solver, software, or even hardware, a simplified tidal discharge model may still be temporally computationally expensive. However, present and future technological advancements in both hard- and software will minimize computational expense. Thus, although not providing real-time estimates of tidal discharge, the computational expenses needed for finite element estimates of discharge may soon become affordable.

To provide a less expensive method (both monetarily and computationally) for recording baseflow tidal discharge, this chapter proposes the introduction of stage-rate-of-change ($\frac{dS}{dt}$) into the classical stage-to-discharge relationship of a tidal rating curve. This new relationship addresses the non-unique tidal stage by pairing stage observations with records of $\frac{dS}{dt}$. The $\frac{dS}{dt}$ measurements describe in which part of the tidal cycle (flood or ebb tide) the stage occurred. For example, if the present tidal stage is 3 m and is associated with a negative $\frac{dS}{dt}$ measurement, we know that this stage magnitude is associated with the falling (i.e., ebb) tide. However, when the 3 m stage returns and is associated with a positive $\frac{dS}{dt}$ value, this new observation occurred during the rising (i.e., flood) tide. Incorporating how each stage measurement relates to the tidal cycle through $\frac{dS}{dt}$ provides an expansion to river gauging methods that accurately enables the estimation of tidal discharge.

An additional obstacle to the tidal rating curve is that tidal river systems experience both riverine and tidal character. For a tidal river, baseflow conditions are likely dominated by tidal character, such as non-unique stage and bidirectional discharge (i.e., discharge oriented upstream and downstream throughout the tidal cycle). However, large increases in riverine discharge may

overwhelm the system's tidal character and cause the system's discharge to emulate riverine behavior [see Chapter 3 and *Jones et al.* 2017, *Ganju et al.* 2004]. Thus, a rating curve designed for a tidal river must be able to encapsulate and provide accurate discharge estimates for both riverine and tidal endmember characters.

We applied the proposed method to the Mission and Aransas Rivers of south Texas, USA, using discharge, stage, and velocity data we collected. Additional analyses were performed on baseflow conditions of discharge and stage from twelve USGS tidal gauging sites to demonstrate replications of the method.

4.2 METHODS

4.2.1 Mission and Aransas River Field Area

The Mission-Aransas (M-A) estuary, along the central Texas Gulf Coast, represents the western gulf biogeographic subregion as a part of the National Estuary Research Reserve (NERR) system [*Evans et al.* 2012]. Two freshwater rivers, the Mission and Aransas Rivers, directly feed the M-A estuary from the west and north flowing into Copano and Mission Bays, respectively. Although typically a diurnal, microtidal system (Copano Bay tidal range is 0.15 m), a highly convoluted tidal signal reaches the Mission and Aransas Rivers due to the geometry-effects of the interconnected bays [*Evans et al.* 2012, *Bianchi et al.* 1999, *Bruesewitz et al.* 2013, *Mooney and McClelland* 2012].

The region's sub-humid to semiarid-subtropical climate generates extreme variability in precipitation (tropical storms, hurricanes, and drought) and strong seasonal oscillations in wind and temperature [*Evans et al.* 2012, *Fulbright et al.* 1990]. The elevated summer temperatures often result in summer evaporation outstripping local annual precipitation [*Mooney and McClelland* 2012, Evans *et al.* 2012, *Ward* 1997]. However, the warm summer waters of the Gulf of Mexico and the impacts of El Niño Southern Oscillation (ENSO) events supply the potential for large, sporadic rains associated with convective thunder storms, tropical storms and hurricanes [*Evans et al.* 2012, *Ropelewski and Halpert* 1986, *Wolter et al.* 1999]. These events often promote

flash flooding in the region and freshets into many of the coastal bays [*Mooney and McClelland* 2012, *Bruesewitz et al.* 2013, *Pollack et al.* 2011]. For example, from 1998 to 2008, the Aransas River experienced an average discharge of 1.39 $m^3 s^{-1}$, peak flow of 829.68 $m^3 s^{-1}$, and minimum flow of 0.0065 $m^3 s^{-1}$ [*Evans et al.* 2012].

The Aransas watershed covers approximately 2,146 km^2 of primarily cropland west of Copano Bay, while the Mission watershed spans approximately 2,675 km^2 of shrub and forest land [*Mooney and McClelland* 2012, *Evans et al.* 2012]. The Aransas and Mission watersheds rest within the Texas Gulf Coastal Plain and have very little relief between the coast and the most downstream USGS river gauges. The Aransas River rises from near sea level at the river mouth to 22.06 m above sea level at the USGS gauge [Station ID: 08189700] that is 94.6 km upstream from the river mouth [*Evans et al.* 2012]. Similarly, the Mission River elevation increases to 0.31 m above sea level along the 36.2 km from the river mouth to the Mission River USGS gauge [Station ID: 08189500] [*Evans et al* 2012]. The minimal baseflow of the two river systems is bolstered by the discharges of thirteen waste water treatment plants (WWTPs). Ten WWTPs contribute 14.4 million liters per day (mld) to the Aransas River, while three WWTPs discharge 1.9 mld into the Mission River [*Mooney and McClelland* 2012, *Johnson* 2009].

The interaction between the strong tidal forces and the minimal riverine baseflow creates a significant river reach that acts tidally. The tidally dominated river reach may create long residence times for outgoing freshwater during periods of low inflow on the order of months, whereas during intervals of high riverine discharge the residence time is much shorter on the order of days [*Evans et al.*, 2012, *Johnson* 2009, *Mooney and McClelland*, 2012, *Jones et al.* 2017, and see Chapter 3]. The length of this tidally influenced reach also varies through time according to riverine and tidal controls [see Chapter 3]. The interaction of hydrologic dynamics and tides in these low-relief coastal river reaches along the Texas Coastal Plain impacts the timing and magnitude of nutrient fluxes to, and hence the biological productivity of, downstream estuarine environments [*Mooney and McClelland* 2012, *Arndt et al.* 2011, *Bruesewitz et al.* 2013, *Palmer et al.* 2011, *Pollack et al.* 2011]. However, to quantify the impacts of the riverine-estuarine

interactions on nutrient fluxes, we need a robust methodology for calculating freshwater inputs to the coastal environment.

4.2.2 Field Data

4.2.2.1 Installed Instruments

Ten monitoring locations along the Mission and Aransas Rivers, five on each river (Figure 4.1), recorded basal stage and conductivity observations, and thalweg velocities. At each site, a *SeaHorse* tilt current meter (TCM) was installed to observe channel thalweg velocity. Previous work with TCMs have investigated the bottom circulation and sediment dynamics in the Gulf of Maine [*Aretxabaleta et al.* 2013, *Maio et al.* 2016], and the current dynamics in Mesquite, Aransas, and Copano Bays [*NERR* 2015]. However, this study provides the first TCM application to rivers [see Chapter 3]. Installed with the TCM, a riverbed sonde (Solinst LTC) recorded the water stage and conductivity.

From the stage observations we calculated the rate of change of stage ($\frac{dS}{dt}$) via the following equation and a *dt* of 15 minutes:

$$\frac{dS_n}{dt} = \frac{Stage_{n+1} - Stage_n}{time_{n+1} - time_n} \tag{4.1}$$

The ten sites recorded observations every 15 minutes, which generated approximately 96 samples per day. *Ruhl and Simpson* [2005] recommend between 50 to 120 samples every 12 to 13 hours to ensure sufficient resolution of the tidal cycle when creating a tidal rating curve using the Index-Velocity Method, consistent with our sampling interval.

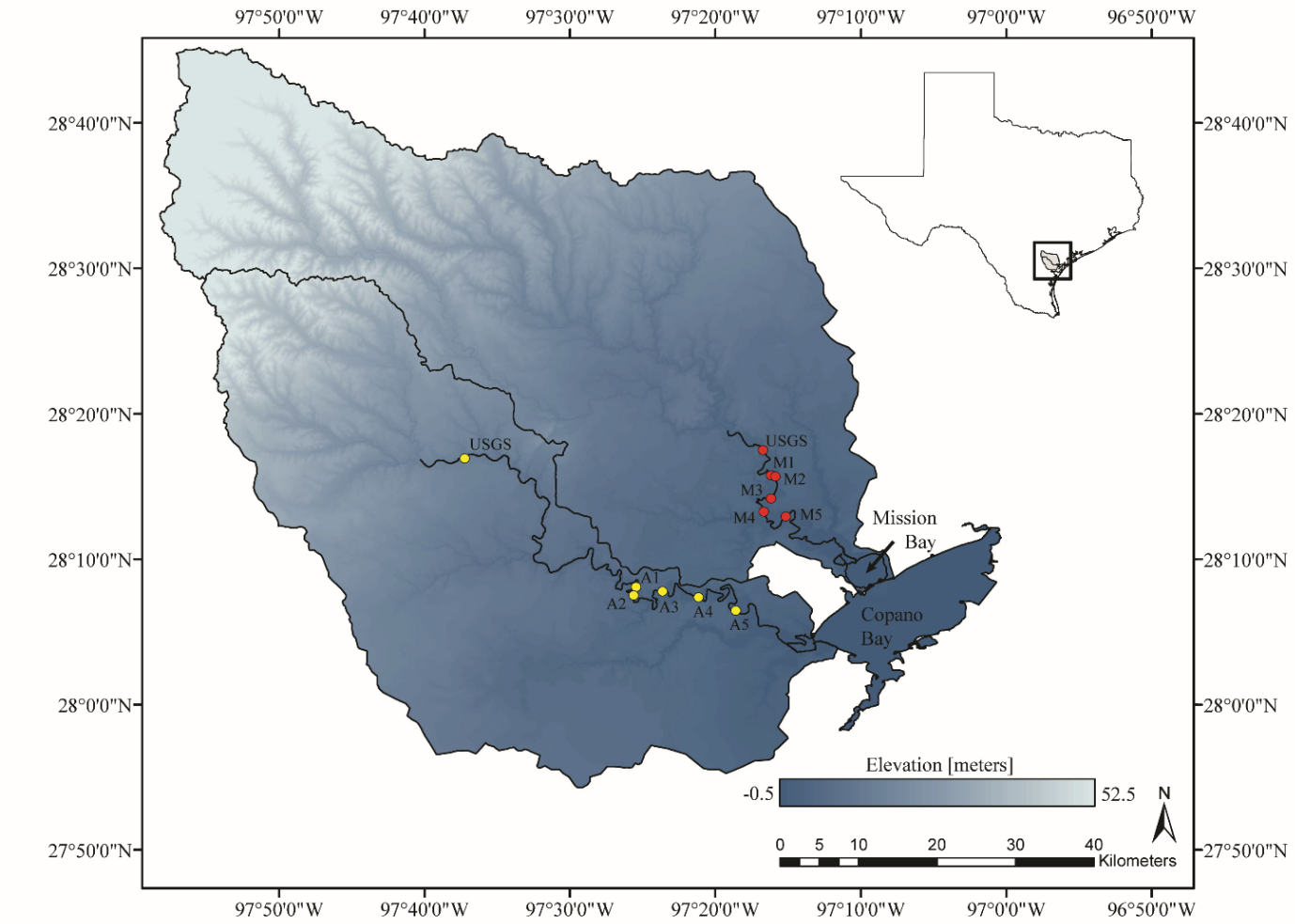

Figure 4.1: Mission and Aransas River watersheds, their topography (see colorbar), and monitoring locations (circles) including each river's USGS gauge (Station ID: 08189500 and 08189700, respectively) [USGS 2017]. Inset: Mission and Aransas watershed locations within Texas, USA.

4.2.2.2 Acoustic Doppler Profiler (ADP) observations

An acoustic doppler profiler (ADP) is an instrument that provides measurement of cross-sectional volumetric discharge based on the Doppler shift between an outgoing and incoming acoustic pulse. The two ADPs used (SonTek RiverSurveyor and Teledyne StreamPro) were both downward-facing profilers that utilize divergent sonar beams to acquire high-resolution velocity measurements that are then amalgamated into a calculation of volumetric discharge. Each beam emits an acoustic signal of known frequency. While traversing the length of the water column, that sonar beam interacts with small particles in the water column that reflect a shifted acoustic signal back to the ADP. Based upon the shift in the return signal, the ADP calculates the direction and magnitude of the reflecting particle's velocity [*Ruhl and Simpson* 2005, *Levesque and Oberg* 2012, *SonTek* 2007, *Teledyne* 2015].

ADP transects were collected multiple times at sites A1 - A4, M1, and M3-M5 throughout the course of the field study between 01 July 2015 and 01 July 2017. In total, 435 transects were recorded during both spring and neap tidal conditions throughout the summer and winter months of 2016 and 2017. To obtain a discharge observation with either instrument, the ADP was mounted to a small dinghy and towed slowly across the channel width, perpendicular to flow, via pulleys stationed opposite one another at each shoreline. These transects accumulated both cross-sectional discharge and spatial velocity data. The surveys completed with the SonTek RiverSurveyor were cleaned as per the manufacturer's recommendations, where each valid transect should have a ratio of measured discharge to estimated discharge of at least 50 [*SonTek* 2007]. Teledyne transects were also cleaned according to a similar metric; we removed all transects containing more than 50% bad ensembles (i.e., binned water column observations), as well as any transects with obvious tacking errors (i.e., ADP inaccurately recorded its own location).

ADP transects were not completed at site A5 due to safety concerns, nor were they completed at site M2 due to issues with the installed instrumentation.

4.2.3 TCM Calibration and data cleaning for tidal river applications

Raw TCM accelerometer data are recorded as X, Y, and Z coordinates. Calibrating and normalizing the raw data are the first steps in translating from raw X, Y, Z coordinates into local velocity measurements. Calibration tests for each TCM provide the maximum observable X, Y, and Z coordinates, as well as the X, Y, and Z coordinates the accelerometer observes during zero velocity conditions. Throughout each of the 2-3 minute long calibration tests, the TCMs should record observations at a sampling rate ≥ 10 Hz [*Sheremet et al.* 2009, *Sheremet* 2013]. The maximum X, Y, and Z coordinates are determined through *roll* and *swing* calibration tests. The *roll* test identifies the maximum X and Y coordinates while the TCM is rolled slowly along a flat surface. In the *swing* test, a tether attaches the TCM to a vertical wall, and the TCM, remaining flat against the wall, is swung in a circular arc about the tether. The *swing* test identifies the maximum Z coordinate. Each of these tests result in sinusoids of the respective coordinates. The maximum coordinates are calculated as an average of the magnitudes recorded during the crest/trough for each coordinate sinusoid [*Sheremet et al.* 2009, *Sheremet* 2013]. The TCM-specific X, Y, and Z zero-velocity coordinates are empirically derived from average laboratory observations of each TCM submerged in a bucket of water [*Sheremet et al.* 2009, *Sheremet* 2013].

Using a TCM's maximum and zero-velocity endmembers, that TCM's field observations may be normalized within this expected range. Thus, post normalization, ideally, zero velocity conditions register as the coordinate vector [0, 0, 1] (i.e., the vertically buoyant TCM is motionless above the X-Y plane's origin), and maximum discharge conditions, where the TCM would be pointed horizontally in the direction of flow, would register as a coordinate vector of [x, y, 0], where $x^2 + y^2 = 1$.

However, the submerged field installations of the TCMs introduce errors, e.g., spatial offsets from the true thalweg or rotation of the TCM. These may cause the observed coordinate axes to be out of alignment with the ideal axes corresponding to the primary flow direction (Figure 4.2a). This axial offset can be corrected using pitch, roll, and yaw corrections similar to those used in eddy flux observations (e.g., *Wilczak et al.* [2001], *Heinesch* [2006], *Yuan et al.* [2007]). The

pitch and roll corrections align the zero velocity conditions of the empirical observations (blue dots in Figure 4.2a) to the ideal X-Y origin (black dots in Figure 4.2a). The yaw correction rotates the data around the ideal origin and aligns the data with the axis denoting the primary flow direction (i.e., positive y-axis relates to downstream flow, and the negative y-axis denotes upstream flow). To determine the proper flow direction from the field observations, we isolated data associated with large storm events, as these flood discharges would overwhelm the tidal signal and provide a clear indication of the downstream direction. The tilt data associated with storm discharges represented the least common 5% of the data. A k-means cluster analysis (where k=2) partitioned this 5% of the data into two primary groups: one closer and one farther from the origin (yellow and cyan points, respectively, in Figure 4.2b). From these clusters, the downstream direction (red arrow in Figure 4.2b) was identified as in line with the cluster centroid farthest from the origin (cyan centroid marked with black 'X' in Figure 4.2b). The yaw correction rotated this downstream orientation to align with the y-positive axis (Figure 4.2c). From the pitch, roll, and yaw corrected data (Figure 4.2c), we determined the angle of each coordinate vector from the vertical, which corresponded to a laboratory-derived relationship between angle-from-vertical and velocity (Figure 4.2d) [*Sheremet et al.* 2009, *Sheremet* 2013]. From this relationship, we obtained a velocity time series for each TCM installation (Figure 4.2e). For greater detail on the TCM calibration and methods, see Appendix G.

The resulting TCM velocity times series is accurate down to a magnitude of approximately 2 cm s^{-1} [*Sheremet et al.* 2009, *Sheremet* 2013]. Although the exact accuracy of velocities with magnitude less than 2 cm s^{-1} is uncertain, the timing of tidal oscillations in discharge is sufficiently accurate to provide insight into the impact of diurnal and semidiurnal tidal cycles on the river reach's discharge regime [*Maio et al.* 2016, *Aretxabaleta et al.* 2014].

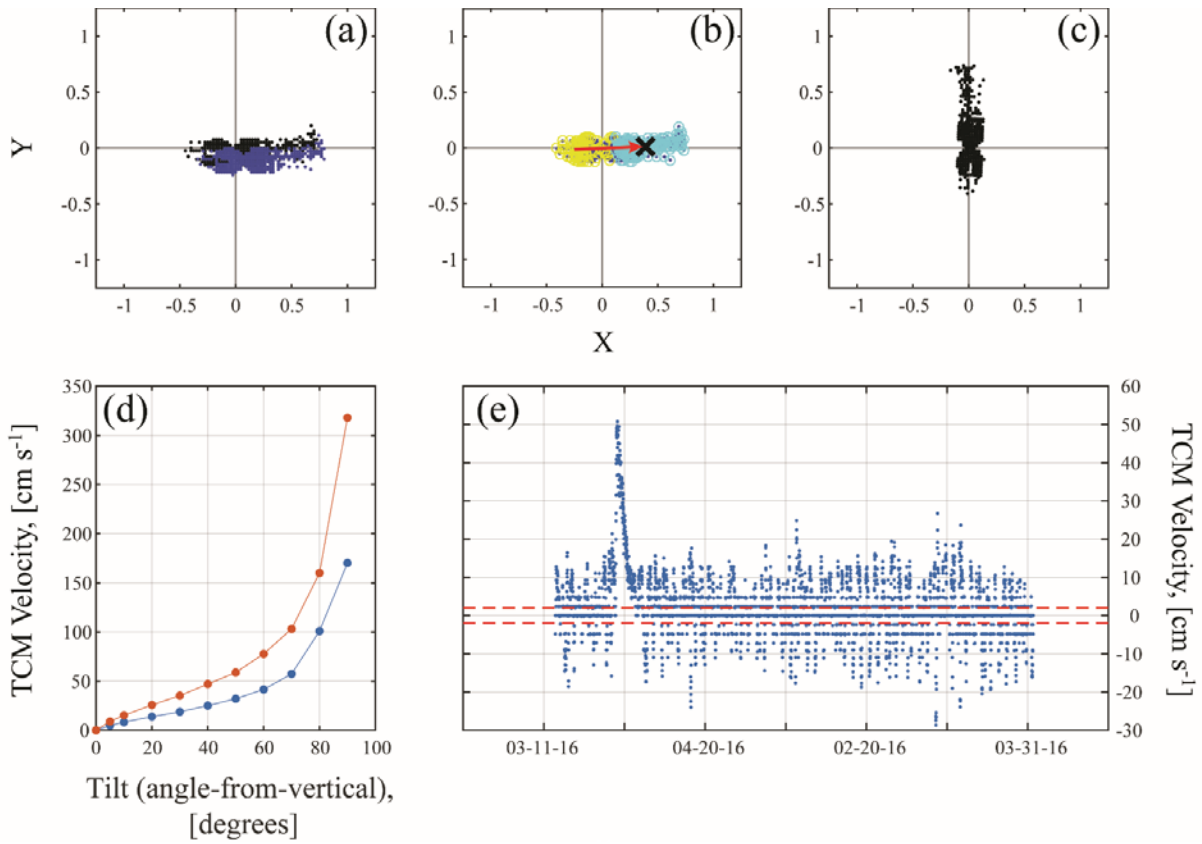

Figure 4.2: Pitch, roll, and yaw corrections for TCM data and resulting corrected velocity time series. The data presented were observed at site A4 between 02 March and 30 April 2016. The pitch, roll, and yaw corrections align the potentially offset or rotated raw data with the proper downstream flow direction, which we oriented along the positive y-axis. The pitch and roll corrections align the observed, normalized TCM coordinate data (blue dots in (a)) to the ideal X-Y origin (black dots in (a)). The isolated storm data (cyan and yellow data in (b)) are used to determine the primary direction of downstream flow (red arrow in (b)). This downstream trend is yaw-rotated to align with the positive y-axis (c). From the cleaned, normalized, and properly oriented TCM coordinate observations (c), an empirical relationship between tilt (angle-from-vertical) and local velocity (d) create a final velocity time series (e). In (d), the orange and blue lines refer to the tilt-velocity relationship for the 'p50' and 'b15' SeaHorse TCMs, respectively. The red dashed lines in (e) outline the TCM detection limit of ± 2 cm s^{-1}.

4.2.4 Determination of Phase Offset (φ)

For each M-A site, we identified the phase offset (φ) between the cyclic signals of tidal stage and tidal velocity through the use of a Fast Fourier Transform (FFT) from Matlab's Discrete Fourier Transform (DFT) package. The phase offset analysis was repeated for comparison on twelve tidal USGS river gauging sites (Figure 4.3, Table 4.1). These twelve USGS sites represent all of the publically available continuous tidal discharge and stage data sufficient for the phase offset analysis [*USGS* 2017]. The twelve sites span both standing wave and mixed wave-type systems. Progressive wave discharge and stage data were unavailable among USGS gauging stations labeled 'Tidal Stream' or 'Estuary'. All velocity (or discharge for the USGS sites) and stage data underwent a 6-hour moving average before the FFT and phase offset analysis to remove noise (e.g., wind) from the data and improve the isolation of correct tidal harmonic phases.

Using each field site's longest continual dataset (e.g., two years, one year, or several months), we used an FFT to isolate the magnitude and phase of the five most influential tidal harmonics. For Copano Bay, the National Oceanic and Atmospheric Administration (NOAA) identified these harmonics as solar semiannual - SSA, solar annual - SA, lunar diurnal – O_1, a second lunar diurnal – K_1, and principal lunar semidiurnal – M_2 [*NOAA* 2017c]. Of these five most influential harmonics only the semidiurnal and diurnal harmonics (i.e., M_2, O_1, K_1) will impact the immediate discharge regime and characterize the system as dominated by a standing, mixed, or progressive waveform. Similarly for the USGS sites, an FFT identified their two strongest diurnal and single strongest semidiurnal harmonics for comparison and calculation of phase offset. The identified tidal harmonics of the USGS sites may not necessarily match those of the M-A sites. The dominant harmonics of the M-A sites are all equivalent due to the shared estuarine geometry and tidal signal. The analysis of phase offset only included the major harmonics with a diurnal or semidiurnal period. Other long-term harmonics of stage and velocity, such as the annual and semiannual constituents, should be nearly in phase, and do not provide any information towards a system's standing, mixed, or progressive wave character.

An FFT provides the fundamental components of each important harmonic, namely amplitude or power, frequency, and phase (ε), and enables the calculation of φ. The FFTs determined ε for stage and ε for velocity at each important semidiurnal or diurnal frequency (e.g., for the M-A sites, for M_2, O_1, K_1, periods of 12.42, 23.94, and 25.80 hours). We determined the offset between phases of stage, ε_s, and velocity, ε_v, for each semidiurnal or diurnal frequency, *f*, using the following equation:

$$\varphi_f = \left|\varepsilon_{s,f} - \varepsilon_{v,f}\right| \quad (4.2)$$

Because there are three major frequencies analyzed, eq. 4.2 provides three phase offsets; these were averaged to obtain the final characterization of the site's phase offset. (The three phase offsets were often very similar; see Appendix H for details.) The calculated average phase offset determines each site's long-term waveform characterization, whether standing ($\varphi = \frac{\pi}{2}$), progressive ($\varphi = \pi$), or mixed ($\frac{\pi}{2} < \varphi < \pi$).

4.2.4.1 Standing vs. Mixed vs. Progressive Waves

Depending upon the geometry and the balance between riverine and tidal discharge within an estuarine system, tidal energy will be transported upstream under one of three waveforms: standing, mixed, or progressive [*Savenije* 2005]. Simplistically, each waveform differs from the others based upon the relationship between stage and discharge, specifically the phase offset between each variable's cyclic signal.

Classically, standing, mixed, and progressive waves are defined on an estuarine discharge coordinate plane, where positive discharge relates to upstream or inland discharge. Thus, in this theory, the offset between stage and discharge should be between $\varphi = 0$ (progressive wave endmember) and $\varphi = \frac{\pi}{2}$ (standing wave endmember) [*Savenije* 2005]. However, since this study is interested in calculating riverine discharge, we have rotated the coordinate plane to have positive discharge denote flow oriented downstream. Thus, the expected phase offset of a progressive wave traveling upstream is now $\varphi = \pi$ (Figure 4.3a). Within the newly rotated riverine coordinate plane, a progressive wave system relates high stage with upstream (negative) discharges and vice versa.

Thus, within the new coordinate system, discharge should negatively correlate with stage for a purely progressive wave system (Figure 4.3a).

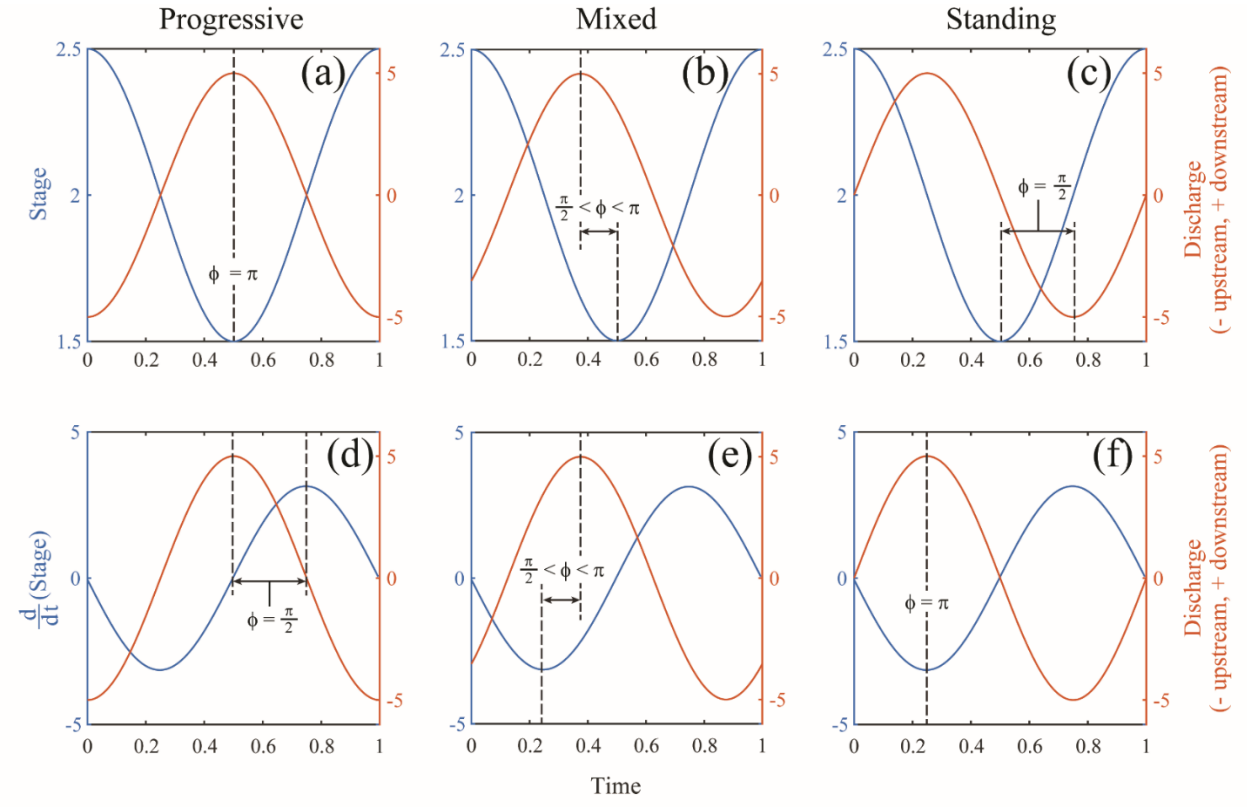

Figure 4.3: Schematic of the relationships between stage and discharge (first row) and between stage-rate-of-change and discharge (second row) for progressive (a, d), mixed (b, e), and standing (c, f) waveforms. Each subfigure has two y-axes; the left axis is stage or its derivative, and the right axis is discharge, with the curves color-coded to match the associated axis. The absolute phase offset between stage and discharge is represented by ϕ.

This coordinate plane rotation does not impact the standing wave offset between stage and discharge, but does affect the lag. Within the estuarine coordinate plane, the discharge is lagged by $\frac{\pi}{2}$ behind stage. However, with the coordinate rotation to riverine coordinates, discharge is lagged behind stage by $\frac{3\pi}{2}$. These different phase lags represent the same magnitude of phase offset calculated by eq. (4.2) since phase offsets of $\frac{3\pi}{2}$ and - $\frac{\pi}{2}$ are equivalent. Thus, the expected phase offset between stage and discharge remains the absolute value of $\frac{\pi}{2}$ for a standing wave system

Figure 4.3c). This means that standing wave discharge is inversely related to the rate of change of stage ($\frac{dS}{dt}$), with actively falling stage (negative $\frac{dS}{dt}$) corresponding to outgoing (positive, downstream-oriented) riverine discharge and actively rising stage (positive $\frac{dS}{dt}$) corresponding to incoming (negative, upstream-oriented) tidal flood waters (Figure 4.3f). Note that returning to an estuarine discharge coordinate plane orientation, a standing wave system would result in a positive relationship between discharge and $\frac{dS}{dt}$. However, since this work is primarily focused on gauging the discharge from terrestrial sources to estuarine sinks, the coordinate system herein will be oriented downstream, with upstream flow corresponding to negative discharge.

A mixed wave is an intermediary between the standing and progressive wave endmembers, with absolute phase offset $\frac{\pi}{2} < \varphi < \pi$ (Figure 4.3and 4.3e). Thus, conceptually, for systems experiencing a mixed waveform, we should expect discharges to relate to some combination of $\frac{dS}{dt}$ and stage.

4.2.5 Creation of the Tidal Rating Curve

To model volumetric discharge, Q, over all conditions, we created a piecewise rating curve. One portion of the rating curve models discharge during tidal baseflow conditions, where flow is potentially bidirectional and coordinated with tidal motion. The other portion of the rating curve approximates volumetric discharge during storm conditions, when riverine forces have overwhelmed tidal influence. During such times, discharge is predominantly unidirectional and oriented downstream.

4.2.5.1 Relating Q observations to Stage and Stage-rate-of-change

Before relating discharge to stage and $\frac{dS}{dt}$, a 3-hour moving average was performed on the raw TCM velocity, stage, and $\frac{dS}{dt}$ data to remove excess noise (e.g., wind). Since, the M-A Rivers' tides are often semidiurnal during neap tide, we selected a 3-hour moving average window that represents a quarter, or $\frac{\pi}{2}$, of this tidal cycle. This is the largest window we could average over without potentially overwriting a semidiurnal signal and so influencing the relationships between stage, $\frac{dS}{dt}$, and discharge.

For baseflow conditions, we fit the following model at each site:

$$Q_i = k_1 S_i^2 + k_2 S_i + k_3 (\frac{\mathrm{d}S_i}{\mathrm{dt}})^2 + k_4 \frac{dS_i}{dt} \quad (4.3)$$

where Q_i, S_i, and $\frac{dS_i}{dt}$ are the calculated volumetric discharge, water stage, and rate of change of stage, respectively, at time, t_i, and coefficients k_1 through k_4 are calculated long-term characterizations of the site. The model must not include an intercept as a y-intercept would imply that when no stage is present flow is still occurring, which is not possible. We repeated the baseflow regression on the publicly available data from the same twelve tidal USGS gauging stations analyzed for phase offset (Tables 4.1 and 4.2) [*USGS* 2017].

For each site (both those along the M-A Rivers and the USGS sites), the significant terms in the regression model of equation (4.3) were determined via model comparison. Given the four proposed terms of the model, there are 15 different combinations composed of one to four terms. Each of the 15 potential combinations was modeled for each site's data. Modeled combinations were discarded if they exhibited insignificant p values (i.e., using a 95% confidence, $p > 0.05$) for the difference of any regression coefficient from zero. For the remaining models containing significant p values (i.e., $p < 0.05$) for all coefficients, the model with the greatest r^2 value was selected to represent the site's tidal baseflow regime. The final model for most stations included all four terms, but a few sites only required three or fewer terms.

4.2.5.2 Discharge approximation during storm periods

In addition to baseflow conditions, the tidal rating curve for each M-A site must handle periods of increased discharge, or "storm periods". The M-A tidal rating curves classify a "storm period" as a time where a given site's measured TCM velocity, v_i, is greater than the 90th percentile of that site's velocity measurements. This definition of a storm period reflects the flashy discharge regime, of long periods of minimal baseflow punctuated by large runoff events, that characterizes the Mission and Aransas Rivers [*Jones et al* 2017, *Mooney and McClelland* 2012, *Bruesewitz et*

al. 2013]. In other words, we are isolating only the strongest storm events within the top 10% of velocity observations.

For these periods of increased velocity, we will approximate discharge at each site by using the following equation:

$$Q_i = v_i * S_i * w \quad (4.4)$$

where, v_i, S_i, and Q_i are the observations of velocity, stage, and calculated discharge, respectively, for time, t_i, and w is a measurement of the channel width at the particular M-A site. This discharge calculation assumes a rectangular cross-sectional geometry with fixed-width, but could be expanded to incorporate more complex geometries.

4.3 RESULTS

4.3.1 M-A and USGS baseflow characterization

4.3.1.1 Baseflow phase offset (φ) comparison

We performed the FFT analysis to identify phase offset (section 4.2.4) on nine of the ten M-A installations, as well as twelve tidal USGS monitoring stations. Site M2 did not record enough field velocity measurements for a reliable FFT and phase analysis due to problems with the TCM instrumentation. Table 4.1 provides the sites' phase offset between stage and discharge, and resulting classification as experiencing predominantly standing, mixed, or progressive wave types. The labels from Table 4.1 correspond to the labels in Figure 4.4. Within Figure 4.4 and Table 4.1 there is a ± 0.087 radian (5 degree) margin (gray dashed lines in Figure 4.4) surrounding the definitions of phase offset to account for noise within FFT calculations.

While the USGS sites span most of the spectrum of possible phase offsets, eight of the nine analyzed M-A sites were dominated by a standing waveform with a phase offset of approximately $\frac{\pi}{2}$ (Figure 4.4, Table 4.1). The remaining M-A site, A2, exhibited a mixed wave that was very nearly standing wave character. Thus, the M-A sites' discharge regimes are likely related to both $\frac{dS}{dt}$ and stage, and we should expect that many of the M-A sites will require at least one of the $\frac{dS}{dt}$ coefficients, if not both.

The twelve USGS sites spanned a range of standing to mixed wave conditions with phase offsets ranging from 0.939 $\frac{\pi}{2}$ (Plum Island River) to 1.64 $\frac{\pi}{2}$ (Shark River). This range of phase offsets described two strongly standing and ten mixed wave systems. None of the available tidal USGS gauging stations that provided both stage and discharge observations exhibited a progressive wave offset. Appendix H includes figures summarizing of each M-A and USGS site's phase offset analysis; specifically, the figures depict each site's isolated semi- and diurnal harmonics and their resulting phase offsets.

4.3.1.2 baseflow tidal rating curve

Table 4.2 presents the model coefficients for baseflow discharge conditions for the eight M-A sites and twelve USGS sites. Overall, the adjusted r^2 values of the tidal sites spanned a wide range from 0.17 at M1 (Mission river, most upstream site) to 0.97 at the Crystal and Savannah River USGS sites. Seven of the eight baseflow tidal rating curves for the M-A sites displayed r^2 values greater 0.40 (all except M1), showing a decent fit between the model and observed ADP discharge. Sites A3 and A4 presented the best fits of the M-A sites with r^2 values of 0.94 and 0.83, respectively. The twelve USGS locations all had r^2 values > 0.60, which implies a strong agreement between the USGS-recorded discharge observations and our model estimations.

The regression coefficients (k_1 to k_4) included in the final models were all significantly different from zero (with 95% confidence, $p < 0.05$). Each of the determined k_4 coefficients showed an inverse relationship with discharge (i.e., a negative $\frac{dS}{dt}$ coefficient) as expected from section 4.2.4.1. Also, several other sites contained an inverse relationship with $(\frac{dS}{dt})^2$ (A2, M3, and the USGS sites on the Crystal, and Shark Rivers). All M-A sites, except for M1 and M5, included $\frac{dS}{dt}$ as an important variable (i.e., included a k_3 and/or k_4 value), as expected from each site's φ values (Table 4.1). However, the site with the weakest r^2 ($r^2 = 0.17$), site M1 at the most upstream location on the Mission River, did not include a relationship to $\frac{dS}{dt}$ or $(\frac{dS}{dt})^2$, nor did site M5 relate to $\frac{dS}{dt}$ or $(\frac{dS}{dt})^2$, contrary to our expectations given the site's phase offset. Appendix J graphically

presents each site's (M-A and USGS) regression model, the tidal rating curve coefficients (k_1 trough k_4) of which are presented in Table 4.2.

4.3.2 Mission and Aransas Rivers' discharge time series

After identifying and isolating periods of baseflow and storm conditions, a complete discharge time series for each of the eight M-A sites was calculated using equations (4.3) and (4.4). A summary of each site's overall discharge regime, as well as baseflow and storm periods, is presented in Table 4.3. Appendix K graphically presents the calculated discharge time series of the eight M-A sites.

During baseflow, the average and median discharges for each M-A site described negligible flow conditions ranging from a minimum of -2.05 $m^3 s^{-1}$ at A3 to a max of 1.29 $m^3 s^{-1}$ at M4. These low net discharge conditions are expected for tidal systems, especially in this semiarid-subtropical climate [*Ensign et al.* 2013, *Mooney and McClelland 2012, Jones et al. 2017*]. Additionally, the standard deviation of baseflow discharge increased downstream. The increased range of likely discharges at downstream sites is indicative of increasing tidal influence on the downstream discharge regimes.

In storm conditions, the mean discharge increased downstream. This reflects our understanding of watershed response to precipitation events. Sites farther downstream experience greater discharge than sites upstream due to increased watershed area supplying runoff to those downstream sites.

For each site's overall discharge time series, the average and median conditions strongly reflected the low baseflow conditions, rather than the sporadic storm events. However, in comparing the storm and baseflow discharges, we observe that most of the freshwater transport occurs during storm events. The average storm discharges are one to two orders of magnitude larger than those of baseflow (e.g., 15.45 $m^3 s^{-1}$ compared to 0.17 $m^3 s^{-1}$ at A4).

4.4 DISCUSSION

4.4.1 Model Caveats

4.4.1.1 Assumptions

The tidal rating curve model developed in this chapter requires several assumptions. The proposed tidal rating curve assumes a non-stratified velocity field and describes the analyzed sites' discharge as vertically and horizontally averaged. However, this assumption is a necessary simplification for gauging a river. Traditional riverine rating curves also provide a one dimensional calculation of discharge, without providing information about cross-sectional variability. The Index-Velocity Method attempts to address the cross-sectional velocity variability within the empirical relationship between the observed "index velocity" and the estimated mean velocity. Whether the "index velocity" is scaled up or down is dependent upon the previous observations of velocity variability [*Ruhl and Simpson* 2005, *Levesque and Oberg* 2012]. However, the resulting discharge estimates from the Index-Velocity Method still describe a vertically and horizontally averaged discharge regime.

Site Name	Site Number	Label	Phase offset [Rad]	Phase Offset [deg]	Wave Type
A1	M-A Site	A1	1.48	84.84	*Standing
A2	M-A Site	A2	1.68	96.34	Mixed
A3	M-A Site	A3	1.49	85.36	Standing
A4	M-A Site	A4	1.49	85.54	Standing
A5	M-A Site	A5	1.58	90.77	Standing
M1	M-A Site	M1	1.53	87.88	Standing
M2	M-A Site	M2	-**	-**	-**
M3	M-A Site	M3	1.36	78.04	*Standing
M4	M-A Site	M4	1.47	84.28	*Standing
M5	M-A Site	M5	1.64	94.20	Standing
Connecticut River	01193050	CON	2.26	129.20	Mixed
Murderkill River	01484085	MUR	2.53	144.68	Mixed
Middle River	02198950	MID	1.93	110.31	Mixed
Savannah River	02198980	SAV	2.00	114.55	Mixed
Ogeechee River	02203536	OGE	1.97	112.88	Mixed
St. Mary's River	02231254	STM	2.39	136.72	Mixed
Chassahowitzka River	02310663	CHA	1.78	101.90	Mixed
Halls River	02310689	HAL	1.90	108.59	Mixed
Crystal River	02310747	CRY	1.57	90.08	Standing
Mobile River	02470629	MOB	2.46	140.78	Mixed
Shark River	252230081021300	SHA	2.58	147.92	Mixed
Plum Island River	424752070491701	PLU	1.46	83.61	*Standing

Table 4.1: List of USGS and Mission-Aransas tidal river sites analyzed, site numbers, figure labels, the calculated φ, and the assessed waveform.
* - Phase offsets are likely of strongly standing character, even though slightly beyond ± 5 degree margin.
** - Insufficient TCM velocity data to accurately determine φ.

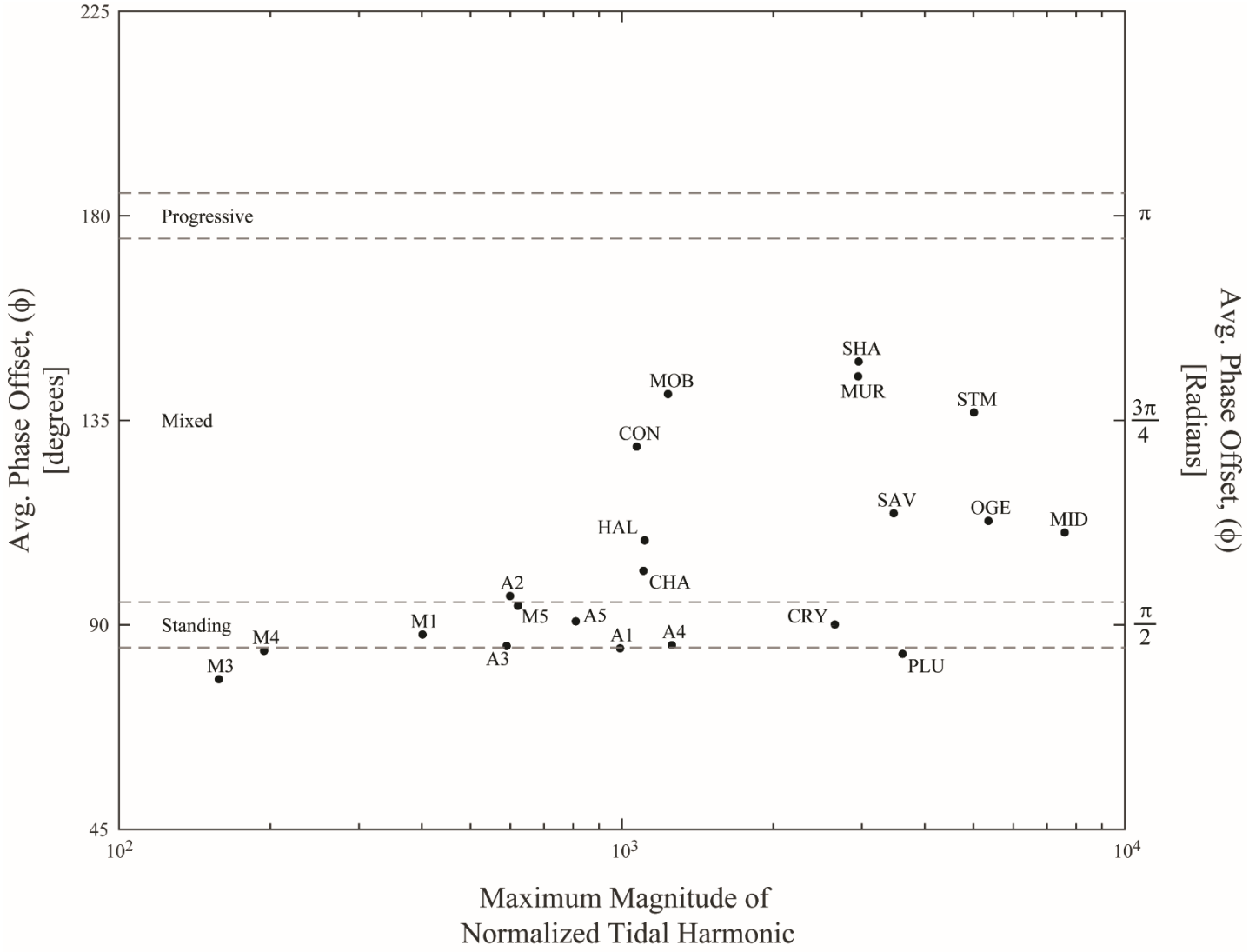

Figure 4.4: Comparison of phase offset and FFT tidal signal magnitude for the Mission-Aransas and USGS sites. The labels and φ values for each site correspond to the "label" column in Table 4.1.

Site Label	k_1 ± SE (tStat; p)	k_2 ± SE (tStat; p)	k_3 ± SE (tStat; p)	k_4 ± SE (tStat; p)	r^2
A1	0.67 ± 0.15 (4.44; 2.83e-05)	-1.06 ± 0.27 (-4.00; 1.36e-04)	0.00	-2.59 ± 0.38 (-6.73; 2.10e-09)	0.44
A2	0.00	0.39 ± 0.10 (3.96; 1.99e-04)	-2.22 ± 0.92 (-2.42; 1.85e-02)	-1.11 ± 0.27 (-4.09; 1.27e-04)	0.50
A3	-3.43 ± 0.37 (-9.20; 3.59e-12)	7.39 ± 0.85 (8.73; 1.75e-11)	0.00	-8.76 ± 0.32 (-27.05; 1.04e-30)	0.94
A4	-2.22 ± 0.62 (-3.60; 5.68e-04)	5.63 ± 1.50 (3.74; 3.65e-04)	4.40 ± 1.60 (2.75; 7.45e-03)	-10.47 ± 0.63 (-16.67; 1.34e-26)	0.83
A5	-*	-*	-*	-*	-*
M1	-0.30 ± 0.03 (-8.90; 1.00e-10)	0.00	0.00	0.00	0.17
M2	-**	-**	-**	-**	-**
M3	0.63 ± 0.15 (4.22; 1.41e-04)	-1.01 ± 0.24 (-4.28; 1.19e-04)	-4.35 ± 0.48 (-9.10; 3.48e-11)	0.00	0.69
M4	0.28 ± 0.05 (5.48; 1.25e-05)	0.00	0.00	-5.58 ± 0.80 (-7.00; 3.06e-07)	0.81
M5	-6.23 ± 1.29 (-4.83; 9.07e-05)	18.84 ± 3.92 (4.81; 9.45e-05)	0.00	0.00	0.51
CON	-2408.66 ± 32.63 (-73.83; 0.00)	1784.70 ± 28.36 (62.94; 0.00)	7.20 ± 0.52 (13.78; 2.68e-42)	-99.22 ± 1.14 (-87.32; 0.00)	0.82
MUR	-140.95 ± 7.96 (-17.71; 2.59e-67)	53.54 ± 10.78 (4.97; 7.14e-07)	1.14 ± 0.06 (18.79; 3.45e-75)	-12.60 ± 0.17 (-74.53; 0.00)	0.79
MID	62.20 ± 2.48 (25.06; 7.90e-114)	-99.29 ± 2.64 (-37.63; 1.71e-211)	1.05 ± 0.02 (63.66; 0.00)	-21.87 ± 0.21 (-106.60; 0.00)	0.90
SAV	690.80 ± 34.86 (19.82; 2.14e-77)	-2937.24 ± 28.13 (-104.40; 0.00)	4.82 ± 0.24 (19.86; 1.16e-77)	-444.94 ± 2.30 (-193.05; 0.00)	0.97
OGE	-55.68 ± 3.62 (-15.39; 1.38e-49)	0.00	2.79 ± 0.08 (34.80; 1.46e-192)	-43.15 ± 0.49 (-88.61; 0.00)	0.85
STM	82.77 ± 11.05 (7.49; 1.19e-13)	-771.16 ± 5.93 (-130.03; 0.00)	2.87 ± 0.08 (37.40; 8.36e-214)	-67.99 ± 0.48 (-142.39; 0.00)	0.96
CHA	-100.89 ± 3.13 (-32.25; 1.28e-172)	57.69 ± 1.72 (33.49; 1.01e-182)	0.00	-9.30 ± 0.11 (-88.57; 0.00)	0.85
HAL	-73.56 ± 4.89 (-15.05; 2.31e-47)	13.88 ± 1.31 (10.59; 3.33e-25)	1.21 ± 0.12 (10.38; 2.64e-24)	-5.24 ± 0.07 (-79.84; 0.00)	0.85
CRY	-20.50 ± 0.56 (-36.33; 4.40e-205)	82.46 ± 2.21 (37.31; 4.73e-213)	-1.62 ± 0.11 (-14.79; 3.73e-46)	-41.17 ± 0.21 (-200.16; 0.00)	0.97
MOB	-2748.87 ± 41.75 (-65.84; 0.00)	1848.70 ± 23.15 (79.87; 0.00)	0.00	-109.26 ± 2.66 (-41.03; 1.18e-270)	0.62
SHA	-1230.88 ± 36.00 (-34.19; 5.12e-191)	-919.98 ± 16.40 (-56.09; 0.00)	-9.10 ± 0.26 (-34.81; 2.91e-196)	-22.94 ± 0.60 (-38.08; 4.79e-224)	0.85
PLU	1.69 ± 0.55 (3.09; 2.03e-03)	2.02 ± 0.61 (3.34; 8.69e-04)	0.06 ± 0.00 (16.76; 5.63e-58)	-4.82 ± 0.04 (-129.99; 0.00)	0.92

Table 4.2: Baseflow regression coefficient estimates (with standard error, t-statistic, and p value) and adjusted r^2 for each monitoring site on the Mission and Aransas Rivers and twelve USGS stations.
* - No ADP transects were collected at site A5 due to safety concerns.
** - Insufficient data were collected at site M2, due to issues with the installed instrumentation.

Site Name	Mean (Median) ± St. Dev. (min; max)		
	Baseflow	**Storm**	**Overall**
A1	0.12 (0.14) ± 1.09 (-4.03; 3.79)	6.76 (3.62) ± 8.25 (1.57; 64.09)	0.79 (0.31) ± 3.44 (-4.03; 64.09)
A2	0.21 (0.46) ± 0.69 (-24.70; 0.97)	5.16 (3.58) ± 4.16 (2.02; 23.06)	0.71 (0.52) ± 2.10 (-24.70; 23.06)
A3	-1.92 (-2.05) ± 3.56 (-17.64; 9.26)	11.42 (8.81) ± 7.91 (5.41; 64.40)	-0.58 (-1.48) ± 5.80 (-17.64; 64.40)
A4	0.17 (-0.42) ± 3.78 (-9.84; 33.92)	15.45 (13.49) ± 7.51 (8.36; 74.15)	1.70 (0.18) ± 6.29 (-9.84; 74.15)
A5	-*	-*	-*
M1	-0.77 (-0.79) ± 0.18 (-1.54; -0.25)	7.70 (3.83) ± 9.66 (1.40; 59.20)	0.07 (-0.76) ± 3.98 (-1.54; 59.20)
M2	-**	-**	-**
M3	-0.30 (-0.16) ± 0.84 (-61.78; 1.34)	10.55 (4.75) ± 14.01 (1.62; 84.03)	0.78 (-0.10) ± 5.56 (-61.78; 84.03)
M4	1.29 (1.29) ± 1.78 (-16.56; 8.16)	17.85 (9.44) ± 19.43 (3.65; 98.68)	2.95 (1.57) ± 8.09 (-16.56; 98.68)
M5	0.97 (1.27) ± 2.75 (-11.72; 8.43)	11.57 (10.76) ± 2.73 (7.82; 20.61)	2.03 (1.68) ± 4.20 (-11.72; 20.61)

Table 4.3: Summary of the eight Mission-Aransas sites' discharge ($m^3 s^{-1}$) regime during identified baseflow and storm conditions, and over all conditions.
* - No ADP transects were collected at site A5 due to safety concerns.
** - Insufficient data were collected at site M2, due to issues with the installed instrumentation.

The calculation of phase offset for M-A sites is dependent upon the assumption that the cyclic timing of the thalweg velocity is synchronous with the cross-sectional discharge regime. In other words, the phase offset analysis assumes that the TCM velocities are directed upstream and downstream synchronously with the actual cross-sectional tidal discharge. Although only representative of the basal thalweg velocity, the TCM velocities provide our best estimate of the tidal discharge regime, especially with regards to the temporal relationship between stage and discharge.

The calculation of discharge during storm periods assumes that thalweg velocity represents mean cross-sectional velocity and that there is no change in channel width, only changes in stage, during storm periods (i.e., a rectangular channel). The TCM velocities recorded during the storm periods are well above the resolution limit of the TCM (e.g., 50 cm $s^{-1} \gg 2$ cm s^{-1}, Figure 4.2e) and are therefore reliable. However, as stage rises during a storm hydrograph, the area of maximal cross-sectional velocity will change location, at the very least rising with stage from its baseflow position. Thus, it is likely that our TCM observations do not capture the maximum cross-sectional velocities of most storms and thereby may underestimate the storm discharges. As stage rises during storms, the river may also spill over the banks into the adjacent floodplain, changing the cross-sectional area and channel geometry. During storm periods, our approximation of channel width does not change with rising stage. This might lead to an underestimation of volumetric discharge during storms. Future method iterations may incorporate an aspect of changing river channel geometry with changes in stage, similar to the USGS Index-Velocity Method [*Ruhl and Simpson* 2005, *Levesque and Oberg* 2012].

4.4.1.2. Piecewise rating curve issues

The average and median discharge results in Table 4.3 are reasonable given our knowledge of baseflow for the semiarid-subtropical physiographic setting of the M-A estuary. However, the extreme values (i.e., minimum and maximum) of baseflow discharge conditions are unrealistic. For example, the calculated discharges of -61.78, -24.70, -17.64 and 33.92 $m^3 s^{-1}$ at sites M3, A2, A3, and A4, respectively, are much too great a magnitude for the drought-laden M-A rivers' minimal baseflow and relatively small tidal amplitude. These unrealistic baseflow extremes are due to discharge being calculated using the baseflow coefficients (Table 4.2) for conditions within a transition between baseflow and storm flow.

Large storm events impact the surface water stage before significantly altering the TCM velocity regime and being identified as a storm period. Thus, the initial impacts of the storm event, such as the dramatic stage increase during the early part of the hydrograph's rising limb, are unintentionally included within the baseflow discharge calculations of this method. For example, the -61.78 $m^3 s^{-1}$ calculation at M3 occurs during the rising limb of a storm during 15-16 May 2016. The rapid rise of stage associated with the rising limb of hydrograph causes the baseflow model portion, which is inversely related to $\frac{dS}{dt}$ (eq. 4.3), to estimate a dramatic surge in upstream flow (i.e., an extremely negative discharge). Effectively, this means that discharge during the transitions between baseflow and storm conditions will require a more nuanced future approach to improve accuracy.

The discharge miscalculations during the transitions into (and possibly out of) storm periods are due to the piecewise nature of our tidal rating curve. The transitions between storm and baseflow periods are more complex than a binary division between tidal and riverine controls on discharge. The hydrology in a tidal river system does not snap from one endmember to the other instantaneously, but rather exhibits a subtly changing

mixture of riverine and tidal forces before arriving at one endmember. For example, a sufficiently large hydrograph peak should exhibit entirely riverine character. Throughout the recession limb of that hydrograph, riverine character is increasingly replaced by tidal forcings. Potentially, upon return to baseflow, the tidal forces have entirely replaced the riverine character and now control the discharge regime (or, at a minimum, some intermediate balance is struck between tidal and riverine forces during baseflow conditions). To further complicate matters, the transitions between tidal and riverine dominance may happen at different rates. For example, the rising limb of a hydrograph may rapidly shift from tidal to riverine domination as opposed to the longer, more gradual transition during the hydrograph's recession limb. Thus, a simplistic piecewise prediction system is not sufficient to resolve the complexity of these gradual transitions.

A rating curve describing all discharge dynamics of tidal rivers will need to exhibit the two different endmember behaviors that may dominate the system over time, *tidal* during baseflow, and *riverine* during periods of increased inflow, as well as the rising and falling limbs of a storm hydrograph. Using a piecewise prediction system to isolate these different time periods is not uncommon. For example, *Moftakhari et al.* [2013] used a breakpoint of 1000 m^3 s^{-1} to differentiate between "high and low flow" conditions when estimating tidal discharges in the Sacramento River. Therefore, although perhaps not atypical, using a piecewise measure for determining periods of unique character should be recognized as somewhat simplistic and an area for potential improvement.

Rating curves on non-tidal rivers must also address baseflow and storm conditions, but may do so through the use of a power law relationship [*Kennedy* 1984]. Such a relationship allows substantial increases from typical stage conditions to estimate elevated storm or flood discharges, while minimal fluctuations from typical stage model baseflow-

magnitude discharge. In addition, the power law relationship results in a continuous model between baseflow and storm conditions.

A first iteration at an improved calculation of a tidal river's transitional conditions from the bimodal approach developed here may be the creation of a trimodal gauging relationship. In such an approach, one set of discharge calculations is during tidal conditions, another describes obvious transitional periods (e.g., the rising and recession limbs of hydrograph peaks), and the final mode occurs during riverine flooding events (similar to suggestions by *Ruhl and Simpson* [2005]).

4.4.2 Why not relate discharge to TCM velocity?

The original goal of the TCM installations was to relate thalweg velocity (as obtained from the TCM point-data) directly to periodic ADP volumetric discharge measurements to obtain a two-year record of discharge. However, many of the baseflow velocity observations, especially at far upstream sites (e.g., A1 and A2), were of a magnitude smaller than the sensitivity of the TCM instrument (i.e., < 2 cm s^{-1}) because of the M-A Rivers' minimal baseflow. To create a rating curve that was applicable for all sites at all discharge conditions, we could not use only TCM velocity in our baseflow model.

At downstream sites, such as A4, the observations of the TCM velocity were larger than the instrument's sensitivity and so could provide a potential relationship between volumetric discharge and TCM velocity. Figure 4.5 displays the correlations and regressions between discharge and TCM velocity for sites A1 (Figure 4.5a), A3 (Figure 4.5b), and A4 (Figure 4.5c). The gray dashed lines in each subfigure portray the 2 cm s^{-1} sensitivity of the TCM.

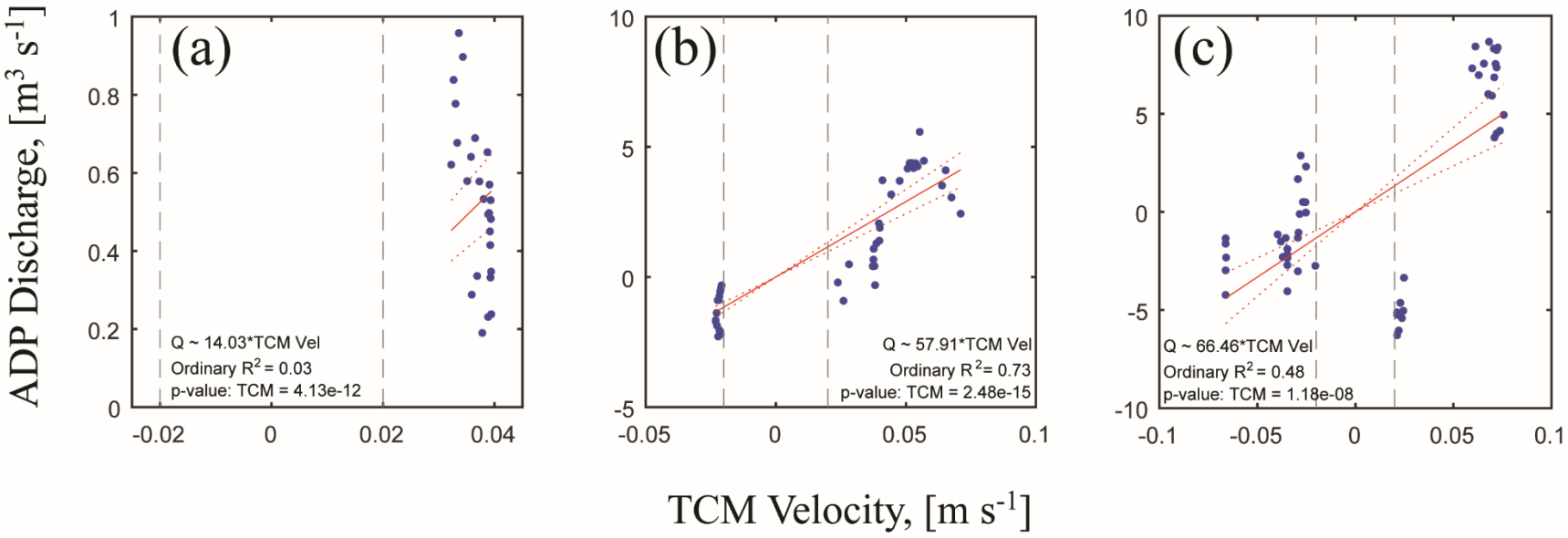

Figure 4.5: Linear model relating TCM velocity to ADP discharge observations at three sites along the Aransas River, Texas. TCM velocities for sites A1 (a), A3 (b), and A4 (c) increase in magnitude with increased distance downstream (toward A4). The regressions for the two downstream sites, A3 and A4, present much better coefficients of determination (r^2 = 0.73 and 0.48, respectively) than the upstream-most site, A1 (r^2 = 0.03). This is primarily due to the velocity observed at A1 often falling below the TCM sensitivity and, therefore, being unreliable in the model.

Each site's regression coefficient is significantly different from zero when using an intercept at the origin, with all $p < 0.05$ (4.13×10^{-12}, 2.48×10^{-15}, and 1.18×10^{-8}, respectively). However, the regression fit (i.e., r^2) varies substantially between upstream (i.e., A1) and downstream (i.e., A3 and A4) sites. The downstream sites exhibit coefficients of determination of 0.73 and 0.48, respectively, as opposed to the r^2 of 0.03 at site A1. The discrepancy in the r^2 values between the sites is primarily due to the removal of unreliable velocity observations (i.e., $| v_i | < 2$ cm s^{-1}) at A1 because of insufficient instrument sensitivity. The overall larger magnitude of velocity observations at downstream sites led to better regressions.

In other systems, where thalweg velocity is large enough to overcome resolution issues, TCM observations of velocity may be sufficient to relate directly to discharge and so create a tidal rating curve for the site using a simple linear regression. Or, where applicable, TCM velocity observations may be incorporated as an additional variable into eq. (4.3) to increase the accuracy of the model. In the M-A systems, due to the minimal, drought-stricken baseflow conditions, many of the completed ADP transects were associated with TCM velocities smaller than the TCM sensitivity (i.e., $| v_i | < 2$ cm s^{-1}). When including the TCM velocities into the regression, any ADP transects (and the associated stage and $\frac{dS}{dt}$ conditions) that corresponded to below sensitivity velocities could not be incorporated into the analysis. Thus, the below-sensitivity TCM velocities served to reduce the quantity of viable data and made identifying significant coefficients and relationships more difficult.

4.4.3 Model Insights

The results from this study indicated that the majority of the Mission and Aransas Rivers' freshwater transport occurs during storm events, similar to the findings of

Bruesewitz et al. [2013], *Mooney and McClelland* [2012], and *Jones et al.* [2017]. During baseflow, the average and median discharge for all M-A sites did not exceed 1.5 $m^3 s^{-1}$. On the other hand, average and median discharge conditions for storm periods increased substantially, up to a full order of magnitude larger than baseflow, e.g., 17.85 $m^3 s^{-1}$ at M4. The maximum discharges observed during storms far exceeded typical baseflow conditions, nearly eclipsing an additional order of magnitude, e.g., 96.86 $m^3 s^{-1}$ at M4 (Table 4.3). This disparity in discharge indicates that most of the nutrient transport occurs during these storm periods, as observed by other studies in these and similar south Texas systems (e.g., *Mooney and McClelland* [2012], *Bruesewitz et al.* [2013], *Palmer et al.* [2011], *Pollack et al.* [2011]).

The fact that storm discharge contributes the majority of the freshwater discharge to nearby bays agrees with our understanding of the interaction between the M-A Rivers and the climate of south Texas. During our study period, 01 July 2015 to 01 July 2017, NOAA confirmed the presence of an El Niño Southern Oscillation (ENSO) event, which brings cooler temperatures and increased precipitation and flooding to south Texas [*NOAA* 2017a, *NOAA* 2017b]. The elevated magnitude of storm discharges may be in part due to the ENSO's influence of increased precipitation and flooding.

Although storm periods may contribute the majority of freshwater to the coasts, baseflow temporally dominates the discharge regime for the M-A Rivers ("Overall" column in Table 4.3). During baseflow, nutrients may be trapped along the length of each river in response to the combination of negligible riverine discharge and the approximately zero net tidal discharge. Although a given site (e.g., A4) may instantaneously experience a range of discharges during tidal baseflow (e.g., between ~ ± 4 $m^3 s^{-1}$), the average net transport is negligible, or near-zero. Thus, the negligible baseflow discharge results in minimal freshwater and nutrient transport to the estuary downstream.

The standard deviation (SD) of baseflow increased downstream for both M-A Rivers (Table 4.3). Coupled with the near zero magnitude of typical discharge, the increasing SD at each subsequent site downstream indicates that we observed a broader range of positive and negative (i.e., downstream- and upstream-oriented) discharges. The more instances of negative discharge imply that tidal forces are becoming more influential in downstream discharge regimes. For example, during baseflow conditions, a non-tidal river's discharge should remain fairly consistent (i.e., a low SD) and in the positive, downstream direction. In fact, *Teledyne* [2015] recommends ensuring a < 5% change between multiple non-tidal discharge observations before validating a given discharge measurement. However, *Teledyne* [2015] warns that this consistency (i.e., low SD) may not be possible when observing a tidal river. The continually changing tidal discharge will present a broader array of flow conditions that will result in larger SD. Thus, a wider spectrum of possible discharges and an associated increase in observations of negative discharge at downstream sites (e.g., A4) indicates an increasingly tidal regime.

In addition, this trend of increasing SD during baseflow indicates that our rating curve upholds the law of conservation of mass. With most mean and median discharges near zero, the SD describes the range of typical discharge observations at each site. Over a tidal cycle at A1 we might expect a discharge range between ±1 m^3 s^{-1}, while farther downstream at site A4 we might expect to observe discharges ranging between ±4 m^3 s^{-1}. Thus, the magnitude of the modeled discharges increases downstream. The increasing magnitude of discharge downstream respects the law of conservation of mass by replicating the expected longitudinal discharge trend for non-tidal rivers. Theoretically, for non-tidal rivers, increasingly large watershed areas contribute to stream flow at sites farther downstream and result in discharge increasing downstream [*Dingman* 2008].

A further insight of our tidal rating curve method is that tidal discharge relates to $\frac{dS}{dt}$ measurements as well as stage observations. This insight leads to a simple expansion to typical rating curve methods for gauging non-tidal rivers. This expansion does not require comprehensive modeling of tidal hydrodynamics to obtain estimates of tidal discharge and/or longitudinal trends in discharge. Our tidal rating curve empirically identifies the importance of both stage and $\frac{dS}{dt}$ on tidal river discharge. The tidal datasets for the M-A Rivers and USGS sites provided a wealth of opportunity to explore the relationship between tidal discharge, stage, and $\frac{dS}{dt}$. The analyzed two weeks of baseflow conditions at the twelve USGS sites exhibited a dual dependence on stage and $\frac{dS}{dt}$. Figure 4.6 presents scatter plots of five USGS sites' tidal discharge, stage, and $\frac{dS}{dt}$. The discharges of Crystal and Plum Island River were highly related to $\frac{dS}{dt}$ (Figure 4.6h and 4.6k, respectively). In fact, a linear model fitting only discharge and $\frac{dS}{dt}$ provides an r^2-value of 0.94 and 0.90, respectively. This strongly mirrors the expectations based upon our classification of these USGS gauges as a standing wave (Table 4.1). However, for the remaining sites, the scatter plots display elliptic relationships between discharge and stage, and discharge and $\frac{dS}{dt}$.

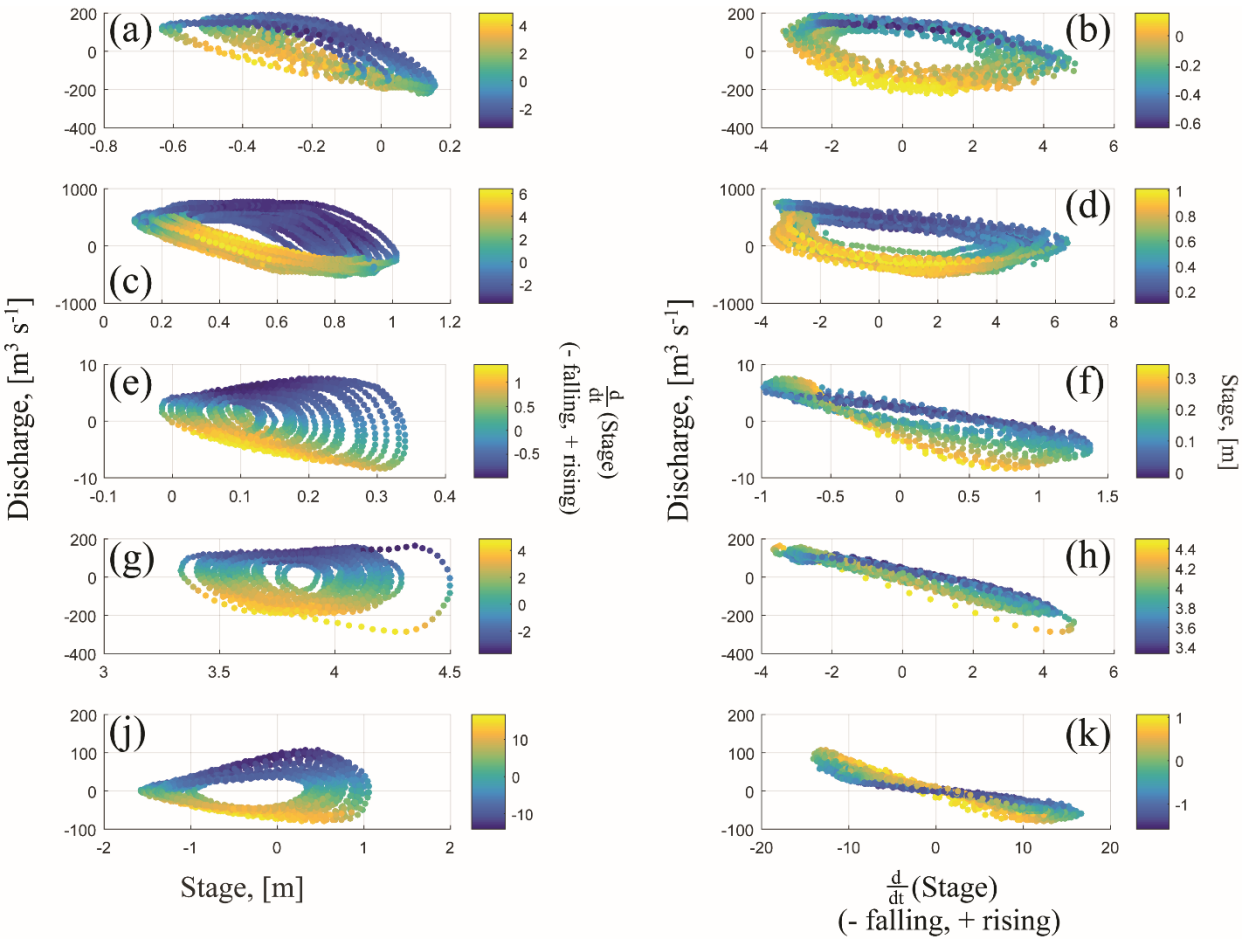

Figure 4.6: Scatter plots of five of the twelve analyzed USGS sites' discharge (observed by USGS), stage, and stage-rate-of-change. Two weeks of baseflow data are shown for each site. The left-hand column (a, c, e, g, and j) plot discharge against stage and are colored with respect to stage-rate-of-change conditions. The right-hand column (b, d, f, h, and k) compare discharge against stage-rate-of-change conditions and are colored by stage. Each row represents a different USGS site; the Shark River's conditions are depicted in (a) and (b), the Connecticut River's conditions are shown in (c) and (d), the Halls River's details are described in (e) and (f), the Crystal River's data are provided in (g) and (h), and the Plum Island River's data are illustrated in (j) and (k). The Shark, Halls, and Plum Island Rivers presented stage relative to a zero MSL datum (hence positive and negative stage).

The repetition of stage values (as seen in the ellipses of a, c, and e) prohibits traditional rating curve methods (i.e., relating discharge to stage alone) from being accurately used on such tidal sites [*Ruhl and Simpson* 2005, *Smoot and Novak* 1969]. However, by expanding the traditional methods to incorporate $\frac{dS}{dt}$ conditions as proposed herein, any discharge observation may be identified with a unique set of stage and $\frac{dS}{dt}$ conditions. This tidal rating curve could be further expanded to gain resolution within the discharge ellipse by adding an additional variable that further resolves the site's discharge (e.g., mean cross-sectional velocity). However, this initial expansion to include the impacts of $\frac{dS}{dt}$ enables a simple and potentially cost-effective methodology for gauging tidal discharge using only stage data and minimal ADP surveys for initial model calibration.

4.4.3.1 Phase offset insights

The phase offset analysis determined each site's tidal waveform, whether *standing*, *mixed*, or *progressive* (Table 4.1). Unfortunately, for our phase offset analysis, none of the sites analyzed (M-A nor USGS) exhibited truly progressive wave conditions. *Savenije* [2005] claims that a purely progressive waveform "only occurs in a frictionless channel of constant cross-section and infinite length." Thus, progressive wave tidal systems may be rare in the natural world (most natural systems exhibit a *mixed* wave type) and may require anthropogenic influence to create, such as "deep man-made (shipping) channels of constant cross-section" [*Savenije* 2005].

In addition to determining a tidal system's dominant waveform (i.e., standing, mixed, or progressive), the phase offset could be used theoretically to predict whether a given tidal site's discharge regime is more strongly related to $\frac{dS}{dt}$, stage, or a mixture of both. For example, the Crystal River USGS site was classified by our phase offset analysis as a standing wave ($\varphi = \sim \frac{\pi}{2}$ or 90.08°, Table 4.1) and its discharge is highly dependent

upon $\frac{dS}{dt}$ conditions (Figure 4.6h). In fact, a linear regression between discharge and $\frac{dS}{dt}$ on the Crystal River returned an r^2-value of 0.94, leaving an improvement of just ~0.03 in the correlation coefficient upon adding the stage, stage^2, and $(\frac{dS}{dt})^2$ terms. Thus, for systems exhibiting a phase offset indicative of a specific waveform, a baseflow tidal rating curve might be roughly and very rapidly estimated by fitting a linear model between observed volumetric discharge and the synchronous variable (i.e., $\frac{dS}{dt}$ for standing waves, and stage for progressive waves).

For example, all the M-A sites depicted strong standing wave character (Figure 4.4, Table 4.1). Thus, the discharge regimes of the M-A rivers should be more closely linked to the $\frac{dS}{dt}$ conditions, rather than stage. To demonstrate this point, we constructed linear models relating only $\frac{dS}{dt}$ conditions to ADP discharge observations for each of the eight ADP-monitored M-A sites (Figure 4.7). That is, we fit the model:

$$Q_{ADP} = k'_4 \frac{dS_i}{dt} \tag{4.5}$$

Each linear model assumes the origin is the y-intercept, which assumes that no change in stage relates to zero discharge. For a standing wave system, a $\frac{dS}{dt}$ value of zero corresponds to either high or low tide (HW/LW), where stage momentarily halts before reversing directions. This moment of zero tidal discharge during the reversal of the stage is known as *slack water* (SW). For mixed wave systems, SW will not be synchronous with HW/LW but will occur between HW/LW and mean tidal stage. Progressive wave systems will experience SW lagged theoretically by $\frac{\pi}{2}$ after HW/LW, occurring near mean tidal stage [*Savenije* 2005]. Our use of a zero intercept in the one-term regression of equation (4.5) therefore enforces a standing waveform model.

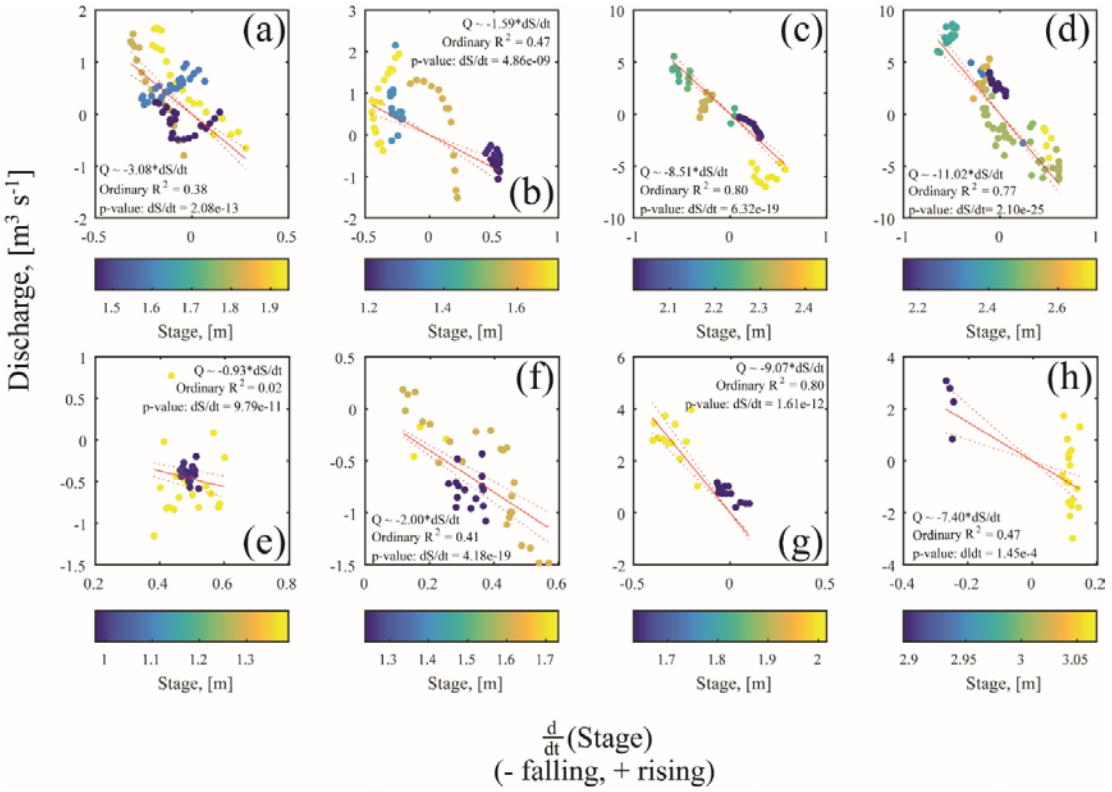

Figure 4.7: Linear models relating the stage-rate-of-change to ADP discharge observations along the Aransas and Mission Rivers, Texas. Each linear model assumes the origin is the y-intercept. The Aransas River sites, A1-4, are depicted in the top row of subfigures (a-d), while the Mission River sites M1 and M3-5 are portrayed on the lower row (subfigures e-h), respectively. In general, each site shows a fair-to-strong relationship between discharge and stage-rate-of-change conditions, which reflects each site's φ values and strongly standing wave-like character; for an ideal standing wave we should expect a linear relationship. The data are colored in reference to their corresponding stage values.

These simplified models resulted in significant p values ($p < 0.05$) and the expected inverse relationship between discharge and $\frac{dS}{dt}$ (subsection 4.2.4). Also, several sites showed a strong relationship (i.e., $r^2 > 0.45$) between the $\frac{dS}{dt}$ and ADP observations (specifically, A2, A3, A4, M3 and M5). The exceptionally low r^2 from site M1 is likely due to many ADP observations occurring under similar $\frac{dS}{dt}$ conditions, i.e., insufficient variance in the data.

The results of Table 4.2 and Figure 4.7 share many similarities with regards to r^2 and the values of modeled coefficients, specifically k_4 and k_4'. In both the more complex model (eq. 4.3) and the simpler standing wave model (eq. 4.5), sites M4 and A3 exhibited the greatest r^2 values. In both models, the most upstream sites (A1 and M1) exhibited the lowest r^2 values (Table 4.2). The weak correlations at sites A1 and M1 was likely due to minimal discharge magnitude at these sites and the lack of a variety in $\frac{dS}{dt}$ conditions observed at site M1. The five k_4 values from Table 4.2 were very similar to the corresponding k_4' values in Figure 4.7, especially for the Aransas River. A ratio of the coefficients, $\rho = k_4 : k_4'$, ranged from 0.62 at M4 to 1.03 at A3, with all of the Aransas River sites exhibiting $\rho \geq 0.70$ (i.e., $\rho_{A1} = 0.84$, $\rho_{A2} = 0.70$, $\rho_{A3} = 1.03$, and $\rho_{A4} = 0.97$). A ρ value of 1 would indicate matching coefficients. The close similarity of the k_4 and k_4' confirms that for these five sites much of the modeled fit using eq. (4.3) is related to the $\frac{dS}{dt}$ term, as expected for strongly standing wave systems.

Finally, the phase offset analysis may provide a method for tracking the impacts of rising sea level on estuarine systems. As sea level continues to rise, estuarine geometries will change and potentially result in different waveforms transporting tidal energy upstream. By monitoring several selected systems' discharge and stage over time, we may witness a temporal shift in waveform character (e.g., from near progressive through mixed to standing wave). Any shift in waveform character will have ramifications for the transport

and timing of nutrients and freshwater discharging from terrestrial headwaters to the coastal environment.

4.4.4 Tidal Rating Curve regression

4.4.4.1 Model Equations

Equation (4.3) can be broken into two parts: the progressive and standing wave controls of tidal systems. The k_1 and k_2 terms correspond to the "progressive" portion of the eq. (4.3) as they relate stage to discharge. Similarly, the k_3 and k_4 terms are associated with the "standing" portion of the equation. Both halves of the equation are characterized by second-order polynomials in an attempt to mimic the power law relationship relating non-tidal riverine stage to discharge. The USGS riverine rating curve methodology attempts to relate discharge measurements to observations of stage through a power law relationship [*Kennedy* 1984] similar to the following:

$$Q_i = a * (S_i - b)^c \quad (4.6)$$

Where Q_i and S_i are the discharge and stage at time, t_i, the value of *b* represents the stage measurement for which no discharge occurs, and the value of *a* is a fit coefficient.

However, a power law relationship cannot be determined for a variable that contains negative values such as $\frac{dS}{dt}$. This fact becomes apparent when determining the value of the exponent, *c*, either empirically or analytically. For example, for an empirical determination, the data is plotted in log-log space and the slope of a linear trend characterizes the exponent, *c* [*Kennedy* 1984]. However, $\frac{dS}{dt}$ conditions cannot be plotted in Real log-log space due to negative values. Additionally, the first step in determining the analytical solution for the power-law parameters is to deconstruct eq. (4.6) using logarithms. Assuming $b = 0$ and substituting $\frac{dS}{dt}$ observations for stage conditions, the

resulting eq. (4.7) is invalid as negative $\frac{dS}{dt}$ values within the logarithmic functions will result in complex imaginary solutions.

$$\log(Q_i) = \log(a) + c * \log(\frac{dS_i}{dt}) \quad (4.7)$$

Instead, we used two second-order polynomials to address the immiscibility of logarithms and negatives, while attempting to describe the elliptical relationship between tidal discharge, stage, and $\frac{dS}{dt}$ (Figure 4.6). Linear regressions of stage and $\frac{dS}{dt}$ would be insufficient to accurately estimate tidal discharge. In addition, *Moftakhari et al.* [2013] estimated tidal river discharges using a power law (on a "tidal property ratio") whose exponent, γ, ranged between $\frac{2}{3} \leq \gamma \leq 2$. At the upper extreme, this power law would mimic a second-order polynomial. However, the symmetrical character of second-order polynomials pose a potential problem as conditions outside those observed (e.g., sharply rising stage relating to $\frac{dS}{dt} > 2$) may produce erroneous discharge estimates.

Each second-order polynomial represented the potential conditions of an endmember condition, i.e., standing or progressive. Equation (4.3) seeks to address the discharge regime of mixed wave systems (e.g., Shark, Connecticut, and Halls Rivers in Figure 4.6) by combining the impacts of both endmember conditions. The combination of the two second-order polynomials represent the amalgamation of standing and progressive wave character and their combined impact on system discharge. Thus, each modeled coefficient (k value) should reflect the expected waveform properties and relationships between tidal discharge, stage, and $\frac{dS}{dt}$ identified by the phase offset analysis.

4.4.4.2 Model coefficients (k_i) vs. waveform expectations

Conceptually, for a standing wave system, $\frac{dS}{dt}$ conditions should inversely relate to discharge (for our coordinate system with positive discharge oriented downstream). Meanwhile, the relationship between stage and discharge should be effectively negligible,

since these two variables are offset by $\frac{\pi}{2}$. However, for the opposite waveform endmember, a progressive wave will inversely relate stage to discharge conditions, while the correlation between $\frac{dS}{dt}$ and discharge should be negligible. A mixed wave system likely represents an intermediate combination of both endmember conditions, inversely relating discharge to both stage and $\frac{dS}{dt}$ conditions.

For the ten strongly standing wave sites identified by our phase analysis (M-A sites and the Crystal and Plum Island Rivers, Table 4.1), we should expect an inverse $\frac{dS}{dt}$ to discharge relationship and a mild-to-negligible inverse stage to discharge relationship. All sites that included the $\frac{dS}{dt}$ term in the model showed a negative k_4 coefficient, indicative of the expected inverse $\frac{dS}{dt}$ to discharge relationship.

Sites M1 and M5, although standing wave systems, do not include a relationship with $\frac{dS}{dt}$. This is likely why site M1 presents such a poor model fit ($r^2 = 0.17$). One possible explanation for this is the lack of ADP data at this site during diverse $\frac{dS}{dt}$ conditions (Figure 4.7e). Unfortunately, due to resolution issues with one of the ADP instruments, the majority of the valid M1 ADP transects occurred during January and February of 2017. The steady, low flows during those monitoring times produced a cluster of negligible discharge measurements (Figure 4.7e), where small sampling errors may have a large impacts. Similarly, insufficient variability in $\frac{dS}{dt}$ conditions during M5 ADP observations led to two clusters of observations (Figure 4.7h) that were described slightly better by stage ($r^2 = 0.51$, Table 4.2) than $\frac{dS}{dt}$ ($r^2 = 0.47$, Figure 4.7h). Longer periods of ADP data and more regular sampling intervals throughout the year at sites M1 and M5 would likely provide a relationship between discharge, stage, and $\frac{dS}{dt}$ that better coincides with standing wave theory.

The phase analysis identified ten USGS sites exhibiting mixed wave character (Connecticut, Murderkill, Middle, Savannah, Ogeechee, St. Mary's, Chassahowitzka,

Halls, Mobile, and Shark Rivers, Table 4.1). For these mixed wave sites, we expect coefficients describing inverse relationships between tidal discharge, and both $\frac{dS}{dt}$ and stage. Indeed as expected, each site's model includes at least one coefficient that describes an inverse stage to discharge relationship (i.e., negative k_1 or k_2), as well as at least one coefficient that characterizes an inverse $\frac{dS}{dt}$ to discharge relationship (i.e., negative k_3 or k_4).

4.5 Summary and Conclusion

This study expanded the classic method for gauging rivers to a similarly simple model for tidal river systems. Classic methods for gauging non-tidal rivers estimate discharge with a regression to stage. Our method incorporates $\frac{dS}{dt}$ into the regression model to account for tidal impacts on stage and discharge.

For the ten M-A sites and twelve USGS sites, we used an FFT to compare the semidiurnal and diurnal harmonic phases and identify the phase offset between tidal stage and velocity fluctuations. This analysis determined that the M-A monitoring sites experience nearly standing wave energy propagation (Table 4.1), meaning that stage and discharge (or velocity conditions) are offset by approximately $\frac{\pi}{2}$.

This relationship between stage and velocity for the M-A sites indicated that $\frac{dS}{dt}$ (i.e., the stage-rate-of-change) was important to include, along with stage, in our tidal rating curves. The phase analysis was also completed for twelve USGS tidal gauging stations, where the Index-Velocity Method is presently used by the USGS to calculate discharge [*Ruhl and Simpson* 2005, *Levesque and Oberg* 2012]. The analysis of the USGS sites resulted in φ values that spanned a wide range of possible offsets (i.e., $\frac{\pi}{2}$ to π). Unfortunately, none of the data exhibited fully progressive wave character (i.e., $\varphi = \pi$). Also, the analysis of phase offset may provide a means for observing the temporal physical changes in estuaries as a consequence of rising sea level.

We combined stage, $\frac{dS}{dt}$, and velocity data collected over two years (i.e., 01 July 2015 to 01 July 2017) at the M-A sites with ADP volumetric discharge observations to create piecewise tidal rating curves. For the 8 M-A sites with ADP observations, we devised a two-part tidal rating curve model (eq. 4.3 and 4.4) that differentiates storm and baseflow periods and calculates discharge accordingly. During baseflow, discharge was calculated from site-specific regression coefficients of stage, stage^2, $\frac{dS}{dt}$, and $(\frac{dS}{dt})^2$. These site-specific coefficients were determined from a regression to each site's associated ADP observations. During storm conditions, when riverine forces have overrun tidal forces, we used observations of thalweg velocity to approximate discharge through a rectangular cross-section. We also performed the baseflow model analysis on two weeks of baseflow data from twelve USGS sites to verify the methodology across broader empirical conditions.

The baseflow regression analysis resulted in fourteen sites (both USGS and M-A) exhibiting strong fits to the proposed discharge models (i.e., $r^2 > 70$). In addition, the discharge results as a whole agreed with the observations of *Bruesewitz et al.* [2013], *Mooney and McClelland* [2012], and *Jones et al*. [2017], with the majority of the discharge through the M-A Rivers occurs during storm periods, even though the typical discharge conditions are overwhelmingly characterized by baseflow.

This new method to estimate the discharge of tidal rivers based only on continuous stage data and minimal ADP calibration measurements provides a simple and inexpensive alternative to existing instrumentation or computationally expensive approaches. Instead, for less money, a study may even install numerous stage monitoring sites, create tidal rating curves at each location, and so monitor the longitudinal variations in discharge regime for a tidal river of interest as done in this study. Future expansions of this methodology may be able to increase the regression agreement between observed and estimated discharge by

including additional variables, such as mean channel velocity. Future studies may also work to more accurately calculate discharges occurring during the transition between baseflow and storm conditions, improving upon this method's piecewise composition.

4.6 Acknowledgements

This material is based upon work supported by the National Science Foundation under Grant No. 1417433. Any opinions, findings, and conclusions or recommendations expressed in this material are those of the authors and do not necessarily reflect the views of the National Science Foundation.

4.7 REFERENCES

Aretxabaleta, A. L., Butman, B., Signell, R. P., Dalyander, P. S., Sherwood, C. R., Sheremet, V. A., & McGillicuddy, D. J. (2014). Near-bottom circulation and dispersion of sediment containing Alexandrium fundyense cysts in the Gulf of Maine during 2010–2011. *Deep Sea Research Part II: Topical Studies in Oceanography*, *103*, 96–111. https://doi.org/10.1016/j.dsr2.2013.11.003

Arndt, S., Lacroix, G., Gypens, N., Regnier, P., & Lancelot, C. (2011). Nutrient dynamics and phytoplankton development along an estuary–coastal zone continuum: A model study. *Journal of Marine Systems*, *84*(3), 49–66. https://doi.org/10.1016/j.jmarsys.2010.08.005

Bianchi, T. S., Pennock, J. R., & Twilley, R. R. (Eds.). (1999). *Biogeochemistry of Gulf of Mexico estuaries*. New York: John Wiley.

Bruesewitz, D. A., Gardner, W. S., Mooney, R. F., Pollard, L., & Buskey, E. J. (2013). Estuarine ecosystem function response to flood and drought in a shallow, semiarid estuary: Nitrogen cycling and ecosystem metabolism. *Limnol. Oceanogr*, *58*(6), 2293–2309. Retrieved from http://www.researchgate.net/publication/258440362_Estuarine_ecosystem_function_response_to_flood_and_drought_in_a_shallow_semiarid_estuary_Nitrogen_cycling_and_ecosystem_metabolism/file/3deec5283d62f52ef0.pdf

Dingman, S. L. (2008). *Physical hydrology* (2nd ed. / reissue). Long Grove, IL: Waveland Press Inc.

Dottori, F., Martina, M. L. V., & Todini, E. (2009). A dynamic rating curve approach to indirect discharge measurement. Hydrology and Earth System Sciences, 13(6), 847. Retrieved from http://search.proquest.com/openview/854ef6955be6af7e35a010c574f673b0/1?pq-origsite=gscholar&cbl=105724

Ensign, S. H., Doyle, M. W., & Piehler, M. F. (2013). The effect of tide on the hydrology and morphology of a freshwater river: TIDAL RIVER HYDROLOGY AND MORPHOLOGY. *Earth Surface Processes and Landforms*, *38*(6), 655–660. https://doi.org/10.1002/esp.3392

Evans, A., Madden, K., & Palmer, S. M. (Eds.). (2012). *The Ecology and Sociology of the Mission-Aransas Estuary* (1st ed.). Port Aransas, Texas: Mission-Aransas National Estuarine Research Reserve.

Fulbright, T. E., Diamond, D. D., Rappole, J., & Norwine, J. (1990). The coastal sand plain of southern Texas. *Rangelands*, 337–340. Retrieved from http://www.jstor.org/stable/4000522

Ganju, N. K., Schoellhamer, D. H., Warner, J. C., Barad, M. F., & Schladow, S. G. (2004). Tidal oscillation of sediment between a river and a bay: a conceptual model. Estuarine, Coastal and Shelf Science, 60(1), 81–90. https://doi.org/10.1016/j.ecss.2003.11.020

Heinesch, B. (2006, July). *Coordinate Rotation*. Oral Presentation presented at the Summer school "eddy-covariance flux measurements," Namur, Belgium. Retrieved from http://hdl.handle.net/2268/60780

Heniche, M., Secretan, Y., Boudreau, P., & Leclerc, M. (2000). A two-dimensional finite element drying-wetting shallow water model for rivers and estuaries. *Advances in Water Resources*, *23*(4), 359–372. Retrieved from http://www.sciencedirect.com/science/article/pii/S0309170899000317

Hittle, C., Patino, E., & Zucker, M. (2004). Hydrologic Characteristics of Estuarine River Systems within Everglades National Park. *US Department of the Interior US Geological Survey*, (2004–3129). Retrieved from https://pubs.usgs.gov/fs/2004/3129/

Huhta, C. (2002). Handheld Acoustic Doppler Velocimeter (ADV) for Water Velocity Surveys. *Hydraulic Measurements and Experimental Methods*. https://doi.org/10.1061/40655(2002)30

Humphries, P., Keckeis, H., & Finlayson, B. (2014). The River Wave Concept: Integrating River Ecosystem Models. *BioScience*, *64*(10), 870–882. https://doi.org/10.1093/biosci/biu130

Johnson, S. L. (2009). *A general method for modeling coastal water pollutant loadings* (Ph.D. Dissertation). The University of Texas at Austin, Austin, TX. Retrieved from http://search.proquest.com/docview/856598483/abstract?accountid=7118

Jones, A. E., Hodges, B. R., McClelland, J. W., Hardison, A. K., & Moffett, K. B. (2017). Residence-time-based classification of surface water systems. *Water Resources Research*. https://doi.org/10.1002/2016WR019928

Kennedy, E. J. (1984). *Discharge Ratings at Gauging Stations* (U.S. Geological Survey Techniques of Water-Resources Investigations No. Book 3, Chap. A10) (p. 59). Washington, D.C., USA: United States Geological Survey. Retrieved from https://pubs.usgs.gov/twri/twri3-a10/pdf/TWRI_3-A10.pdf

Levesque, V. A. (2004). *Water Flow and Nutrient Flux from Five Estuarine Rivers along the Southwest Coast of the Everglades National Park, Florida, 1997-2001* (Scientific Investigations Report No. 2004–5142). Reston, VA: US Department of the Interior US Geological Survey.

Levesque, V. A., & Oberg, K. A. (2012). *Computing Discharge Usin the Index Velocity Method* (Techniques and Methods No. 3-A23) (p. 148). Reston, Virginia: U.S. Geological Survey. Retrieved from http://pubs.usgs.gov/tm/3a23/

Maio, C. V., Donnelly, J. P., Sullivan, R., Madsen, S. M., Weidman, C. R., Gontz, A. M., & Sheremet, V. A. (2016). Sediment dynamics and hydrographic conditions during storm passage, Waquoit Bay, Massachusetts. *Marine Geology*, *381*, 67–86. https://doi.org/10.1016/j.margeo.2016.07.004

Moftakhari, H. R., Jay, D. A., Talke, S. A., Kukulka, T., & Bromirski, P. D. (2013). A novel approach to flow estimation in tidal rivers. *Water Resources Research*, *49*(8), 4817–4832. https://doi.org/10.1002/wrcr.20363

Mooney, R. F., & McClelland, J. W. (2012). Watershed Export Events and Ecosystem Responses in the Mission–Aransas National Estuarine Research Reserve, South Texas. *Estuaries and Coasts*, *35*(6), 1468–1485. https://doi.org/10.1007/s12237-012-9537-4

National Estuarine Research Reserve (NERR) (2015). Tunnell, J., Buskey, E. J. & Peterson, T. (Eds.) *Freshwater Inflows: Determining Flow Regimes in the Face of Land Use Change, Climate Change, and Other Unknowns*. 47 (National Estuarine Research Reserve, 2015).

National Oceanic and Atmospheric Administration (NOAA) (2017a). Climate Prediction Center - Monitoring & Data: ENSO Impacts on the U.S. - Previous Events. *National Weather Service - Climate Prediction Center* (2017). Available at: http://www.cpc.ncep.noaa.gov/products/analysis_monitoring/ensostuff/ensoyears.shtml. (Accessed: 19th July 2017)

National Oceanic and Atmospheric Administration (NOAA) (2017b). El Niño Southern Oscillation (ENSO). *Earth System Research Laboratory: Physical Sciences Division* (2017). Available at: https://www.esrl.noaa.gov/psd/enso/enso_101.html. (Accessed: 19th July 2017)

National Oceanic and Atmospheric Administration (NOAA) Tides & Currents (2017c), Station Selection—NOAA Tides & Currents NOAA Tides & Currents—Station Selection, National Oceanic and Atmospheric Administration, Washington, D. C. [Available at https://tidesandcurrents.noaa.gov/stations.html?type5Water1Levels#Texas, accessed 19th July 2017.]

Palmer, T. A., Montagna, P. A., Pollack, J. B., Kalke, R. D., & DeYoe, H. R. (2011). The role of freshwater inflow in lagoons, rivers, and bays. *Hydrobiologia*, *667*(1), 49–67. https://doi.org/10.1007/s10750-011-0637-0

Pollack, J. B., Kim, H.-C., Morgan, E. K., & Montagna, P. A. (2011). Role of Flood Disturbance in Natural Oyster (Crassostrea virginica) Population Maintenance in an Estuary in South Texas, USA. *Estuaries and Coasts*, *34*(1), 187–197. https://doi.org/10.1007/s12237-010-9338-6

Ropelewski, C. F., & Halpert, M. S. (1986). North American Precipitation and Temperature Patterns Associated with the El Niño/Southern Oscillation (ENSO). *Monthly Weather Review*, *114*(12), 2352–2362. https://doi.org/10.1175/1520-0493(1986)114<2352:NAPATP>2.0.CO;2

Ruhl, C. A., & Simpson, M. R. (2005). *Computation of Discharge Usin the Indexd-Velocity Method in Tidally Affected Areas* (Scientific Investigations Report No. 2005–5004) (p. 31). Reston, Virginia: U.S. Geological Survey.

Savenije, H. H. G. (2005). *Salinity and tides in alluvial estuaries* (1st ed). Amsterdam ; Boston: Elsevier.

Shen, J., & Haas, L. (2004). Calculating age and residence time in the tidal York River using three-dimensional model experiments. *Estuarine, Coastal and Shelf Science*, *61*(3), 449–461. https://doi.org/10.1016/j.ecss.2004.06.010

Sheremet, V. (2013, February). *Building Observing System Deployed on Lobster Traps along the Northeast Atlantic Shelf*. Presented at the Fishermen & Scientist Research Society: 20th Annual Conference, Truro, Nova Scotia. Retrieved from http://www.fsrs.ns.ca/docs/Building%20Observing%20Systems%20Vitalii%20SharemetManning_PubRelease.pdf

Sheremet, V., Manning, J., & Pelletier, E. (2009). *Environmental monitors on lobster traps (eMOLT) Phase VI: Bottom Currents* (Annual Report). Northeast Fisheries Science Center. Retrieved from http://www.northeastconsortium.net/pdfs/awards_2007/Sheremet%2007/Sheremet%2007%20Final%20Report.pdf

Smoot, G. F., & Novak, C. E. (1969). *Measurement of discharge by the moving-boat method* (USGS Numbered Series No. 03-A11). U.S. Govt. Print. Off.,. Retrieved from http://www.comm-tec.com/Library/technical_papers/USGS/twri_3-A11_a.pdf

Soballe, D. M., & Kimmel, B. L. (1987). A Large-Scale Comparison of Factors Influencing Phytoplankton Abundance in Rivers, Lakes, and Impoundments. *Ecology*, *68*(6), 1943. https://doi.org/10.2307/1939885

SonTek. (2007). *RiverSurveyor System Manual* (System Manual) (p. 189). San Diego, CA: SonTek/YSI Inc. Retrieved from http://www.sontek.com

Teledyne. (2015). *StreamPro ADCP Guide* (ADCP Guide No. 95B–6003–00) (p. 101). Poway, CA: Teledyne RD Instruments. Retrieved from http://www.rdinstruments.com

United States Geological Survey (USGS) (2017), USGS Current Water Data for Texas, USGS NWIS United States Geological Survey, Reston, Va. [Available at http://waterdata.usgs.gov/tx/nwis/rt, accessed July 2017.]

Wilczak, J. M., Oncley, S. P., & Stage, S. A. (2001). Sonic anemometer tilt correction algorithms. *Boundary-Layer Meteorology*, *99*(1), 127–150. Retrieved from http://www.springerlink.com/index/p32123684246g213.pdf

Wolter, K., Dole, R. M., & Smith, C. A. (1999). Short-term climate extremes over the continental United States and ENSO. Part I: Seasonal temperatures. *Journal of Climate; Boston*, *12*(11), 3255–3272. Retrieved from https://search-proquest-com.ezproxy.lib.utexas.edu/docview/222898488?pq-origsite=summon

Yuan, R., Kang, M.-S., Park, S.-B., & Hong, J.-K. (2007). The Effect of Coordinate Rotation on the Eddy Covariance Flux Estimation in a Hilly KoFlux Forest Catchment. *Korean Journal of Agricultural and Forest Meteorology*, *9*(2), 100–108. https://doi.org/10.5532/KJAFM.2007.9.2.100

Chapter 5: Conclusion

5.1 MOTIVATION

The purpose of the preceding chapters was to provide the foundation for investigations into residence time dynamics of the *riverine tidal freshwater zone* (RTFZ). Although a transitional environment along the river-estuary continuum, the RTFZ has yet to be formally defined with a consistent nomenclature. An RTFZ is a river reach upstream of the river mouth composed of freshwater chemistry, while experiencing tidal physics. Similar tidal freshwater environments have been discussed previously in the literature, however mostly regarding freshwater wetlands and swamps [*Odum* 1988, *Day et al.* 2007, *Doyle et al.* 2007]. No consistent nomenclature nor framework has described tidal freshwater environments contained within the river channel. Sometimes noted as a "transitional" environment (e.g., *Yankovsky et al.* [2012]), these tidal freshwater zones (TFZs) may control the timing and magnitude of freshwater and nutrient transport to the downstream estuary.

Before investigating the RTFZ's residence time dynamics, a consistent and fundamental definition of an RTFZ is needed. The work presented in Chapters 2 and 3 provide that necessary foundation upon which to build more in-depth RTFZ analyses. Chapter 2 isolates systems that may contain an RTFZ via their temporal residence time conditions. After investigating a specific system identified by the work of Chapter 2, an RTFZ is isolated and observed in Chapter 3. Chapter 3 includes a discussion of both empirical RTFZ observations and an RTFZ conceptual model.

With the RTFZ conceptual model and nomenclature in place, a method was needed for translating field measurements of tidal stage into estimates of tidal discharge. Chapter 4 presents a method for estimating tidal discharges from tidal stage time series. With these

modeled tidal discharges, the necessary puzzle pieces have been accumulated to begin investigations into RTFZ residence time dynamics.

Although Chapter 2 presents an initial residence time study to identify potential RTFZ sites, future studies may investigate RTFZ residence time dynamics with greater resolution. For example, Chapter 2 determines bulk water residence times through the tidal freshwater portion of 15 Texas tidal rivers. However, newly modeled tidal discharges (Chapter 4) enable analysis of residence times between observed locations of λ_3 and λ_1 (Chapter 3). In addition, boundaries of systems analyzed in Chapter 2 did not change location, while RTFZ boundaries (i.e., λ_3 and λ_1) observed in Chapter 3 translated over time (e.g., λ_1 moving upstream with saline intrusion). With modeled tidal discharges and temporal RTFZ λ locations, we may analyze residence time dynamics throughout the temporally variable RTFZ length. We may also analyze the residence time dynamics across different RTFZ reaches (i.e., λ_3 to λ_2 versus λ_2 to λ_1).

Each chapter works toward the ultimate goal of investigating RTFZ residence time conditions. The chapters, both individually and in conjunction, provide numerous scientific and methodologic contributions that make future longitudinal residence time analyses possible. The following provides a summary of each chapter and highlights their combined contributions. I also discuss potential future research that builds upon the foundation laid by these chapters.

Future studies should work to tease out the effects of the RTFZ and its temporal dynamics (e.g., lengthening, shortening, or translation along river length) on freshwater and nutrient residence times. RTFZ residence time dynamics may influence the estuarine ecology [*Palmer et al.* 2011, *Pollack et al.* 2001] and, with looming impacts of future climate change, RTFZs will become the nexus of two primary consequences of climate change: rising temperatures altering the hydrologic cycle and sea level rise.

5.2 SUMMARY OF CHAPTER 2

Chapter 2 presents a framework for classifying fresh surface water bodies as *lentic*/*lotic*/*intermediate* and *oscillic*/*nonoscillic* based upon temporal residence time conditions. The presented Freshwater Continuum Classification (FCC) framework seeks to consistently quantify the classification of a given water body as either *lentic* (reservoir-like) or *lotic* (riverine). The FCC also expands classic *lentic*/*lotic* nomenclature by introducing the *oscillic* and *nonoscillic* terms to describe a system's temporal behavior. A system may be described as *oscillic* if it experiences both *lotic* and *lentic* behavior over the period of analysis. The FCC attempts to translate the previously qualitative *lentic* and *lotic* definitions into a quantitative framework that is universally descriptive. With the FCC, all systems defined as *lentic* or *lotic* will exhibit similar hydrodynamics and residence time properties.

As an initial case study, Chapter 2 also presents the application of the FCC to 15 tidal rivers along Texas' Gulf of Mexico coastline. The region's minimal baseflow, due to extensive summer evaporation, coupled with potential flooding from tropical storm deluges creates the opportunity for *lentic, oscillic* systems. The minimal baseflow promotes extended residence times that are indicative of *lentic* (reservoir-like) environments, while flooding promotes *lotic* (river-like) conditions. Over the multi-year period of record, we expected to observe primarily *lentic* conditions punctuated by periodic episodes of *lotic* character, which would result in a final *lentic, oscillic* classification. In fact, eight of the fifteen systems analyzed were described as *lentic, oscillic* as predicted. The subsequent study that attempted to identify, isolate, and observe an RTFZ within one of those *lentic, oscillic* systems: the Aransas River.

5.3 SUMMARY OF CHAPTER 3

Chapter 3 provides the first formal conceptual and empirical definition of an RTFZ. Although TFZs have been previously discussed (e.g., *Yankovsky et al.* [2012], *Knights et al.* [2017], *Ganju et al.* [2004], *Odum* [1988]), a formal framework for describing such a system has not yet materialized. A TFZ entirely upstream of the river mouth but contained within the river banks, i.e., an RTFZ, has also not been discussed in the literature. Chapter 3 attempts to rectify this oversight by proposing an RTFZ conceptual model and contributes the first empirical identification and observation of an RTFZ.

The RTFZ conceptual model consists of three λ locations that mark the extent of certain points of interest along the river-estuary continuum. The conceptual model describes a vertically and horizontally averaged river-estuary continuum (i.e., one dimensional). This continuum is discretized into four segments of importance separated by three λ values. Each λ position is recorded as distance upstream from the river mouth. Conceptually, the extent of tidal surface waves is denoted by λ_3. That is, everything downstream of λ_3 experiences rising and falling stage that is a result of flood and ebb tides. Conversely, river reaches upstream of λ_3 maintain stage conditions reminiscent of a non-tidal river (i.e., rising stage with increased flow, and fairly consistent stage during baseflow). The upstream extent of tidal bidirectional velocities is denoted by λ_2. Sites downstream of λ_2 will experience changes in the orientation of discharge. These sites' discharge will switch between flowing downstream and upstream throughout the tidal cycle. Sites upstream of λ_2 will experience only downstream-oriented discharge (i.e., unidirectional flow). This does not mean that the tidal cycle does not impact these upstream sites' discharge regime. Their discharge magnitude may decrease or increase in response to the tidal cycle; however, these sites' discharge is never (or rarely) negative (i.e., directed upstream). The downstream boundary of the RTFZ is marked by λ_1, which denotes the

upstream extent of estuarine brackish waters (identified with a threshold of 2.0 PSU in Chapter 3). Thus, λ_1 divides the terrestrial freshwaters from the estuarine brackish waters. The RTFZ is defined as the river reach between λ_3 and λ_1, under the caveat that λ_1 must be upstream of the river mouth for an RTFZ to exist. The RTFZ length and position (i.e., specific location along the river length) may shift in response to perturbations in the balance of riverine and tidal forcings that creates the RTFZ.

As observed on the Aransas River, large precipitation events may collapse and even eliminate the RTFZ. A rapid increase in inflow may cause riverine conditions (i.e., unidirectional discharge and non-tidally fluctuating stage) to override all indications of tidal influence. This riverine domination rapidly translates λ_3 and λ_2 downstream, potentially beyond λ_1 and the river mouth. As λ_3 is pushed downstream, the length of the RTFZ is rapidly shortened. As mass transport occurs more slowly than energy transport, λ_1 will eventually move downstream as advection removes the estuarine salt from the river. If a large enough inflow pulse, the RTFZ may be destroyed as λ_1 is extruded beyond the river mouth. If λ_1 was not removed beyond the river mouth, upon the post-storm return to baseflow, the RTFZ will be reestablished as tidal forces return upstream. If λ_1 was indeed moved downstream but remained upstream of the river mouth, the reestablished RTFZ will be longer than the immediately pre-storm RTFZ. As baseflow conditions continue over the long-term, tidal forces will intrude salt (and with it λ_1) farther upstream, which will slowly shorten the RTFZ length. The rate of RTFZ shortening is related to the rate of inland estuarine salt transport.

The residence time conditions of the RTFZ likely also respond to these same perturbations and are altered by translations in λ location. To investigate the residence times of the transient RTFZ and its λs, a method is needed for recording long-term observations of tidal discharge.

5.4 SUMMARY OF CHAPTER 4

Chapter 4 presents a simple methodologic expansion to classic river gauging methods to create a tidal rating curve. Non-tidal rivers are typically gauged by relating stage to discharge observations via a power function [*Kennedy* 1984]. However, tidal rivers cannot be described by such a relationship, because tidal influence makes the stage to discharge relationship non-unique. Stage magnitudes are repeated throughout the tidal cycle, but each repetition of stage is not associated with identical discharges. Measurements of $\frac{dS}{dt}$, and specifically its sign, isolate when during the tidal cycle each stage observation occurred (e.g., rising or falling tide). By incorporating $\frac{dS}{dt}$ as a factor that influences tidal discharge, we eliminate the non-unique stage problem and may estimate tidal discharge.

As an initial case study, the method for developing a tidal rating curve was applied to several sites along the Mission and Aransas (M-A) Rivers of south Texas, and twelve tidal USGS gauging sites. The rating curve's estimates of tidal discharge showed strong agreement with measurements of discharge with 14 of 20 sites analyzed exhibiting $r^2 > 0.70$. This initial case study provides evidence of an accurate method for gauging tidal rivers without needing permanent expensive installations. In addition, the resulting modeled discharge for the M-A rivers reflected the expected discharge dynamics of these systems. Specifically, although minimal tidal baseflow dominates the temporal majority of the discharge regime, the majority of freshwater transport occurs during storm periods [*Bruesewitz et al.* 2013, *Mooney and McClelland* 2012, and *Jones et al.* 2017].

Chapter 4 also discussed the waveform stage to discharge relationships between standing and progressive waves. Within a riverine coordinate system (i.e., positive discharge oriented downstream), progressive waves should theoretically inversely relate stage and discharge, while standing waves should inversely relate discharge and $\frac{dS}{dt}$. These

relationships have been described previously (e.g., *Savenije* [2005]), but have not been used to estimate tidal discharge.

5.5 SCIENTIFIC AND METHODOLOGIC CONTRIBUTIONS

The analyses presented in this dissertation provide numerous scientific and methodologic contributions. This work contributes both to hydrology in general and to our understanding of tidal systems. Herein I provide several explicit examples of the potential impacts of this work.

The work presented in Chapter 2 expanded the *lentic/lotic* nomenclature to include hydrologic temporal variability through the introduction of the *oscillic* term. The analysis updated what was previously a binary, qualitative assessment of a system's hydrologic character. Previously, *Soballe and Kimmel* [1987] had called for hydrologic character to be viewed as a spectrum of potential conditions, rather than the discrete, binary *lentic*/*lotic* classifications. The work of Chapter 2 attempts to move the *lentic*/*lotic* ideology toward a spectrum-like discussion by incorporating an additional *intermediate* typical condition and accounting for temporal variability (*oscillic*).

As a scientific contribution, Chapter 3 conceptually and empirically defines an RTFZ. This definition provides a much needed common nomenclature that may be used to discuss and investigate RTFZ dynamics. Previously, to describe TFZs, studies have used such terms as "transitional zone" [*Yankovsky et al.* 2012], "transitional regime" [*Ganju et al.* 2004], or "tidal river estuary" [*Shen and Haas* 2004]. Chapter 3 provides a consistent and explicit framework for describing RTFZs that until now has not been realized. Such a framework will likely become increasingly useful as climate change threatens to alter the balance between river and tidal forcings, and potentially impact RTFZs worldwide.

Chapters 2 and 3 present methods that may be used in resource management. Both chapters present a method for classifying or identifying the presence of a certain quality within a given system. Chapter 2 presents the FCC that identifies *lentic*/*lotic*/*oscillic* character, while Chapter 3 provides the methodology for identifying the presence of an RTFZ within a river-estuary continuum. Each of these methods may prove useful for monitoring anthropogenic impacts on our coastal resources. For example, the construction of a dam to create a freshwater reservoir will likely reduce downstream discharge. Diminishing the freshwater inputs to the coastal system may cause a shift in the *lentic*/*lotic*/*oscillic* character and/or may alter the location or presence of an RTFZ. The presented methods may be used to monitor the RTFZ position and *lentic*/*lotic*/*oscillic* character of the system throughout the installation of the dam and its subsequent management. Similarly, the installation of a salt sill to prevent saline intrusion upstream will likely alter a system's RTFZ and may impact a system's *lentic*/*lotic*/*oscillic* character. A salt sill may reduce the impact of the tide, which reduces saline intrusion, and may potentially truncate the movement of λ_1 upstream. This would create an artificially long RTFZ. The decreased tidal influence may also make some originally *lentic* tidal systems exhibit *lotic* or *intermediate* conditions. This shift in typical system character may also result in a change in the system's *oscillic* nature. By monitoring the system's RTFZ and *lentic*/*lotic*/*oscillic* character, we may minimize anthropogenic impacts on our coastal systems.

As an additional methodological contribution of this dissertation, Chapters 3 and 4 present the first application of SeaHorse tilt current meters (TCMs) to tidal river environments. To date, TCMs have been installed only in estuarine or coastal shelf environments [*Aretxabaleta et al.* 2013, *Maio et al.* 2016, *NERR* 2015]. The minimal baseflow observed in Chapters 3 and 4 often corresponded to minimal velocities below tilt

meter sensitivity limits (i.e., $| v_i | < 2$ cm s^{-1}). However, these velocity sensitivity issues may be resolved with improved accelerometer technologies. The new technology may allow for increased sensitivity of newer TCMs. Another way to resolve the velocity issues is to be more selective about installation location. For example, if you need a majority of velocity measurement magnitudes to be reliable, install TCMs in tidal systems that experience stronger flow (e.g., A4 rather than A1). However, if monitoring a tidal system, TCMS may always record some semi-unreliable velocity measurements, specifically during slack water (SW) when tidal discharge momentarily ceases. Thus, unless tilt meter sensitivity increases dramatically, tilt meters will likely always record some semi-unreliable velocity data in tidal systems. However, the cyclic timing of tidal velocity fluctuations during baseflow was reliably captured by TCMs. Although the magnitude of some velocities remained questionable, the overall cyclic discharge character of TCM sites could be monitored. TCMs will reliably monitor velocity oscillations between upstream and downstream orientations. These oscillating discharge observations could be used to diagnose the energy waveform of a tidal system (when paired with stage observations - Chapter 4), or differentiate reach lengths that contain primarily bi- or unidirectional velocity regimes (Chapter 3).

For future TCM deployments in unidirectional riverine environments (i.e., upstream of λ_2 and/or λ_3), researchers should be aware of the maximum velocity sensitivity of the TCMs. Any velocities that exceed the TCM maximum will be reported as the TCM's maximum observable velocity, which will lead to an underestimation of discharge and velocity conditions. In other words, the TCM has a reliable sensitivity range between exceptionally low and high flow rates, but beyond that range, the accuracy of the TCM observations is debatable. However, if one keeps the instrument's sensitivity range in mind,

TCMs deployed in riverine environments should provide accurate, reliable, and inexpensive continuous observations of thalweg velocity.

The tidal rating curve method of Chapter 4 contributes a simple approach for estimating tidal discharge by expanding typical methods for gauging non-tidal rivers. Before this, the estimation of tidal discharge relied on computationally expensive numerical models or permanent installations of acoustic doppler instrumentation. The new method proposes the inclusion of $\frac{dS}{dt}$ to eliminate problems with non-unique correlations between tidal stage and discharge. Since measurements of $\frac{dS}{dt}$ temporally describe the tidal cycle (e.g., positive $\frac{dS}{dt}$ relates to rising tidal stage), the relationships between coupled stage and $\frac{dS}{dt}$ descriptors, and discharge are unique. Thus, a simple expansion to classic river gauging methods enables the estimation of tidal discharge. Furthermore, while the additive second-order polynomial relationship described in Chapter 4 (eq. 4.3) is adequate for estimating tidal discharge, the actual relationship between tidal discharge, stage, and $\frac{dS}{dt}$ may be elliptic (Figure 4.6 in Chapter 4). This ellipse may rotate in three dimensional space with respect to the waveform of the tidal system. For example, the systems depicted in Figure 4.6 are plotted in order with respect to their system waveforms, with most *progressive*-like at the top to most *standing*-like at the bottom. Potentially, as the waveform type moves toward one endmember (i.e., progressive or standing), the discharge relationship approaches a linear relationship with either stage or $\frac{dS}{dt}$ (respectively). For example, in Figure 4.6 we see that the relationship between $\frac{dS}{dt}$ and discharge becomes increasingly linear as you approach a standing wave when moving from Figure 4.6b to 4.6d to 4.6f to finally reach the linear relationships in Figures 4.6h and 4.6k. The systems depicted in Figures 4.6h and 4.6k were both defined as standing wave systems in Chapter 4 (Crystal and Plum Island Rivers in Table 4.1). If investigated properly, this elliptic insight

may provide increasingly accurate estimations of tidal discharge without expensive permanent installations.

5.6 FUTURE WORK

Several potential future studies will build off the analyses presented in preceding chapters. For example, tidal discharge estimates produced in Chapter 4 may be used to analyze the Aransas River RTFZ's discharge and residence time regime. Specifically, Aransas River sites' (A1-A5) discharge estimates may be compared against RTFZ λ locations to empirically investigate longitudinal trends in RTFZ discharge and residence time.

Empirically verified modelling efforts may also help to tease out the residence time implications of the RTFZ. A one-dimensional (1D) river-estuary continuum model would allow for a sensitivity analysis on the controls of the length and position of an RTFZ. The model results may be verified with the λ locations from Chapter 3 and discharge estimates from Chapter 4, yet may provide insight into the residence time dynamics along the RTFZ.

From the residence time predictions, either from the 1D modeling study or the empirical analysis, we may compare the Aransas River RTFZ within the FCC framework presented in Chapter 2. This analysis would determine whether the Aransas River RTFZ (or potentially RTFZs in general) typically acts as a *lentic*/*lotic*/*intermediate* system and is *oscillic*/*nonoscillic*.

Chapter 4 introduced the idea that the relationship between tidal discharge, stage, and $\frac{dS}{dt}$ may be elliptic. As a tangential future endeavor, the relationship described by this ellipsoidal plane in 3D space may be investigated to provide more accurate estimations of tidal discharges. Additionally, such an investigation may increase our understanding of waveform energy transport.

In general, future analyses should focus on the RTFZ as an important transitional environment between rivers and the coastal environment. Not only has the RTFZ been largely overlooked until recently, but, with increasing global temperatures altering the hydrologic cycle, and global sea level rise, RTFZs reside at the nexus two primary consequences of climate change.

5.7 Acknowledgments

This material is based upon work supported by the National Science Foundation under Grant No. 1417433. Any opinions, findings, and conclusions or recommendations expressed in this material are those of the authors and do not necessarily reflect the views of the National Science Foundation.

5.8 REFERENCES

Aretxabaleta, A. L., Butman, B., Signell, R. P., Dalyander, P. S., Sherwood, C. R., Sheremet, V. A., & McGillicuddy, D. J. (2014). Near-bottom circulation and dispersion of sediment containing Alexandrium fundyense cysts in the Gulf of Maine during 2010–2011. *Deep Sea Research Part II: Topical Studies in Oceanography*, *103*, 96–111. https://doi.org/10.1016/j.dsr2.2013.11.003

Bruesewitz, D. A., Gardner, W. S., Mooney, R. F., Pollard, L., & Buskey, E. J. (2013). Estuarine ecosystem function response to flood and drought in a shallow, semiarid estuary: Nitrogen cycling and ecosystem metabolism. *Limnol. Oceanogr*, *58*(6), 2293–2309. Retrieved from http://www.researchgate.net/publication/258440362_Estuarine_ecosystem_function_response_to_flood_and_drought_in_a_shallow_semiarid_estuary_Nitrogen_cycling_and_ecosystem_metabolism/file/3deec5283d62f52ef0.pdf

Day, R. H., Williams, T. M., & Swarzenski, C. M. (2007). Hydrology of Tidal Freshwater Forested Wetlands of the Southeastern United States. In *Ecology of Tidal Freshwater Forested Wetlands of the Southeastern United States* (pp. 29–63). Springer Netherlands. Retrieved from http://link.springer.com/chapter/10.1007/978-1-4020-5095-4_2

Doyle, T. W., O'Neil, C. P., Melder, M. P. V., From, A. S., & Palta, M. M. (2007). Tidal Freshwater Swamps of the Southeastern United States: Effects of Land Use, Hurricanes, Sea-level Rise, and Climate Change. In *Ecology of Tidal Freshwater Forested Wetlands of the Southeastern United States* (pp. 1–28). Springer Netherlands. Retrieved from http://link.springer.com/chapter/10.1007/978-1-4020-5095-4_1

Ganju, N. K., Schoellhamer, D. H., Warner, J. C., Barad, M. F., & Schladow, S. G. (2004). Tidal oscillation of sediment between a river and a bay: a conceptual model. *Estuarine, Coastal and Shelf Science*, *60*(1), 81–90. https://doi.org/10.1016/j.ecss.2003.11.020

Jones, A. E., Hodges, B. R., McClelland, J. W., Hardison, A. K., & Moffett, K. B. (2017). Residence-time-based classification of surface water systems. *Water Resources Research*. https://doi.org/10.1002/2016WR019928

Kennedy, E. J. (1984). *Discharge Ratings at Gauging Stations* (U.S. Geological Survey Techniques of Water-Resources Investigations No. Book 3, Chap. A10) (p. 59). Washington, D.C., USA: United States Geological Survey. Retrieved from https://pubs.usgs.gov/twri/twri3-a10/pdf/TWRI_3-A10.pdf

Knights, D., Sawyer, A. H., Barnes, R. T., Musial, C. T., & Bray, S. (2017). Tidal controls on riverbed denitrification along a tidal freshwater zone: Tides on Riverbed Denitrification. *Water Resources Research*, *53*(1), 799–816. https://doi.org/10.1002/2016WR019405

Maio, C. V., Donnelly, J. P., Sullivan, R., Madsen, S. M., Weidman, C. R., Gontz, A. M., & Sheremet, V. A. (2016). Sediment dynamics and hydrographic conditions during storm passage, Waquoit Bay, Massachusetts. *Marine Geology*, *381*, 67–86. https://doi.org/10.1016/j.margeo.2016.07.004

Mooney, R. F., & McClelland, J. W. (2012). Watershed Export Events and Ecosystem Responses in the Mission–Aransas National Estuarine Research Reserve, South Texas. *Estuaries and Coasts*, *35*(6), 1468–1485. https://doi.org/10.1007/s12237-012-9537-4

National Estuarine Research Reserve (NERR) (2015). Tunnell, J., Buskey, E. J. & Peterson, T. (Eds.) *Freshwater Inflows: Determining Flow Regimes in the Face of Land Use Change, Climate Change, and Other Unknowns*. 47 (National Estuarine Research Reserve, 2015).

Odum, W. E. (1988). Comparative Ecology of Tidal Freshwater and Salt Marshes. *Annual Review of Ecology and Systematics*, *19*, 147–176. https://doi.org/10.2307/2097151

Palmer, T. A., Montagna, P. A., Pollack, J. B., Kalke, R. D., & DeYoe, H. R. (2011). The role of freshwater inflow in lagoons, rivers, and bays. *Hydrobiologia*, *667*(1), 49–67. https://doi.org/10.1007/s10750-011-0637-0

Pollack, J., Kim, H.-C., Morgan, E., & Montagna, P. (2011). Role of Flood Disturbance in Natural Oyster (Crassostrea virginica) Population Maintenance in an Estuary in South Texas, USA. *Estuaries and Coasts*, *34*(1), 187–197. https://doi.org/10.1007/s12237-010-9338-6

Shen, J., & Haas, L. (2004). Calculating age and residence time in the tidal York River using three-dimensional model experiments. *Estuarine, Coastal and Shelf Science*, *61*(3), 449–461. https://doi.org/10.1016/j.ecss.2004.06.010

Soballe, D. M., & Kimmel, B. L. (1987). A Large-Scale Comparison of Factors Influencing Phytoplankton Abundance in Rivers, Lakes, and Impoundments. *Ecology*, *68*(6), 1943. https://doi.org/10.2307/1939885

Yankovsky, A. E., Torres, R., Torres-Garcia, L. M., & Jeon, K. (2012). Interaction of Tidal and Fluvial Processes in the Transition Zone of the Santee River, SC, USA. *Estuaries and Coasts*, *35*(6), 1500–1509. https://doi.org/10.1007/s12237-012-9535-6

Appendix A: Description of lentic/lotic threshold calculations

Conceptually, the lentic/lotic iT_R threshold calculations approximate the lentic/lotic conditions for a range from large to small possible natural system volumes. The calculations are completed by approximating and interpolating between the lentic and lotic iT_R behaviors at the largest and smallest natural volumes. This requires four volume-iT_R threshold endpoints, e.g. *lentic* threshold for the *largest* plausible natural volume, etc: (1) *large lotic*, (2) *small lotic*, (3) *large lentic* and (4) *small lentic*. Interpolating between the large and small system lotic coordinates (conditions 1 and 2) and lentic endpoints (conditions 3 and 4) results in the iT_R threshold conditions for any system volume within the natural world.

A.1 Volume Approximations

As a conservative estimate, we approximated the smallest natural study site volume as one cubic meter – a 1m x 1m x 1m cube. We reasoned that any smaller body of freshwater would not likely be analyzed to determine lentic or lotic character.

On the opposite end of the natural spectrum, we used simple geometric measurements of the world's largest river systems. The product of the Nile River's length (6853 km), the maximum width of the Amazon River (4800 m), and the maximum depth of the Congo River (220 m) provided the volume approximation of the largest natural freshwater system to be studied for lentic/lotic behavior.

When approximating the iT_R conditions at each spectrum endmember, we will build upon and incorporate aspects of these volume conditions. Each estimated volume is also incorporated into the lentic and lotic coordinates for that given end of the spectrum (Figure A.2).

A.2 INTEGRATED RESIDENCE TIME APPROXIMATIONS

Since discharge and volume time-series do not exist for each volumetric extreme, we cannot calculate iT_R using the integration methodology (Figure 2.1). However, if we assume steady-state conditions, where there is no change in system volume or discharge over time,

$$\frac{d}{dt}Q = \frac{d}{dt}V = 0 \qquad \text{(A1)}$$

the endmember iT_R conditions may be approximated by instantaneous residence time calculations (T_R =V/Q).

The iT_R is calculated as the difference between $t_{initial}$ and t_{final}, the time when the accumulated discharge equals the system volume, V, or in other words, the time necessary, given variable discharge conditions, to accumulate the system volume (see Section 2.2.1). However, under steady-state conditions, the discharge magnitude will not change over time. As such, the "accumulated" volume of discharge is Q*iT_R = Vac, and when Vac = V, the calculations of iT_R are equivalent to those of instantaneous residence time (T_R). Because the iT_R calculations for a system at steady-state replicate T_R calculations, the following expansion of equation (2.1) holds true,

$$iT_R = t_{final} - t_{initial} = \frac{Vol}{Q} = \frac{l*w*d}{q*A_{in}} = \frac{l*A_{avg}}{q*A_{in}} = \frac{l}{q} * (\frac{A_{avg}}{A_{in}}) = T_R \qquad \text{(A2)}$$

where t_{final} and $t_{initial}$ are obtained from the time-series calculations of iT_R conditions (**Figure A.1**).

Examination of the final portion of equation (A2) reveals only three terms need approximation to estimate iT_R conditions:

1. Specific discharge, *q*, at the upstream end of the system of interest
2. The system length, *l*
3. The cross-sectional area ratio, $\frac{A_{avg}}{A_{in}}$, of average to smallest upstream cross sections of the system of interest.

To specify specific discharge, q, we obtained water velocities associated with lentic and lotic conditions from the literature: 0.01 m s-1 and 0.4 m s-1, respectively [Hein et al., 2003; Baranyi et al. 2002] (for further detail, see Section 2.2.1.1). We calculated two separate iTR thresholds at each volumetric endmember using these two velocities.

We used our volume approximations' length measurements for the system lengths, with the largest plausible study site having the length of the Nile River (6853 km) and the smallest having a length of one meter.

The final variable needed to estimate the iT_R conditions is the cross-sectional area ratio, which describes how the cross-sectional area changes along the length of the water body. At the small end of the natural volume spectrum, the cross-sectional area of a system is unlikely to change over the meter length. Thus, we approximate the area ratio of the small end of the natural spectrum as 1:1.

However, for most natural systems the inflow cross-sectional area at the most upstream end of the system is likely to be different from the average cross-sectional area. For the largest plausible natural study site, the cross-sectional area of flow should change substantially throughout the traverse length and must be greater than 1:1. We described the area ratio of the large end of the natural spectrum as 60:1.

One reason for the area ratio of 60:1 for largest conceivable natural system is the area ratios of the analyzed Texas Rivers. An empirical analysis of the area ratios for the

analyzed Texas Rivers revealed an approximate median and mean ratios of 8:1 and 15:1, respectively. Area of the inflow cross-section was calculated with rectangular geometry via the measured width at the United States Geological Survey (USGS) gauge and river stage recorded by the USGS gauge. The average cross-sectional area was determined by averaging between the inflow and river mouth cross-sectional areas. We calculated the river mouth cross-sectional area, approximated with rectangular geometry, via a channel width measurement and tidal stage recorded at the nearest National Oceanic and Atmospheric Administration's (NOAA) gauging station. If the average area ratio for these systems is 15:1, quadrupling the area ratio provides a reasonable estimate for characterizing the largest natural system. Note that this does not mean the area ratio or method is specific to Texas rivers; rather, the selected study reaches happen to provide 15 examples and that the assumptions and analysis should hold elsewhere provided hydrology and geomorphology operate according to consistent global governing factors.

The Amazon River provides good agreement with the 60:1 area ratio via the comparison of two upstream sites to central Amazon River mean observations. Trigg et al. [2009] collected bathymetry transects along 430 km along the central Amazon River and observed an average water depth and channel width of 27.7 meters and 3711 meters. The upper Amazon River is composed of two tributaries: the Ucayali and Marañón rivers. Cross-sectional width measurement of the confluence of the Marañón and the Rio Crisnejas is 60.3 meters; approximately 70 times less than the average channel width reported by Trigg et al. [2009]. In addition, the width of the headwaters of the Ucayali River (the confluence of the Tambo and Urubamba Rivers) is 304 meters. From this inflow width, the average width, and average depth of the central Amazon River we can predict that ~5.6 meters inflow depth is necessary to maintain the 60:1 area ratio. An Amazon River survey, commissioned by the Peru navy, reported water depths along the Ucayali River between 3

and 12 meters [Sullivan, 2013]. Thus, the proposed area ratio of 60:1 is representative of the geometry of the largest natural freshwater systems.

Using the longitudinal length and area ratio for each volume endmember, and the lentic/lotic flow rates, we calculated the lentic/lotic iT_R thresholds for each end of the natural spectrum. **Figure A.2** summarize the calculations and the resulting four coordinates.

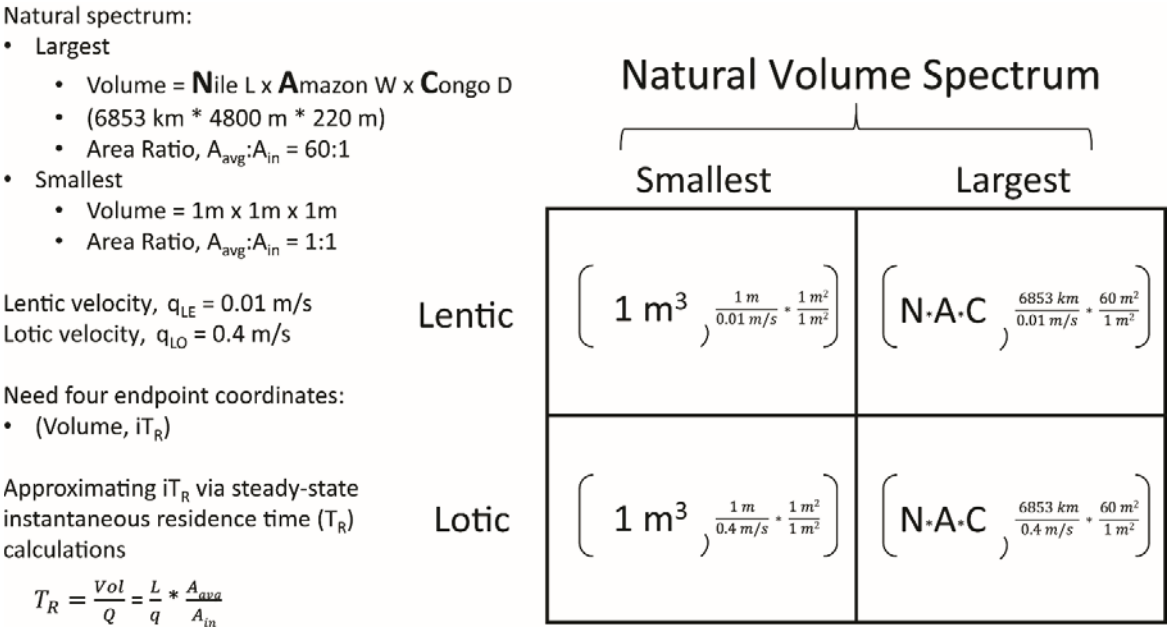

Figure A.2: Summary of large-/small-volume, lentic/lotic coordinate calculation. Lentic and lotic velocities remain constant at both volumetric endmembers. The largest volume is approximated by the product of the length of the Nile River, the maximum width of the Amazon River, and the maximum depth of Congo River, while the smallest volume is 1 m^3. The area ratio at the large volume approximation is 60:1 while 1:1 at the smallest. From the volume traverse length, the lentic/lotic velocity and the area ratio, we estimate and pair the iT_R conditions at each endmember with the respective volume to form our spectrum endpoints.

The spectrum coordinates were created by pairing the respective endmember volume and iT_R condition. For example, to describe the lentic conditions at largest plausible natural volume, we paired the following volume and iT_R conditions (**Figure A.2**):

$$(\text{Volume, } iT_R) = \left(N * A * D,\ \ \frac{N}{0.01\ m\ s^{-1}} * \frac{60\ m^2}{1\ m^2}\right) \quad \text{(A3)}$$

where *N* is the length of the Nile River, *A* is the maximum width of the Amazon River, and *D* is the maximum depth of the Congo River.

A power law interpolation between the two sets of lentic and lotic endpoints extrapolates the iT_R thresholds through spectrum of natural volumes. These interpolated curves allow us to determine the lentic/lotic iT_R thresholds for any plausible natural volume. Each volume within the spectrum of possible natural volumes is associated with a unique set of lentic/lotic thresholds. The power law interpolation accurately reproduced the literature's thresholds for our analyzed data (**Figure A.3**). In contrast, linear interpolation neither fit the empirical data nor, more importantly, resulted in threshold values similar to the literature. Equations (A4) and (A5) are the final, interpolated lentic and lotic thresholds, respectively.

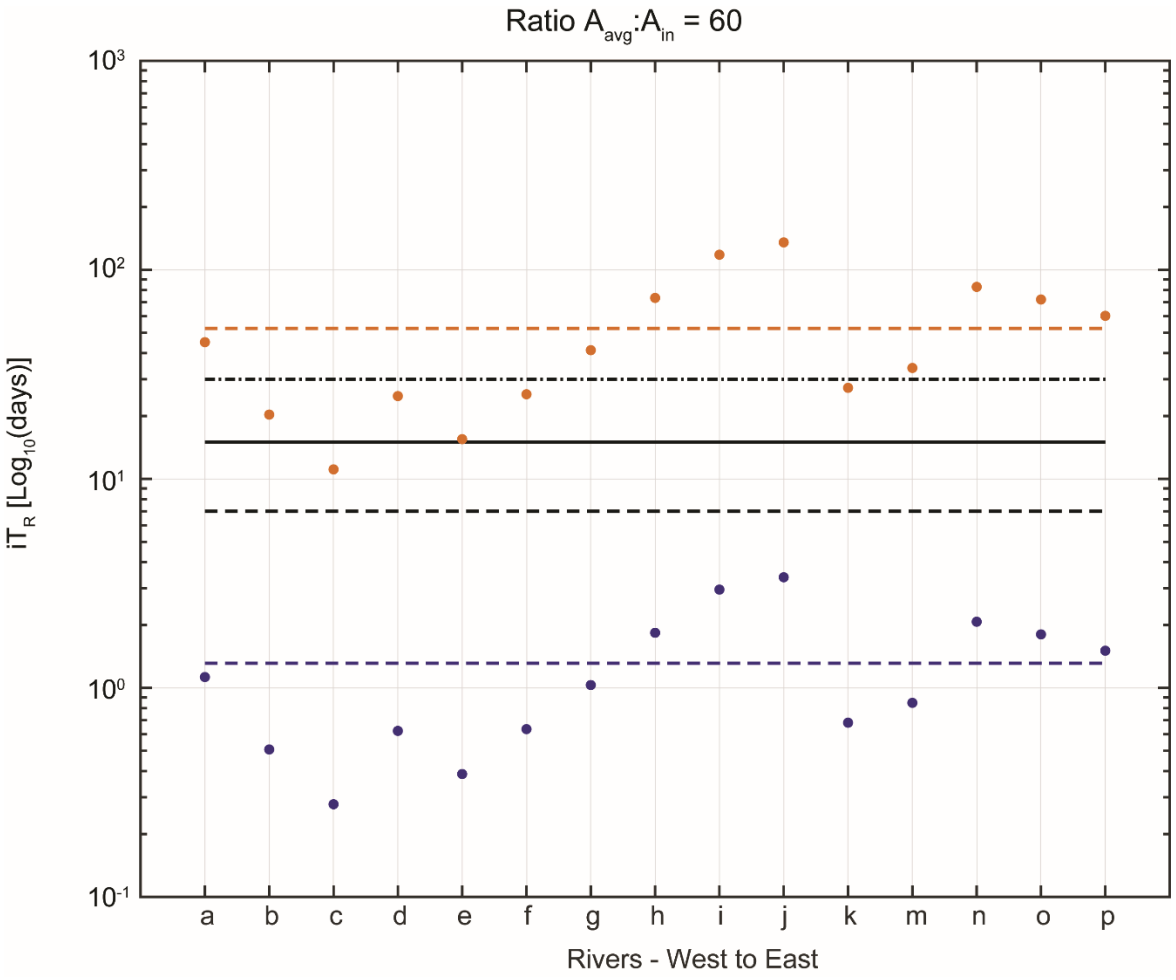

Figure A.3: Comparison of calculated iT_R thresholds to literature observations. For the 15 rivers analyzed in this study, each river's calculated lentic/lotic iT_R thresholds (orange/blue dots, respectively) were compared against some threshold values between lentic and lotic behaviors from the literature: 30 days (dot-dashed line, from Hein et al., [2003] and Baranyi et al., [2002]), 15 days (solid line, from Rennella and Quirós [2006]) and 7 days (black dashed line, from Baranyi et al., [2003]). The letter labels along each plot's x-axis are associated with the tidal reaches of the rivers named in Table 2.1. This comparison shows that the derived power laws, which generated the orange and blue dots, divide systems into lentic/intermediate/lotic around the same iT_R values that prior (non-scalable) methods would have (although they lacked the intermediate class).

Appendix B: Quantitative classification framework guide

The following descriptions and Matlab coding snippets will guide those interested through a simplified version of the lentic/intermediate/lotic and oscillic/nonoscillic classifications. There are two companion Matlab scripts, "ClassificationFramework_Example.m" and "intersections.m", to this Appendix B of the supplement. Please view both the "ClassificationFramework_Example.m" Matlab script and section A of this supplement together for a thorough example. This guide will accomplish the following tasks:

1. Recreate a simplistic Figure 2.1 using example data
2. Calculate *integrated residence time* (iT_R) for the example system
3. Classify and plot the data within Figure 2.3 framework

B.1 How to recreate Figure 2.1

B.1.1 Obtain the proper data

The first goal of this guide is to recreate a plot similar to Figure 2.1. Working to assemble Figure 2.1 ensures that all the proper data is present for the analysis. The variables necessary to complete this classification analysis are:

- Time stamps for each observation
- Time series of inflow (volumetric discharge) observations
- Time series of volume measurements

This framework implicitly assumes that the system's inflow is equivalent to its outflow. Thus, an outflow is not used in this analysis. Although a volume time series is

necessary, temporal volume measurements may be unavailable. The following data sets will enable a volume time series approximation if necessary:

- Time series of inflow depth measurements
- Time series of outflow depth measurements
- Time series/single measurement of inflow width
- Time series/single measurement of outflow width
- Single measurement of the traverse length

Note this guide assumes that the volume to be approximated is that of a river. Furthermore, this guide will assume that the river cross-sectional area is rectangular. However, other freshwater volumes (e.g., a reservoir) may be incorporated into the model.

The data necessary to approximate volume may not all be time series measurements. The inflow and outflow widths were stationary measurements in the pilot study. However, if geometric relationships between system depth and width exist, using a time series of widths would increase the accuracy of the volume time series approximations.

The example will perform two different analyses: one on a set of steady-state data, where this is no change in parameters over time, and a second on a transient system. Lines 31-64 of the "ClassificationFramework_Example.m" script (now on referred to as the *Main Script*, which can be found in Appendix C), presented below, initialize the necessary datasets to complete these simplistic example analyses.

```
31. %% Obtain the proper data
32. % hourly timestamps from Jan. 1, 2015 to Mar. 1, 2015
33. time_period = [datenum('01/01/2015 00:00', 'mm/dd/yyyy HH:MM'):...
34. 1/24:...
35. datenum('03/01/2015 00:00', 'mm/dd/yyyy HH:MM')]';
36.
37. % Steady-state Discharge
38. Qss = 12*ones(size(time_period)); % constant discharge of 12 m^3/s
39.
40. % Discharge 2: Transient
41. Q2_timeseries = linspace(9, 15, length(time_period))'; % vector of linearly changing
    discharge
42.
43. % If time series volume measurements exist, those may be used during the
44. % iTR calculations. However, if the volume time series does not exit, it
45. % may be created from several geometric measurements.
46.
47. % steady_state Volume - if time series volume is unavailable
48. Vss = 3e7*ones(size(time_period)); % constant 30 million cubic meters over time
49.
50. % If volume time series is unavailable, then calculate the volume time
51. % series from the following variables:
52. % - Inflow depth (time series)
53. % - Outflow depth (time series)
54. % - Inflow width (time series or single measurement)
55. % - Outflow width (time series or single measurement)
56. % - Traverse length (single measurement)
57.
58. % In this example, all applicable variables will be represented by a "single
59. % measurement", for the sake of simplicity.
60. inflow_depth   = linspace(5, 10, length(time_period))'; % vector of linearly rising inflow
    stage
61. outflow_depth  = linspace(10, 20, length(time_period))'; % vector of linearly rising
    outflow stage
62. inflow_width   = 45; % inflow cross-section is ~45 meters across
63. outflow_width  = 175; % inflow cross-section is ~175 meters across
64. traverse_length = 25e3; % 25km long water particle's journey from inflow to outflow
```

When reading Matlab code, any text that appears in green, or preceded by a percentile symbol (%), are comments. This means those lines are not executed by the software, but instead serve as notes about the script. Please read through the executable script lines and the comments for a complete explanation of the framework's calculations.

Lines 33-35 initialize a vector of time stamps, representing the hourly observations for the fictitious data obtained between January 1, 2015 and March 1, 2015. Line 38

initializes the steady-state discharge time series: a constant discharge of 12 cubic meters per second (cms) for this example. Whereas, line 41 creates a second discharge time series that changes linearly over the study, ranging from 9 cms in January to 15 cms in March. Line 48 records a steady-state volume time series, while lines 60-64 prepare the necessary variables (listed previously) to create a transient volume time series.

The next step in this guide is the creation of a volume time series from the above variables. Skip to section **B.1.3 – Calculating integrated discharge** if a volume time series approximation is unnecessary.

B.1.2 Approximating Volume if time series unavailable

Lines 72-95 of the *Main Script* present the approximation of a volume time series.

```
72. %% Calculating Volume - if time series is UNavailable
73. % these volume calculations will be used in calculations with
74. % non-steady state Q2 ("Discharge 2")
75.
76. % Step V1 - interpolate widths at meter resolution along the traverse length
77. resolution = 1;
78. riv_widths = linspace(inflow_width, outflow_width,...
79. round(traverse_length/resolution))';
80.
81. % step V2 - interpolate the depth profile along the traverse length at one
82. % meter resolution for every timestep
83. for iii = 1:length(time_period)
84.   all_depths(iii,:) = linspace(inflow_depth(iii), outflow_depth(iii),...
85.     round(traverse_length/resolution));
86. end
87. % resulting matrix of the depth profile (each rows) for all timesteps
88.
89. % Step V3 - find the summed area of each cross-section by multiplying depth
90. % and width for each time step
91. system_areas = all_depths * riv_widths;
92.
93. % Step V4 - find volume by multiplying summed cross-sectional area by
94. % the resolution
95. V2_timeseries = system_areas * resolution;
```

To approximate the volume from the depth, width, and traverse length measurements, first select the longitudinal discretization interval. The example analysis

uses one meter resolution (line 77) for the volume approximation. This means that the analysis will calculate the system's cross-sectional volume over every meter of length. An interval of one meter is conservative for a long study reach and will ensure that the volume between subsequent cross-sections is not significantly different. However, such a fine interval over the 25 km length of this example may be highly computationally expensive. If the *Main Script* takes too long to run, increase the interval as necessary (e.g., 10 or 20 meters). However, ensure during application to real data that the chosen interval does not oversimplify the system volume.

Conceptually, to approximate the system volume for any time step, we will sum the volume of adjacent cross-sectional rectangular prisms every meter (or the chosen interval) along the system length. The combined volume is

$$V = L_1*W_1*D_1 + L_2*W_2*D_2 + \ldots + L_n*W_n*D_n \quad \text{(B1)}$$

where n is the number of adjacent rectangles that is determined by dividing the total length by the interval length. However, we may simplify these calculations, because the length of each rectangular cross-section is the interval length (R). Thus,

$$L_1 = L_2 = L_n = R \quad \text{(B2)}$$

After incorporating equation (B2) into equation (B1),

$$V = R*(W_1*D_1 + W_2*D_2 + \ldots + W_n*D_n) \quad \text{(B3)}$$

where the statement enclosed in parentheses may be calculated through matrix multiplication as in equation (B4).

$$[D_1 \ldots D_n] * \begin{bmatrix} W_1 \\ \cdots \\ W_n \end{bmatrix} = (W_1*D_1 + W_2*D_2 + \ldots + W_n*D_n) \quad \text{(B4)}$$

Building on equation (B4), the system's depths may be recorded in a matrix, where each row is the depth profile for an associated time step (column), to allow for the expansion

$$\begin{bmatrix} D_{1,1} & \cdots & D_{1,n} \\ \vdots & \ddots & \vdots \\ D_{t,1} & \cdots & D_{t,n} \end{bmatrix} * \begin{bmatrix} W_1 \\ \cdots \\ W_n \end{bmatrix} = \begin{bmatrix} (W_1 * D_{1,1} \ + \ \ldots \ + \ W_n * D_{1,n}) \\ \cdots\cdots\cdots\cdots\cdots \\ (W_1 * D_{t,1} \ + \ \ldots \ + \ W_n * D_{t,n}) \end{bmatrix} \quad \text{(B5)}$$

where *t* is the number of time steps in the analysis. Multiplying the column vector resulting from equation (B5) by the chosen resolution, effectively a substitution into equation (B3), calculates a column vector of volumes for each time step.

Lines 78-79 and 84-85 interpolate the between the inflow and outflow widths and depths, respectively, along the traverse length and create a vector of width or depth measurements for every meter. In addition, lines 84-85 repeat the depth interpolation process for every inflow and outflow depth available and stores each interpolated vector as a row in the matrix titled "all_depths". Line 91 calculates and sums the cross-sectional areas by performing matrix multiplication between the *all_depths* matrix and the *riv_widths* column vector, as in equation (B5). The volume time series calculations are completed as line 95 by multiplying the summed areas by the chosen resolution.

B.1.3 Calculating integrated discharge

Lines 105-149 provide the calculations of integrated discharge for both discharge time series.

```
105. %% Calculating the integrated discharge for every time step
106. % Using trapezoidal summation, we determine the accumulated discharge from
107. % the initial timestep for all time steps.
108.
109. %Step 1 - Timestep integration beneath discharge curve.
110. for iii = 2:length(time_period)
111.
112.   % Equation for area of a trapezoid = ((b1 + b2)*h)/2.
113.   % Here, 'b1' and 'b2' are two sequential discharge measurements and 'h'
114.   % is the time between each observation.
115.
```

```
116.   % ***** STEADY-STATE CALCULATIONS ************************************
117.   b1 = Qss(iii-1);
118.   b2 = Qss(iii);
119.   h  = (time_period(iii)-time_period(iii-1))*(24*3600); % converted from [days] to [sec]
120.
121.   % integrated discharge for each time step
122.   integrated_Qss(iii-1,1) = ((b1 + b2)*h)/2;
123.
124.
125.   % ***** TRANSIENT CALCULATIONS ***************************************
126.   b1 = Q2_timeseries(iii-1);
127.   b2 = Q2_timeseries(iii);
128.   h  = (time_period(iii)-time_period(iii-1))*(24*3600); % converted from [days] to [sec]
129.
130.   % integrated discharge for each time step
131.   integrated_Q2(iii-1,1) = ((b1 + b2)*h)/2;
132.
133. end
134.
135. % Step 2 - Perform a cumulative summation on the time step integrated data,
136. % to obtain the accumulated discharge curve.
137.
138. % Notice that the integrated data is 1 value shorter in length than all the
139. % other time series. To address this, store a '0' value before the
140. % integrated discharge area, because at time step #1, no discharge has
141. % been accumulated.
142.
143. accum1_Qss = cumsum([0; integrated_Qss]); % steady-state accumulated Q
144. accum1_Q2  = cumsum([0; integrated_Q2]);  % Transient accumlated Q
145.
146. % ****** NOTE:
147. % This cumulative summation only calculated the accumulated discharge
148. % from the FIRST time step. The FOR loop will complete this
149. % calcuation for each timestep when calculating iTR.
```

The analysis performs trapezoidal summation to approximate integration of the discharge time series. This summation provides the volume of water fluxing through the system with each time step, by calculating the area of a trapezoid (A = [b1+b2]*h/2) created by two subsequent discharge observations (b1, b2) and the amount of time between each observation (h). The FOR loop, beginning on line 110, iterates through each time step, starting from the second and ending at the final time step, and calculates the volume traversing the system during that time step.

To finish Figure 2.1, we need to calculate the cumulative volume discharged through the system for a given time step. Lines 143 and 144 calculate the accumulated discharge volume starting at the first time step. A cumulative sum returns the sum of all the cells from the original vector with index lower than or equal to the current index of the new vector.

B.1.4 Re-creating Figure 2.1

Lines 155-188 draw a plot similar to Figure 2.1 from the sample data calculated throughout this guide. The resulting plot should resemble Figure B.1.

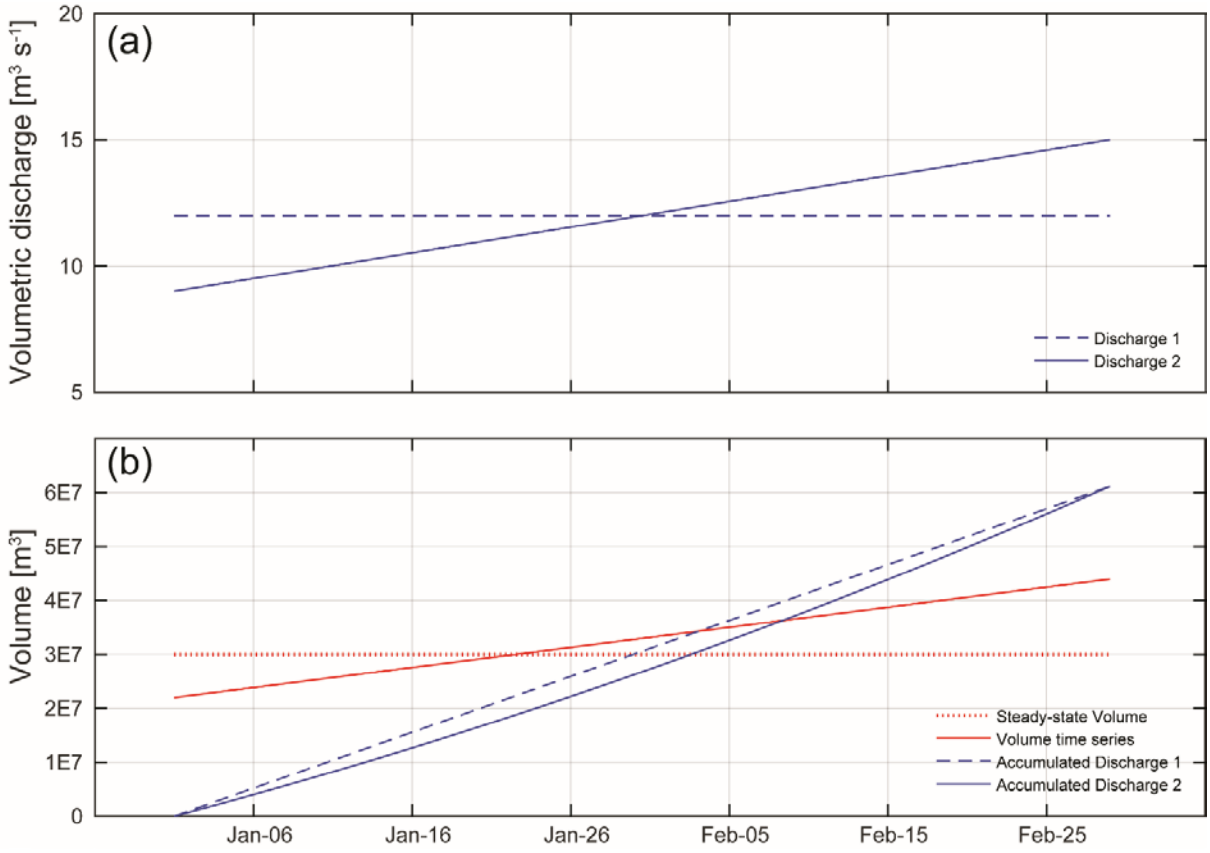

Figure B.1: Initial replication of conceptual Figure 2.1. For simplicity, the example analysis uses a constant (steady-state) and simple linearly increasing discharge time series (a); the same goes for the volume time series (b).

B.2 CALCULATING iT_R FOR ALL TIME STEPS FROM DISCHARGE AND VOLUME TIME SERIES

Lines 205-330 provide the iT_R calculations for both the steady-state and transient time series. However, only the steady-state calculations are included within this section. The full Matlab script (Section C) includes how to work with transient data.

```
205. %% Calculating iTR from the discharge and volume time series
206. %%%%%%%%%%%% iTR calculations %%%%%%%%%%%%%
207. % The second goal of this analysis will be to calculate iTR conditions for
208. % each time step. This process will use the same accumulated discharge
209. % calculations as a part of the analysis, but apply it for every time step.
210.
211. % Analysis will be carried out over each time step; we use a FOR loop to
212. % perform the analysis on each time step.
213. for ttt = 1:length(time_period)
214.
215.   % obtaining time stamp for time step's calculations
216.   t_initial = time_period(ttt);
217.
218.   % ***** STEADY-STATE CALCULATIONS ******
219.   % calculating all possible accumulated discharge from current time step
220.   accum_Qss   = cumsum([0; integrated_Qss(ttt:end)]);
221.
222.   % With every time step, the number of accumulated discharge values
223.   % decreases. To compare vectors and vector indices accurately, all
224.   % vectors are shortened to the same length. In other words, we are
225.   % updated all vectors to begin at the same time step.
226.   clipped_Vss  = Vss(ttt:end);
227.   clipped_time = time_period(ttt:end);
228.
229.   % find where accumulated discharge is just above and below
230.   below_index  = max(find(accum_Qss < clipped_Vss));
231.   above_index  = min(find(accum_Qss > clipped_Vss));
232.
233.
234.   if isempty(above_index)
235.     % If there are no time steps with an accumulated discharge above the
236.     % sytem volume, we return a 'NaN' value as the iTR value for that time
237.     % step.
238.     iTRss(ttt,1) = nan;
239.
240.   else
241.     % Find intersection between points
242.     [intersect_time, intersect_vol] = ...
243.     intersections(...
244.     clipped_time(below_index:above_index), accum_Qss(below_index:above_index),...
245.     clipped_time(below_index:above_index), clipped_Vss(below_index:above_index),   1);
246.     % Can calculate the intersection yourself or use the "intersections.m"
247.     % function written by Douglas M. Schwarz available from MatLab File
```

```
248.      % Exchange here:
249.      % http://www.mathworks.com/matlabcentral/fileexchange/11837-fast-and-robust-curve-
intersections
250.      % A copy of the function is included with the supplemental MatLab files.
251.
252.        % marking the best end time
253.        if ~isempty(intersect_time)
254.          t_final = intersect_time(1);
255.
256.          % adding the iTR value to the tracking variable
257.          iTRss(ttt,1) = t_final – t_initial; % recorded in [days]
... ** An 'else' statement outputting an error, should anything go wrong in the calculations. **
264.        end
265.      end
... *** break where Transient calculations are in Matlab script.***
330. end
```

The calculations of iT_R conditions are performed for each time step. As such, the actual calculations, lines 216-330, are performed within a FOR loop iterating over all timesteps. When the iT_R calculations begin anew for each time step, the current time stamp is recorded as $t_{initial}$ (line 216).

Since the iT_R calculations use the observations that follow the current time step, the time series data need to be "clipped" to reflect only the current time step's future conditions. Lines 220, 226, and 227 select the appropriate time series data (i.e. the current time step and all future conditions until the end of the data set).

After obtaining the current-future accumulated discharge and volume time series with the proper associated time stamps, lines 230 and 231 find indices for the accumulated discharge values most immediately less than (*below_index*) and greater than (*above_index*) the volume time series. If no intersection between the accumulated discharge and volume time series occur, meaning that the remaining future discharge conditions do not input enough water to exceed the system's volume, a 'NaN' ('Not a Number') value is returned for that time step's iT_R conditions (lines 234-238). However, if an intersection is found, the time and volume coordinates of the intersection are calculated (lines 242-245). One may calculate the coordinates of this intersection themselves; however, this analysis used

a function ("intersections.m") written by Douglas M. Scwarz made available by the Matlab File Exchange[1] that returns the intersection coordinates. The time coordinate of the intersection is recorded as t_{final} (Line 254) and the current time step's iT_R behavior is calculated as: $iT_R = t_{final} - t_{initial}$ (line 257).

B.2.1 Adding the iT_R lines to Figure B.1

Upon completing the FOR loop, the iT_R calculations for each time step for both the steady-state and transient data are finished. Thus, we may add the descriptions of the iT_R calculations to Figure B.1 to obtain a Figure B.2 (lines 338-404). The script only plots the iT_R calculations for the first time step. As such, no data is present before, or to the left, of the left most vertical line, marking $t_{initial}$. The other two vertical lines represent t_{finsl} for the steady-state and transient time series and cross the respective intersections of each data's accumulated discharge and volume time series (Figure B.2b).

[1] The "intersections.m" function may be downloaded at the following URL:
http://www.mathworks.com/matlabcentral/fileexchange/11837-fast-and-robust-curve-intersections

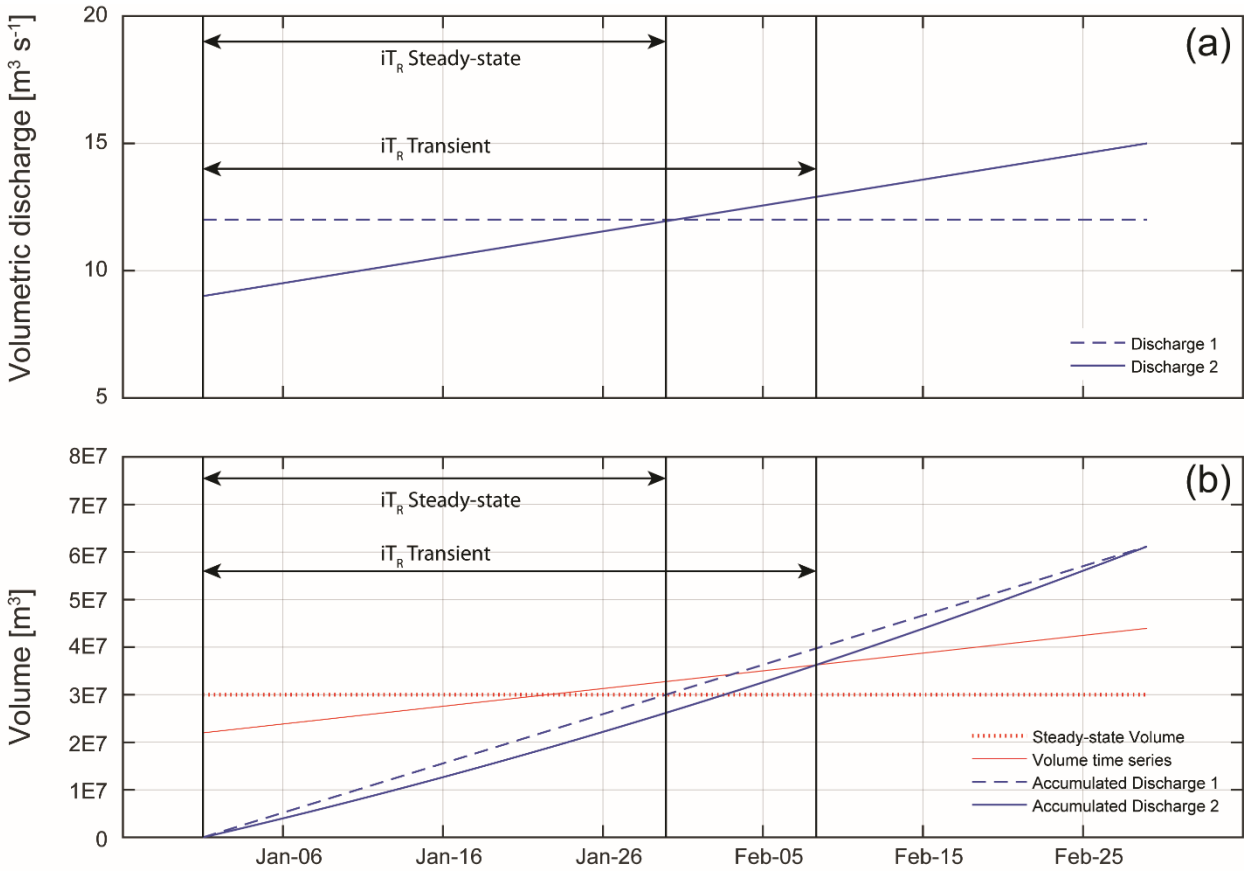

Figure B.2: Replication of Figure 2.1 including the iT_R calculation descriptions. The left-most vertical line, marking $t_{initial}$, is the first time step (a). Although the plots only display the iT_R calculations for the first time step, the vertical lines representing the placement of t_{final} cross the intersections between the steady-state and transient accumulated discharge and volume time series (b).

B.3 CLASSIFYING THE EXAMPLE SYSTEMS

B.3.1 Determine the iT_R thresholds across all possible natural volumes

Appendix A of this supplementary material provides an in-depth explanation of the threshold calculations. As such, this section will only provide the calculation highlights. Please read Appendix A and lines 410-452 of the *Main Script* for a more thorough explanation of the threshold calculations.

The threshold calculation process scales the lentic/lotic specific discharges through geometric relationships to volumetric discharges related to the largest and smallest natural volumes. The lentic and lotic threshold velocities in this study are: 0.4 m s^{-1} and 0.01 m s^{-1}. Please see section 2.2.2.1) for an explanation of how these velocities were determined from the literature.

*****IMPORTANT NOTE*****

Line 428 is where the lentic/lotic threshold velocities may be updated if improved specific discharges become available.

```
427. % threshold velocities from literature
428. q_thresh = [0.01, 0.4]; % m/s [row vector]
```

*****IMPORTANT NOTE*****

When using an alternate set of lentic/lotic threshold velocities within the *Main Script*, ensure that the first value is the **LENTIC** threshold. Also, should more appropriate area ratios (A_{avg}:A_{in}) be determined for the volume endmembers, those values may be incorporated into the *Main Script* at line 439, with the small volume endmember value first.

```
438. % Area ratios - Aavg:Ain for volume spectrum endmembers
439. AavgAin    = [1, 60];
```

Currently, the endmember extremes are interpolated via a single-term power law in lines 451 and 452. However, should a more accurate relationship between iT_R and volume be discovered, that relationship may be incorporated into the *Main Script* by changing the "fit" specifications.

```
450. % creating fit objects for threshold lines
451. [iTR_001, gof, params] = fit(hyp_vols, instant_RT_approx(:,1), 'power1'); % lentic fit
452. [iTR_04,  gof, params] = fit(hyp_vols, instant_RT_approx(:,2), 'power1'); % lotic fit
```

The calculation and interpolation process yields equations (2.3) and (2.4), which are used to calculate each system's unique iT_R thresholds.

B.3.2 Classify systems from unique iT_R thresholds

Lines 457-527 determine the lentic/intermediate/lotic and oscillic/nonoscillic classifications for both the steady-state and transient datasets. Only the steady-state classification commands are presented in this section since the process for classifying the transient data is identical.

```
457. % Classify - Step 2: Determine the Lentic/Lotic thresholds
458. % To calculate the Lentic/Lotic thresholds, first determine the median
459. % volume of your systems. Then use the fit object (or interpolated
460. % equation) to determine the proper iTR threshold. The if-else statements
461. % that follow enact the decision tree included in the supplemental
462. % information packet.
463.
464. % ***** STEADY-STATE CALCULATIONS ************************************
465. medVss = nanmedian(Vss);   % median steady-state volume
466. LenThresh_ss = iTR_001(medVss);   % lentic steady-state threshold
467. LotThresh_ss = iTR_04(medVss);    % lotic steady-state threshold
468. mediTRss = nanmedian(iTRss); % median iTR conditions of steady-state system
469.
470. % comparison of median iTR conditions with thresholds
471. % determining lentic/int./lotic classification
472. if mediTRss > LenThresh_ss
473.    LIL_class = 'Lentic';
474.
475. elseif mediTRss < LotThresh_ss
476.    LIL_class = 'Lotic';
477.
478. else
479.    LIL_class = 'Intermediate';
480. End
481.
482. % determining the oscillic classification - max and min iTR
483. maxi = nanmax(iTRss);
484. mini = nanmin(iTRss);
485. if maxi > LenThresh_ss && mini < LotThresh_ss
486. osc_class = 'Oscillic';
```

```
487. else
488. osc_class = 'Nonoscillic';
489. end
490.
491. % outputting the results
492. classification  = ['The steady-state system is classified as: '];
493. output = sprintf('%s\n %s%s %s\n', classification, LIL_class, ',', osc_class);
494. fprintf(output)
```

Once the iT_R time series has been obtained, there are two separate classifications completed from that time series of data: lentic/intermediate/lotic and oscillic/nonoscillic classifications (Figure B.3). To complete these classifications the system-specific iT_R thresholds are calculated from the interpolated equations (2.3 and 2.4) using a system's median volume (lines 465-467). The system-specific iT_R thresholds are compared against the system's median iT_R conditions (calculated in line 468) to determine typical lentic, intermediate, or lotic character. If the median iT_R value is greater than the lentic threshold, the system is typically *lentic* (lines 472-473). However, if the median iT_R is less than the lotic threshold, the system is *lotic* (lines 475-476). If neither of the previous two conditions are true, then the system must be *intermediate* (lines 478-479). This decision making process is depicted in the left limbs of the Figure B.3.

To complete the oscillic/nonoscillic classification, the maximum and minimum values of the iT_R time series are compared against the same lentic and lotic thresholds (right limb of Figure B.3).

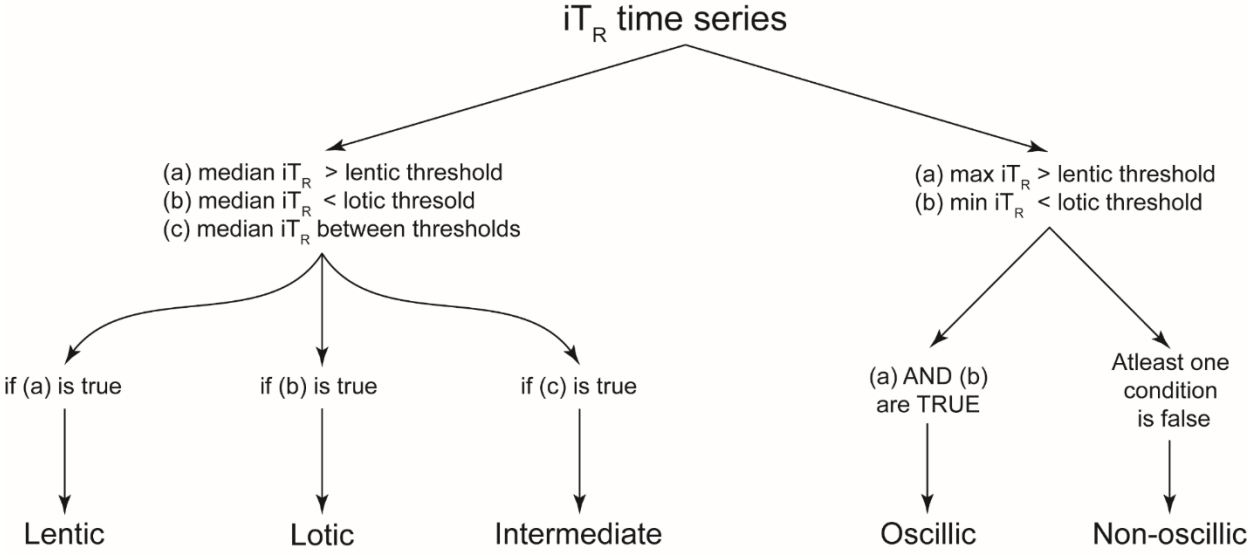

Figure B.3: The decision tree of the proposed classification framework. Beginning with a system's iT_R time series, there are two separate classifications to complete: lentic/lotic/intermediate and oscillic/nonoscillic. The former classification examines how the system's median, or typical, iT_R conditions relate to the system-specific lentic/lotic thresholds. The oscillic classification analyzes how the extremes of the time series relate to the iT_R thresholds. The left limb of the decision tree can be graphically represented as Figures 2.3a and 2.6, while the right limb is depicted in Figures 2.3b and 2.7.

The maximum and minimum values of the iT_R time series are calculated on lines 483 and 484, and compared to the lentic/lotic thresholds, through an if/else statement, on lines 485-489. If the maximum iT_R is greater than the lentic threshold AND the minimum iT_R is less than the lotic threshold, the system is *oscillic*. Note, that both conditions must be true in order for a system to be defined as oscillic. If either of the conditional statements is false, the system is defined as *nonoscillic* (Figure B.3).

For this simplistic example, both the steady-state and Transient time series represented “Intermediate, nonoscillic” systems. The final classifications are printed to the command window via lines 492-494.

B.3.3 Plotting the classifications similar to Figure 2.3a and 2.3b

Lines 532-611 plot the example classifications in a style similar to Figure 2.3. Figure B.4 depicts the output of the *Main Script*. Both systems’ typical conditions plot within the intermediate region (Figure B.4a) and their iT_R time series do not cross both thresholds (Figures B.4b and c), confirming the aforementioned “Intermediate, nonoscillic” classification.

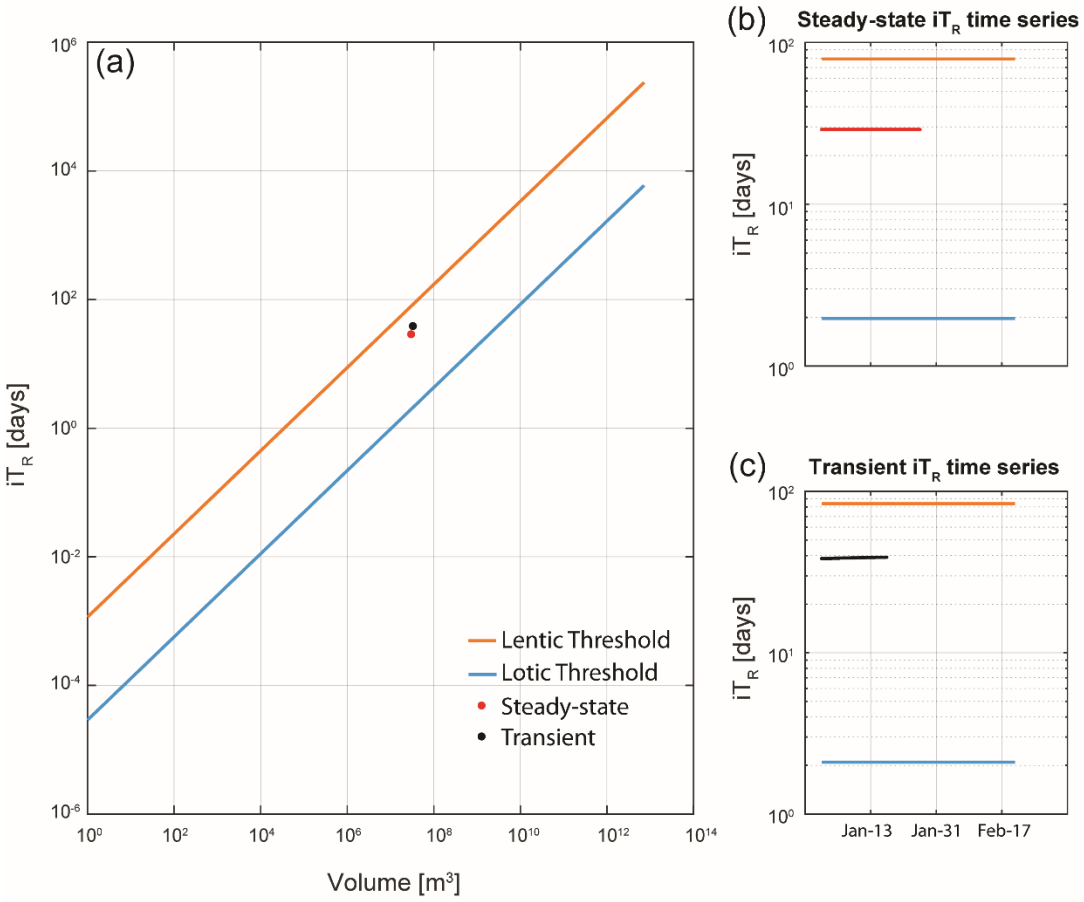

Figure B.4: Example data plot replicating conceptual Figure 2.3. The orange line represents the lentic threshold conditions for all volumes in (a), while representing the system-specific lentic thresholds for the steady-state time series in (b), and the *Transient* time series in (c). Similarly, the blue line represents the spectrum (a) and system-specific ((b) and (c)) lotic threshold conditions. The purple lines (b) and (c) represent the iT_R time series for the steady-state and transient hydrologic conditions, respectively.

This completes the guide to the quantitative lentic/lotic classification framework. If you have any questions, please contact Allan Edward Jones (allan.e.jones@utexas.edu).

B.4 AN ADDITIONAL NOTE

If one would like to see how the classification framework acts under less simplistic discharge conditions, replace the 'Q2_timeseries' variable in line 41, with either of the following lines.

- ```
  Q2_timeseries = 3*randn(size(time_period))+12;
  ```

- ```
  Q2_timeseries = 2*randn(size(time_period))+3;
      Q2_timeseries(Q2_timeseries <= 0) = 0.005;
      num_of_ind = round(rand(1)*0.05*length(time_period));
      rand_ind   = unique(round(rand(num_of_ind,1)*length(time_period)));
      Q2_timeseries(rand_ind,1) =
      Q2_timeseries(rand_ind,1).*(1000*rand(length(rand_ind),1));
  ```

The five new lines creates a faux-flashy discharge regime. This will make the transient iT_R time series vary a bit more over time when compared to the initial linear discharge time series. The plots created with the faux-flashy discharge regime will be similar to Figures B.5, B.6, and B.7. Please note that each iterations plots with pseudo-flashy discharge will not be the same, since the script creates the discharge time series from random values.

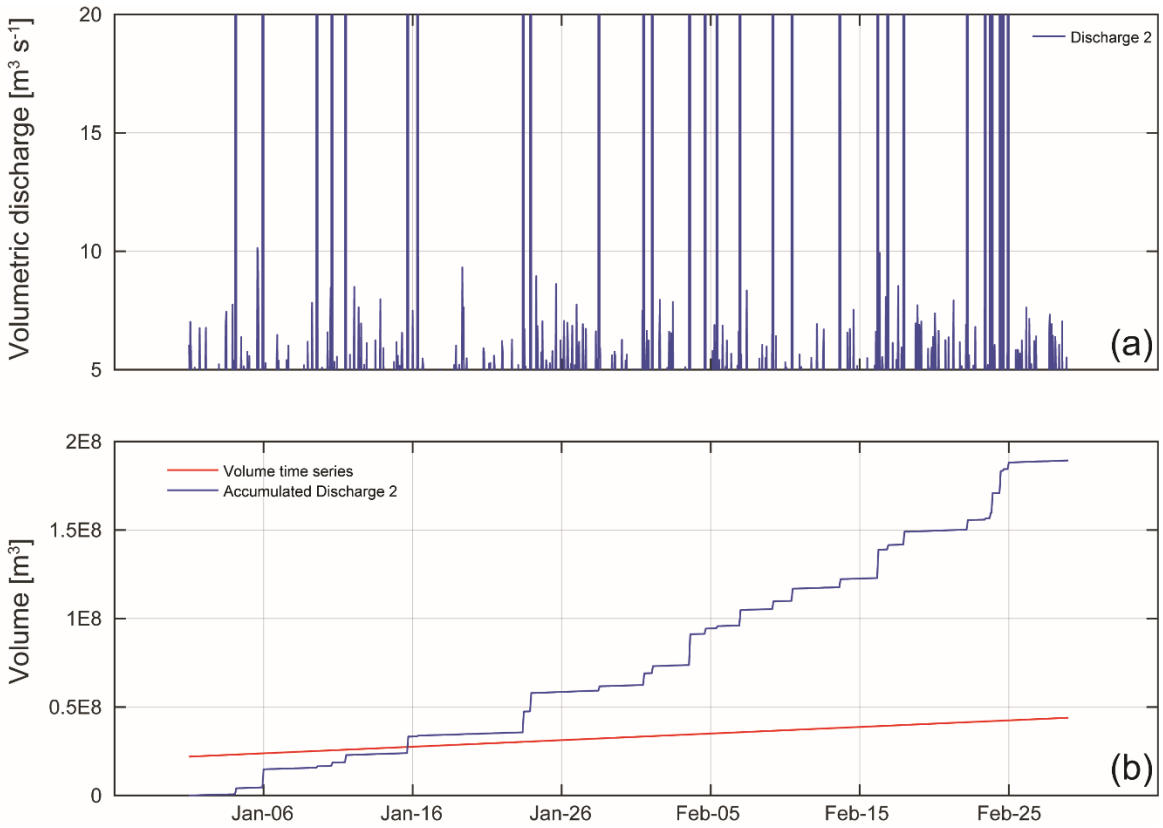

Figure B.5: Replication of Figure 2.1 using a faux-flashy discharge regime. Due to the "storm" peaks in (a) alter the "Accumulated Discharge 2" curve in (b), translating the intersection with the Transient volume time series to near Jan-10 as opposed to after Feb-05 for the initial analysis.

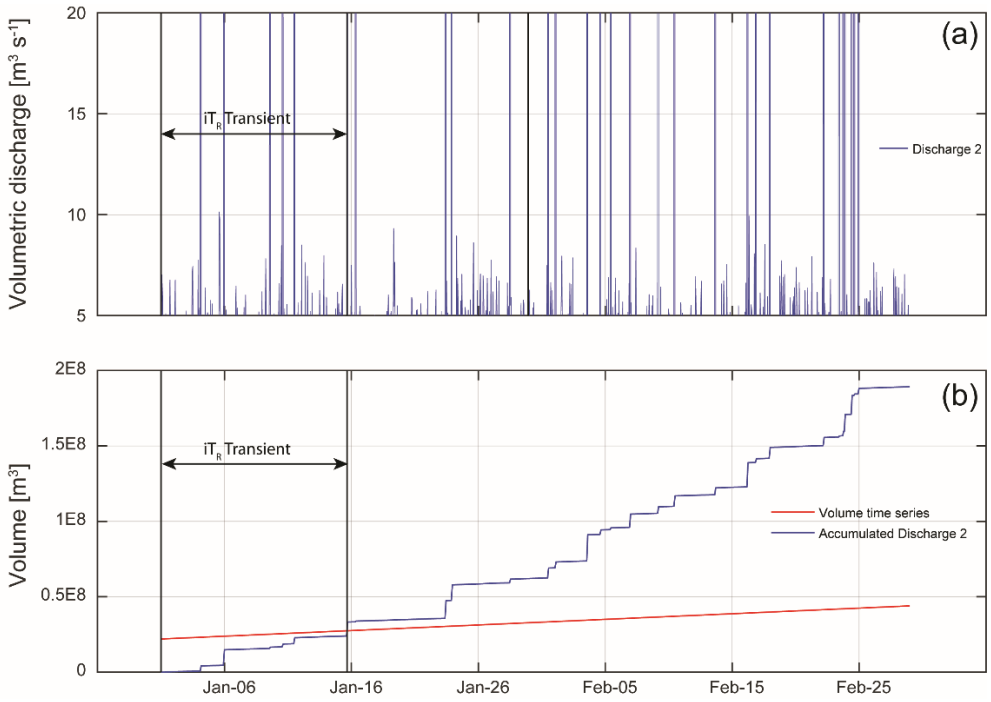

Figure B.6: Replication of Figure 2.1 with faux-flashy discharge regime and iT_R calculations lines. Although the "storm" peaks in (a) alter the "Accumulated Discharge 2" curve in (b), and translate the intersection with the Transient volume time series to earlier, the iT_R calculations still correctly identified t_{final} for the Transient data (intersection between solid blue and red lines in b).

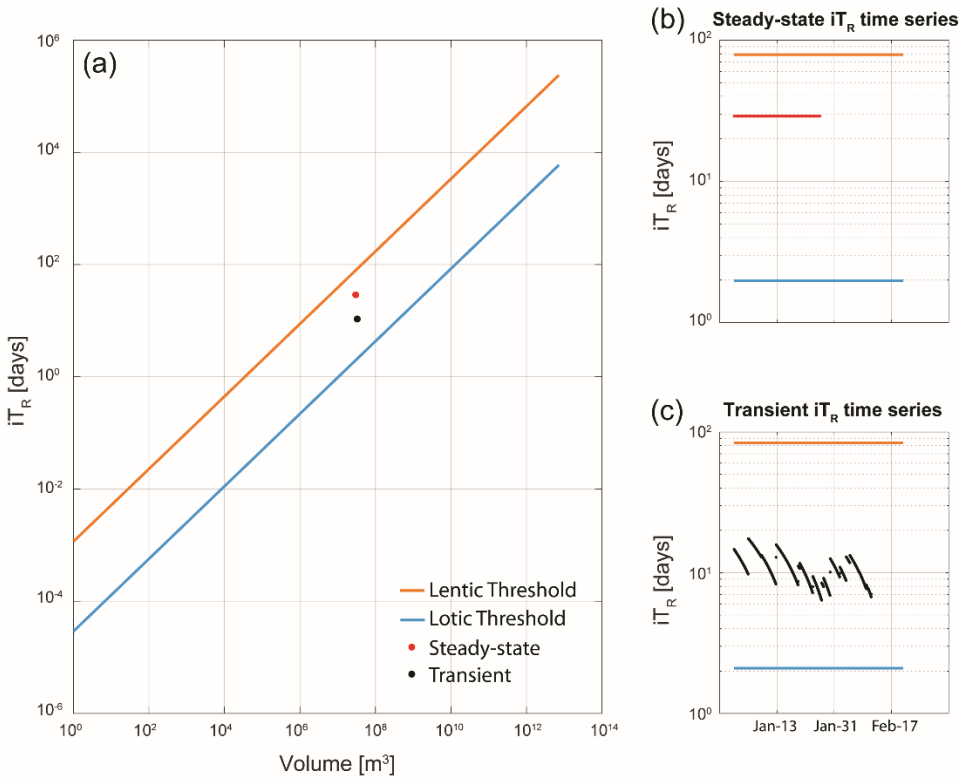

Figure B.7: Faux-flashy discharge regime plotted with Figure 2.3 conceptual framework. Although the intermediate (a) and nonoscillic classifications ((b) and (c)) did not change, the Transient iT_R time series changed to accommodate the increased discharge dynamics (c).

Appendix C: Matlab *Main Script*

The matlab script referred to as the *Main Script* in Appendix B with line numbers included.

```
1   %{
2   This script will serve as an example to guide interested parties through
3   a
4   simplistic form of the lentic/intermediate/lotic and oscillic/nonoscillic
5   classification.
6
7   Author: Allan Edward Jones
8   Date: 5/16/2016
9
10  ** Disclaimers **
11  1) All values are made-up and kept simple for the purpose of instruction.
12  When
13  performing your own analysis, of course, make each measurement as accurate
14  as possible.
15
16  2) The volumetric time series calculations assumes that the system of
17  interest is a river and will be approximated with a rectangular
18  cross-section.
19
20  %}
21
22  clear; close all; clc
23  save_check = 'no';
24
25
26
27  %      GOAL      1:      Re-create      conceptual      Figure      1
28  %%%%%%%%%%%%%%%%%%%%%%%%%%%%%%%%%%%%%%%%
29  % The first goal of this script will be to reproduce the the conceptual
30  % plot describing the calculation of integrated residence time (iTR)
31  % (Figure 1 in the main article). This will ensure we have a simplistic
32  set
33  % of example data to complete this analysis.
34
35  %% Obtain the proper data
36  % hourly timestamps from Jan. 1, 2015 to Mar. 1, 2015
37  time_period = [datenum('01/01/2015 00:00', 'mm/dd/yyyy HH:MM'):...
38      1/24:...
39      datenum('03/01/2015 00:00', 'mm/dd/yyyy HH:MM')]';
40
41  % Steady-state Discharge
42  Qss = 12*ones(size(time_period)); % constant discharge of 12 m^3/s
43
44  % Discharge 2: Transient
45  Q2_timeseries  =  linspace(9,  15,  length(time_period))';  %  vector  of
46  linearly changing discharge
```

```
47
48  % If time series volume measurements exist, those may be used during the
49  % iTR calculations. However, if the volume time series does not exit, it
50  % may be created from several geometric measurements.
51
52  % steady_state Volume - if time series volume is unavailable
53  Vss = 3e7*ones(size(time_period)); % constant 30 million cubic meters
54  over time
55
56  % If volume time series is unavailable, then calculate the volume time
57  % series from the following variables:
58  % - Inflow depth (time series)
59  % - Outflow depth (time series)
60  % - Inflow width (time series or single measurement)
61  % - Outflow width (time series or single measurement)
62  % - Traverse length (single measurement)
63
64  % In this example, all applicable variables will be represented by a
65  "single
66  % measurement", for the sake of simplicity.
67  inflow_depth     = linspace(5, 10, length(time_period))'; % vector of
68  linearly rising inflow stage
69  outflow_depth    = linspace(10, 20, length(time_period))'; % vector of
70  linearly rising outflow stage
71  inflow_width    = 45; % inflow cross-section is ~45 meters across
72  outflow_width   = 175; % inflow cross-section is ~175 meters across
73  traverse_length = 25e3; % 25km long water particle's journey from inflow
74  to outflow
75
76
77
78
79
80
81
82  %% Calculating Volume - if time series is UNavailable
83  % these volume calculations will be used in calculations with
84  % non-steady state Q2 ("Discharge 2")
85
86  % Step V1 - interpolate widths at meter resolution along the traverse
87  length
88  resolution = 1;
89  riv_widths = linspace(inflow_width, outflow_width,...
90      round(traverse_length/resolution))';
91
92  % step V2 - interpolate the depth profile along the traverse length at
93  one
94  % meter resolution for every timestep
95  for iii = 1:length(time_period)
```

```
96      all_depths(iii,:)           =           linspace(inflow_depth(iii),
97  outflow_depth(iii),...
98          round(traverse_length/resolution));
99  end
100 % resulting matrix of the depth profile (each rows) for all timesteps
101
102 % Step V3 - find the summed area of each cross-section by multiplying
103 depth
104 % and width for each time step
105 system_areas = all_depths * riv_widths;
106
107 % Step V4 - find volume by multiplying summed cross-sectional area by
108 % the resolution
109 V2_timeseries = system_areas * resolution;
110
111 % clearing variables to preserve memory
112 clear all_depths system_areas crossSectional_vols riv_widths resolution
113
114
115
116
117
118
119 %% Calculating the integrated discharge for every time step
120 % Using trapezoidal summation, we determine the accumulated discharge
121 from
122 % the initial time step for all time steps.
123
124 %Step 1 – Time step integration beneath discharge curve.
125 for iii = 2:length(time_period)
126
127     % Equation for area of a trapezoid = ((b1 + b2)*h)/2.
128     % Here, 'b1' and 'b2' are two sequential discharge measurements and
129 'h'
130     % is the time between each observation.
131
132     %             *****             STEADY-STATE             CALCULATIONS
133 ************************************
134     b1 = Qss(iii-1);
135     b2 = Qss(iii);
136     h   = (time_period(iii)-time_period(iii-1))*(24*3600);  % converted
137 from [days] to [sec]
138
139     % integrated discharge for each time step
140     integrated_Qss(iii-1,1) = ((b1 + b2)*h)/2;
141
142
143     %              *****              TRANSIENT              CALCULATIONS
144 ****************************************
145     b1 = Q2_timeseries(iii-1);
```

```
146       b2 = Q2_timeseries(iii);
147       h    =  (time_period(iii)-time_period(iii-1))*(24*3600);  % converted
148   from [days] to [sec]
149
150       % integrated discharge for each time step
151       integrated_Q2(iii-1,1) = ((b1 + b2)*h)/2;
152
153   end
154
155   % Step 2 - Perform a cumulative summation on the time step integrated
156   data,
157   % to obtain the accumulated discharge curve.
158
159   % Notice that the integrated data is 1 value shorter in length than all
160   the
161   % other time series. To address this, store a '0' value before the
162   % integrated discharge area, because at time step #1, no discharge has
163   % been accumulated.
164
165   accum1_Qss = cumsum([0; integrated_Qss]); % steady-state accumulated Q
166   accum1_Q2  = cumsum([0; integrated_Q2]);  % Transient accumlated Q
167
168   % ****** NOTE:
169   % This cumulative summation only calculated the accumulated discharge
170   % from the FIRST time step. The FOR loop will complete this
171   % calcuation for each timestep when calculating iTR.
172
173
174
175
176
177   %% Re-plotting Figure 1
178   % Based on the time-series data available, we can now reproduce figure
179   very
180   % similar to conceptual Figure 1.
181
182   figure(1)
183   % plotting Figure 1a
184   subplot(2,1,1)
185   plot(time_period, Qss, '--b') % plotting the steady-state "Discharge 1"
186   hold on
187   plot(time_period, Q2_timeseries, 'b') % plotting "Discharge 2"
188   % labeling the plot
189   set(gca, 'xticklabel', [])
190   set(gca, 'ylim', [5 20])
191   ylabel('Volumetric discharge [m^3 s^{-1}]')
192   grid on
193   legend('Discharge 1', 'Discharge 2',...
194       'Location', 'SouthEast')
195
```

```
196
197 % plotting Figure 1b
198 subplot(2,1,2)
199 plot(time_period, Vss, ':r') % plotting the steady-state volume time
200 series
201 hold on
202 plot(time_period, V2_timeseries, 'r') % plotting changing volume time
203 series (not in original Figure 1)
204 plot(time_period, accum1_Qss, '--b') % plotting the cumulative steady-
205 state "Discharge 1"
206 plot(time_period, accum1_Q2, 'b') % plotting the cumulative "Discharge 2"
207 % labeling the plot
208 xlabel('Time')
209 set(gca, 'xticklabel', datestr(get(gca, 'xtick'), 'mmm-dd'))
210 ylabel('Volume [m^3]')
211 grid on
212 legend('Steady-state Volume', 'Volume time series',...
213     'Accumulated Discharge 1', 'Accumulated Discharge 2',...
214     'Location', 'SouthEast')
215
216 % saving figure
217 if strcmp(save_check,'yes')
218
219     % SAVING THE PLOT
220     % makes sure the saved pdf fits within a landscape document
221     set(gcf,'PaperOrientation','landscape');
222     set(gcf,'PaperUnits','normalized');
223     set(gcf,'PaperPosition', [0 0 1 1]);
224
225     % Saving within the main folder not an individual river name folde
226     print(gcf, '-dpdf' , ['initial_Figure1_recreate.pdf']);
227 end
228
229
230
231 %% Calculating iTR from the discharge and volume time series
232 %%%%%%%%%%%%                    iTR                    calculations
233 %%%%%%%%%%%%%%%%%%%%%%%%%%%%%%%%%%%%%%%%%%%%%%%%%%%%%%%%%%%%%%%%%%%%%%%
234 % The second goal of this analysis will be to calculate iTR conditions
235 for
236 % each time step. This process will use the same accumulated discharge
237 % calculations as a part of the analysis, but apply it for every time
238 step.
239
240 % Analysis will be carried out over each time step; we use a FOR loop to
241 % perform the analysis on each time step.
242 for ttt = 1:length(time_period)
243
244     % obtaining time stamp for time step's calculations
245     t_initial = time_period(ttt);
246
```

```
247      %             *****             STEADY-STATE             CALCULATIONS
248  ************************************
249      % calculating all possible accumulated discharge from current time
250  step
251      accum_Qss    = cumsum([0; integrated_Qss(ttt:end)]);
252
253      % With every time step, the number of accumulated discharge values
254      % decreases. To compare vectors and vector indices accurately, all
255      % vectors are shortened to the same length. In other words, we are
256      % updated all vectors to begin at the same time step.
257      clipped_Vss  = Vss(ttt:end);
258      clipped_time = time_period(ttt:end);
259
260      % find where accumulated discharge is just above and below
261      below_index  = max(find(accum_Qss < clipped_Vss));
262      above_index  = min(find(accum_Qss > clipped_Vss));
263
264
265      if isempty(above_index)
266          % If there are no time steps with an accumulated discharge above
267  the
268          % sytem volume, we return a 'NaN' value as the iTR value for that
269  time
270          % step.
271          iTRss(ttt,1) = nan;
272
273      else
274          % Find intersection between points
275          [intersect_time, intersect_vol] = ...
276          intersections(...
277          clipped_time(below_index:above_index),
278  accum_Qss(below_index:above_index),...
279          clipped_time(below_index:above_index),
280  clipped_Vss(below_index:above_index),   1);
281          %  Can  calculate  the  intersection  yourself  or  use  the
282  "intersections.m"
283          % function written by Douglas M. Schwarz available from MatLab
284  File
285          % Exchange here:
286          %     http://www.mathworks.com/matlabcentral/fileexchange/11837-
287  fast-and-robust-curve-intersections
288          % A copy of the function is included with the supplemental MatLab
289  files.
290
291              % marking the best end time
292              if ~isempty(intersect_time)
293                  t_final = intersect_time(1);
294
295                  % adding the iTR value to the tracking variable
296                  iTRss(ttt,1) = t_final - t_initial; % recorded in [days]
297              else
```

```
                % return an error if there is no intersect found
                error(['A steady-state intersect was not found. Possibly,
'...
                    'the script is '...
                    'not finding the proper indices before beginning the
'...
                    'intersection calculations.'])
            end
    end
```

```
    %              *****              TRANSIENT              CALCULATIONS
**************************************
    % calculating all possible accumulated discharge from current time
step
    accum_Q2     = cumsum([0; integrated_Q2(ttt:end)]);

    % With every time step, the number of accumulated discharge values
    % decreases. To compare vectors and vector indices accurately, all
    % vectors are shortened to the same length. In other words, we are
    % updated all vectors to begin at the same time step.
    clipped_V2   = V2_timeseries(ttt:end);
    clipped_time = time_period(ttt:end);

    % find where accumulated discharge is just above and below
    below_index  = max(find(accum_Q2 < clipped_V2));
    above_index  = min(find(accum_Q2 > clipped_V2));

    if ~isempty(above_index) && below_index > above_index
        % Sometimes the accumulated discharge and the volume time series
        % intersect multiple times. If so, the first intersection marks
the
        % correct t_final for iTR calculations.
        below_index = min(find(diff(find(accum_Q2 < clipped_V2)) > 1));

        if below_index > above_index % still.... oops!
            error('The correct intersection indices were not found.')
        end

    end


    if isempty(above_index)
        % If there are no time steps with an accumulated discharge above
the
        % sytem volume, we return a 'NaN' value as the iTR value for that
time
```

```
348             % step.
349             iTR2(ttt,1) = nan;
350 
351         else
352             % Find intersection between points
353             [intersect_time, intersect_vol] = ...
354             intersections(...
355             clipped_time(below_index:above_index),
356     accum_Q2(below_index:above_index),...
357             clipped_time(below_index:above_index),
358     clipped_V2(below_index:above_index),   1);
359             %  Can  calculate  the  intersection  yourself  or  use  the
360     "intersections.m"
361             % function written by Douglas M. Schwarz available from MatLab
362     File
363             % Exchange here:
364             %     http://www.mathworks.com/matlabcentral/fileexchange/11837-
365     fast-and-robust-curve-intersections
366             % A copy of the function is included with the supplemental MatLab
367     files.
368 
369                 % marking the best end time
370                 if ~isempty(intersect_time)
371                     t_final = intersect_time(1);
372 
373                     % adding the RT value to the tracking variable
374                     iTR2(ttt,1) = t_final - t_initial; % recorded in [days]
375                 else
376                     % return an error if there is no intersect found
377                     error(['An intersect was not found. Possibly, the script
378     is '...
379                         'not finding the proper indices before beginning the
380     '...
381                         'intersection calculations.'])
382                 end
383         end
384     end
385 
386 
387 
388 
389 
390 
391     %% Add iTR lines to Figure 1
392     figure(1)
393     subplot(2,1,1)
394     hold on
395     % plotting line for 't_initial'
396     plot([time_period(1) time_period(1)], get(gca, 'ylim'), 'k')
397     % plotting second line for 't_final' at steady-state
```

```
plot([time_period(1)+iTRss(1)     time_period(1)+iTRss(1)],     get(gca,
'ylim'), 'k')
% plotting second line for 't_final' at Transient
plot([time_period(1)+iTR2(1) time_period(1)+iTR2(1)], get(gca, 'ylim'),
'k')

% steady-state iTR arrows
quiver(time_period(1),          0.95*max(get(gca, 'ylim')),...
    iTRss(1), 0, 0, 'k') % steady-state right arrow
quiver(time_period(1)+iTRss(1), 0.95*max(get(gca, 'ylim')),...
    -iTRss(1), 0, 0, 'k') % steady-state right arrow
% labeling the arrow
text(mean([time_period(1)  time_period(1)+iTRss(1)]),  0.95*max(get(gca,
'ylim')),...
    'iT_R Steady-state', 'VerticalAlignment', 'Top')

% Transient iTR arrows
quiver(time_period(1),         0.70*max(get(gca, 'ylim')),...
    iTR2(1), 0, 0, 'k') % Transient right arrow
quiver(time_period(1)+iTR2(1), 0.70*max(get(gca, 'ylim')),...
    -iTR2(1), 0, 0, 'k') % Transient right arrow
% labeling the arrow
text(mean([time_period(1)  time_period(1)+iTR2(1)]),  0.70*max(get(gca,
'ylim')),...
    'iT_R Transient', 'VerticalAlignment', 'Bottom')


subplot(2,1,2)
hold on
% plotting line for 't_initial'
plot([time_period(1) time_period(1)], get(gca, 'ylim'), 'k')
% plotting second line for 't_final' at steady-state
plot([time_period(1)+iTRss(1)     time_period(1)+iTRss(1)],     get(gca,
'ylim'), 'k')
% plotting second line for 't_final' at Transient
plot([time_period(1)+iTR2(1) time_period(1)+iTR2(1)], get(gca, 'ylim'),
'k')

% steady-state iTR arrows
quiver(time_period(1),          0.95*max(get(gca, 'ylim')),...
    iTRss(1), 0, 0, 'k') % steady-state right arrow
quiver(time_period(1)+iTRss(1), 0.95*max(get(gca, 'ylim')),...
    -iTRss(1), 0, 0, 'k') % steady-state right arrow
% labeling the arrow
text(mean([time_period(1)  time_period(1)+iTRss(1)]),  0.95*max(get(gca,
'ylim')),...
    'iT_R Steady-state', 'VerticalAlignment', 'Top')

% Transient iTR arrows
quiver(time_period(1),         0.70*max(get(gca, 'ylim')),...
    iTR2(1), 0, 0, 'k') % Transient right arrow
```

```
quiver(time_period(1)+iTR2(1), 0.70*max(get(gca, 'ylim')),...
    -iTR2(1), 0, 0, 'k') % Transient right arrow
% labeling the arrow
text(mean([time_period(1)   time_period(1)+iTR2(1)]),   0.70*max(get(gca,
'ylim')),...
    'iT_R Transient', 'VerticalAlignment', 'Bottom')

% saving figure again
if strcmp(save_check,'yes')
    % SAVING THE PLOT
    % makes sure the saved pdf fits within a landscape document
    set(gcf,'PaperOrientation','landscape');
    set(gcf,'PaperUnits','normalized');
    set(gcf,'PaperPosition', [0 0 1 1]);

    % Saving within the main folder not an individual river name folde
    print(gcf, '-dpdf' , ['Figure1_recreate_iTRlines.pdf']);
end









%% Classifying the steady-state and Transient systems
%%%%%%%%%%%%                                                    Classifications
%%%%%%%%%%%%%%%%%%%%%%%%%%%%%%%%%%%%%%%%%%%%%%%%%%%%%%%%%%%%%%%%%%%%%%%%%%%%%%%
% The final goal of this analysis is to classify the systems as
% lentic/intermediate/lotic and oscillic/nonoscillic. This analysis will
% re-create Figures 3a and 3b.



% Classify - Step 1:
% We need to determine the iTR thresholds for the natural volume spectrum.
% The variables necessary for the following calculations are:
% - lentic/lotic threshold velocities
% - traverse lengths
% - largest/smallest system width
% - largest/smallest system depth
% - area ratios at smallest and largest volumes

% threshold velocities from literature
q_thresh = [0.01, 0.4]; % m/s [row vector]

% lengths of interest in meters [1m, Nile]
traverse_length = [1, 6853e3]; % meters

% width and depth scaling area
amazonW  = 4.8e3; % average low season width -> meters
congoD   = 220; % meters
```

```
scalingA = [1, congoD*amazonW]; % m^2

% Area ratios - Aavg:Ain for volume spectrum endmembers
AavgAin     = [1, 30];

% hypothetical volumes that represent the smallest and largest possible
% freshwater bodies in the world
hyp_vols    = [traverse_length.*scalingA]'; % column vector

% calculating the instantaneous residence time values
instant_RT_approx  = (traverse_length' * [1./q_thresh]) ./ (3600*24); %
in seconds ->> to days
instant_RT_approx  = [instant_RT_approx(1,:) .* AavgAin(1);...
                instant_RT_approx(2,:) .* AavgAin(2)];

% creating fit objects for threshold lines
[iTR_001, gof, params] = fit(hyp_vols, instant_RT_approx(:,1), 'power1');
% lentic fit
[iTR_04,  gof, params] = fit(hyp_vols, instant_RT_approx(:,2), 'power1');
% lotic fit




% Classify - Step 2: Determine the Lentic/Lotic thresholds
% To calculate the Lentic/Lotic thresholds, first determine the median
% volume of your systems. Then use the fit object (or interpolated
% equation) to determine the proper iTR threshold. The if-else statements
% that follow enact the decision tree included in the supplemental
% information packet (Figure A.3).

% ***** STEADY-STATE CALCULATIONS ***********************************
medVss       = nanmedian(Vss);   % median steady-state volume
LenThresh_ss = iTR_001(medVss);   % lentic steady-state threshold
LotThresh_ss = iTR_04(medVss);    % lotic steady-state threshold
mediTRss     = nanmedian(iTRss); % median iTR conditions of steady-state
system

% comparison of median iTR conditions with thresholds
% determining lentic/int./lotic classification
if mediTRss > LenThresh_ss
    LIL_class = 'Lentic';

elseif mediTRss < LotThresh_ss
    LIL_class = 'Lotic';

else
    LIL_class = 'Intermediate';
end

```

```
% determining the oscillic classification - max and min iTR
maxi = nanmax(iTRss);
mini = nanmin(iTRss);
if maxi > LenThresh_ss && mini < LotThresh_ss
    osc_class = 'Oscillic';
else
    osc_class = 'Nonoscillic';
end

% outputting the results
classification  = ['The steady-state system is classified as: '];
output  =  sprintf('%s\n  %s%s  %s\n',  classification,  LIL_class,  ',',
osc_class);
fprintf(output)


%               *****               TRANSIENT               CALCULATIONS
****************************************
medV2       = nanmedian(V2_timeseries);   % median steady-state volume
LenThresh_2 = iTR_001(medV2);   % lentic steady-state threshold
LotThresh_2 = iTR_04(medV2);    % lotic steady-state threshold
mediTR2      = nanmedian(iTR2); % median iTR conditions of steady-state
system

% comparison of median iTR conditions with thresholds
% determining lentic/int./lotic classification
if mediTR2 > LenThresh_2
    LIL_class = 'Lentic';

elseif mediTR2 < LotThresh_2
    LIL_class = 'Lotic';

else
    LIL_class = 'Intermediate';
end

% determining the oscillic classification - max and min iTR
maxi = nanmax(iTRss);
mini = nanmin(iTRss);
if maxi > LenThresh_2 && mini < LotThresh_2
    osc_class = 'Oscillic';
else
    osc_class = 'Nonoscillic';
end

% outputting the results
classification  = ['The Transient system is classified as: '];
output  =  sprintf('%s\n  %s%s  %s\n',  classification,  LIL_class,  ',',
osc_class);
fprintf(output)

```

```
600
601
602
603   % Classify - Step 3: Create Figure 3 for each river
604   % Plot each system by the median volume and iTR values, along with the
605   iTR
606   % thresholds, to create Figure 3a. Then plot the iTR time series against
607   % the lentic/lotic thresholds (horizontal lines) to graphically depict
608   the
609   % oscillic classification.
610
611   % creating the vector of volume for plotting
612   vector_len  = 1e2;
613   vol_vector     =   logspace(log10(min(hyp_vols)),   log10(max(hyp_vols)),
614   vector_len);
615
616   %FIGURE 3A
617   figure(2)
618   subplot(2, 3, [1 2 4 5])
619   hold on
620   grid on
621   % plotting 0.01 threshold
622   hhh = loglog(vol_vector, iTR_001(vol_vector),  'color', [245/255 128/255
623   32/255]);
624   set(hhh, 'linewidth', 2)
625
626   % plotting 0.4 threshold
627   hhh = loglog(vol_vector, iTR_04(vol_vector),   'color', [26/255 158/255
628   217/255]);
629   set(hhh, 'linewidth', 2)
630
631   % plotting the steady-state data - red
632   loglog(medVss, mediTRss, '.r', 'markersize', 15)
633   % plotting the Transient data - black
634   loglog(medV2, mediTR2, '.k', 'markersize', 15)
635
636   % setting scale on axes
637   set(gca, 'yscale', 'log')
638   set(gca, 'xscale', 'log')
639
640   % labeling axes
641   ylabel('iT_R [days]')
642   xlabel('Volume [m^3]')
643   legend('Lentic    Threshold',    'Lotic    Threshold',    'Steady-state',
644   'Transient',...
645       'Location','SouthEast')
646
647
648
649   % FIGURE 3B
```

```
% ***** STEADY-STATE iTR timeseries plot
subplot(2,3,3)
semilogy(time_period, iTRss, '.b') % plotting the data
hold on
% plotting lentic steady-state threshold
ppp    =    plot([min(time_period)    max(time_period)],    [LenThresh_ss
LenThresh_ss],...
    'color', [245/255 128/255 32/255]);
set(ppp, 'linewidth', 2)
% plotting lotic steady-state threshold
ppp    =    plot([min(time_period)    max(time_period)],    [LotThresh_ss
LotThresh_ss],...
    'color', [26/255 158/255 217/255]);
set(ppp, 'linewidth', 2)
grid on

% labeling plot
ylabel('iT_R [days]')
set(gca, 'xticklabel', datestr(get(gca, 'xtick'), 'mmm-dd'))
title('Steady-state iT_R time series')



% ***** Transient iTR timeseries plot
subplot(2,3,6)
semilogy(time_period, iTR2, '.b') % plotting the data
hold on
% plotting lentic steady-state threshold
ppp    =    plot([min(time_period)    max(time_period)],    [LenThresh_2
LenThresh_2],...
    'color', [245/255 128/255 32/255]);
set(ppp, 'linewidth', 2)
% plotting lotic steady-state threshold
ppp    =    plot([min(time_period)    max(time_period)],    [LotThresh_2
LotThresh_2],...
    'color', [26/255 158/255 217/255]);
set(ppp, 'linewidth', 2)
grid on

% labeling plot
ylabel('iT_R [days]')
set(gca, 'xticklabel', datestr(get(gca, 'xtick'), 'mmm-dd'))
title('Transient iT_R time series')







% final figure save
```

```
700  if strcmp(save_check,'yes')
701      % SAVING THE PLOT
702      % makes sure the saved pdf fits within a landscape document
703      set(gcf,'PaperOrientation','landscape');
704      set(gcf,'PaperUnits','normalized');
705      set(gcf,'PaperPosition', [0 0 1 1]);
706
707      % Saving within the main folder not an individual river name folde
708      print(gcf, '-dpdf' , ['Figure3.pdf']);
709  end
710
711
712
713
714  %% Classification complete.
715  % The lentic/intermediate/lotic and oscillic/nonoscillic classifications
716  % are complete. If you have any questions, please to
717  % email Allan Edward Jones at allan.e.jones@utexas.edu. Thank you.
718  fprintf(sprintf('\n\n%s\n%s\n%s\n%s\n',...
719      'The lentic/intermediate/lotic and oscillic/nonoscillic ',...
720      'classifications are complete. If you have any questions, ',...
721      'please do not hesitate to email Allan Edward Jones at ',...
722      'allan.e.jones@utexas.edu. Thank you.'))
723
724  % To see different iTR time series, change up the 'Q2_timeseries'
725  % variable. A possible simple entry includes:
726  %
727  % Q2_timeseries = 3*randn(size(time_period))+12;
728  %
729  % Or the following replicates a "flashy" discharge regime within this
730  % classification framework. Copy the following 5 lines, and replace the
731  % 'Q2_timeseries' initialization line at the beginning of this script.
732  %
733  % Q2_timeseries = 2*randn(size(time_period))+3;
734  % Q2_timeseries(Q2_timeseries <= 0) = 0.005;
735  % num_of_ind = round(rand(1)*0.05*length(time_period));
736  % rand_ind   = unique(round(rand(num_of_ind,1)*length(time_period)));
737  %                       Q2_timeseries(rand_ind,1)                        =
738  Q2_timeseries(rand_ind,1).*(1000*rand(length(rand_ind),1));
```

Appendix D: Storm λ_3 ID figure

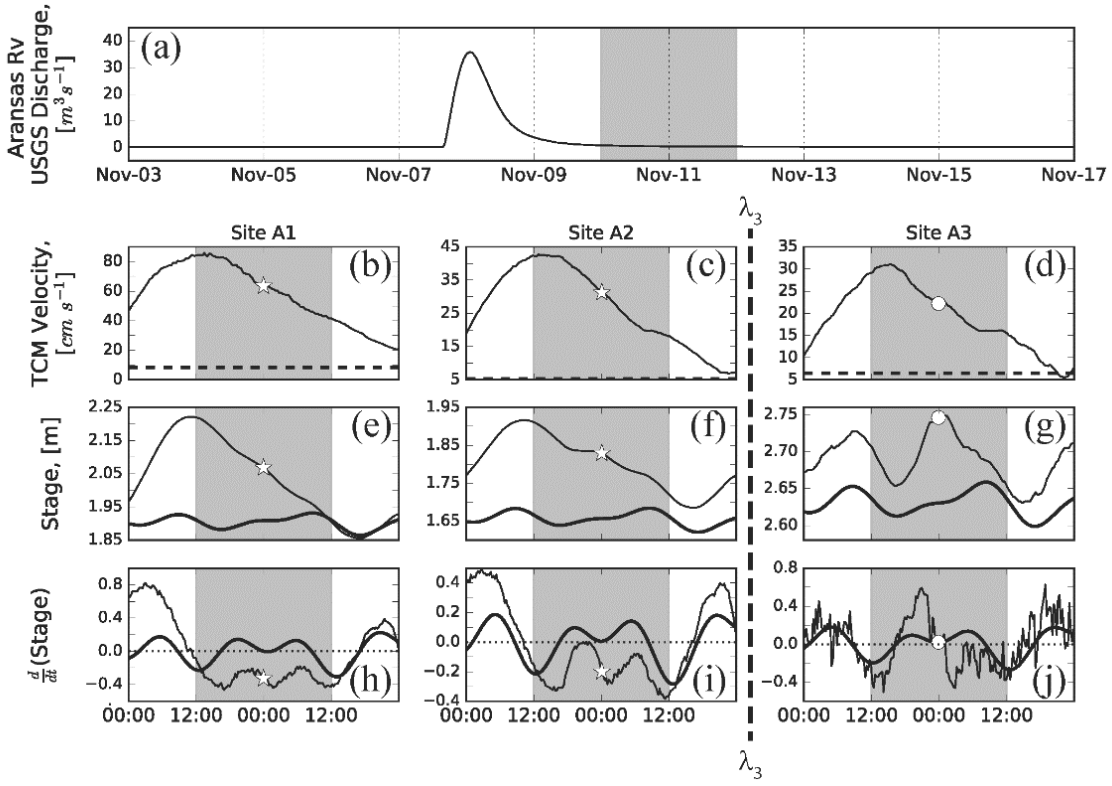

Figure D.1: Methods for identification of λ_3 during a storm period

The storm period presented from 07-13 November 2015, as identified in (a), where the hydrograph peak in discharge is observed by the USGS gauge is due to precipitation only (since the USGS gauge is upstream of all tidal influence). The shaded portion of (a) highlights a 48-hour period presented in each of the following subplots (b-j). Each subplot depicts the conditions (i.e., TCM velocity, stage, or $\frac{dS}{dt}$) at a given long-term monitoring site (i.e, A1, A2, or A3). The shaded region in each subplot (b-j) highlights the 24-hours surrounding the median timestamp within each plot. The in-stream conditions during the highlighted 24-hours are used to determine the relative position of each site to λ_3 (i.e.,

upstream or downstream). Sites above λ_3 at the median timestamp are marked with a star (I.e., sites A1 and A2), while the sites downstream of λ_3 are denoted by an open circle (i.e., A3). At all three sites over the highlighted 24-hours, observed velocities are much greater than the 90th percentile threshold (dashed lines in b, c, and d) indicating a storm period. This storm period was lagged from the USGS observations in (a) due to its time to transit downstream from the far inland gauge. Upon comparison of the expected and actual $\frac{dS}{dt}$ conditions (thick and thin black solid lines in h, i, and j), both sites A1 and A2 do not experience synchronous zeros within the highlighted 24-hour period, and, thus, are upstream of λ_3, while A3 does experience synchronous $\frac{dS}{dt}$ zeros, and is characterized as downstream of λ_3.

Appendix E: Sinusoid derivation

Since tidal signals are cyclic and are often conceptually described as sinusoids (e.g., *NOAA* [2017c], *Savenije*, [2005]), the relationship between $\frac{\mathrm{dS}}{\mathrm{dt}}$ and stage may be described through sinusoidal derivatives. For a theoretical sinusoidal tidal stage (eq. 3.2), $\frac{\mathrm{dS}}{\mathrm{dt}}$ may be calculated via u-substitution, as shown in the following equations:

$$Stage,\ S = A_S * \sin\left(\frac{2\pi}{P} * t + \varphi\right) \quad \text{(E1)}$$

$$u = \left(\frac{2\pi}{P} * t + \varphi\right),\ \frac{du}{dt} = \frac{2\pi}{P} \quad \text{(E2)}$$

$$\frac{dS}{dt} = A_S * \frac{du}{dt} * \cos(u) = A_S * \frac{2\pi}{P} * \cos\left(\frac{2\pi}{P} * t + \varphi\right) = A_{dS} * \cos\left(\frac{2\pi}{P} * t + \varphi\right) \quad \text{(E3)}$$

where A_S is the tidal stage amplitude, φ is the tidal phase offset, and P is the known tidal period (in same units as time, t) and A_{dS} is the amplitude of $\frac{\mathrm{dS}}{\mathrm{dt}}$ sinusoid. Thus, the $\frac{\mathrm{dS}}{\mathrm{dt}}$ amplitude is effectively scaled up by a factor of $\frac{2\pi}{P}$ from the stage amplitude ($A_{dS} = \frac{2\pi}{p} * A_S$). In a system predominantly influenced by a diurnal tidal signal (~ 24 hour period, or 1 day), we may simplify by converting the time units to days and setting P equal to 1. However, for systems dominated by a semidiurnal tidal signal, the tidal period is ~ 12 hours or half-a-day, thus making the tidal amplitude relationship: $A_{dS} = 4\pi * A_S$. Finally, to approximate the tidal range of a system, you must multiply the calculations by 2: $TR_{dS} = 2 * 4\pi * A_S$ (for a semidiurnal tide). For example, in a diurnal system, river reaches with an observed $\frac{\mathrm{dS}}{\mathrm{dt}}$ interquartile range of < 0.31 m d^{-1} relate to river reaches that contain a tidal stage amplitude of < 2.5 cm or a tidal range < 5 cm.

Unfortunately, however, for a “mixed” tidal systems identifying the proper dominant tidal period is less straightforward. For the Aransas River, where tide acts predominantly diurnal during spring tide and potentially semidiurnal during neap tide [*Evans et al.*, 2012; *Mooney and McClelland*, 2012], we address this problem through an FFT on each 24-hour window of baseflow stage analyzed. The dominant tidal period present, whether 12- or 24-hour, is determined via a comparison of the amplitude of each signal produced by the Fourier Transform, the stronger amplitude indicating the dominant signal.

Appendix F: Storm lag and spreading figure

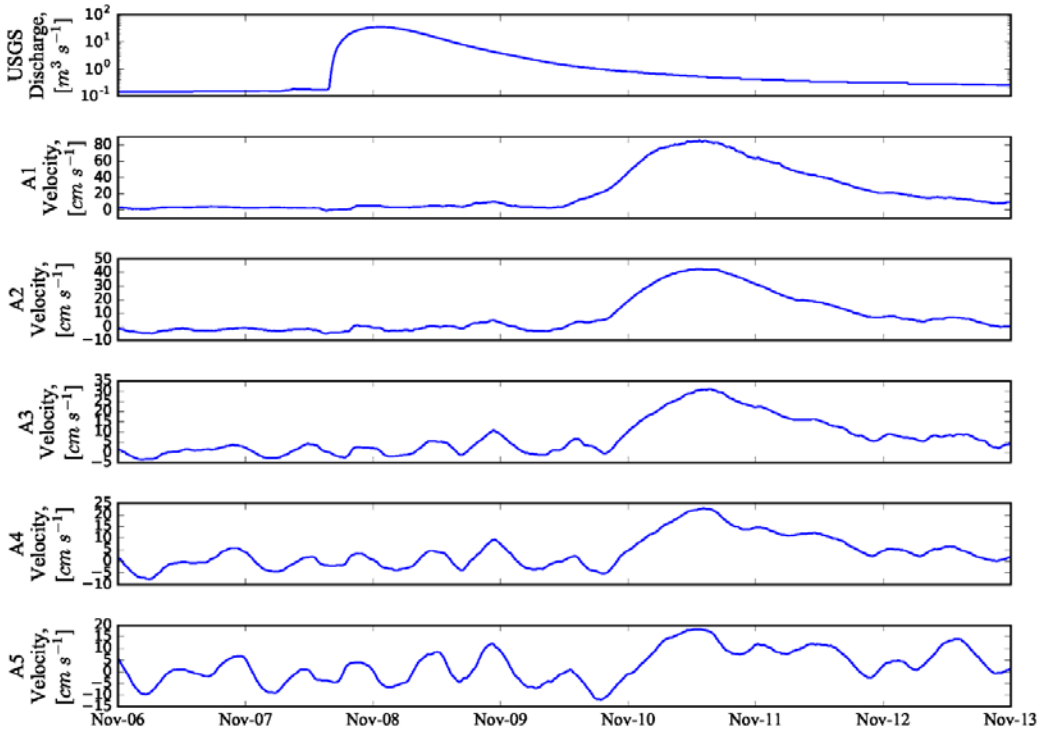

Figure F.1: A storm pulse on the Aransas River in November 2015 that is lagged in transport downstream, decreases in velocity downstream, and is spread over a wider time window.

Appendix G: TCM Coordinate rotation method and Matlab script

The following is a set of bulleted notes describing the TCM calibration and rotations in greater detail. The Matlab code for the rotations follows that.

- Remove the data 1 hour before and after installation of the meters
    - To remove any unintentional human influence when we were installing
- Site/TCM specific configuration files provide the normalization coefficients and zero velocity offsets
    - The minimum X and Y normalization coefficients are experienced during the opposing axes maximum
    - The Z normalization coefficients are determined in relation to the X and Y coefficients
- The raw data from the TCM is presented in a left-hand coordinate system, which needs to be translated into a right-handed coordinate system
- The newly translated data is then normalized using the TCM specific configuration coefficients
- We perform pitch, roll, and yaw rotations about the Y, X, and Z axes respectively to align our data with the downstream flow direction of the river channel
    - The pitch and roll rotations center the data on the zero velocity offsets from the TCM-specific configuration files
        - Any lateral or longitudinal offset from the zero velocity coordinates denote a velocity experienced by the meter
    - The Yaw rotation aligns the major axis of the data with the downstream flow direction
        - Periods of increased storm discharge were isolated and denoted the direction of rotation
            - These storm periods/increased downstream discharge were represented by the least common 5% of the TCM data
            - The slope between the centroids of the two clusters determine from the least common 5% of the data was aligned parallel to the Y-axis.
    - The resulting rotation meant that all positive Y-axis values denote downstream flow, while negative Y-axis values represented upstream flow.
- Tilts away from the origin was determined by the following equation:

$$\theta = tan^{-1}\left(\frac{||vz \text{ x } a||}{vz \,.a}\right)$$ -> where 'vz . a' is the 'scalar/dot product'

where *vz* are the zero velocity observations, and *a* is each [x, y, z] vector observation. All vectors in this calculation have been normalized and rotated with the previous coordinate rotations.

- Flume-derived, empirical curves relate degrees from vertical (0-90) to a local specific discharge
    - Different curve depending upon TCM model
        - Initial purchase was all 1p50s
        - Replaced site M2 with a 1p50b15 in March of 2016
    - Some tilts above 90 degrees observed. However, those values were reset to 90 degrees which is the maximum for which we have empirical flume data.
- We broke down and recorded the discharge vector into its downstream (y-axis) and cross-stream (x-axis) specific discharges.
- The resulting data is a time series of 15 minute data specific discharge data stretching from 20 May 2015 to the present.
- The resulting TCM velocity data is accurate down to approximately 2 cm s^{-1} for any given sampling value [*Sheremet et al.* 2009, *Sheremet and Manning* 2013].
    - Although the exact accuracy of velocities of magnitude less than 2 cm s^{-1} is uncertain, the timing of tidal oscillations in discharge is sufficiently accurate to provide insight into the impact of tidal cycles (i.e., diurnal, semidiurnal) on the river reach's discharge regime [*Maio et al.* 2016, *Aretxabaleta et al.* 2014].

Matlab code:
Any questions should be directed to author, Allan Edward Jones, at email: allan.e.jones@utexas.edu

```
%{
This script will replicate vitalii's python scripts to calibrate and
convert TCM tilt data into secific discharge.

Author: Allan Edward Jones
Date: 6/27/2016
%}

close all; clear; clc;

cur_dir = cd; slashes = regexp(cur_dir, '\');
using_comp = cur_dir(1:slashes(3));

date_save = ['prelim_' datestr(now, 'yyyymmdd')];

plot_check = 01; % 0 for no plot save
fig = 1;

% save path for TCM and LTC data
save_path = [using_comp 'Dropbox\Field Work\Analysis\'...
    'All Long Term Data\Matlab Cleaned Data\Calibrated TCM data\'...
     date_save '\'];...
if ~isdir([save_path])
    mkdir([save_path]);
end

% diary to record the output
diary([using_comp 'Dropbox\Field Work\Analysis\'...
      'All Long Term Data\Matlab Cleaned Data\Calibrated TCM data\'...
      date_save '\Rotation_diary.txt']);

%% correcting datenum python errors
%{
%% obtaining ADP data
disp(['Loading ADP data...'])
ADPdirectory = ['Dropbox\Field Work\'...
    'Analysis\All Long Term Data\ADP_24hr\'];
river_folder = 'Aransas\';
ADPfnames24 = {'AR24_20150810.mat'; 'AR24_20160227.mat'};
for iii = 1:length(ADPfnames24)
    load([using_comp ADPdirectory river_folder ADPfnames24{iii}]);
end


%% obtaining LEVEL data
disp(['Loading LTC data...'])
```

```
LTCdir   = ['Dropbox\Field Work\Analysis\'...
    'All Long Term Data\LTC data corrected\'];
LTCnames = dir([using_comp LTCdir]);
% find and load actual filenames -> 'from' date to data in real titles
for iii = 1:length(LTCnames)
    if ~isempty(regexp(LTCnames(iii).name, 'from'))
        load([using_comp LTCdir LTCnames(iii).name]);
    end
end


%% obtaining TCM data
disp(['Loading TCM data...'])
TCMdir = ['Dropbox\Field Work\Analysis\'...
    'All Long Term Data\TCM data\'];
TCMnames = dir([using_comp TCMdir]);
% find and load actual filenames -> 'from' date to data in real titles
for iii = 1:length(TCMnames)
    if ~isempty(regexp(TCMnames(iii).name, 'from'))
        load([using_comp TCMdir TCMnames(iii).name]);
    end
end


%% obtaining an alphabetical list of the Mission and Aransas variables
AranVars = who('AR*');
MissVars = who('MR*');


%% Cleaning downloaded data - 4/18/2016
disp(['Converting TCM data to double...'])
%making fields of TCM data into doubles
fieldnames = {'X_Accel'; 'Y_Accel'; 'Z_Accel'; 'X_Tilt'; 'Y_Tilt';...
    'Z_Tilt'; 'Sum_Vector'};
% for the Aransas River
for vvv = [find(not(cellfun('isempty',regexp(AranVars, 'TCM'))))]'
    for iii = 1:length(fieldnames)
        % converting string matrices to double
        eval([AranVars{vvv} '.' fieldnames{iii} ' = '...
            'str2num(' AranVars{vvv} '.' fieldnames{iii} ');'])
    end
end


%%%%%%%%%%%%%%%%%%%%%%%%%%%%%%%%%%%%%%%%%%%%%%%%%%%%%%%%%%%%%%%%%%%%%%%%%%%
%%%%
% RPEAT PROCESS FOR MISSION RIVER
%%%%%%%%%%%%%%%%%%%%%%%%%%%%%%%%%%%%%%%%%%%%%%%%%%%%%%%%%%%%%%%%%%%%%%%%%%%
%%%%
% for the Miss River
for vvv = [find(not(cellfun('isempty',regexp(MissVars, 'TCM'))))]'
```

```
    for iii = 1:length(fieldnames)
        % converting string matrices to double
        eval([MissVars{vvv} '.' fieldnames{iii} ' = '...
            'str2num(' MissVars{vvv} '.' fieldnames{iii} ');'])
    end
end


%% Resetting all the date numbers
disp(['Adjusting date numbers...'])
% Aransas River
for vvv = 1:length(AranVars)

    % for the TCM and ADP files
    if ~isempty(regexp(AranVars{vvv}, 'AR24')) ||...
            ~isempty(regexp(AranVars{vvv},'TCM'))

        %resetting datenum variable
        eval([AranVars{vvv} '.Datenum = [];'])
        eval(['lengthy = length(' AranVars{vvv} '.Date_Time);'])

        for iii = 1:lengthy
            %recalculatting date numbers
            eval([AranVars{vvv} '.Datenum(iii,1) = datenum('...
                AranVars{vvv} '.Date_Time(iii,:));'])
        end

    else
        % for the LTC files
        % resetting date num variable
        eval([AranVars{vvv} '.Datenum = [];'])
        eval(['lengthy = length(' AranVars{vvv} '.Date);'])

        % Turning temperature and level into vectors
        eval([AranVars{vvv} '.TEMPERATURE = ' AranVars{vvv}...
            '.TEMPERATURE'';'])
        eval([AranVars{vvv} '.CONDUCTIVITY = ' AranVars{vvv}...
            '.CONDUCTIVITY'';'])
        eval([AranVars{vvv} '.LEVEL = ' AranVars{vvv} '.LEVEL'';'])
        eval([AranVars{vvv} '.ms = ' AranVars{vvv} '.ms'';'])

        for iii = 1:lengthy
            % recalculating date numbers
            eval([AranVars{vvv} '.Datenum(iii,1) = datenum(['...
               AranVars{vvv} '.Date(iii,:) '' '' ' AranVars{vvv}...
               '.Time(iii,:)]);'])
        end
    end
end
```

```
%%%%%%%%%%%%%%%%%%%%%%%%%%%%%%%%%%%%%%%%%%%%%%%%%%%%%%%%%%%%%%%%%%%%%%%%%%%%%%%
%%%%
% REPEAT PROCESS FOR MISSION RIVER
%%%%%%%%%%%%%%%%%%%%%%%%%%%%%%%%%%%%%%%%%%%%%%%%%%%%%%%%%%%%%%%%%%%%%%%%%%%%%%%
%%%%
% for the Miss River
for vvv = 1:length(MissVars)

    % for the TCM and ADP files
    if ~isempty(regexp(MissVars{vvv}, 'AR24')) ||...
            ~isempty(regexp(MissVars{vvv},'TCM'))

        %resetting datenum variable
        eval([MissVars{vvv} '.Datenum = [];'])
        eval(['lengthy = length(' MissVars{vvv} '.Date_Time);'])

        for iii = 1:lengthy
            %recalculatting date numbers
            eval([MissVars{vvv} '.Datenum(iii,1) = datenum('...
                MissVars{vvv} '.Date_Time(iii,:));'])
        end

    else
        % for the LTC files
        % resetting date num variable
        eval([MissVars{vvv} '.Datenum = [];'])
        eval(['lengthy = length(' MissVars{vvv} '.Date);'])

        % Turning temperature and level into vectors
        eval([MissVars{vvv} '.TEMPERATURE = ' MissVars{vvv}...
            '.TEMPERATURE'';'])
        eval([MissVars{vvv} '.CONDUCTIVITY = ' MissVars{vvv}...
            '.CONDUCTIVITY'';'])
        eval([MissVars{vvv} '.LEVEL = ' MissVars{vvv} '.LEVEL'';'])
        eval([MissVars{vvv} '.ms = ' MissVars{vvv} '.ms'';'])

        for iii = 1:lengthy
            % recalculating date numbers
            eval([MissVars{vvv} '.Datenum(iii,1) = datenum(['...
               MissVars{vvv} '.Date(iii,:) '' '' ' MissVars{vvv}...
               '.Time(iii,:)]);'])
        end
    end
end

%% Save and clear ADP 24 hour data
disp(['Saving and clearing 24 hour data...'])
% create a path for saving data
adp_save_path = ['Dropbox\Field Work\Analysis\'...
    'All Long Term Data\Matlab Cleaned Data\'];
```

```
data_saving = '24 Hour ADP Data\';
if ~isdir([using_comp adp_save_path data_saving])
    mkdir([using_comp adp_save_path data_saving])
end

% finding 24 hour study variables
for vvv = find(not(cellfun('isempty',regexp(AranVars, 'AR24'))))'
    % saving 24 hour data
    eval(['save([using_comp   adp_save_path   data_saving   AranVars{vvv}
''.mat''],'...
        '''' AranVars{vvv} ''');'])
end


%%%%%%%%%%%%%%%%%%%%%%%%%%%%%%%%%%%%%%%%%%%%%%%%%%%%%%%%%%%%%%%%%%%%%%%%%%%%
%%%%
% REPEAT PROCESS FOR MISSION RIVER
%%%%%%%%%%%%%%%%%%%%%%%%%%%%%%%%%%%%%%%%%%%%%%%%%%%%%%%%%%%%%%%%%%%%%%%%%%%%
%%%%
% for the Miss River

% finding 24 hour study variables
for vvv = find(not(cellfun('isempty',regexp(MissVars, 'MR24'))))'
    % saving 24 hour data
    eval(['save([using_comp    save_path    data_saving    MissVars{vvv}
''.mat''],'...
        '''' MissVars{vvv} ''');'])
end

% clearing data
eval(['clear '...
    AranVars{find(not(cellfun('isempty',regexp(AranVars, 'AR24'))))'}])
% eval(['clear '...
%   MissVars{find(not(cellfun('isempty',regexp(MissVars, 'MR24'))))'}])
clear fieldnames ADPdirectory ADPfnames24


%% Save datenum corrected data
disp(['Saving datenum fixed data...'])
% create a path for saving data
save_datenum_path = ['Dropbox\Field Work\Analysis\All Long Term Data\'...
    'Matlab Cleaned Data\'];
data_saving = 'Datenum cleaned Data\';
if ~isdir([using_comp save_datenum_path data_saving])
    mkdir([using_comp save_datenum_path data_saving])
end

% obtaining updated list of datenum corrected variables
AranVars = who('AR*');

for vvv = 1:length(AranVars)
```

```
    eval(['save([using_comp save_datenum_path data_saving AranVars{vvv}
'...
        '''_datenum_corrected.mat''],'...
        '''' AranVars{vvv} ''');'])
end

%%%%%%%%%%%%%%%%%%%%%%%%%%%%%%%%%%%%%%%%%%%%%%%%%%%%%%%%%%%%%%%%%%%%%%%%%%%%
%%%%
% REPEAT PROCESS FOR MISSION RIVER
%%%%%%%%%%%%%%%%%%%%%%%%%%%%%%%%%%%%%%%%%%%%%%%%%%%%%%%%%%%%%%%%%%%%%%%%%%%%
%%%%
% for the Miss River
% obtaining updated list of datenum corrected variables
MissVars = who('MR*');

for vvv = 1:length(MissVars)
    eval(['save([using_comp save_datenum_path data_saving MissVars{vvv}
'...
        '''_datenum_corrected.mat''],'...
        '''' MissVars{vvv} ''');'])
end
%}

%% Loading the datenum corrected data
%7{
load_path = ['Dropbox\Field Work\Analysis\All Long Term Data\'...
    'Matlab Cleaned Data\Datenum cleaned Data\'];
load_files = dir([using_comp load_path]);

for vvv = 1:length(load_files)
    if ~isempty(regexp(load_files(vvv).name, '.mat'))
        eval(['load([using_comp   load_path   '''   load_files(vvv).name
''''])'])
    end
end
%}


%% Reading in deployment dates and creating site structure variables
%7{
disp(['Obtaining deployment date information...'])
%opening the .csv deployment file
deployment_path = ['Dropbox\Field Work\Analysis\'...
    'Field Data Analysis\Clean Field data\'];
deploy_file     = 'TCM_deployments.csv';
Dfid            = fopen([using_comp deployment_path deploy_file]);
soi             = {};

%reading the information from each line
dummy = fgetl(Dfid); num = 1;
while ischar(dummy)
```

```
    % pull dates from between commas and create variable of site name
    commas = [1 regexp(dummy, ',') length(dummy)+1];

    for iii = 1:length(commas)-1
        if iii == 1
            % creating variable (sturcture) of site name
            sitevar = dummy(commas(iii):commas(iii+1)-1);
            soi{num,1} = sitevar;
        else
            % storing the dates within the variable
            eval([sitevar '.deploy_dates{iii-1,1} = '....
                dummy(commas(iii)+1:commas(iii+1)-1) ';'])
        end
    end

    % grab new line
    dummy = fgetl(Dfid); num = num+1;
end
fclose(Dfid);

% clear data
clear num commas sitevar
%}


%% creating master matrices
%{

%% Creating trimmed matrix within structures
disp(['Trimming data based on deployment dates...'])
for vvv = 1:length(soi)
    % creating a string to obtain previous variables
    initials = [soi{vvv}(1) 'R_' soi{vvv}(2)];

    % creating a matrices of all the raw data to trim
    eval([initials  '.trimmed_mat  =  ['  initials  '.Datenum,'  initials
'.LEVEL,'...
        initials '.TEMPERATURE,' initials '.CONDUCTIVITY];'])
    eval([initials 'TCM.trimmed_mat = [' initials 'TCM.Datenum,'...
        initials 'TCM.X_Accel,'...
        initials 'TCM.X_Tilt,'...
        initials 'TCM.Y_Accel,'...
        initials 'TCM.Y_Tilt,'...
        initials 'TCM.Z_Accel,'...
        initials 'TCM.Z_Tilt,'...
        initials 'TCM.Sum_Vector];']);

    % find indices to remove observations before initial install
    eval(['remove  = find(' initials '.Datenum < datenum('...
        soi{vvv} '.deploy_dates{1},''yyyymmdd HHMM''));'])
```

```
    eval(['remove_t  = find(' initials 'TCM.Datenum < datenum('...
        soi{vvv} '.deploy_dates{1},''yyyymmdd HHMM''));'])

    % find indices to remove for final observations
    eval(['remove  = [remove;'...
        'find(' initials '.Datenum > datenum('...
        soi{vvv} '.deploy_dates{end},''yyyymmdd HHMM''))];'])
    eval(['remove_t  = [remove_t;'...
        'find(' initials 'TCM.Datenum > datenum('...
        soi{vvv} '.deploy_dates{end},''yyyymmdd HHMM''))];'])

    % removing indices
    eval([initials '.trimmed_mat(remove,:) = [];'])
    eval([initials 'TCM.trimmed_mat(remove_t,:) = [];'])

end


%% Creating master (timestamp aligned) matrix within the site structures
disp(['Creating master matrix of all data for each site...'])
mins15 = 15/(60*24);

for vvv = 1:length(soi)
    % creating blank master matrix
    eval([soi{vvv} '.master = [];'])
    eval(['june15_deploy = datenum(' soi{vvv} '.deploy_dates{2},'...
        '''YYYYmmdd HHMM'');'])
    % obtaining "initials"
    initials = [soi{vvv}(1) 'R_' soi{vvv}(2)];
    %finding length of trimmed matrices
    eval(['lengthy = length(' initials '.trimmed_mat);'])

    for iii = 1:lengthy % searching LTC data for TCM match

        % obtaining LTC timestamp
        eval(['[time_diff,TCM_index] = min(abs(' initials...
            '.trimmed_mat(iii,1)          -          '          initials
'TCM.trimmed_mat(:,1)));'])

% **** UPDATE IF EVER FIGURE OUT HOW TO USE IMPROPER INSTALL DATA ****
        % removing TCM values before June installation
        eval(['timer = ' initials '.trimmed_mat(iii,1);'])
        if timer < june15_deploy
            time_diff = 1e6; % forces next if statement to record nans
        end

% if nearest data point is more than 15 minutes away, store nan values
        if time_diff > mins15
            % storing nan values in the master variable
            eval([soi{vvv} '.master = ['...
                soi{vvv} '.master;'...
```

```
                initials '.trimmed_mat(iii,:),'...
                'nan(1,size(' initials 'TCM.trimmed_mat,2))];'])
        else
            % storing TCM values in the master variable
            eval([soi{vvv} '.master = ['...
                soi{vvv} '.master;'...
                initials '.trimmed_mat(iii,:),'...
                initials 'TCM.trimmed_mat(TCM_index,:)];'])
        end
    end
    %saving header information
    eval([soi{vvv} '.headers = {''LTC Datenum'';'...
        '''LTC Level [m]''; ''LTC Temp [C]''; ''LTC Cond uS/cm'';'...
        '''TCM Datenum''; ''TCM X Accel''; ''TCM X Tilt'';'...
        '''TCM Y Accel''; ''TCM Y Tilt'';'...
        '''TCM Z Accel''; ''TCM Z Tilt'';'...
        '''TCM Sum Vector''};'])

    % remove repeated timesteps - TCM or LTC - sort the matrix by LTC
timestamp
    % removing repeat TCM timestamps
    eval(['[~, ui, ~] = unique(' soi{vvv} '.master(:,5));'])
    eval([soi{vvv} '.master = ' soi{vvv} '.master(ui,:);'])
    % removing repeat LTC timestamps
    eval(['[~, ui, ~] = unique(' soi{vvv} '.master(:,1));'])
    eval([soi{vvv} '.master = ' soi{vvv} '.master(ui,:);'])

end

%% save master matrices
disp(['Saving Master data...'])
% create a path for saving data
save_master_path = ['Dropbox\Field Work\Analysis\All Long Term Data\'...
    'Matlab Cleaned Data\'];
data_saving = 'initial Master matrices\';
if ~isdir([using_comp save_master_path data_saving])
    mkdir([using_comp save_master_path data_saving])
end

for vvv = 1:length(soi)
    eval(['save([using_comp save_master_path data_saving soi{vvv} '...
        '''_initial_master.mat''],'...
        '''' soi{vvv} ''');'])
end
%}

%% load saved Master data
disp(['Loading initial Master data...'])
% create a path for saving data
load_master_path = ['Dropbox\Field Work\Analysis\All Long Term Data\'...
    'Matlab Cleaned Data\'];
data_saving = 'initial Master matrices\';
```

```
for vvv = 1:length(soi)
    eval(['load([using_comp load_master_path data_saving '...
        'soi{vvv} '...
        '''_initial_master.mat''])'])
end


%% removing unneeded data
% removing the unneeded raw tilt and sum vector data
disp(['Removing the unnecessary raw tilt and sum vector data...'])
unneeded_indices = [7 9 11 12];

for vvv = 1:length(soi)
    eval([soi{vvv} '.master(:,unneeded_indices) = [];'])
    eval([soi{vvv} '.headers = {''LTC Datenum'';'...
        '''LTC Level [m]''; ''LTC Temp [C]''; ''LTC Cond uS/cm'';'...
        '''TCM Datenum''; ''TCM X Accel'';'...
        '''TCM Y Accel'';'...
        '''TCM Z Accel''};'])
end




%% cleaning data from install events and storing in a 'split' cell/matrix
disp(['Cleaning out the data from between deployments...'])
for vvv = 1:length(soi)

    eval([soi{vvv} '.split_master ={};'])
    %finding # of deplyments
    eval(['lengthy = length(' soi{vvv} '.deploy_dates);'])
    storage = 1;
    for iii = 1:lengthy-1

        % grabbing date of deployment
        eval(['dateup = ' soi{vvv} '.deploy_dates{iii+1};'])

        if iii == 1
% obtaining the LTC timestamps between the first and second install
timestamp
% (-1 hr for install time)
            eval(['LTC_timestamps = '...
                'intersect('...
                'find(' soi{vvv} '.master(:,1) > datenum('...
                soi{vvv} '.deploy_dates{iii}, ''yyyymmdd HHMM'')),'...
                'find(' soi{vvv} '.master(:,1) < datenum('...
                soi{vvv}   '.deploy_dates{iii+1},   ''yyyymmdd   HHMM'')-
0.25/24));'])
```

```
% obtaining the TCM timestamps between the first and second install
timestamp
            TCM_timestamps = []; % bad first installation in May 2015

% finding and storing the common values
            indices = LTC_timestamps;
            eval([soi{vvv} '.split_master{iii,1} = '...
                soi{vvv} '.master(indices,:);'])

% stripping extra data off of end of July 2016 downloads
        elseif ~isempty(regexp(dateup, '20160716')) ||...
                ~isempty(regexp(dateup, '20160717'))

            % storing nan values for period of calibrations in July 2016
            eval([soi{vvv} '.split_master{iii,1} = nan(10,8);'])

% normal conditions
        else
% obtaining the LTC timestamps between the current
% (+1 hr for install time) and next install timestamp
            eval(['LTC_timestamps = '...
                'intersect('...
                'find(' soi{vvv} '.master(:,1) > datenum('...
                soi{vvv}         '.deploy_dates{iii},         ''yyyymmdd
HHMM'')+0.5/24),'...
                'find(' soi{vvv} '.master(:,1) < datenum('...
                soi{vvv}   '.deploy_dates{iii+1},   ''yyyymmdd   HHMM'')-
0.25/24));'])

% obtaining the TCM timestamps between the current
%(+1 hr for install time) and next install timestamp
            eval(['TCM_timestamps = '...
                'intersect('...
                'find(' soi{vvv} '.master(:,5) > datenum('...
                soi{vvv}         '.deploy_dates{iii},         ''yyyymmdd
HHMM'')+0.5/24),'...
                'find(' soi{vvv} '.master(:,5) < datenum('...
                soi{vvv}   '.deploy_dates{iii+1},   ''yyyymmdd   HHMM'')-
0.25/24));'])

% finding and storing the common values
%             if ~isempty(TCM_timestamps) && ...
%                     abs(length(LTC_timestamps)-length(TCM_timestamps))
< 5
%                 indices = intersect(LTC_timestamps, TCM_timestamps);
%             else
%                 indices = LTC_timestamps;
%             end
% the above script forces a match between indices before saving the data.
% instead, we will take the set of indices that has more points and save
% those in the split_master. the above script assumed the TCMs would be
```

```
% more reliable than they were.
% - i.e., likely LTC will have more points, and we want as much data from
% all sensors, even if that means that the LTC data is unmatched with TCM
% data
            if length(TCM_timestamps) > length(LTC_timestamps)
                indices = TCM_timestamps;
            else
                indices = LTC_timestamps;
            end
            eval([soi{vvv} '.split_master{iii,1} = '...
                soi{vvv} '.master(indices,:);'])
        end
    end
end



%% Creating empirical tilt curves
disp(['Creating the empirical tilt curves...'])
% making tilt curve for the 1p50b15 TCM
b15 = [0    0;... matrix of [tilt (deg), velocity (cm/s)] columns
       5    4.7310;...
      10    8.2004;...
      20    13.8776;...
      30    18.9240;...
      40    25.2320;...
      50    32.1708;...
      60    41.6328;...
      70    57.4028;...
      80    100.9280;...
      90    170.3160];

 % making tilt curve for the 1p50 TCM
 p50 = [0   0;... matrix of [tilt (deg), velocity (cm/s)] columns
        5   8.8320;...
        10  15.3088;...
        20  25.9072;...
        30  35.3280;...
        40  47.1040;...
        50  58.8800;...
        60  77.7216;...
        70  103.0400;...
        80  160.1536;...
        90  317.9520];



% figure(1)
% subplot(1,2,1)
% plot(b15(:,1), b15(:,2), 'marker','.', 'markersize', 20)
% xlabel('Tilt degrees(\circ)')
% ylabel('Velocity, [cm s^{-1}]')
```

```
% title('Ballasted TCM')
%
%
% subplot(1,2,2)
% plot(p50(:,1), p50(:,2), 'marker','.', 'markersize', 20)
% xlabel('Tilt degrees(\circ)')
% ylabel('Velocity, [cm s^{-1}]')
% title('Non-ballasted TCM')

%% translate from accel, g into deg then into q
disp(['Rotating and translating accel (g) to tilt then q...'])
%{
The section performs the following actions:
- normalizes the data first
- centers the data on the normalized V0
- then performs a YAW rotation
    - all rotations also performed on V0 values (should end at origin
- calculates tilt (deg from vert) and velocity
- sets all velocities with direction > 0 as positive, and all those < 0
as
negative
    - denoting downstream and upstream flow, repsectively
%}

% Rotate Cartesian coordinates so y-axis aligns with river flow direction
% y+ points downstream, X+ points toward the right bank, z+ points up
% assuming that Z is properly oriented in the veritical direction
% performing a "yaw" rotation
%   ^^->   Heinesch   2006   -   Coordinate   rotation   presentation
(Rotations_ppt.tif)
% p/slide 9-11 - Rotations 1-3 matrix
rotXY = @(alpha)...
    [cosd(alpha) sind(alpha) 0;...
    -sind(alpha) cosd(alpha) 0;...
    0            0           1];

rotXZ = @(beta)...
    [cosd(beta) 0 sind(beta);...
    0           1          0;...
    -sind(beta) 0 cosd(beta)];

rotYZ = @(gamma)...
    [1           0            0;...
    0   cosd(gamma) sind(gamma);...
    0  -sind(gamma) cosd(gamma)];

% ** we need to perform a YXZ rotation, or pitch, roll, then yaw rotations

% loading the calibration material
calib_path = [using_comp '\Dropbox\Field Work\Analysis\'...
    'All Long Term Data\Configurate TCM\'];
```

```
% loop through sites and translate accel data into tilt
for vvv = 1:length(soi)

    % displaying the current site being worked on
    disp(['Working site ' soi{vvv} '...'])
    eval(['splits = length(' soi{vvv} '.deploy_dates)-1;'])

    for kkk = 1:splits

        % obtaining data for current field installation
        eval(['current_data = ' soi{vvv} '.split_master{kkk,1};'])
        % grabbing date for titles of plots
        eval(['title_date   = ' soi{vvv} '.deploy_dates{kkk,1}(1:8);'])

        % if ALL the values are nan, skip the calculations
        % sum of valid data is greater than 100 points
        if sum(~isnan(current_data(:,5))) > 20

            % TCM has left-handed coordinate system
            % convert to right-handed
            ttt = current_data(:,5); % time stamps
            XYZ_raw     =     [current_data(:,8)     current_data(:,7)
current_data(:,6)];
            % [cross-channel  up\down-stream  vertical]

            % obtaining the calibration/configuration coefficients to
            % normalize the raw data before rotation
            if strcmp(soi{vvv}, 'M2')
                %obtaining proper coefs
                load([calib_path soi{vvv} '_1p50b15_calib_coef.mat']);
                % equation coefficients
                emp_curve = b15;

            elseif datenum(title_date, 'yyyymmdd') > datenum('20160716',
'yyyymmdd')...
                    && strcmp(soi{vvv},'M1')
                disp(['Ballasted logger moved to M1 in summer of 2016.'])
                disp(['Using ballasted configuration coefficients.'])
                %obtaining proper coefs
                load([calib_path 'M2_1p50b15_calib_coef.mat']);
                % equation coefficients
                emp_curve = b15;

            elseif strcmp(soi{vvv},'M1')
                disp(['No cfg data available for M1'])
                disp(['Using M3 configuration coefficients.'])
                % obtaining M3 coefs
                load([calib_path 'M3_1p50_calib_coef.mat']);
                % equation coefficients
                emp_curve = p50;
```

```
            else
                % obtaining correct coefs
                load([calib_path soi{vvv} '_1p50_calib_coef.mat']);
                % equation coefficients
                emp_curve = p50;
            end

% ************* % finding most commonly repeated data
% ************* % with X-,Y-,and Z-data all the same
            iq_test = XYZ_raw;
            ordered_TCM = nan(length(iq_test),2);
            for jjj = 1:length(iq_test)
                if isnan(ordered_TCM(jjj))
                    % find number of cells that all have same X, Y, & Z
                    xi   = find(abs(iq_test(:,1) - iq_test(jjj,1)) < 1e-
10);
                    xyi  = xi(find(abs(iq_test(xi,2) - iq_test(jjj,2)) <
1e-10));
                    xyzi = xyi(find(abs(iq_test(xyi,3) - iq_test(jjj,3))
< 1e-10));

                    % track and store number of cells
                    if length(xyzi) >= 1
                        ordered_TCM(xyzi,1) = jjj;
                        ordered_TCM(xyzi,2) = length(xyzi);

                    elseif isnan(iq_test(jjj,1))
                        ordered_TCM(xyzi,1) = jjj;
                        ordered_TCM(xyzi,2) = nan;
                        % nans wil be removed from dataset to not impact
95%

                    else
                        error(['Data is not finding a match, even to
itself.'])
                    end
                end
            end

            % attach timestep counter to data
            ordered_TCM    = [[1:1:length(ordered_TCM)]', ordered_TCM];
            [~,sorti]      = sort(ordered_TCM(:,3), 'descend');
            ordered_TCM    = ordered_TCM(sorti,:);
            ordered_TCM    = ordered_TCM(~isnan(ordered_TCM(:,2)),:);

            % finding most common 25% points
            iqp100       = 0.25;
            quant_num    = round(length(ordered_TCM(:,1))*iqp100);
            origin_prime = ordered_TCM(1:quant_num,1);
```

```
            % finding median x,y,z values of most common 25% of points
            if strcmp(soi{vvv}, 'A2')
                V0X = nanmean(XYZ_raw(origin_prime, 1));
                V0Y = nanmean(XYZ_raw(origin_prime, 2));
                V0Z = nanmean(XYZ_raw(origin_prime, 3));
            elseif   strcmp(soi{vvv},   'A3')   &&   strcmp(title_date,
'20161203')
                V0X = nanmean(XYZ_raw(origin_prime, 1));
                V0Y = nanmean(XYZ_raw(origin_prime, 2));
                V0Z = nanmean(XYZ_raw(origin_prime, 3));
            end


%********** % Normalizing the data
            XYZ_norm = [(XYZ_raw(:,1)-QX0)./QX1,...
                (XYZ_raw(:,2)-QY0)./QY1,...
                (XYZ_raw(:,3)-QZ0)./QZ1];
            % normalizing the zero velocity data
            vz_norm  =  [(V0X  -  QX0)./QX1;  (V0Y  -  QY0)./QY1;  (V0Z  -
QZ0)./QZ1];
            y_rot_pt = vz_norm;


            % inverting XYZ matrix
            XYZ_norm = XYZ_norm';

% ************* % rotating the XZ coordinate plane about Y!!- AXIS
% ************* % rotating about the most common 25% of points
            centroid_slope    = y_rot_pt(3)/y_rot_pt(1);
            if centroid_slope > 0 % positive
                beta = atand(centroid_slope)-90;
            else % negative
                beta = atand(centroid_slope)+90;
            end
            eval([soi{vvv} '.rotation_degs(kkk,1) = beta;'])
            cartesian_y_rotate = rotXZ(beta)*XYZ_norm;
            x_rot_pt           = rotXZ(beta)*y_rot_pt;
            vz1                = rotXZ(beta)*vz_norm;


% ************* % rotating the YZ coordinate plane about X!!- AXIS
% ************* % rotating about the most common 25% of points
            centroid_slope    = x_rot_pt(3)/x_rot_pt(2);
            if centroid_slope > 0 % positive
                gamma = atand(centroid_slope)-90;
            else % negative
                gamma = atand(centroid_slope)+90;
            end
            eval([soi{vvv} '.rotation_degs(kkk,2) = gamma;'])
            cartesian_yx_rotate = rotYZ(gamma)*cartesian_y_rotate;
            z_rot_pt            = rotYZ(gamma)*x_rot_pt;
```

```
            vz2                 = rotYZ(gamma)*vz1;


% ************* % YAW rotation using median X&Y of the farthest 1 percent
% ************* % rotating the XY coordinate plane about Z!!- AXIS
            % finding least common 5% of points
            iqp100       = 0.95;
            quant_num    = round(length(ordered_TCM(:,1))*iqp100);
            ind05        = ordered_TCM(quant_num:end,1);
            ind95        = ordered_TCM(1:quant_num, 1);
            least_common = cartesian_yx_rotate(:,ind05)';

            % determine if there are two unique clusters of farthest one
percent
            disp([soi{vvv} ': ' title_date])
            [clus_ind, Centroids] = kmeans(least_common(:,1:2), 2,...
                'Replicates', 10, 'Display', 'final');

            % determine rotation slope from centroid data
            % We will rotate with centroid that is further from origin.
            if              sqrt(sum(Centroids(1,:).^2))              >
sqrt(sum(Centroids(2,:).^2))
                interp_pt = Centroids(1,:);
                other_pt  = Centroids(2,:);
                if (vvv == 4 || vvv == 5) && iii == splits
                    interp_pt = Centroids(2,:);
                    other_pt  = Centroids(1,:);
                end
            else
                interp_pt = Centroids(2,:);
                other_pt  = Centroids(1,:);
                if (vvv == 4 || vvv == 5) && iii == splits
                    interp_pt = Centroids(1,:);
                    other_pt  = Centroids(2,:);
                end
            end

            % Manual adjustments to problem sites
            if strcmp(soi{vvv}, 'A2') && strcmp(title_date , '20160111')
                interp_pt = Centroids(find(Centroids(:,2) < 0),:);
                other_pt  = Centroids(find(Centroids(:,2) > 0),:);
            elseif   strcmp(soi{vvv},   'A4')   &&   strcmp(title_date   ,
'20160430')
                interp_pt = Centroids(find(Centroids(:,2) > 0),:);
                other_pt  = Centroids(find(Centroids(:,2) < 0),:);
            elseif   strcmp(soi{vvv},   'A5')   &&   strcmp(title_date   ,
'20150808')
                interp_pt = Centroids(find(Centroids(:,2) < 0),:);
                other_pt  = Centroids(find(Centroids(:,2) > 0),:);
            elseif   strcmp(soi{vvv},   'A5')   &&   strcmp(title_date   ,
'20160430')
                interp_pt = Centroids(find(Centroids(:,1) > 0),:);
```

```
                other_pt  = Centroids(find(Centroids(:,1) < 0),:);
            end



            % obtaining clusters to plot
            plot_clusters       =       {[least_common(clus_ind==1,1),
least_common(clus_ind==1,2)];...
                [least_common(clus_ind==2,1),
least_common(clus_ind==2,2)]};
            cluster_cols = {'om','oc'};

            % find slope from selected interpolation point and rotate
            centroid_slope  =  (interp_pt(2)-other_pt(2))/(interp_pt(1)-
other_pt(1)); % obtaining the slope between centroids
            quad_points   = [interp_pt(2)/centroid_slope, interp_pt(2)];

            if quad_points(1)>0 && quad_points(2)>0  % quadrant 1
                alpha   = atand(centroid_slope)-90;
                plot_slope    =    [-0.25:0.05:0.25;    centroid_slope*(-
0.25:0.05:0.25)];
                no_rot = 0;

            elseif quad_points(1)<0 && quad_points(2)>0 % quadrant 2
                alpha   = atand(centroid_slope)+90;
                plot_slope  =  [0.25:-0.05:-0.25;  centroid_slope*(0.25:-
0.05:-0.25)];
                no_rot = 0;

            elseif quad_points(1)<0 && quad_points(2)<0 % quadrant 3
                alpha   = atand(centroid_slope)+90;
                plot_slope  =  [0.25:-0.05:-0.25;  centroid_slope*(0.25:-
0.05:-0.25)];
                no_rot = 0;

            elseif quad_points(1)>0 && quad_points(2)<0 % quadrant 4
                alpha   = atand(centroid_slope)-90;
                plot_slope    =    [-0.25:0.05:0.25;    centroid_slope*(-
0.25:0.05:0.25)];
                no_rot = 0;

            end
            loc_str = 'SouthOutside';

            % rotating the  XY coordinate plane about Z-axis
            eval([soi{vvv} '.rotation_degs(kkk,3) = alpha;'])
            cartesian_prime = rotXY(alpha)*cartesian_yx_rotate;
            final_origin    = rotXY(alpha)*z_rot_pt;
            vz_final        = rotXY(alpha)*vz2;
```

```
            % Plotting Rotation Procedure
            % SUBPLOT 1 - raw data
            figure(fig)
            subplot(1,3,1)
            plot(XYZ_raw(:,1), XYZ_raw(:,2), '.k')
            hold on
            plot(XYZ_norm(1,:), XYZ_norm(2,:), '.b')
            % plotting most common 25%
            plot(y_rot_pt(1),y_rot_pt(2), '.g', 'markersize',10)
            plot(V0X, V0Y, '*r')
            plot([QX0 QX1], [QY0 QY1], '*m')
            title([soi{vvv} ': ' title_date])
            % plotting  axes
            plot([-50 50], [0 0], 'color', [0.5 0.5 0.5]) % x-axis
            plot([0 0], [-50 50], 'color', [0.5 0.5 0.5]) % y-axis
            axis([-1.5 1.5 -1.5 1.5])
            if strcmp(soi{vvv}, 'A2')
                legend('Raw data', 'Normalized Data',...
                    'Normalized Origin - Raw 25% most repeated',...
                    'original - Vzero',  'original - Q coeffs',...
                    'Location', loc_str)
            else
                legend('Raw data', 'Normalized Data',...
                    'Normalized Origin',...
                    'original - Vzero',  'original - Q coeffs',...
                    'Location', loc_str)
            end

            % SUBPLOT 2 - origin corrected data
            subplot(1,3,2)
            plot(cartesian_yx_rotate(1,:),     cartesian_yx_rotate(2,:),
'.b')
            hold on
            % plotting data of least common 5%
            %                       plot(cartesian_yx_rotate(1,iq3d_ind),
cartesian_yx_rotate(2,iq3d_ind), 'og')
            title([soi{vvv} ': ' title_date])
            % plot centroid/cluster information
            plot(plot_clusters{1}(:,1),           plot_clusters{1}(:,2),
cluster_cols{1})
            plot(plot_clusters{2}(:,1),           plot_clusters{2}(:,2),
cluster_cols{2})
            plot(plot_slope(1,:), plot_slope(2,:), 'r')
            plot(quad_points(1), quad_points(2), '.r', 'markersize', 20)
            plot(Centroids(:,1), Centroids(:,2), 'kx',...
                'MarkerSize',10,'LineWidth',2)
            plot(final_origin(1), final_origin(2), '*g')
            % plotting  axes
            plot([-50 50], [0 0], 'color', [0.5 0.5 0.5]) % x-axis
            plot([0 0], [-50 50], 'color', [0.5 0.5 0.5]) % y-axis
```

```
            axis([-1.5 1.5 -1.5 1.5])
            legend('Pitch/Roll data', '5% Cluster 1', '5% Cluster 2',
'Rotation Line', ...
                'Rotation Point','Cluster centroids','Final Origin',...
                'Location', loc_str)


            % SUBPLOT 3 - the final rotated data
            subplot(1,3,3)
            plot(cartesian_prime(1,:), cartesian_prime(2,:), '.b')
            hold on
            plot(vz_final(1), vz_final(2), '*r')
            plot([-50 50], [0 0], 'color', [0.5 0.5 0.5]) % x-axis
            plot([0 0], [-50 50], 'color', [0.5 0.5 0.5]) % y-axis
            axis([-1.5 1.5 -1.5 1.5])
            if no_rot
                text(0.3, 0.45, 'No rotation occured.')
            end
            title([soi{vvv} ': ' title_date])
            legend('Rotated Data', 'Vzero - final',...
                'Location', loc_str)
            hold on

            if plot_check ~= 0
                % save plot
                % *** SAVING FIGURE BEFORE MOVING ON
                % makes sure the saved pdf fits within a landscape
document
                set(gcf,'PaperOrientation','landscape');
                set(gcf,'PaperUnits','normalized');
                set(gcf,'PaperPosition', [0 0 1 1]);

                % Saving within the main folder not an individual river
name folder
                % legend off
                folders = ['Rotation Method plots\' soi{vvv} '\'];
                if ~isdir([save_path folders])
                    mkdir([save_path folders]);
                end

                % save as .tif
                eval(['print(gcf, ''-dtiff'' , [save_path folders '...
                    '''' soi{vvv} '_' title_date '.tif'']);'])

                % closing figures
                % close all;
            end
            fig = fig +1;

%%%%%%%%%%%%%%%%%%%%%%%%%% - Finished rotating data ^^^
```

```
%%%%%%%%%%%%%%%%%%%%%%%%%%%% - Now calculating tilt and q vvvv

            % creating storage variables
            theta = nan(length(cartesian_prime(1,:)), 1);
            qdis  = nan(length(cartesian_prime(1,:)), 1);

            for iii = 1:length(cartesian_prime(1,:))
                % finding the tilt degress
                dots   = dot(vz_final, cartesian_prime(:,iii));
                norman = norm(cross(vz_final, cartesian_prime(:,iii)));
                theta(iii) = atan2d(norman, dots); % degrees
                if theta(iii) > 90
                    theta(iii) = 90;
                end


                if isnan(theta(iii))
                    qdis(iii) = nan;

                elseif max(theta(iii) == emp_curve(:,1))
                    % recording discharge of an exact calculated tilt
                    ind = find(emp_curve(:,1) == theta(iii));
                    qdis(iii) = emp_curve(ind,2);

                else
                    % finding nearest tilts in the empirical curve
                    nearest      =      [max(find(emp_curve(:,1)      <=
theta(iii))),...
                        min(find(emp_curve(:,1) >= theta(iii)))];

                    % finding discharge data
                    newq             =     interp1(emp_curve(nearest,1),
emp_curve(nearest,2),...
                        [emp_curve(nearest(1),1)        full(theta(iii))
emp_curve(nearest(2),1)]);
                    qdis(iii) = newq(2);
                end

            end

            downstream_flow = nan(size(qdis));
            crossstream_flow = nan(size(qdis));
            % setting q positive (+Y) for downstream flow
            % and negative (-Y) for upstream flow
            cartesian_prime = cartesian_prime'; % transposing data for
easier calculations
            posi = find(cartesian_prime(:,2) > 0);
            nega = find(cartesian_prime(:,2) < 0);
            downstream_flow(posi) = qdis(posi).*cosd(...
```

```
atand(cartesian_prime(posi,1)./cartesian_prime(posi,2)));
            downstream_flow(nega) = -1*qdis(nega).*cosd(...

atand(cartesian_prime(nega,1)./cartesian_prime(nega,2)));

            % recording cross-stream velocities
            % Right bank (X+) = positive q
            % Left bank  (X-) = negative q
            posix = find(cartesian_prime(:,1) > 0);
            negax = find(cartesian_prime(:,1) < 0);
            crossstream_flow(posix) = qdis(posix).*cosd(...

atand(cartesian_prime(posix,2)./cartesian_prime(posix,1)));
            crossstream_flow(negax) = -1*qdis(negax).*cosd(...

atand(cartesian_prime(negax,2)./cartesian_prime(negax,1)));
            cartesian_prime = cartesian_prime'; % re-transposing data to
original form


            % removing obvious outliers
            if strcmp(soi{vvv}, 'M3') && strcmp(title_date , '20150808')
                % finding outlier
                out_ind = find(cartesian_prime(1,:) > 0.7);

                % replacing with nans everywhere
                XYZ_norm(:,out_ind)        = [nan; nan; nan];
                cartesian_prime(:,out_ind) = [nan; nan; nan];
                theta(out_ind)             = nan;
                qdis(out_ind)              = nan;
                downstream_flow(out_ind)   = nan;
                crossstream_flow(out_ind)  = nan;

            elseif   strcmp(soi{vvv},   'M4')   &&   strcmp(title_date   ,
'20150808')
                % finding outlier
                out_ind = find(cartesian_prime(1,:) > 0.35);

                % replacing with nans everywhere
                XYZ_norm(:,out_ind)        = [nan; nan; nan];
                cartesian_prime(:,out_ind) = [nan; nan; nan];
                theta(out_ind)             = nan;
                qdis(out_ind)              = nan;
                downstream_flow(out_ind)   = nan;
                crossstream_flow(out_ind)  = nan;
            end



            %%%% plotting the data if applicable
```

```
            %7{
            % plotting the X Y data
            figure(fig)
            plot(cartesian_prime(1,:), cartesian_prime(2,:), '.')
            hold on
            plot(cartesian_prime(1,nega), cartesian_prime(2,nega),'oc')
            plot(vz_final(1), vz_final(2), '*r')
            lims = [get(gca, 'xlim'); get(gca, 'ylim')];
            plot([-50 50], [0 0], 'color', [0.5 0.5 0.5]) % x-axis
            plot([0 0], [-50 50], 'color', [0.5 0.5 0.5]) % y-axis
            set(gca, 'xlim', lims(1,:))
            set(gca, 'ylim', lims(2,:))
            ylabel('Y')
            xlabel('X')
            title([soi{vvv} ': ' title_date])
            if ~isempty(nega)
                legend('Normalized/Rotated Raw Data','Negative q',...
                    'V-zero','Rotated           Calib           Coeff',
'Location','SouthOutside')
            else
            legend('Normalized/Rotated Raw Data',...
                     'V-zero','Rotated                              Calib
Coeff','Location','SouthOutside')
            end
            grid on

            % saving figures of all major axes
            if plot_check ~= 0;
                % *** SAVING FIGURE BEFORE MOVING ON
                % makes sure the saved pdf fits within a landscape
document
                set(gcf,'PaperOrientation','landscape');
                set(gcf,'PaperUnits','normalized');
                set(gcf,'PaperPosition', [0 0 1 1]);

                % save as .tif
                print(gcf, '-dtiff' , [save_path folders soi{vvv} '_'
title_date '_xVy.tif'])
            end
            fig = fig +1;

            % plotting the discharge data
            figure(fig)
            plot(ttt, downstream_flow, '.')
            hold on
            plot(get(gca, 'xlim'), [ 2  2], '--r')
            plot(get(gca, 'xlim'), [-2 -2], '--r')
            ylabel('Velocity, (cm/s)')
            set(gca,  'xticklabel',  datestr(get(gca,  'xtick'),'mm-dd-
yy'))
            title([soi{vvv} ': ' title_date])
            grid on
```

```
            % saving figures of all major axes
            if plot_check ~= 0;
                % *** SAVING FIGURE BEFORE MOVING ON
                % makes sure the saved pdf fits within a landscape
document
                set(gcf,'PaperOrientation','landscape');
                set(gcf,'PaperUnits','normalized');
                set(gcf,'PaperPosition', [0 0 1 1]);

                % save as .tif
                print(gcf, '-dtiff' , [save_path folders soi{vvv} '_'
title_date '_qVt.tif'])
            end
            fig = fig +1;
            %}


            %%%%%%%%%%% Storing the data
            % storing updated acceleration data, tilt data, and discharge
data
            eval([soi{vvv}     '.split_master{kkk}(:,end+1:end+3)     =
XYZ_norm'';'])
            eval([soi{vvv}     '.split_master{kkk}(:,end+1:end+3)     =
cartesian_prime'';'])
            eval([soi{vvv}       '.split_master{kkk}(:,end+1)       =
full(theta);'])
            eval([soi{vvv} '.split_master{kkk}(:,end+1) = full(qdis);'])
            eval([soi{vvv}       '.split_master{kkk}(:,end+1)       =
downstream_flow;'])
            eval([soi{vvv}       '.split_master{kkk}(:,end+1)       =
crossstream_flow;'])

        % storing nans if the X, Y, and Z values are nan values
        else
            % storing nan values
            eval([soi{vvv} '.split_master{kkk}(:,end+1:end+10)'...
                '= nan(length(current_data(:,5)),10);'])
        end
    end

    % updating headers
    eval([soi{vvv} '.headers{end+1,1} = ''TCM X normalized?'';'])
    eval([soi{vvv} '.headers{end+1,1} = ''TCM Y normalized?'';'])
    eval([soi{vvv} '.headers{end+1,1} = ''TCM Z normalized?'';'])
    eval([soi{vvv} '.headers{end+1,1} = ''X rotated accel,g'';'])
    eval([soi{vvv} '.headers{end+1,1} = ''Y rotated accel,g'';'])
    eval([soi{vvv} '.headers{end+1,1} = ''Z rotated accel,g'';'])
    eval([soi{vvv}    '.headers{end+1,1}    =    ''abs(degrees    from
vetrical)'';'])
```

```
    eval([soi{vvv}  '.headers{end+1,1}  =  ''abs(specific  discharge),
cm/s'';'])
    eval([soi{vvv} '.headers{end+1,1} = ''Specific dis along downstream
'...
                                          '(Y) axis, (cm/s)'';'])
    eval([soi{vvv} '.headers{end+1,1} = ''Specific dis cross-stream '...
                                          '(X) axis, (cm/s)'';'])
    % creating a note
    eval([soi{vvv} '.downstream_flow_note = '...
        '''+ is downstream, - is upstream'';'])
    eval([soi{vvv} '.crossstream_flow_note = '...
        '''+ is Right bank, - is left bank'';'])

    % freeing up memory space
    close all

end


%% save updated matlab structures
disp(['Saving cleaned LTC and rotated TCM data...'])
for vvv = 1:length(soi)
    eval(['save([save_path ''' soi{vvv}...
        '_calib.mat''], ''' soi{vvv} ''')'])
end

% updating user on completion of script
disp(['Done.'])
diary off
```

Appendix H: Individual phase offset analysis plots

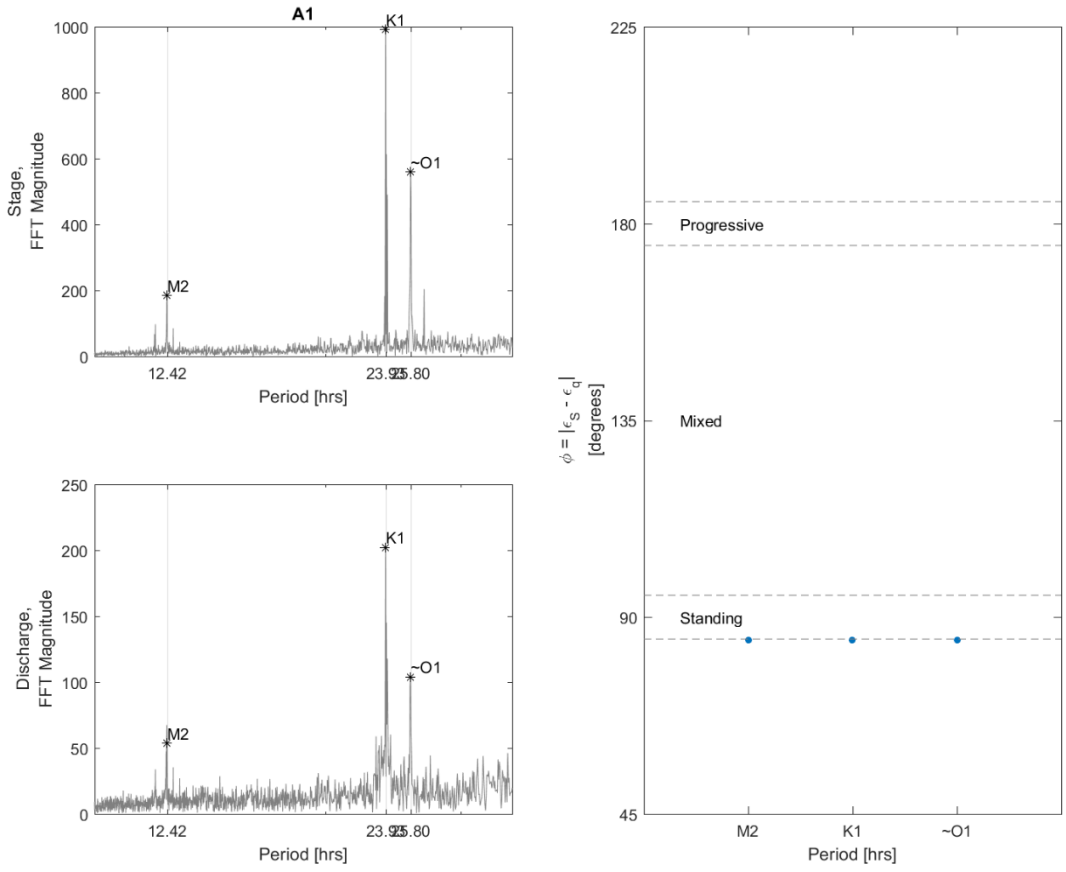

Figure H.1: The phase analysis for M-A site A1. The two subfigures (one atop the other) on the left-hand side of this figure show the FFT magnitudes of the stage (left-top) and discharge (left-bottom) for the identified semidiurnal and diurnal harmonics analyzed for phase offset. The right-hand figure shows the calculated phase offset for each harmonic and compares it to the predicted offsets for a standing, mixed and progressive wave.

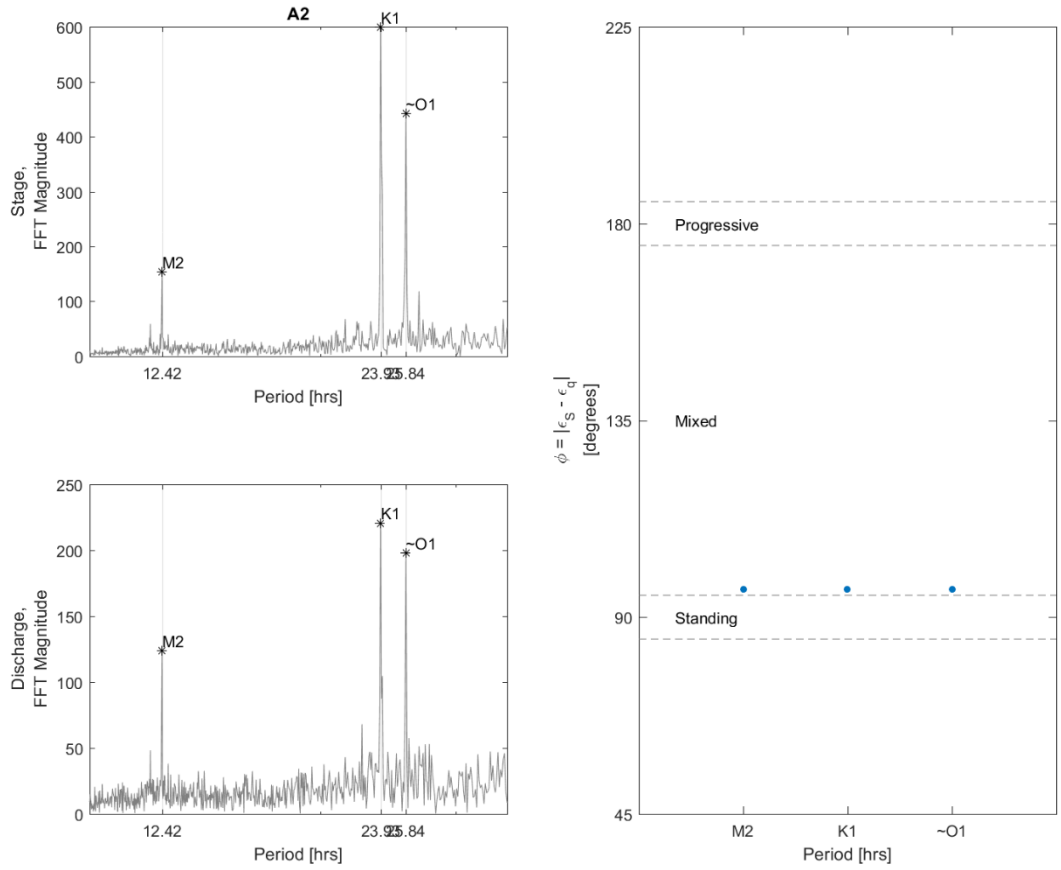

Figure H.2: The phase analysis for M-A site A2. The two subfigures (one atop the other) on the left-hand side of this figure show the FFT magnitudes of the stage (left-top) and discharge (left-bottom) for the identified semidiurnal and diurnal harmonics analyzed for phase offset. The right-hand figure shows the calculated phase offset for each harmonic and compares it to the predicted offsets for a standing, mixed and progressive wave.

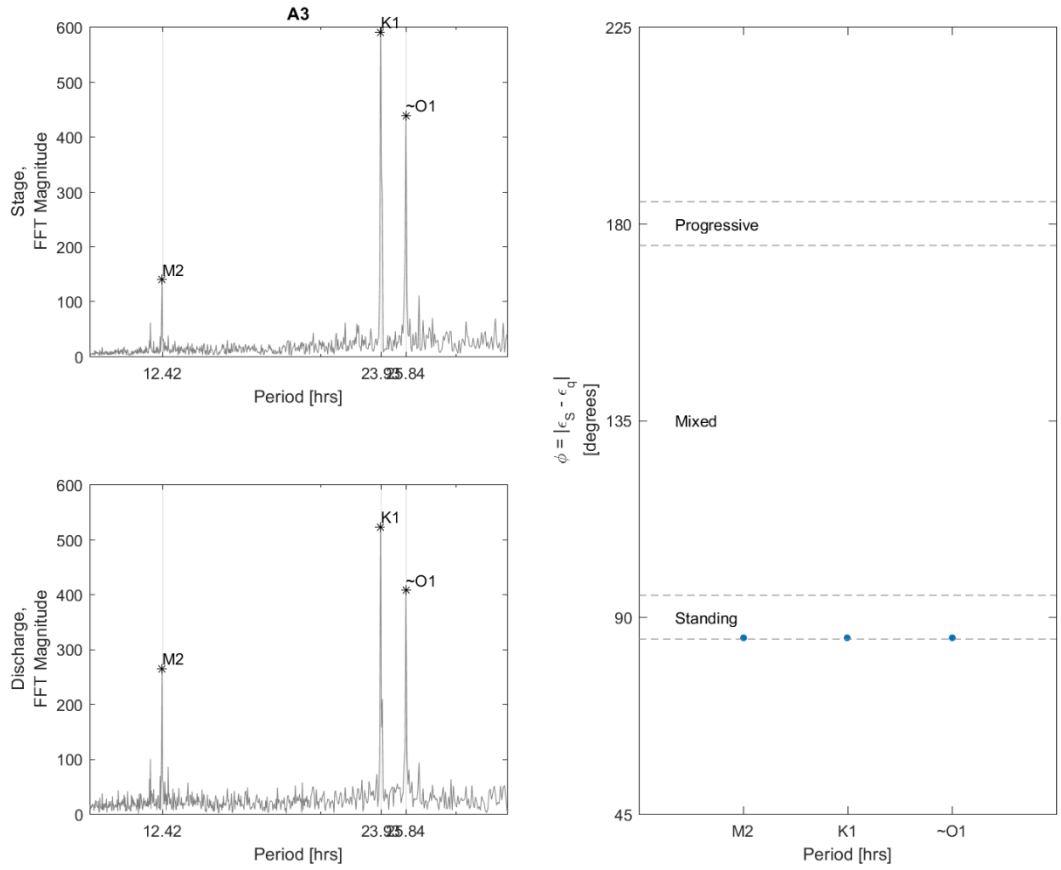

Figure H.3: The phase analysis for M-A site A3. The two subfigures (one atop the other) on the left-hand side of this figure show the FFT magnitudes of the stage (left-top) and discharge (left-bottom) for the identified semidiurnal and diurnal harmonics analyzed for phase offset. The right-hand figure shows the calculated phase offset for each harmonic and compares it to the predicted offsets for a standing, mixed and progressive wave.

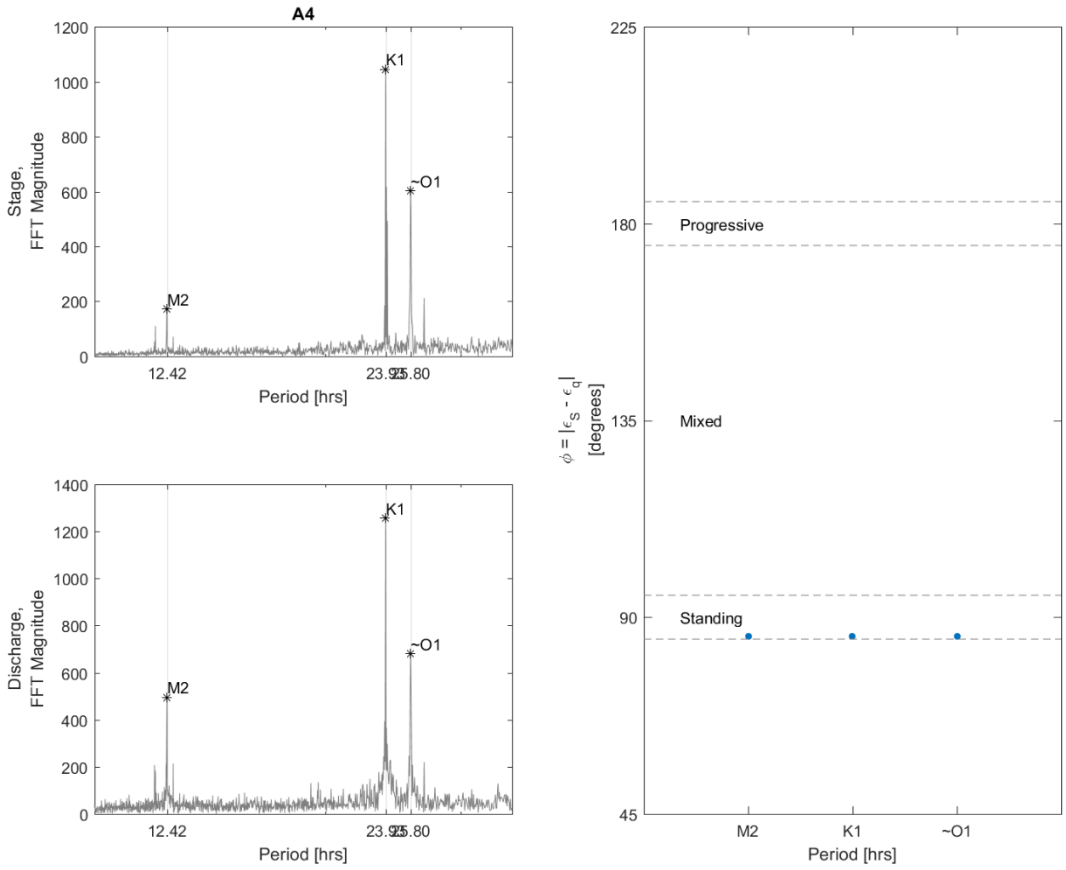

Figure H.4: The phase analysis for M-A site A4. The two subfigures (one atop the other) on the left-hand side of this figure show the FFT magnitudes of the stage (left-top) and discharge (left-bottom) for the identified semidiurnal and diurnal harmonics analyzed for phase offset. The right-hand figure shows the calculated phase offset for each harmonic and compares it to the predicted offsets for a standing, mixed and progressive wave.

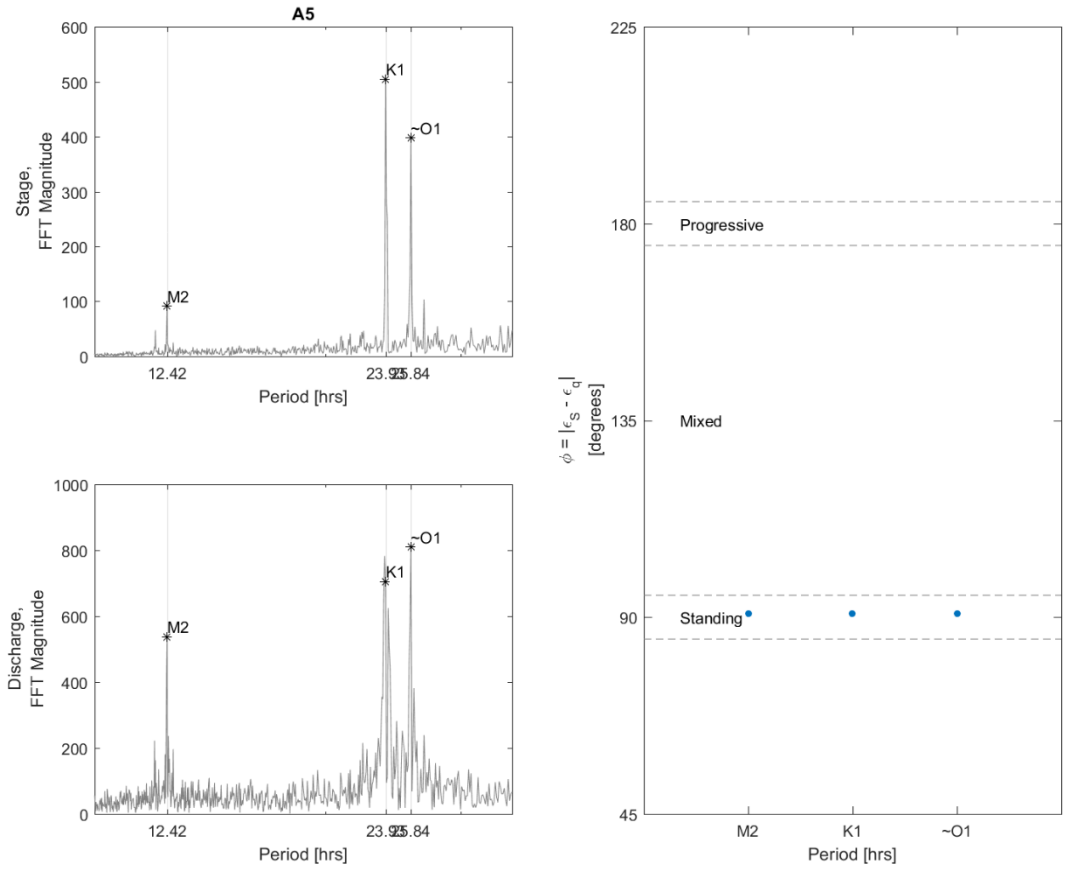

Figure H.5: The phase analysis for M-A site A5. The two subfigures (one atop the other) on the left-hand side of this figure show the FFT magnitudes of the stage (left-top) and discharge (left-bottom) for the identified semidiurnal and diurnal harmonics analyzed for phase offset. The right-hand figure shows the calculated phase offset for each harmonic and compares it to the predicted offsets for a standing, mixed and progressive wave.

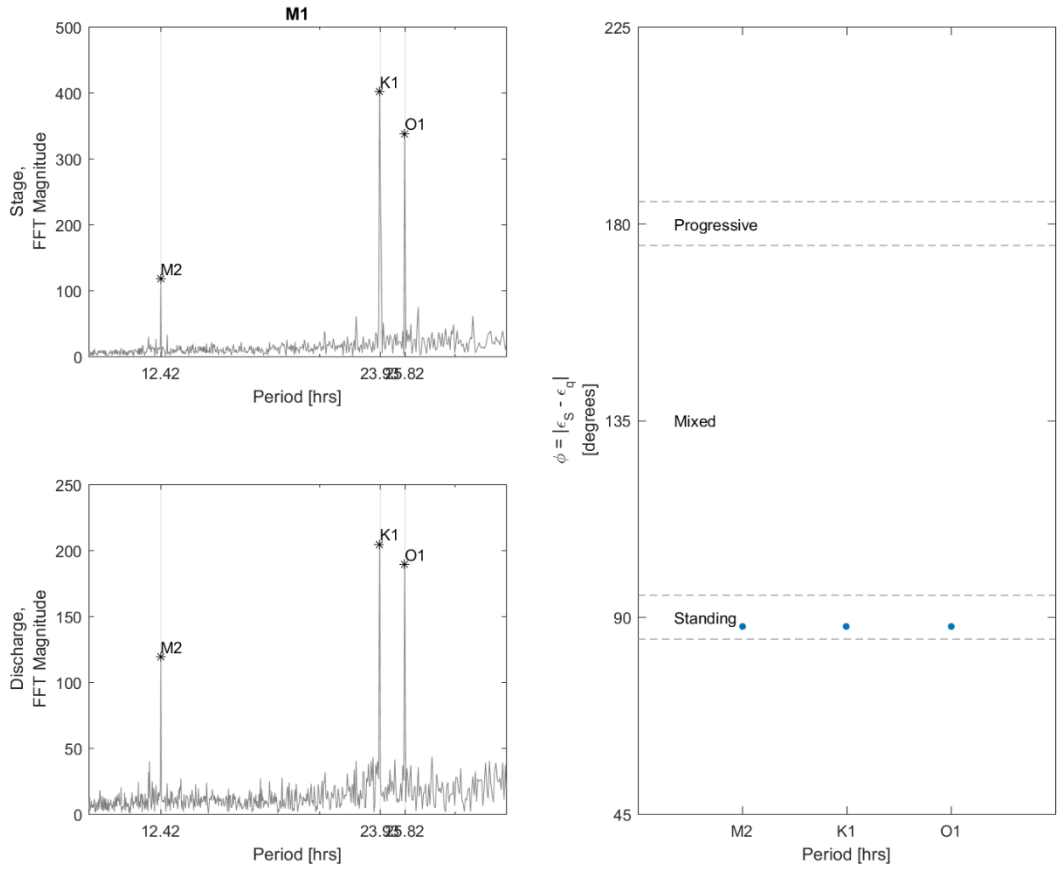

Figure H.6: The phase analysis for M-A site M1. The two subfigures (one atop the other) on the left-hand side of this figure show the FFT magnitudes of the stage (left-top) and discharge (left-bottom) for the identified semidiurnal and diurnal harmonics analyzed for phase offset. The right-hand figure shows the calculated phase offset for each harmonic and compares it to the predicted offsets for a standing, mixed and progressive wave.

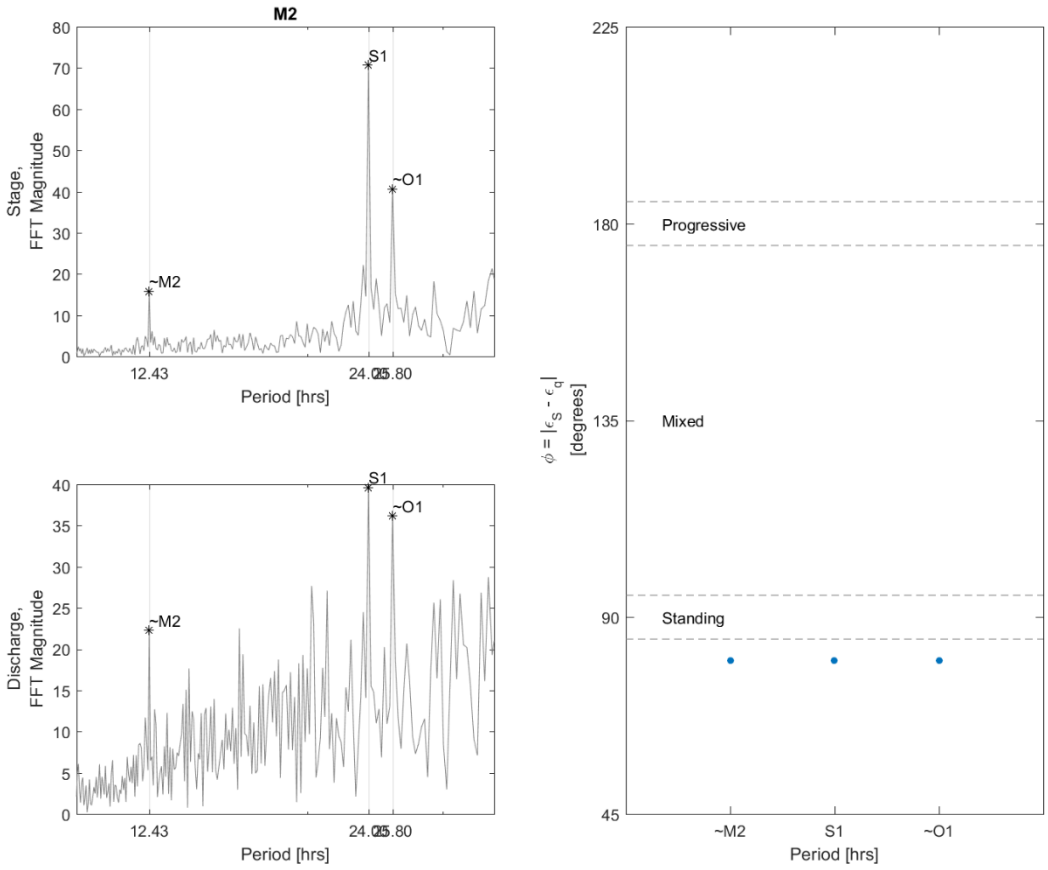

Figure H.7: The phase analysis for M-A site M2. The two subfigures (one atop the other) on the left-hand side of this figure show the FFT magnitudes of the stage (left-top) and discharge (left-bottom) for the identified semidiurnal and diurnal harmonics analyzed for phase offset. The right-hand figure shows the calculated phase offset for each harmonic and compares it to the predicted offsets for a standing, mixed and progressive wave.

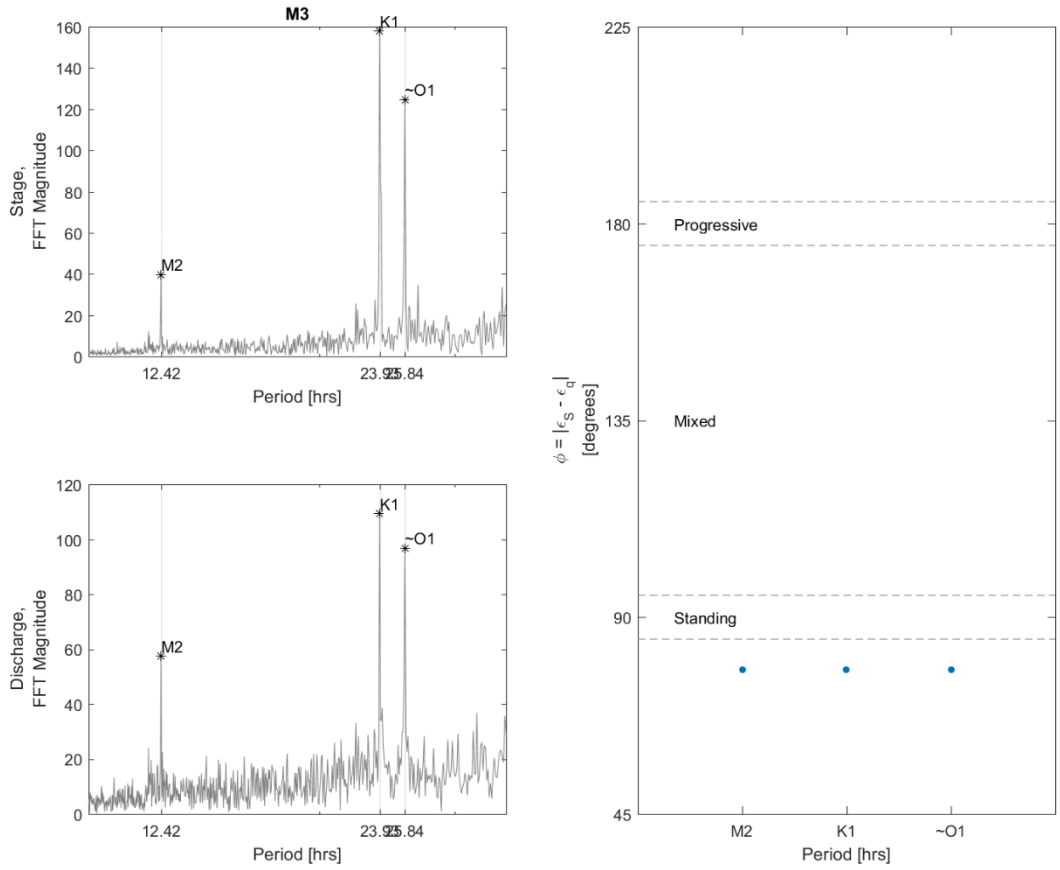

Figure H.8: The phase analysis for M-A site M3. The two subfigures (one atop the other) on the left-hand side of this figure show the FFT magnitudes of the stage (left-top) and discharge (left-bottom) for the identified semidiurnal and diurnal harmonics analyzed for phase offset. The right-hand figure shows the calculated phase offset for each harmonic and compares it to the predicted offsets for a standing, mixed and progressive wave.

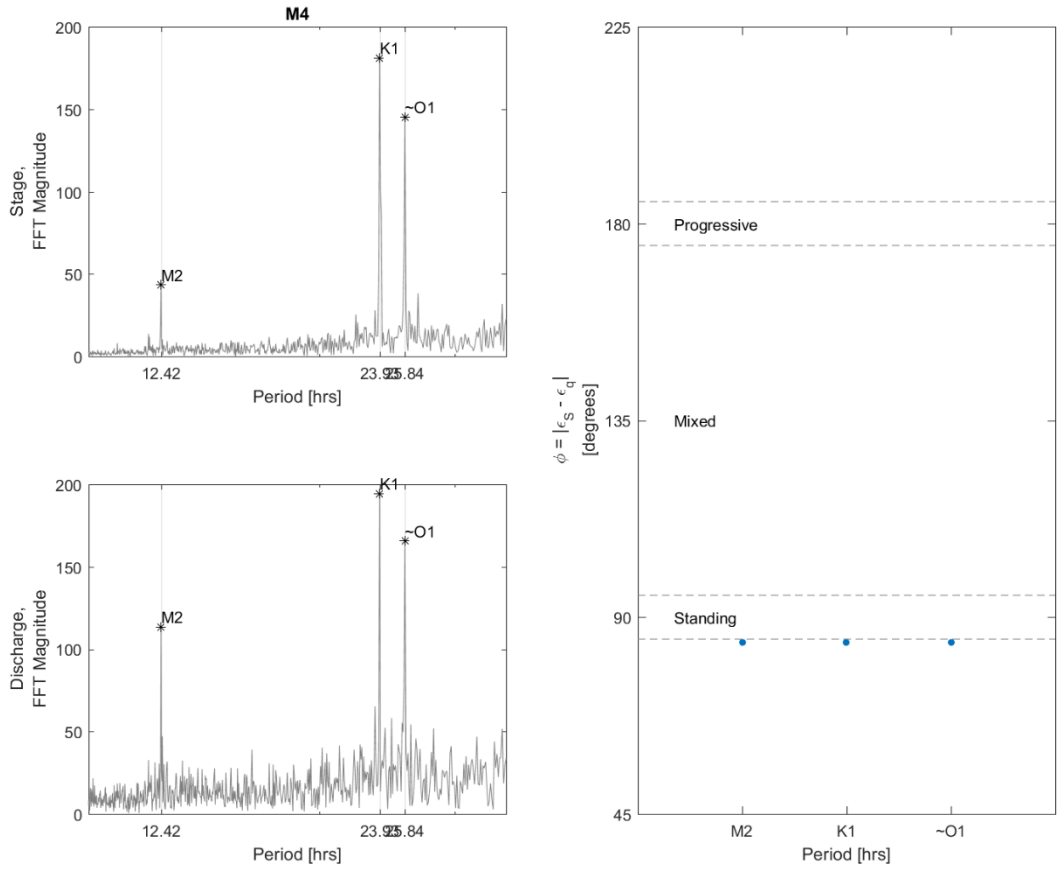

Figure H.9: The phase analysis for M-A site M4. The two subfigures (one atop the other) on the left-hand side of this figure show the FFT magnitudes of the stage (left-top) and discharge (left-bottom) for the identified semidiurnal and diurnal harmonics analyzed for phase offset. The right-hand figure shows the calculated phase offset for each harmonic and compares it to the predicted offsets for a standing, mixed and progressive wave.

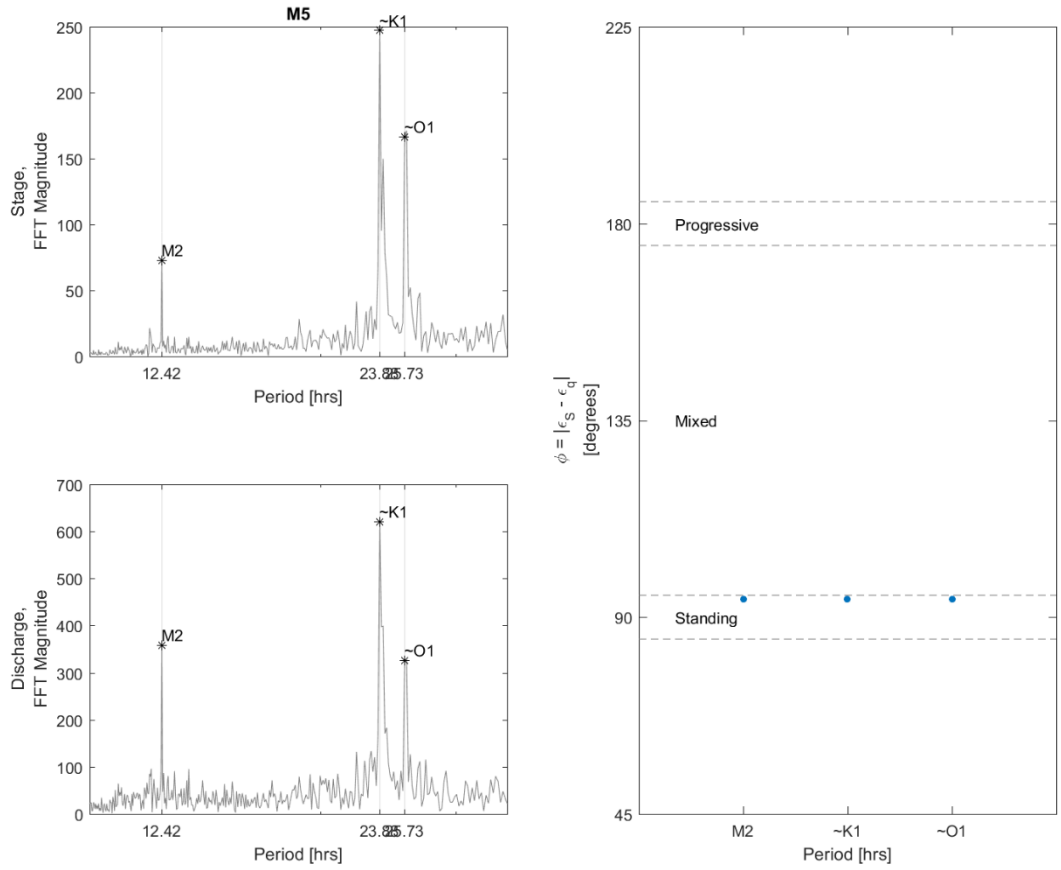

Figure H.10: The phase analysis for M-A site M5. The two subfigures (one atop the other) on the left-hand side of this figure show the FFT magnitudes of the stage (left-top) and discharge (left-bottom) for the identified semidiurnal and diurnal harmonics analyzed for phase offset. The right-hand figure shows the calculated phase offset for each harmonic and compares it to the predicted offsets for a standing, mixed and progressive wave.

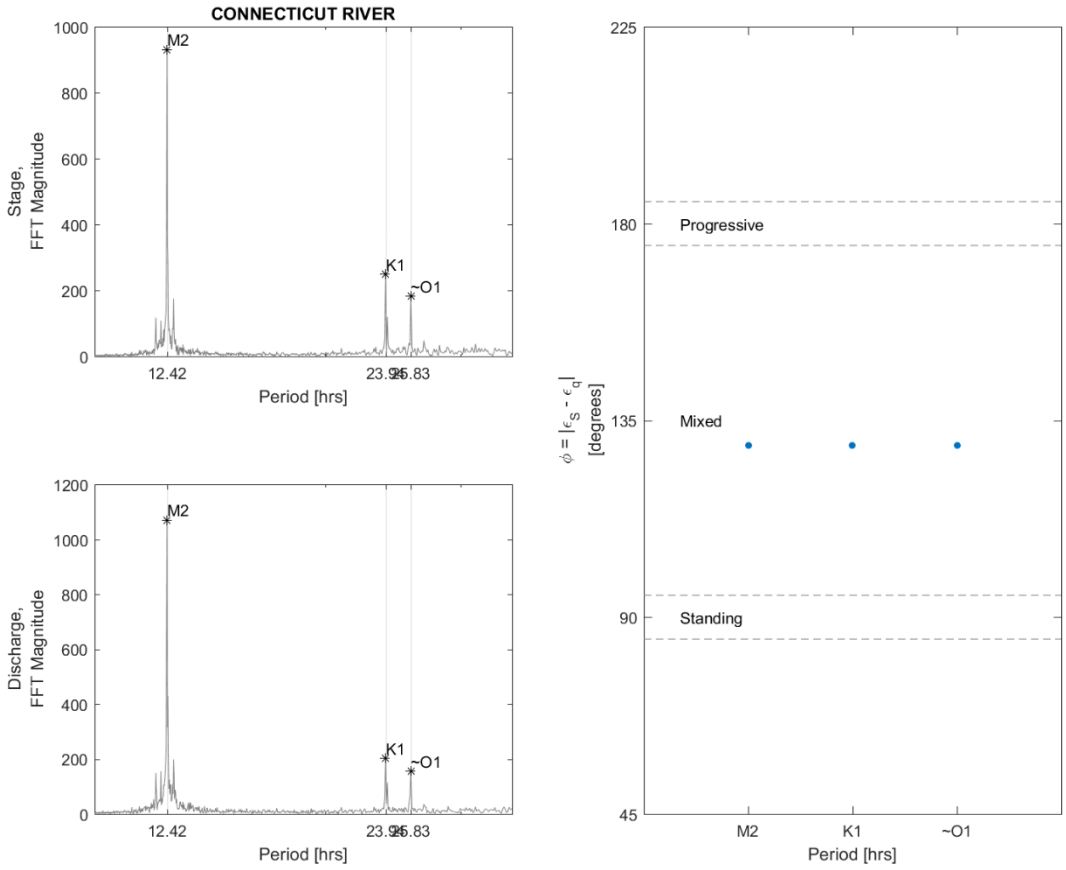

Figure H.11: The phase analysis for USGS site on the Connecticut River [site number: 01193050]. The two subfigures (one atop the other) on the left-hand side of this figure show the FFT magnitudes of the stage (left-top) and discharge (left-bottom) for the identified semidiurnal and diurnal harmonics analyzed for phase offset. The right-hand figure shows the calculated phase offset for each harmonic and compares it to the predicted offsets for a standing, mixed and progressive wave.

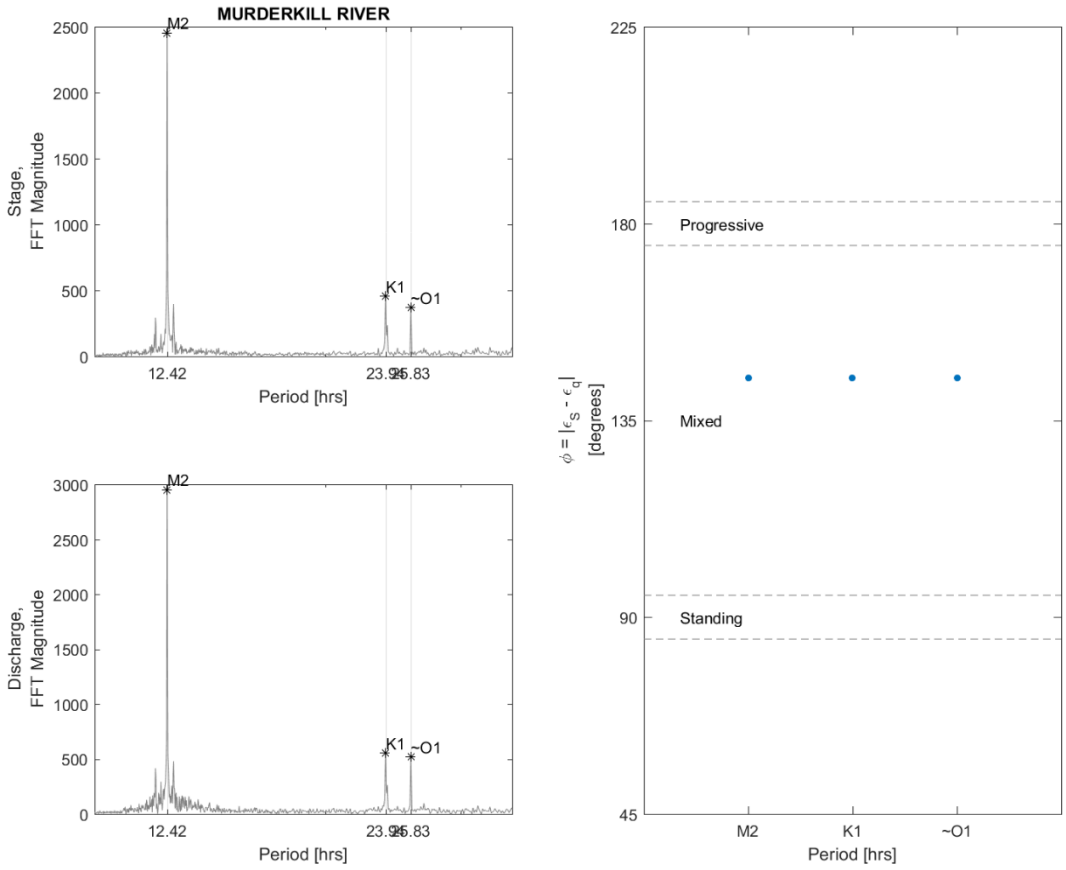

Figure H.12: The phase analysis for USGS site on the Murderkill River [site number: 01484085]. The two subfigures (one atop the other) on the left-hand side of this figure show the FFT magnitudes of the stage (left-top) and discharge (left-bottom) for the identified semidiurnal and diurnal harmonics analyzed for phase offset. The right-hand figure shows the calculated phase offset for each harmonic and compares it to the predicted offsets for a standing, mixed and progressive wave.

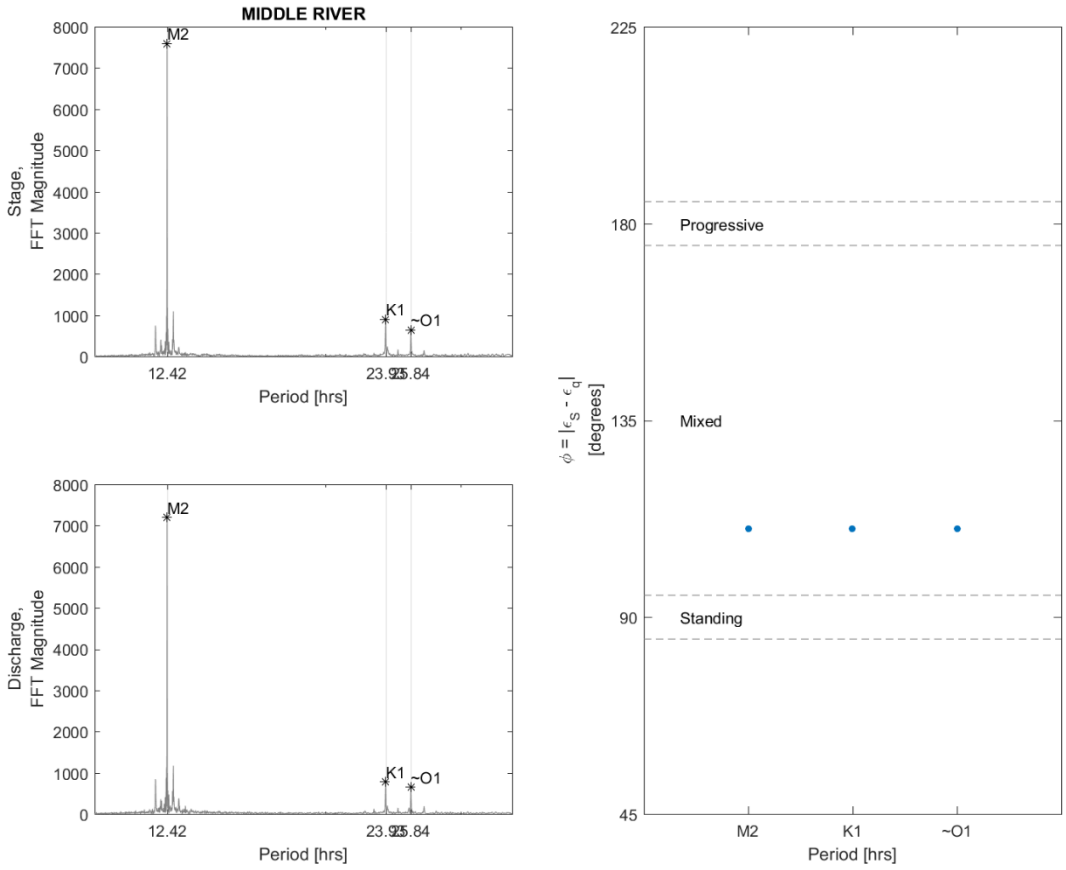

Figure H.13: The phase analysis for USGS site on the Middle River [site number: 02198950]. The two subfigures (one atop the other) on the left-hand side of this figure show the FFT magnitudes of the stage (left-top) and discharge (left-bottom) for the identified semidiurnal and diurnal harmonics analyzed for phase offset. The right-hand figure shows the calculated phase offset for each harmonic and compares it to the predicted offsets for a standing, mixed and progressive wave.

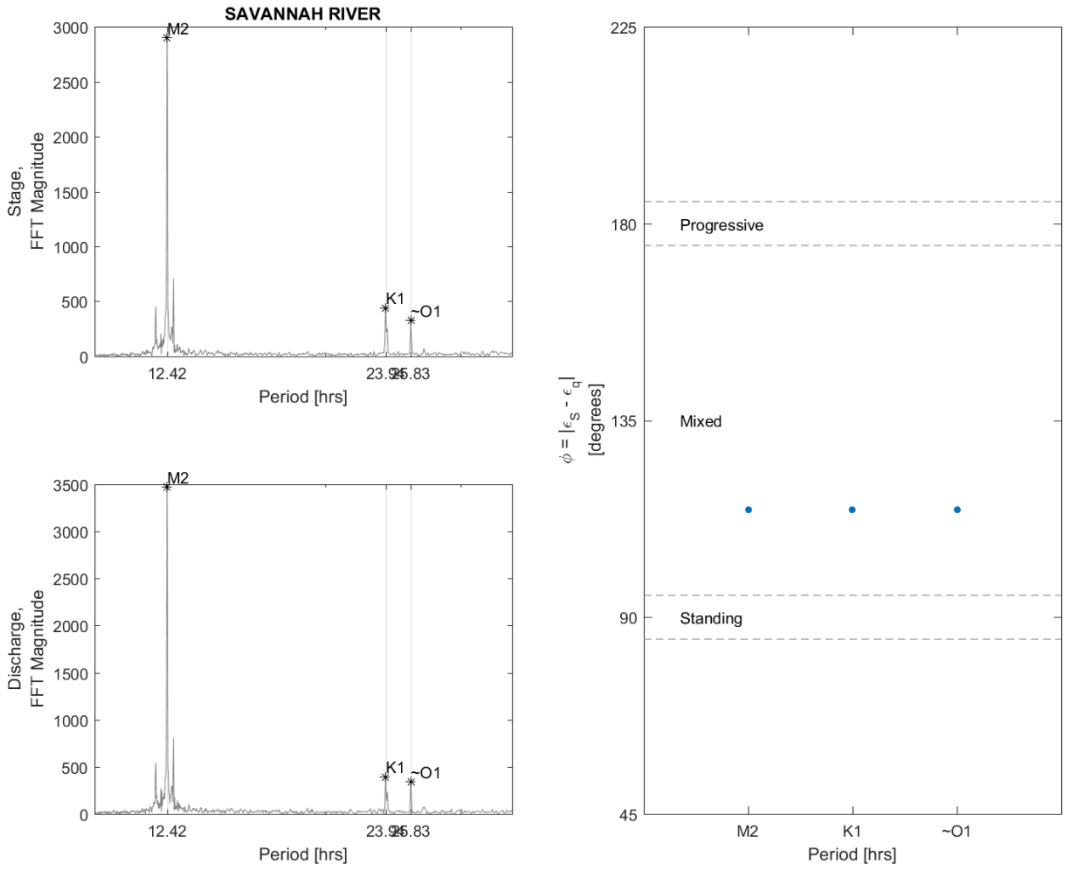

Figure H.14: The phase analysis for USGS site on the Savannah River [site number: 02198980]. The two subfigures (one atop the other) on the left-hand side of this figure show the FFT magnitudes of the stage (left-top) and discharge (left-bottom) for the identified semidiurnal and diurnal harmonics analyzed for phase offset. The right-hand figure shows the calculated phase offset for each harmonic and compares it to the predicted offsets for a standing, mixed and progressive wave.

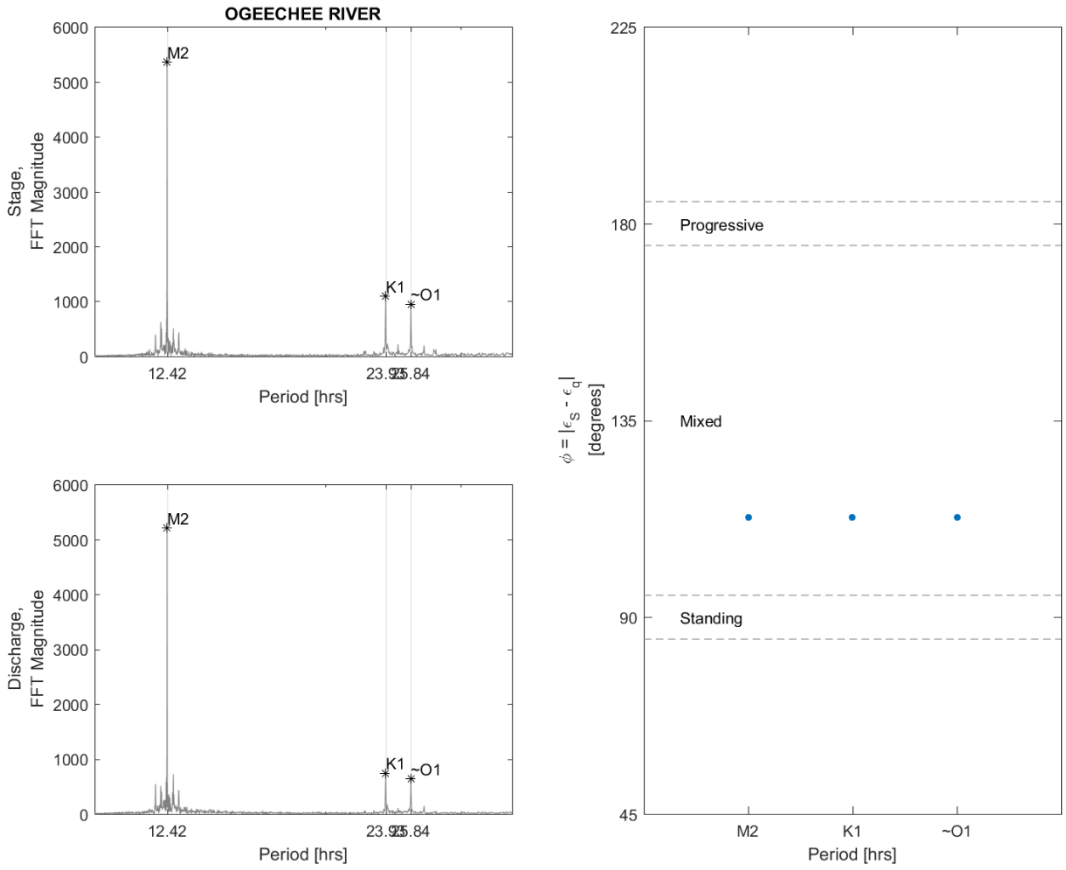

Figure H.15: The phase analysis for USGS site on the Ogeechee River [site number: 02203536]. The two subfigures (one atop the other) on the left-hand side of this figure show the FFT magnitudes of the stage (left-top) and discharge (left-bottom) for the identified semidiurnal and diurnal harmonics analyzed for phase offset. The right-hand figure shows the calculated phase offset for each harmonic and compares it to the predicted offsets for a standing, mixed and progressive wave.

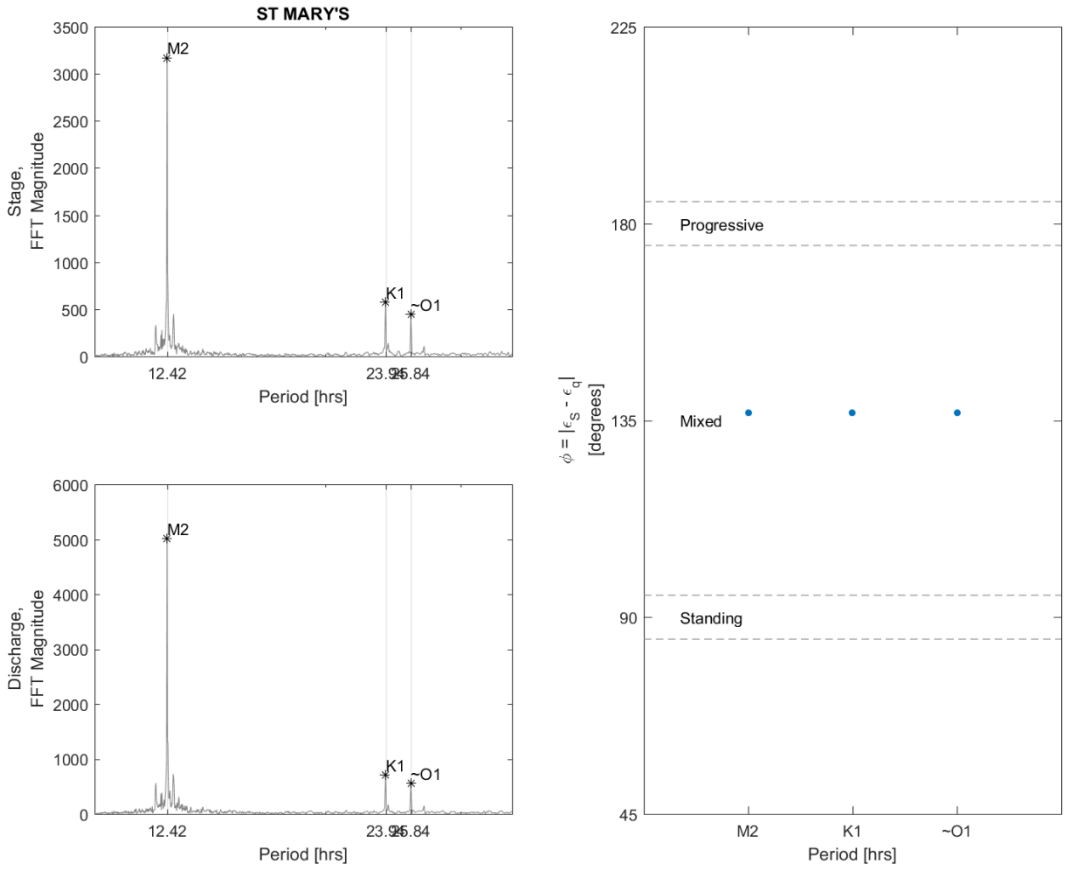

Figure H.16: The phase analysis for USGS site on the St. Mary's River [site number: 02231254]. The two subfigures (one atop the other) on the left-hand side of this figure show the FFT magnitudes of the stage (left-top) and discharge (left-bottom) for the identified semidiurnal and diurnal harmonics analyzed for phase offset. The right-hand figure shows the calculated phase offset for each harmonic and compares it to the predicted offsets for a standing, mixed and progressive wave.

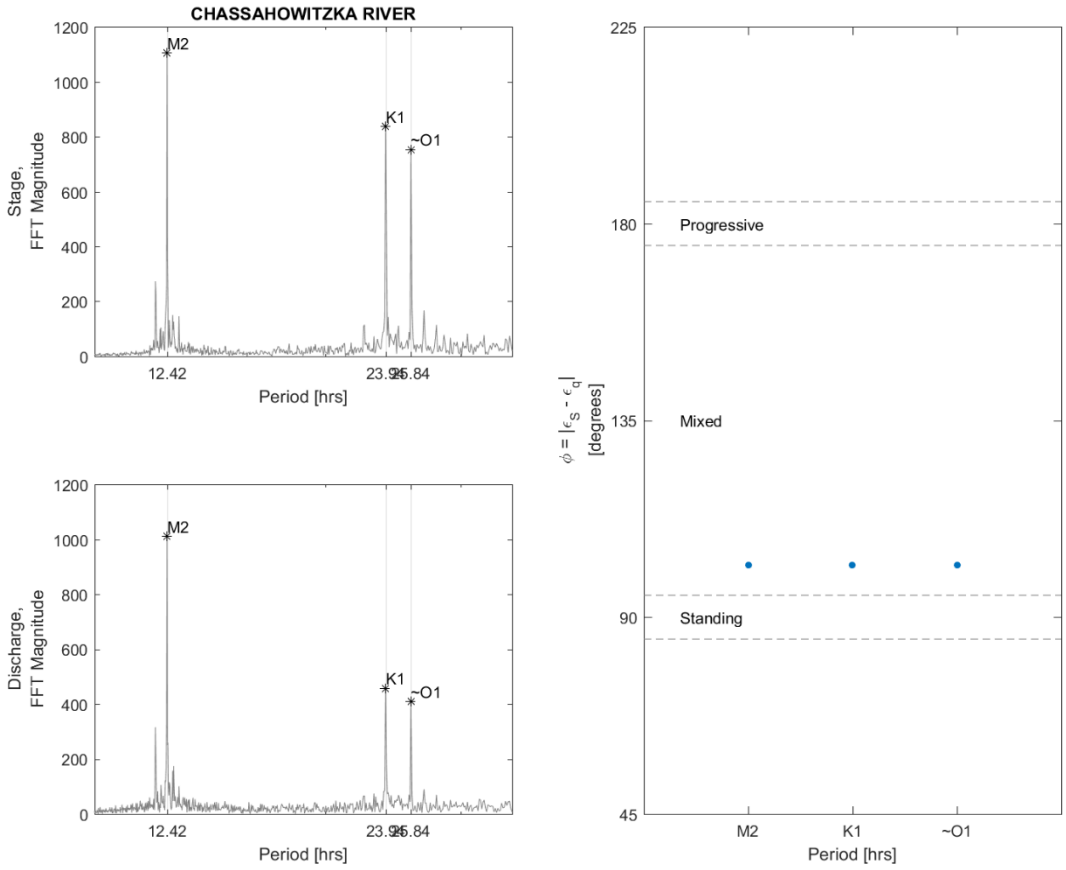

Figure H.17: The phase analysis for USGS site on the Chassahowitzka River [site number: 02310663]. The two subfigures (one atop the other) on the left-hand side of this figure show the FFT magnitudes of the stage (left-top) and discharge (left-bottom) for the identified semidiurnal and diurnal harmonics analyzed for phase offset. The right-hand figure shows the calculated phase offset for each harmonic and compares it to the predicted offsets for a standing, mixed and progressive wave.

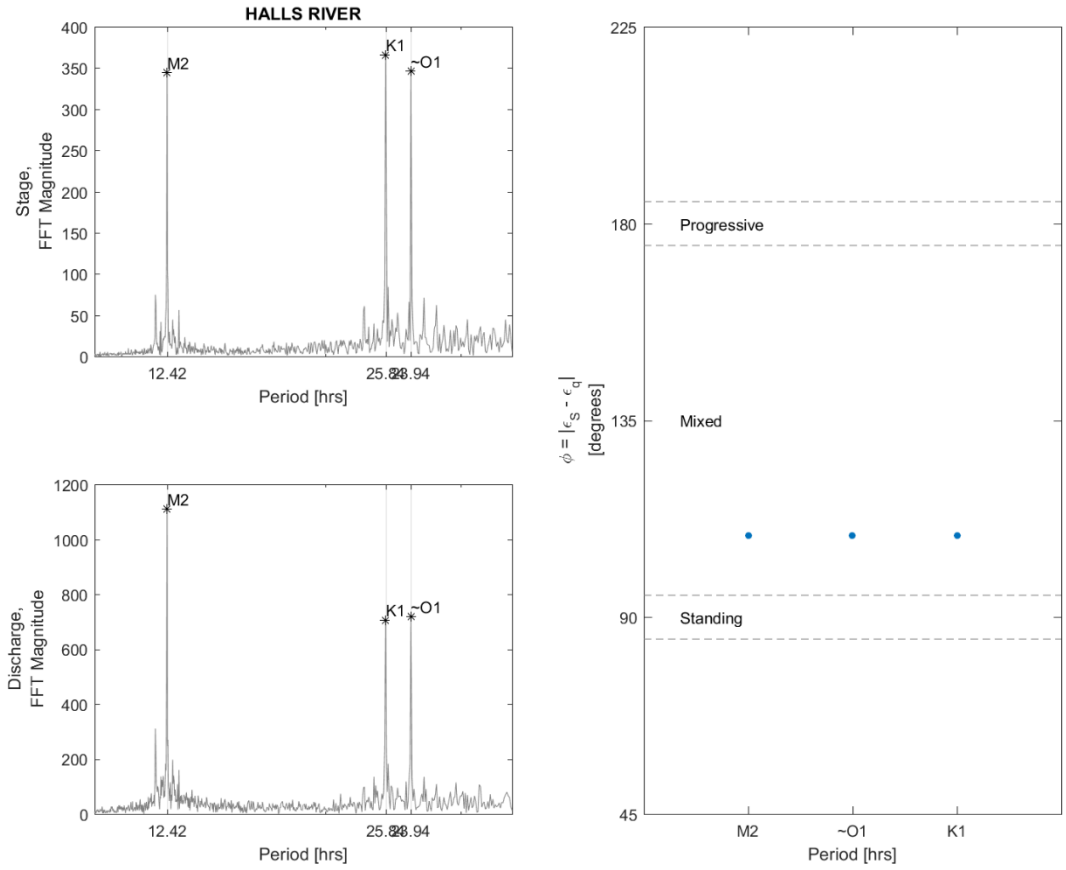

Figure H.18: The phase analysis for USGS site on the Halls River [site number: 02310689]. The two subfigures (one atop the other) on the left-hand side of this figure show the FFT magnitudes of the stage (left-top) and discharge (left-bottom) for the identified semidiurnal and diurnal harmonics analyzed for phase offset. The right-hand figure shows the calculated phase offset for each harmonic and compares it to the predicted offsets for a standing, mixed and progressive wave.

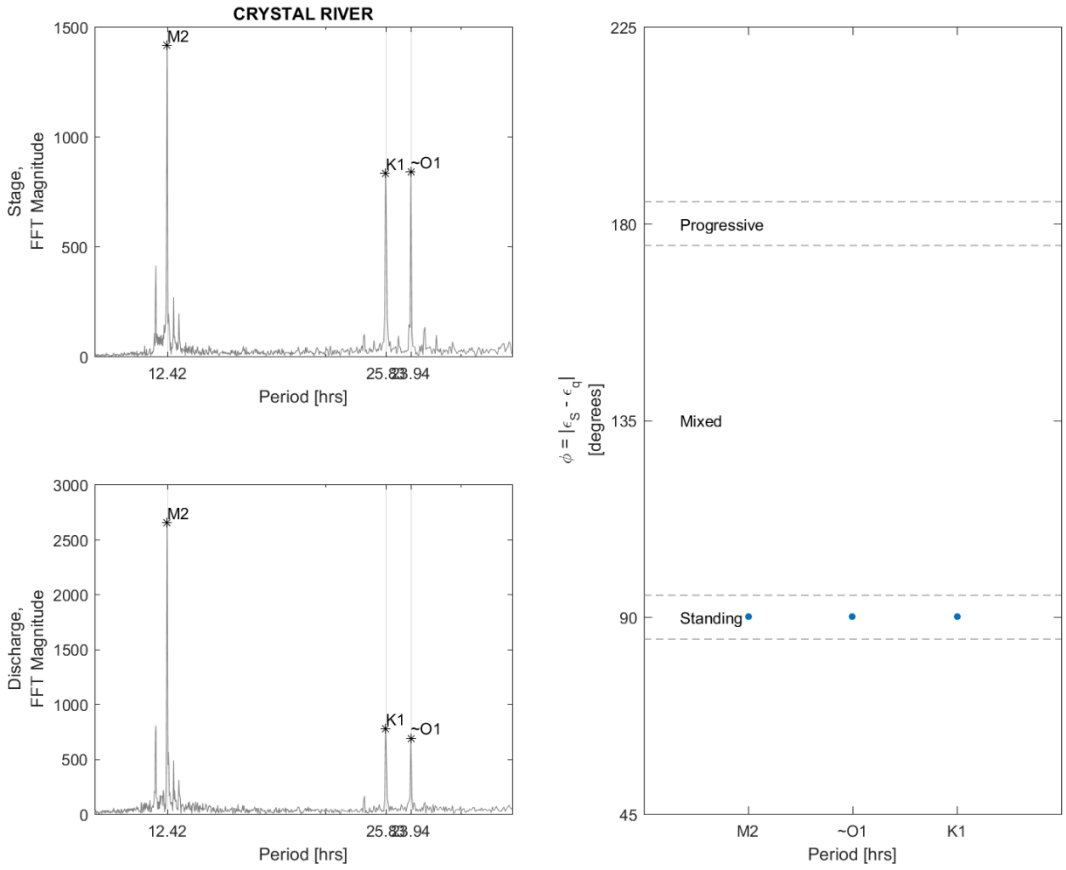

Figure H.19: The phase analysis for USGS site on the Crystal River [site number: 02310747]. The two subfigures (one atop the other) on the left-hand side of this figure show the FFT magnitudes of the stage (left-top) and discharge (left-bottom) for the identified semidiurnal and diurnal harmonics analyzed for phase offset. The right-hand figure shows the calculated phase offset for each harmonic and compares it to the predicted offsets for a standing, mixed and progressive wave.

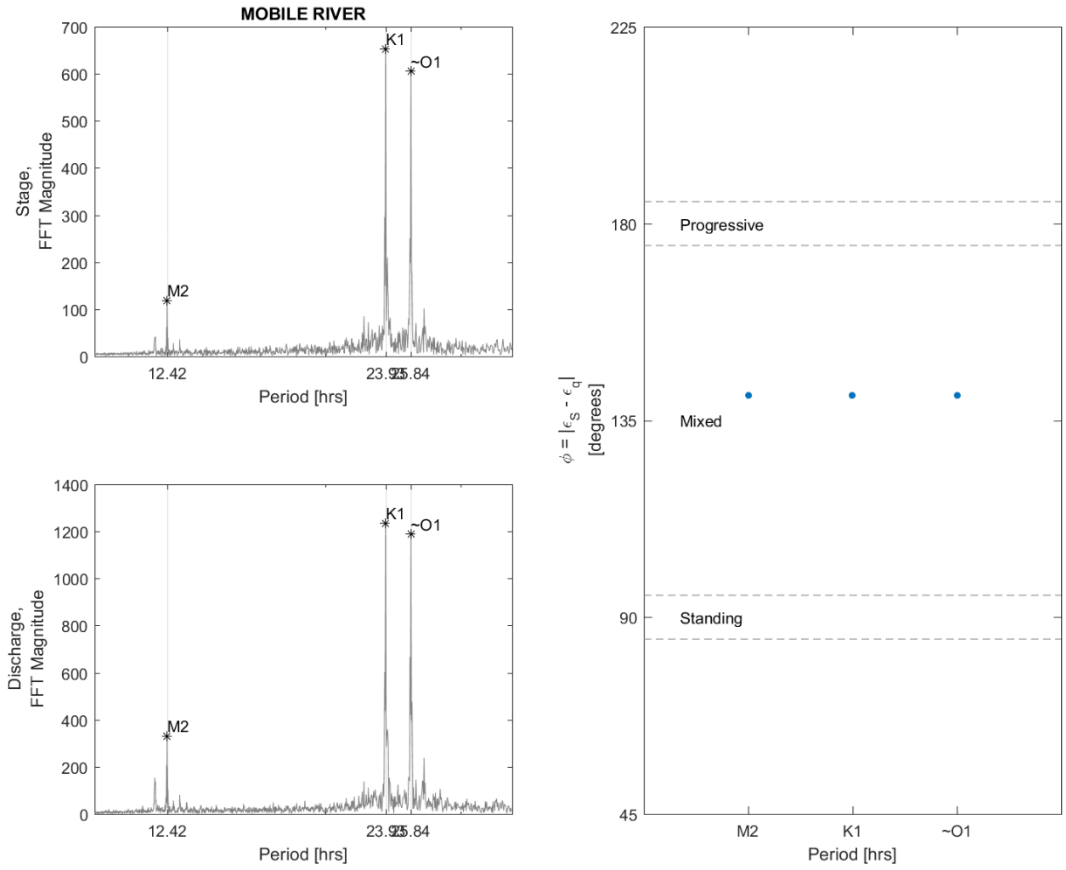

Figure H.20: The phase analysis for USGS site on the Mobile River [site number: 02470629]. The two subfigures (one atop the other) on the left-hand side of this figure show the FFT magnitudes of the stage (left-top) and discharge (left-bottom) for the identified semidiurnal and diurnal harmonics analyzed for phase offset. The right-hand figure shows the calculated phase offset for each harmonic and compares it to the predicted offsets for a standing, mixed and progressive wave.

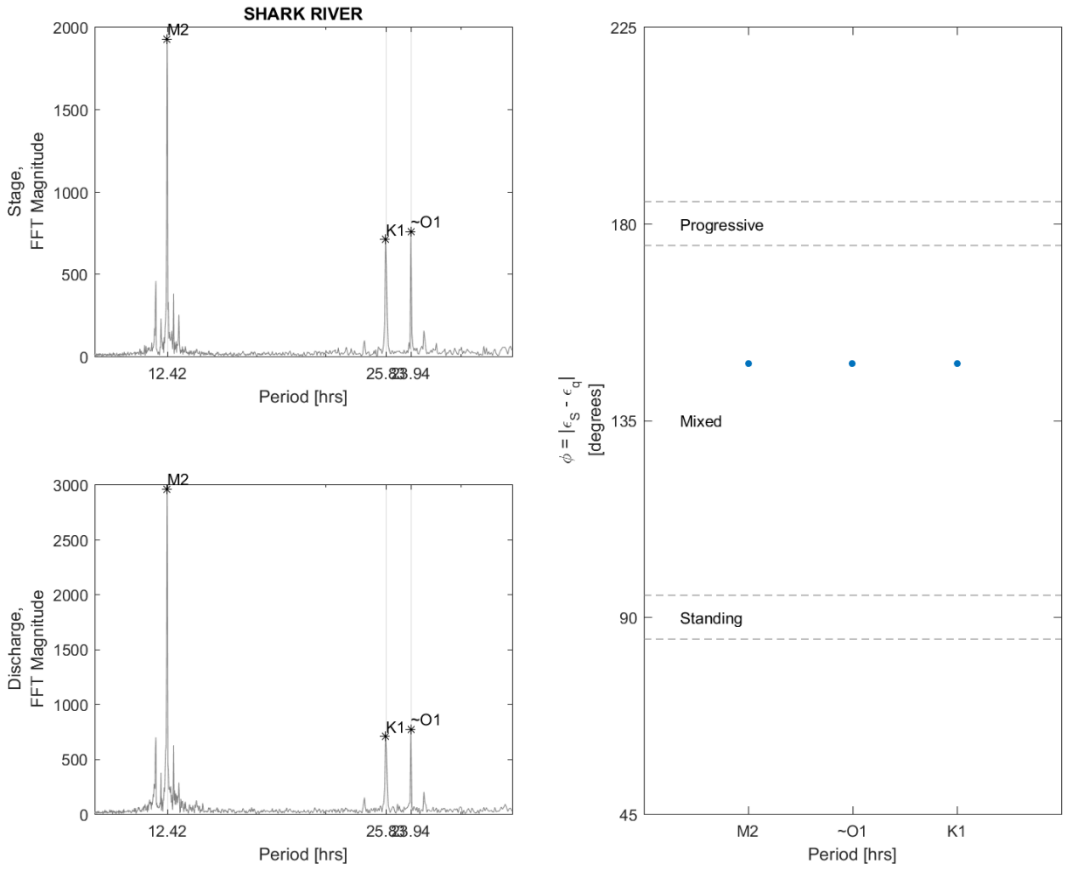

Figure H.21: The phase analysis for USGS site on the Shark River [site number: 252230081021300]. The two subfigures (one atop the other) on the left-hand side of this figure show the FFT magnitudes of the stage (left-top) and discharge (left-bottom) for the identified semidiurnal and diurnal harmonics analyzed for phase offset. The right-hand figure shows the calculated phase offset for each harmonic and compares it to the predicted offsets for a standing, mixed and progressive wave.

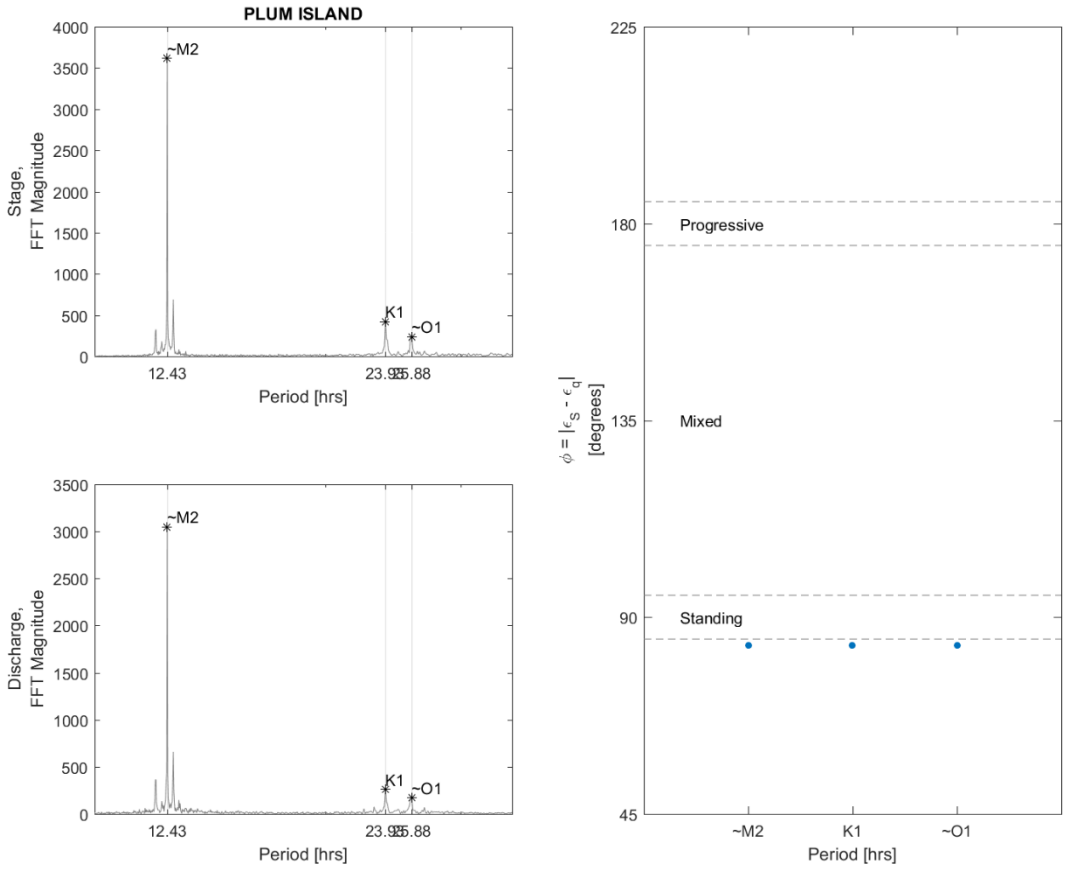

Figure H.22 The phase analysis for USGS site on the Plum Island River [site number: 424752070491701]. The two subfigures (one atop the other) on the left-hand side of this figure show the FFT magnitudes of the stage (left-top) and discharge (left-bottom) for the identified semidiurnal and diurnal harmonics analyzed for phase offset. The right-hand figure shows the calculated phase offset for each harmonic and compares it to the predicted offsets for a standing, mixed and progressive wave.

Appendix J: M-A and USGS site regression plots

Appendix "I" was purposefully skipped to eliminate confusion between the letter "I" and the Roman Numeral one.

The following figures are provide a visual representation of the best linear model of equation (3) fit to each M-A site and the four USGS sites. The exact value of the coefficients, k_1-k_4, are listed in Table 4.2. For those sites with a coefficient(s) that were not significantly different than zero, the equation within the figure title will not include that variable. For example, the title of Figure J.1 does not include a *dldt^2* (referring to the $(\frac{dS}{dt})^2$ variable), because, as is seen in Table 4.2, k_1 for site A1 is not significantly different from zero.

To clarify, the title equations will use the terms *dldt* and *dldt^2* to represent $\frac{dS}{dt}$ and $(\frac{dS}{dt})^2$, respectively. The terms *dldt* and *dldt^2* are the names of the variables within the Matlab script. They still represent observations of $\frac{dS}{dt}$ over time.

These figures are the results of plotting the raw output from the Matlab *fitlm* function. The *adjusted* term in each axis refers to a averaging function performed by the *plot* function when utilizing the out *fitlm* function's output. From the *Adjusted Response Plot* documentation page, "[t]he adjusted response plot shows the fitted response as a function of var, with the other predictors averaged out by averaging the fitted values over the data used in the fit. Adjusted data points are computed by adding the residual to the adjusted fitted value for each observation."

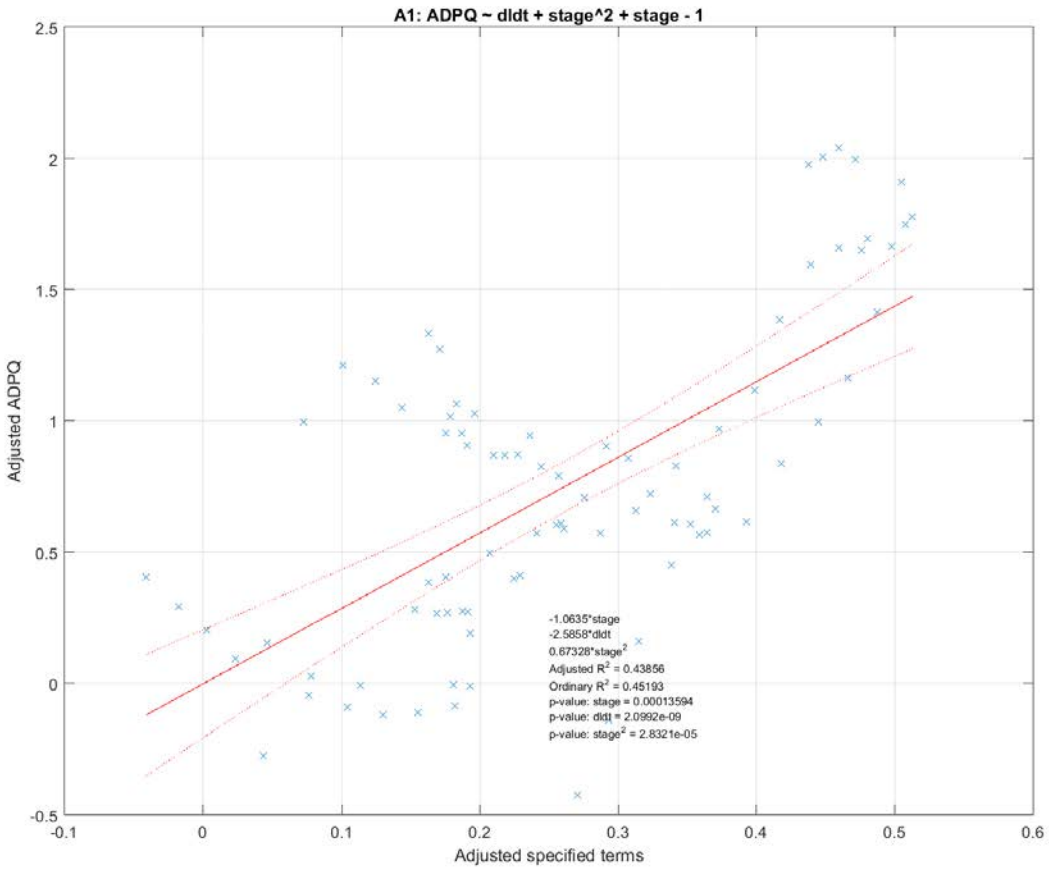

Figure J.1: The linear regression data for site A1.

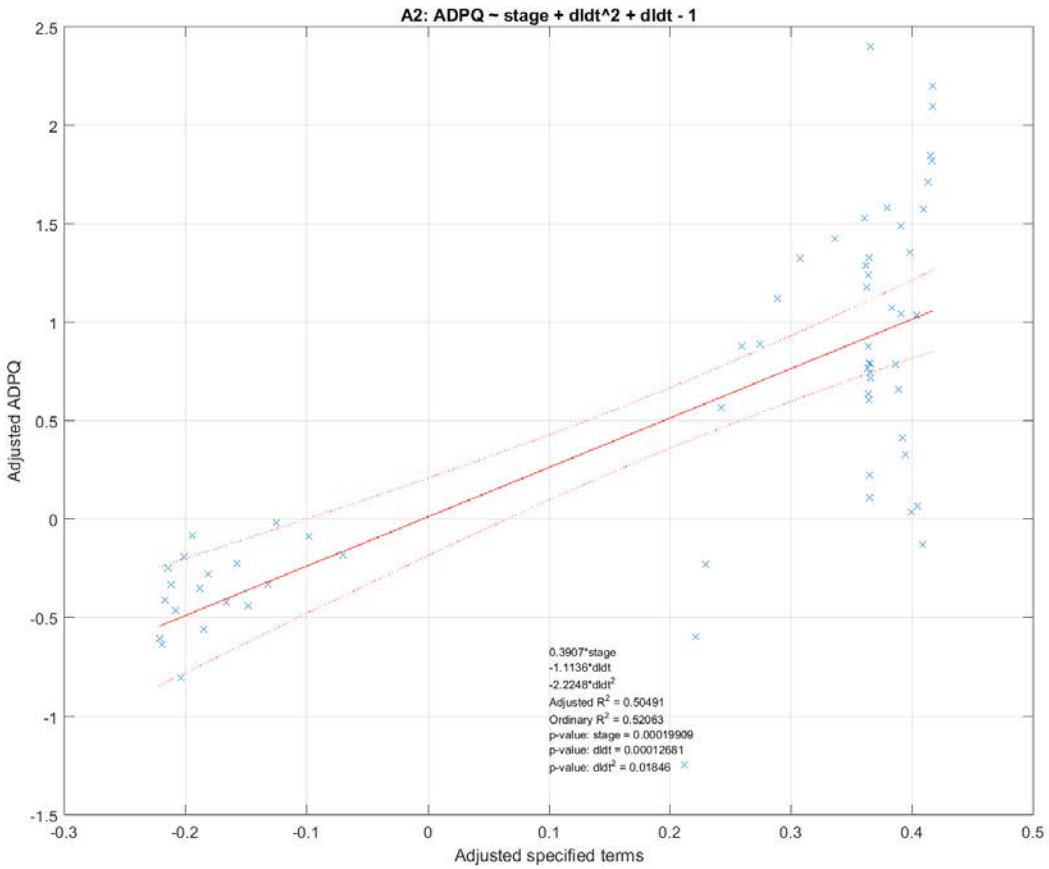

Figure J.2: The linear regression data for site A2.

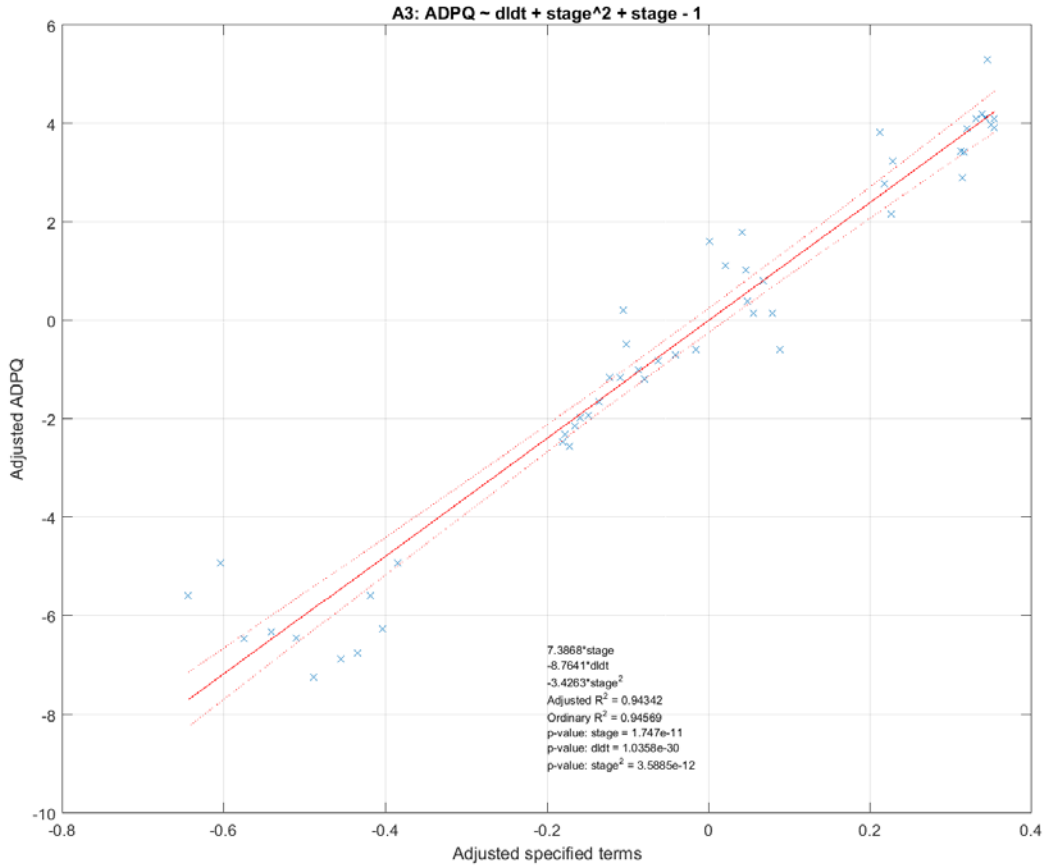

Figure J.3: The linear regression data for site A3.

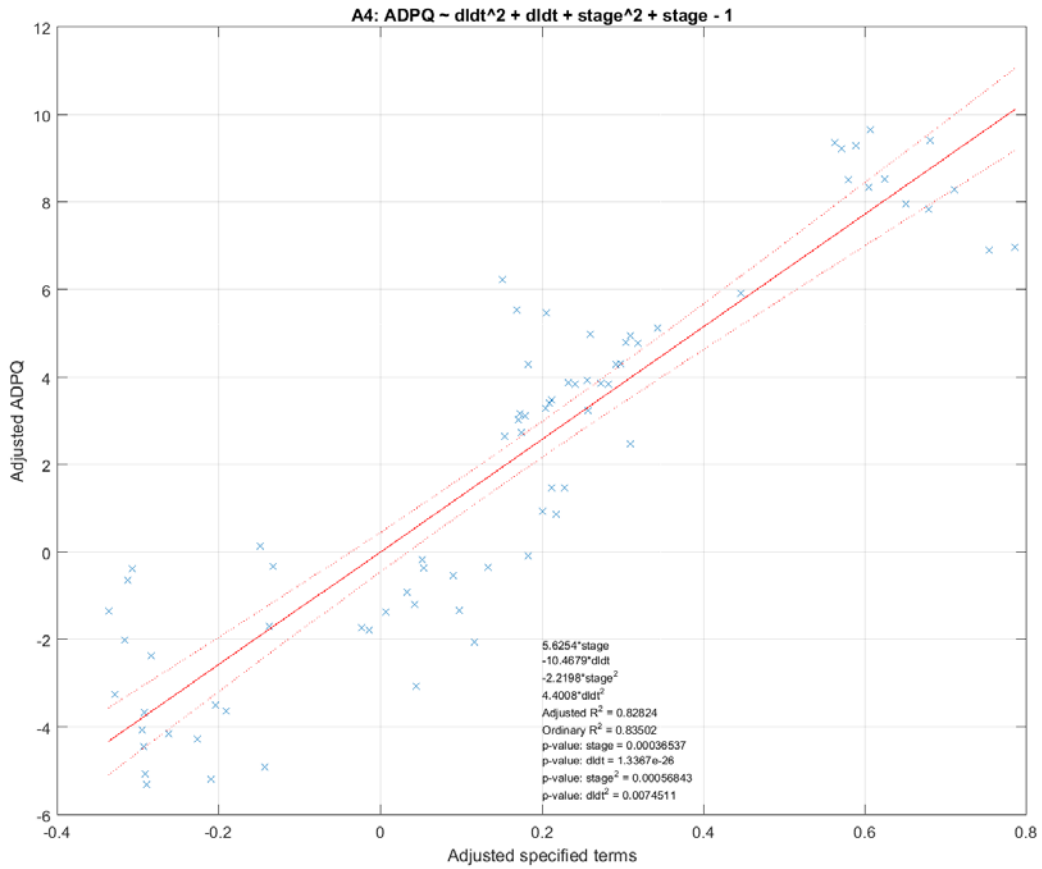

Figure J.4: The linear regression data for site A4.

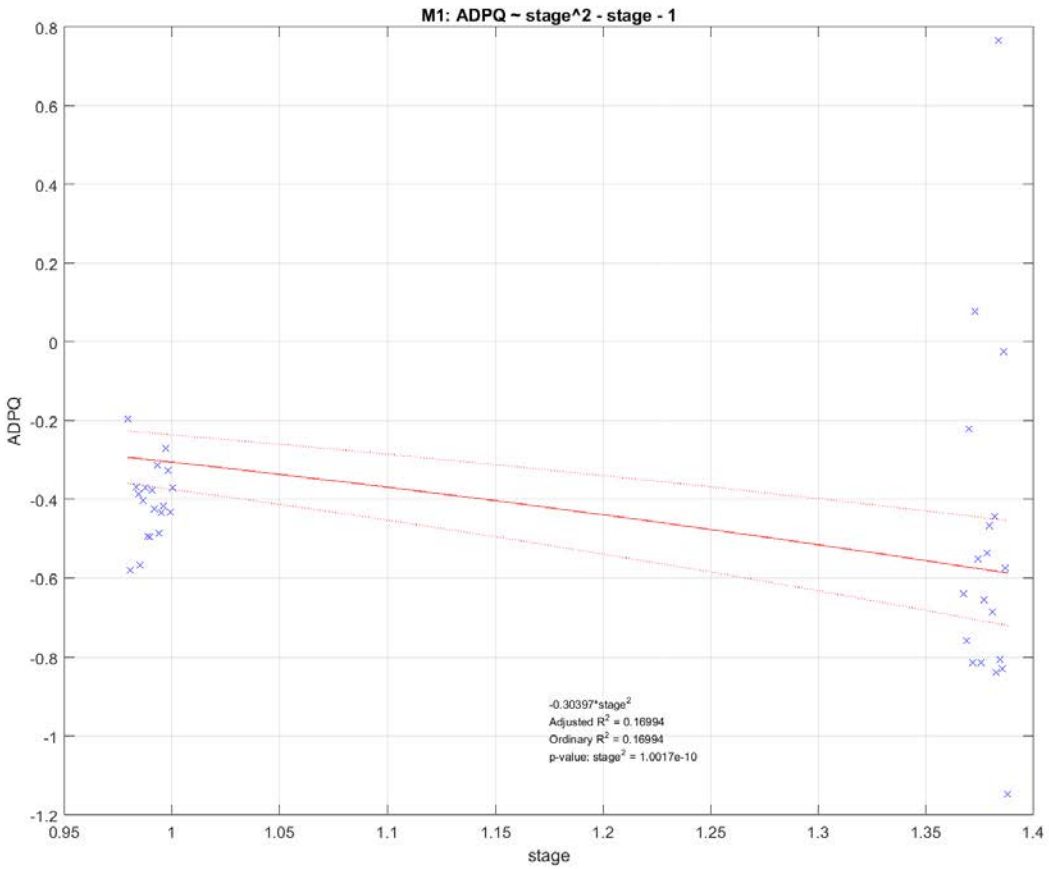

Figure J.5: The linear regression data for site M1.

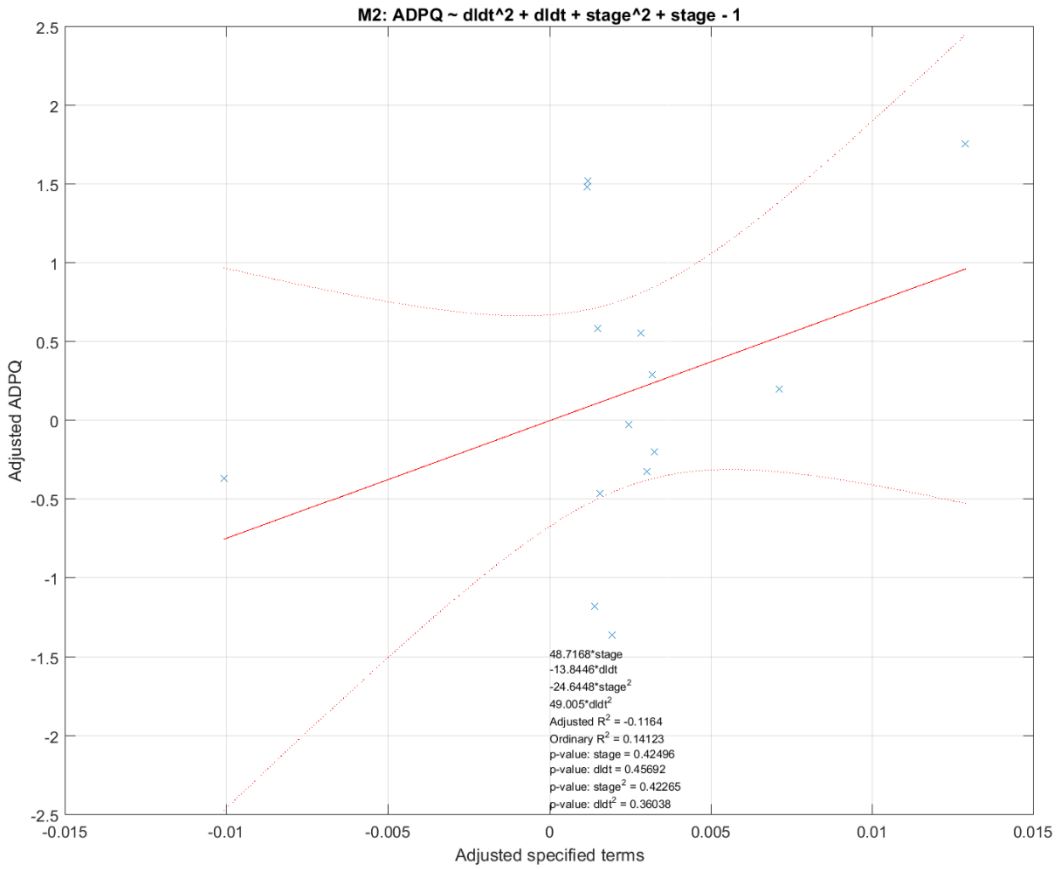

Figure J.6: The linear regression data for site M2. Because this linear regression produced an r^2 less than 0, these results were not included in Chapter 4. The poor nature of this fit is likely due to limited ADP observations and installation data. Evidence suggests that our installation was stolen.

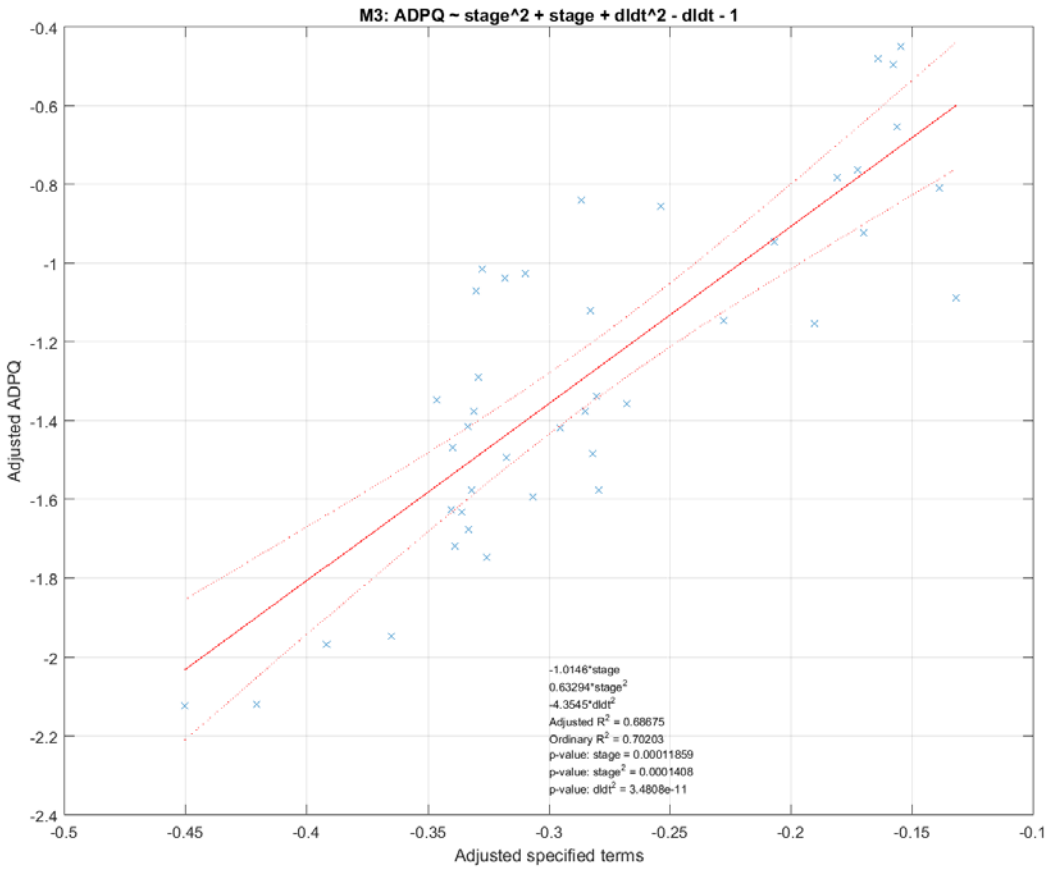

Figure J.7: The linear regression data for site M3.

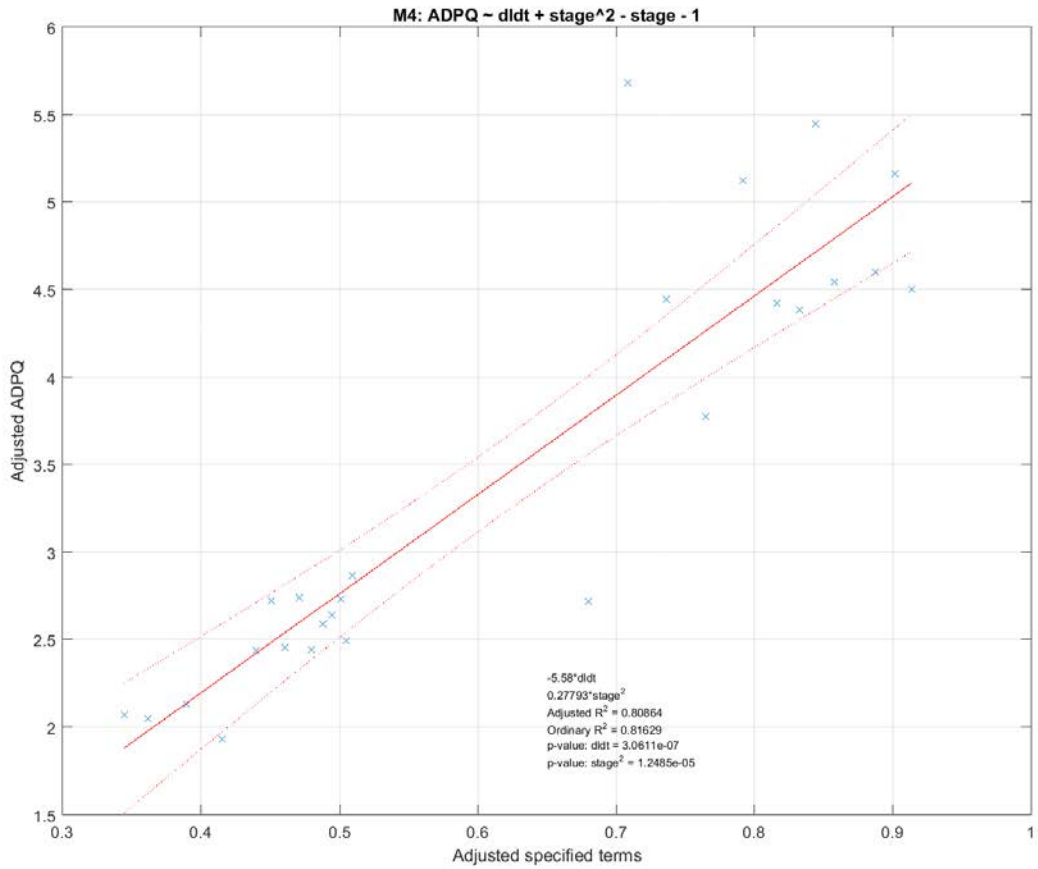

Figure J.8: The linear regression data for site M4.

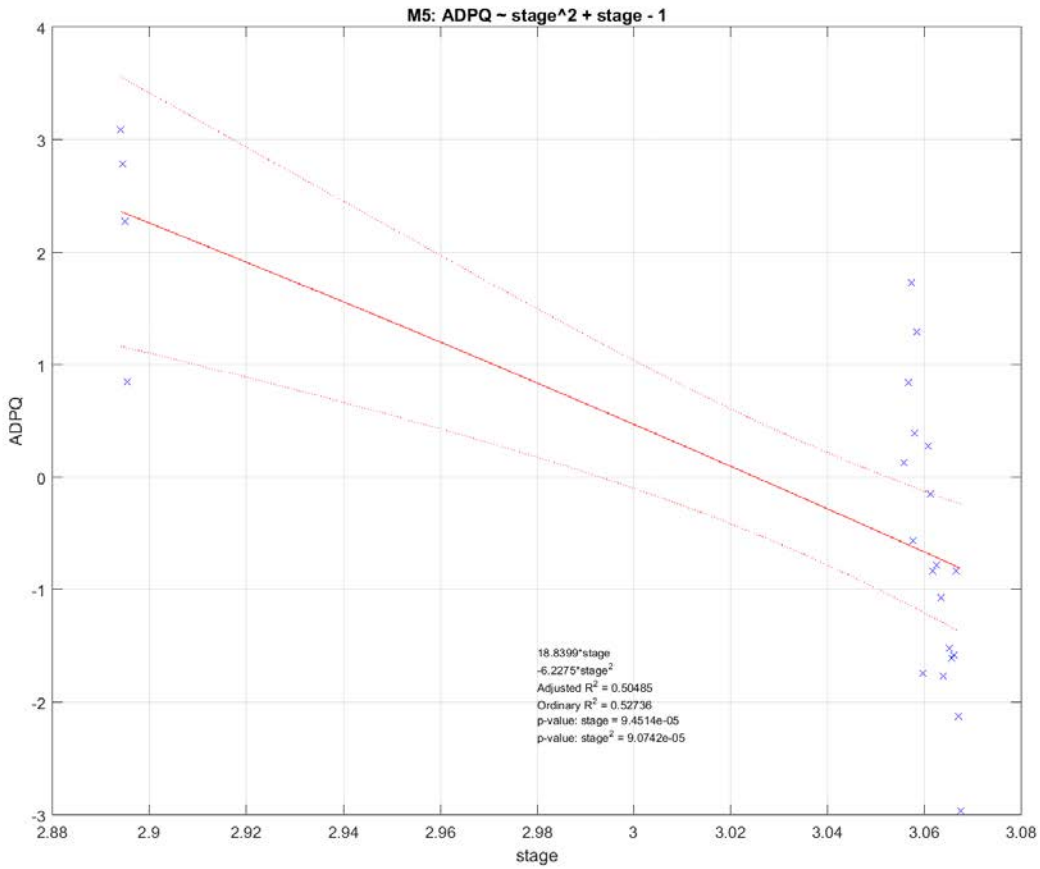

Figure J.9: The linear regression data for site M5.

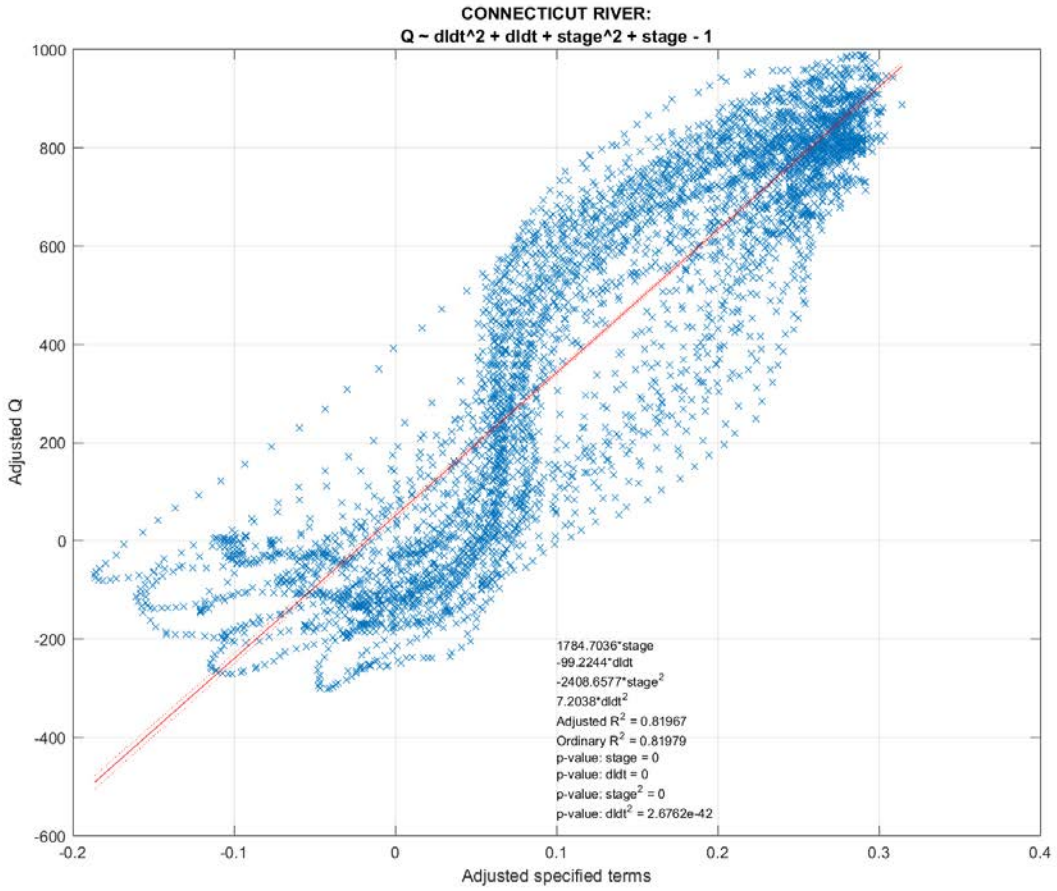

Figure J.10: The linear regression data for USGS site on the Connecticut River [site number: 01193050].

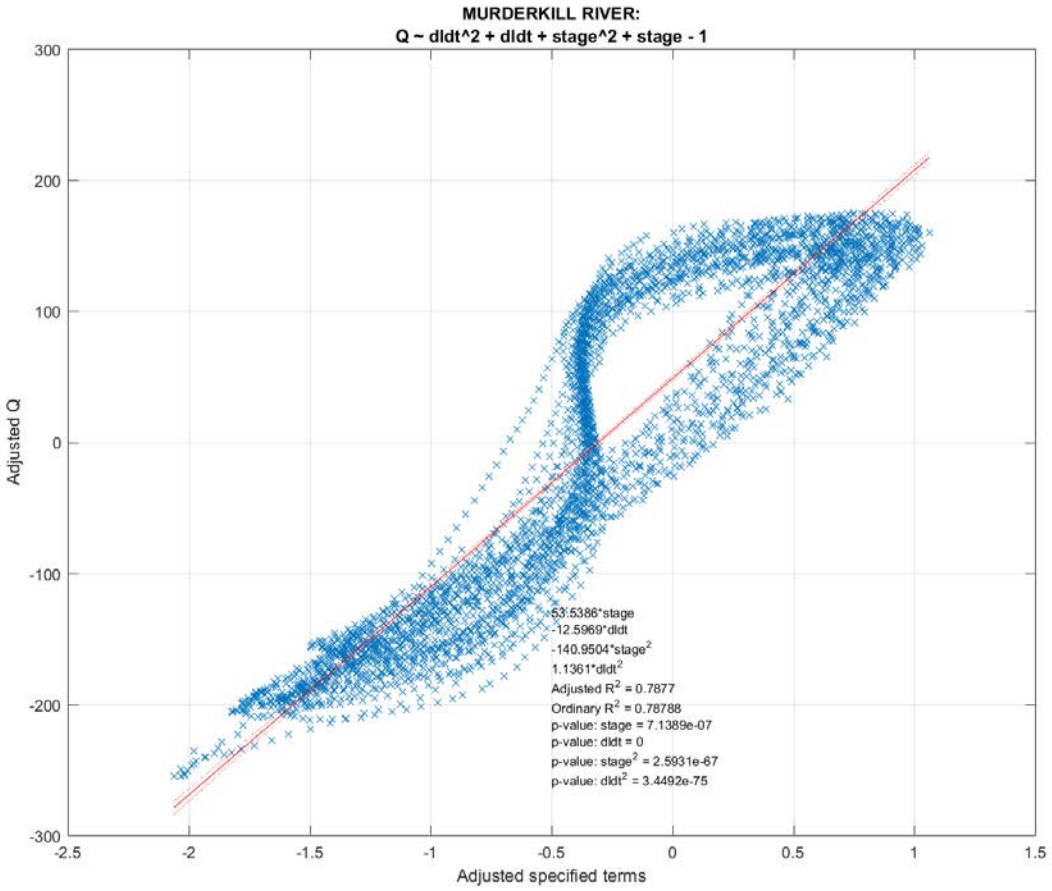

Figure J.11: The linear regression data for USGS site on the Murderkill River [site number: 01484085].

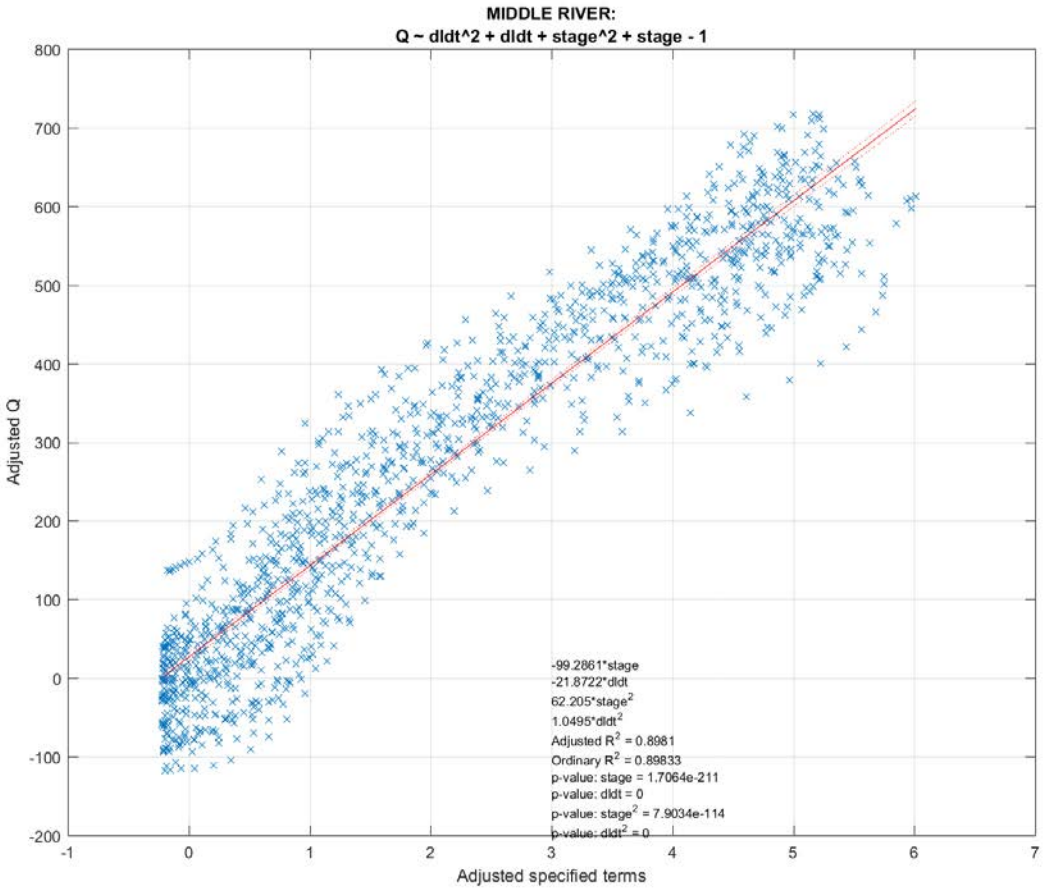

Figure J.12: The linear regression data for USGS site on the Middle River [site number: 02198950].

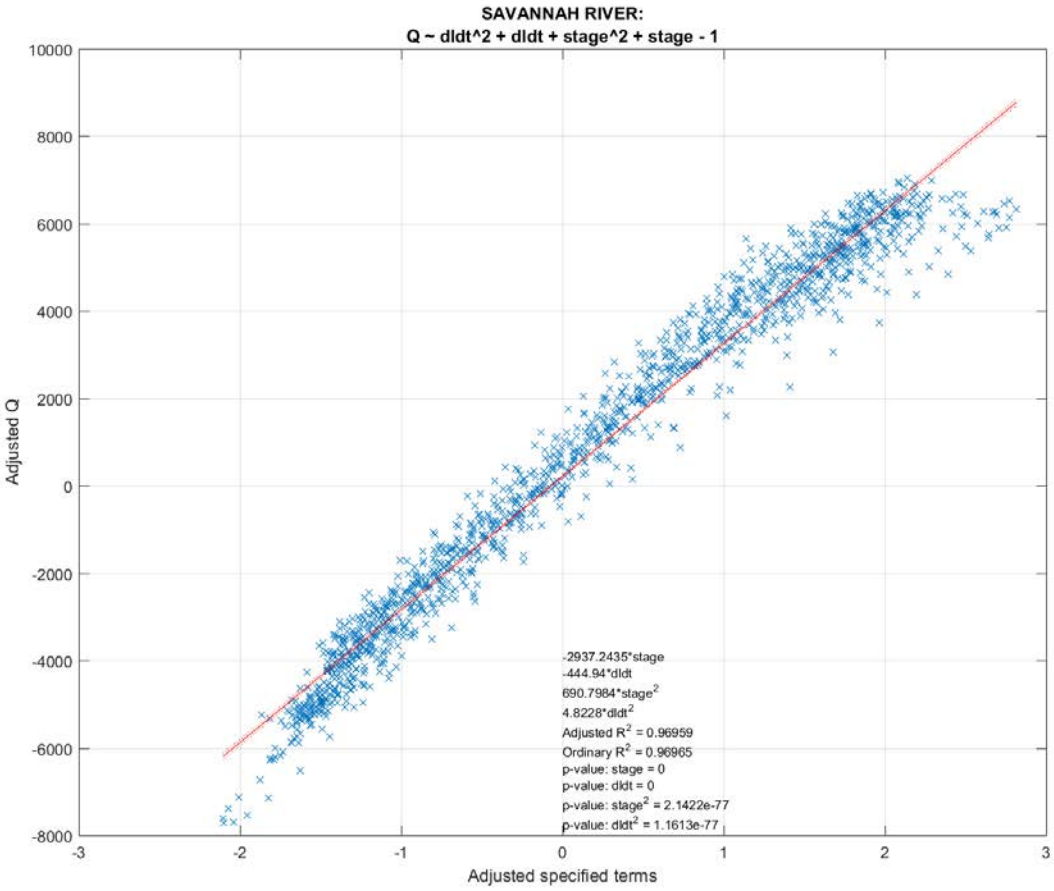

Figure J.13: The linear regression data for USGS site on the Savannah River [site number: 02198980].

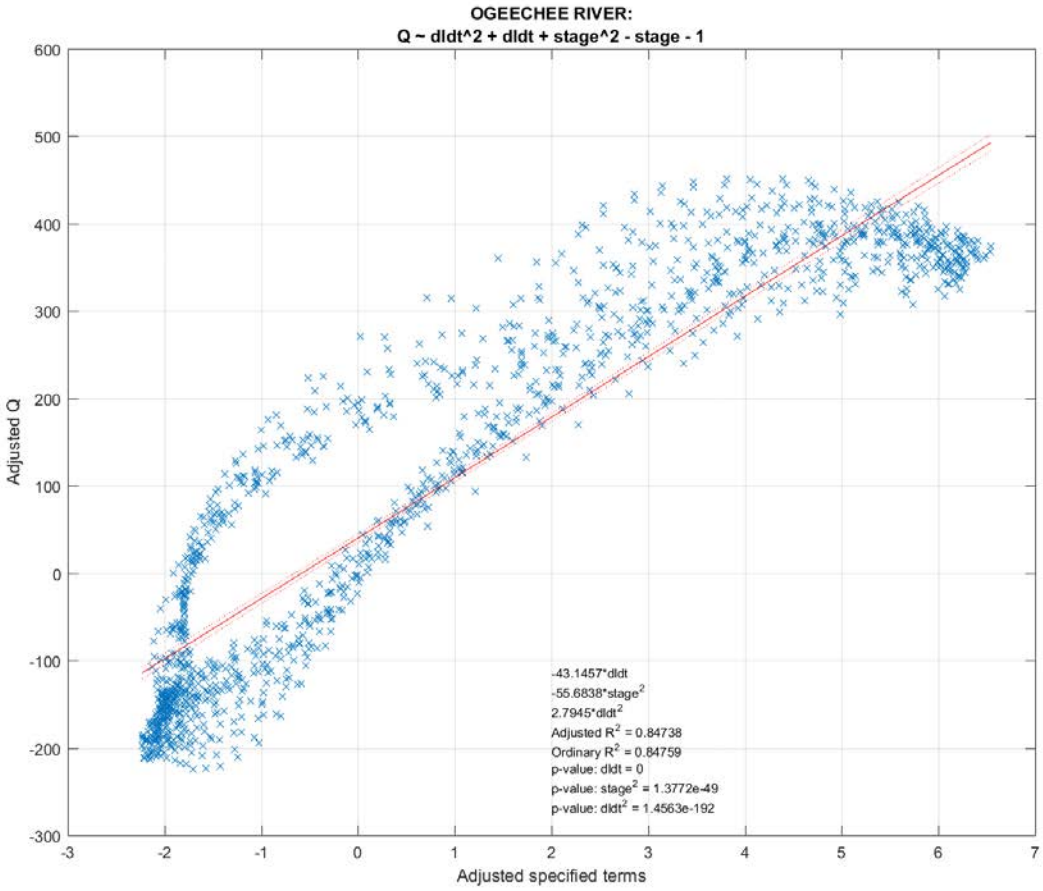

Figure J.14: The linear regression data for USGS site on the Ogeechee River [site number: 02203536].

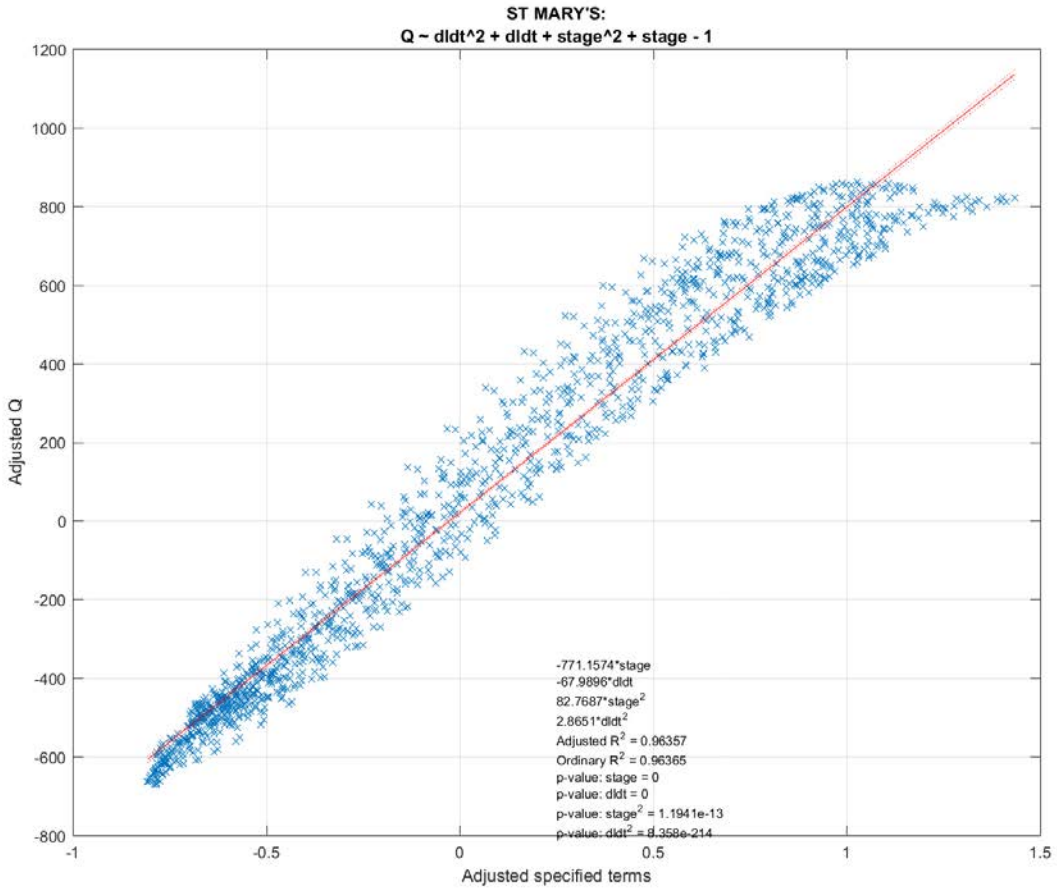

Figure J.15: The linear regression data for USGS site on the St. Mary's River [site number: 02231254].

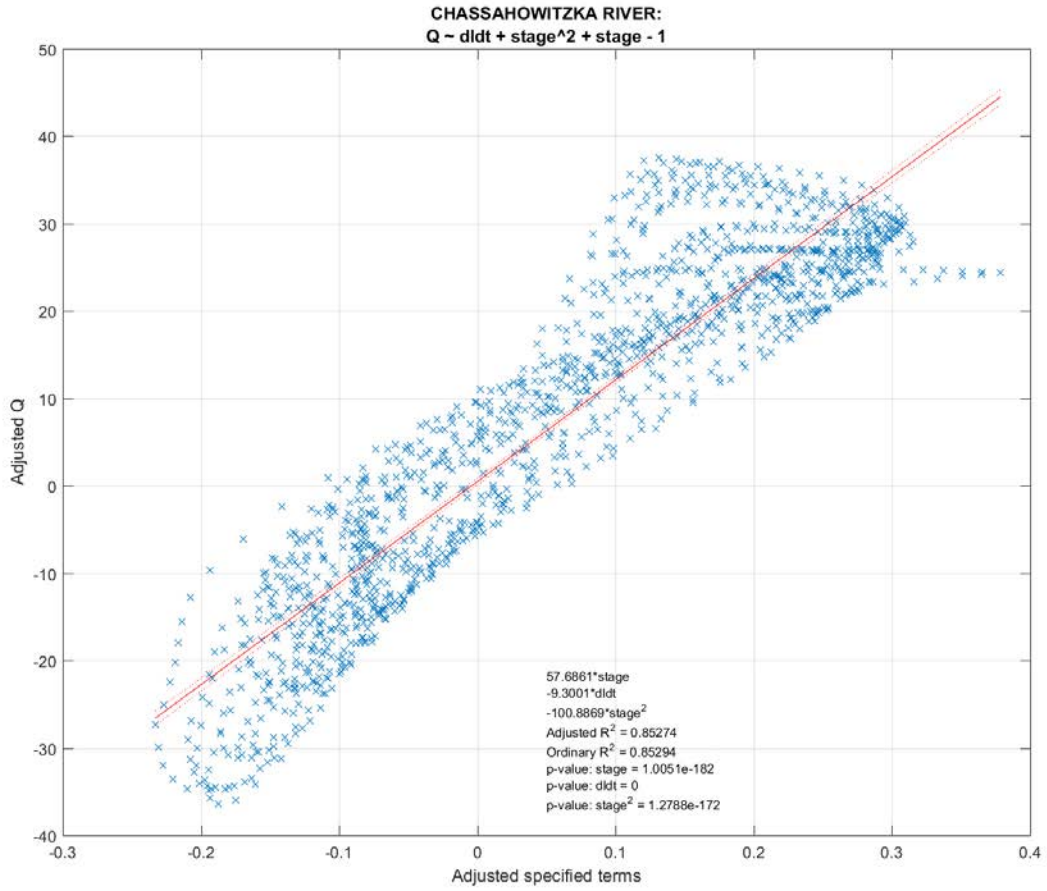

Figure J.16: The linear regression data for USGS site on the Chassahowitzka River [site number: 02310663].

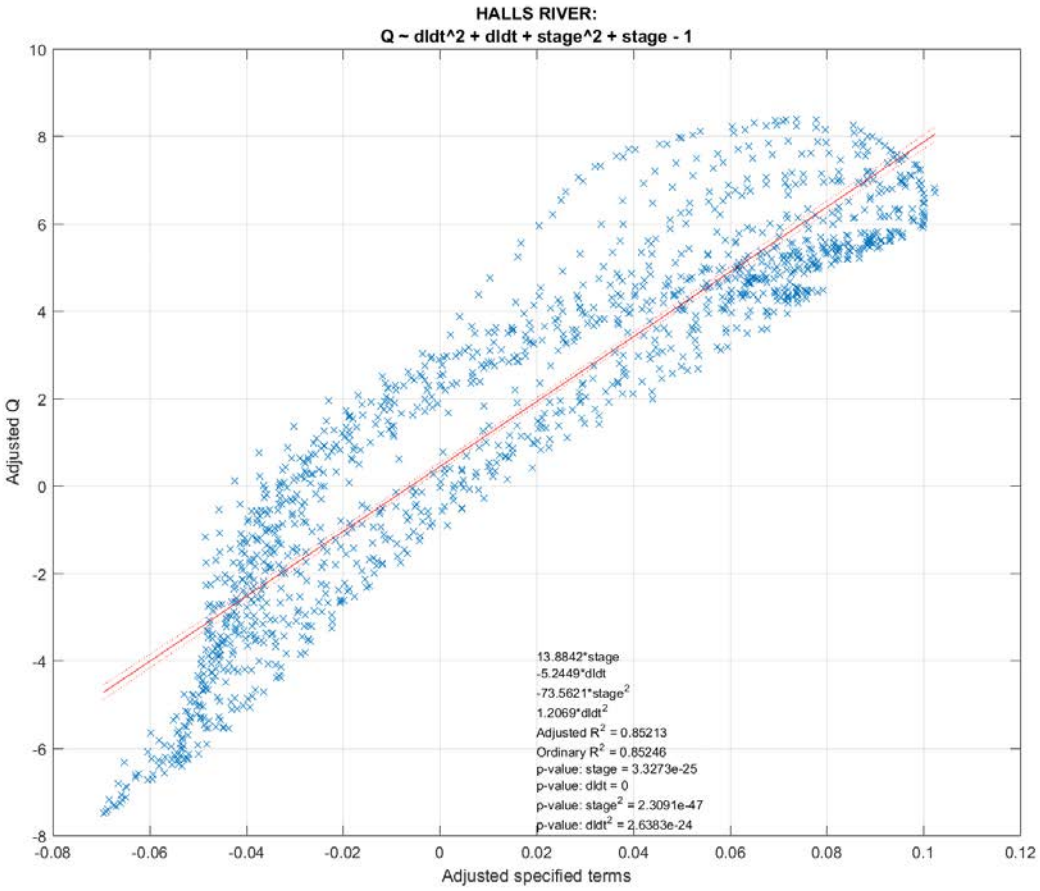

Figure J.17: The linear regression data for USGS site on the Halls River [site number: 02310689].

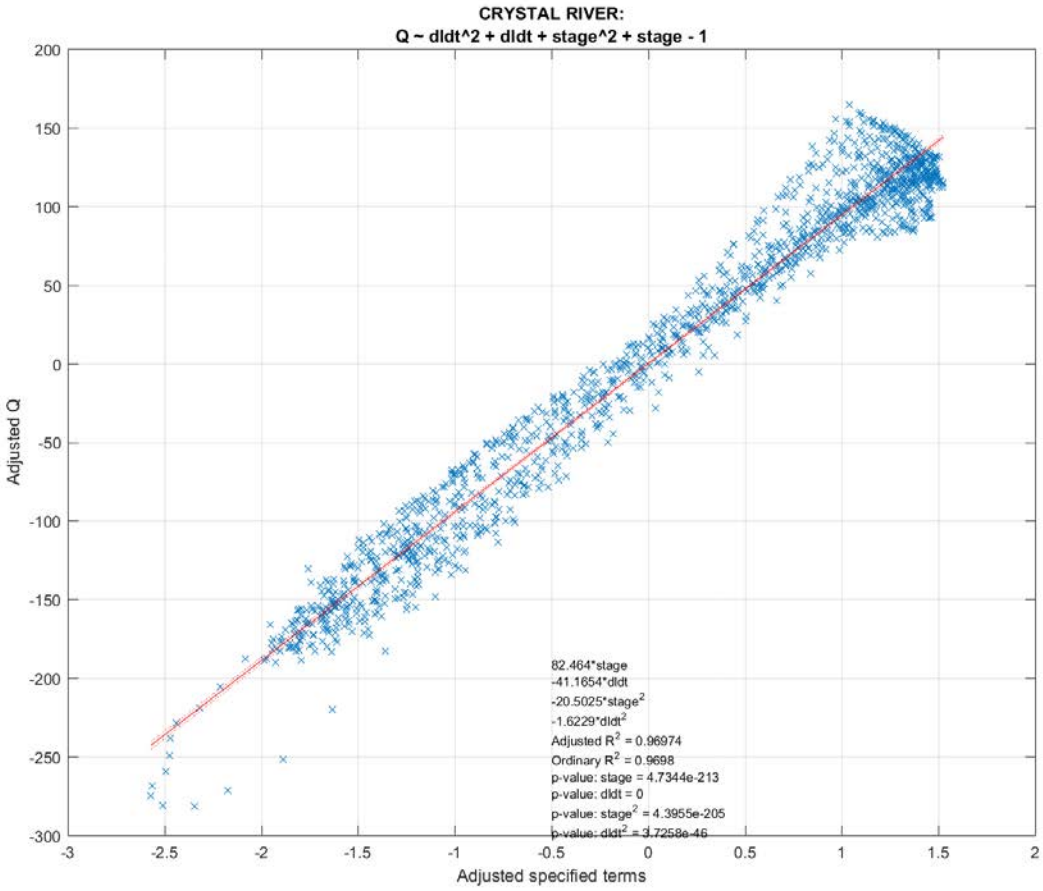

Figure J.18: The linear regression data for USGS site on the Crystal River [site number: 02310747].

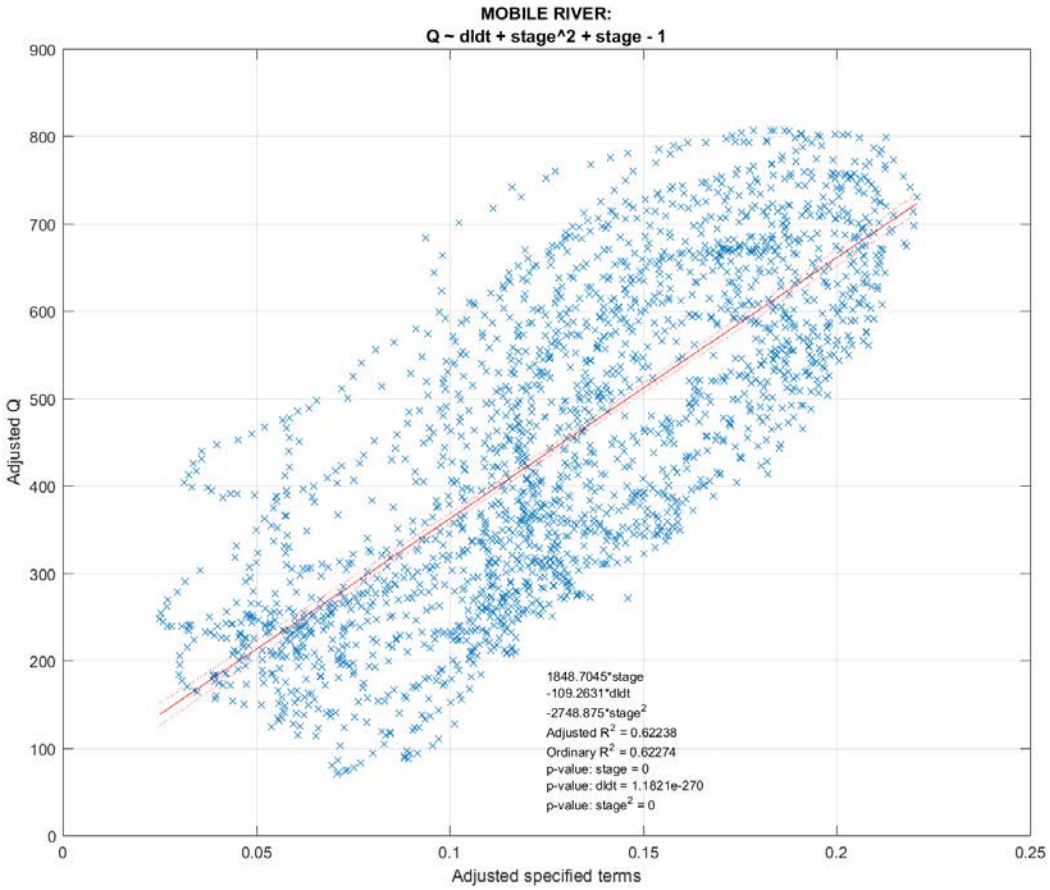

Figure J.19: The linear regression data for USGS site on the Mobile River [site number: 02470629].

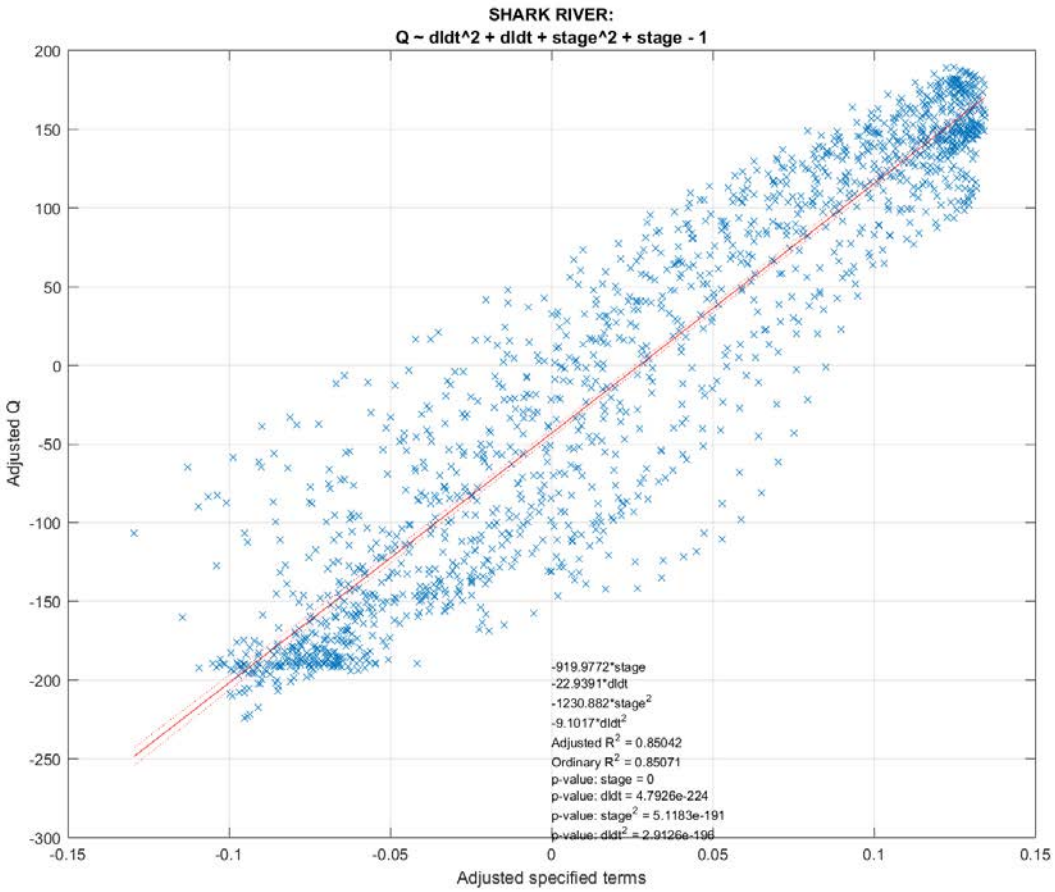

Figure J.20: The linear regression data for USGS site on the Shark River [site number: 252230081021300].

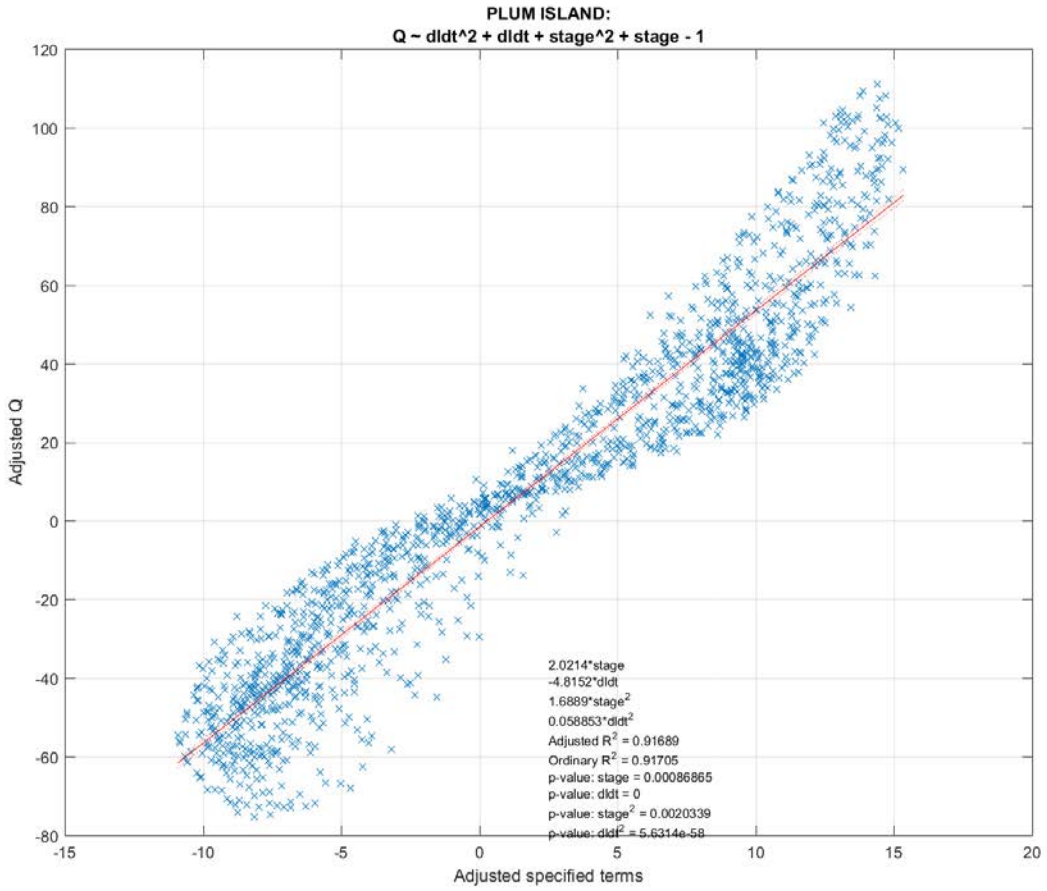

Figure J.21: The linear regression data for USGS site on the Shark River [site number: 424752070491701].

Appendix K: M-A discharge time series from tidal rating curve

The following are the calculated discharge time series for each M-A site.

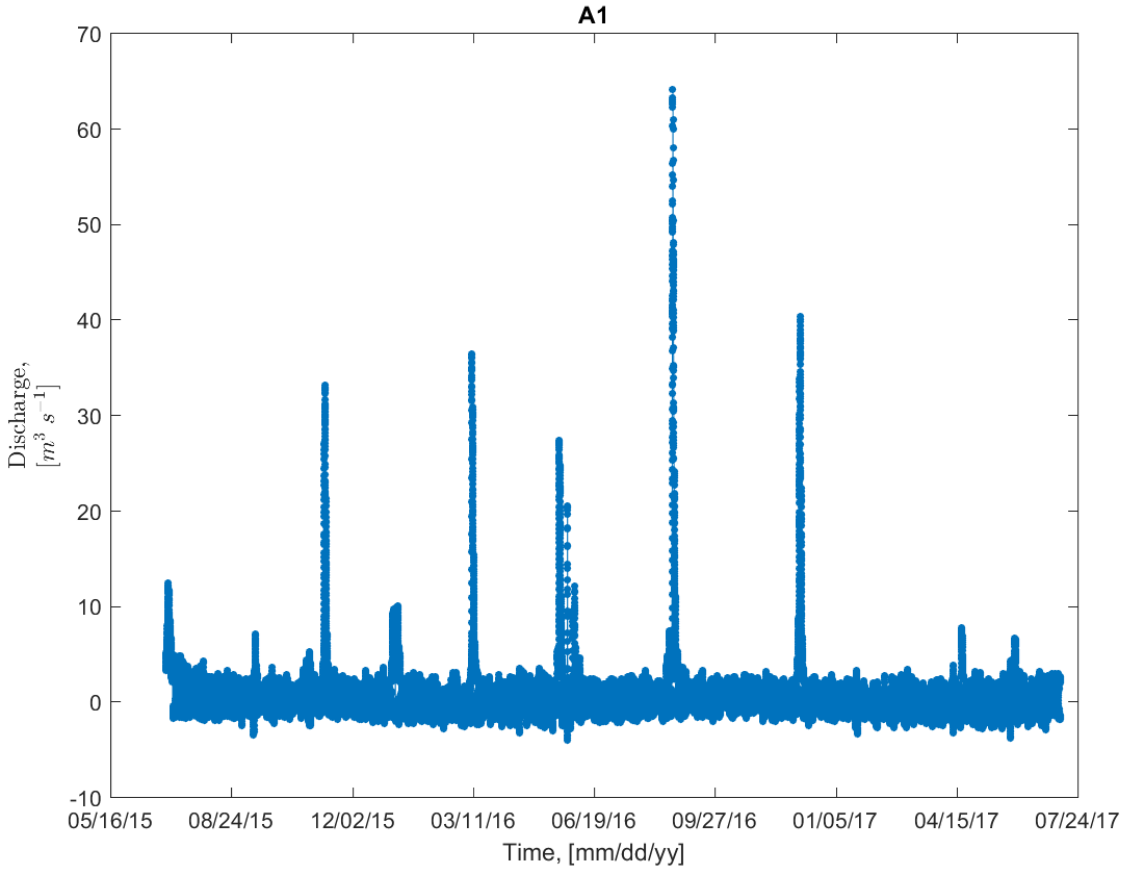

Figure K.1: The calculated discharge time series for M-A site: A1.

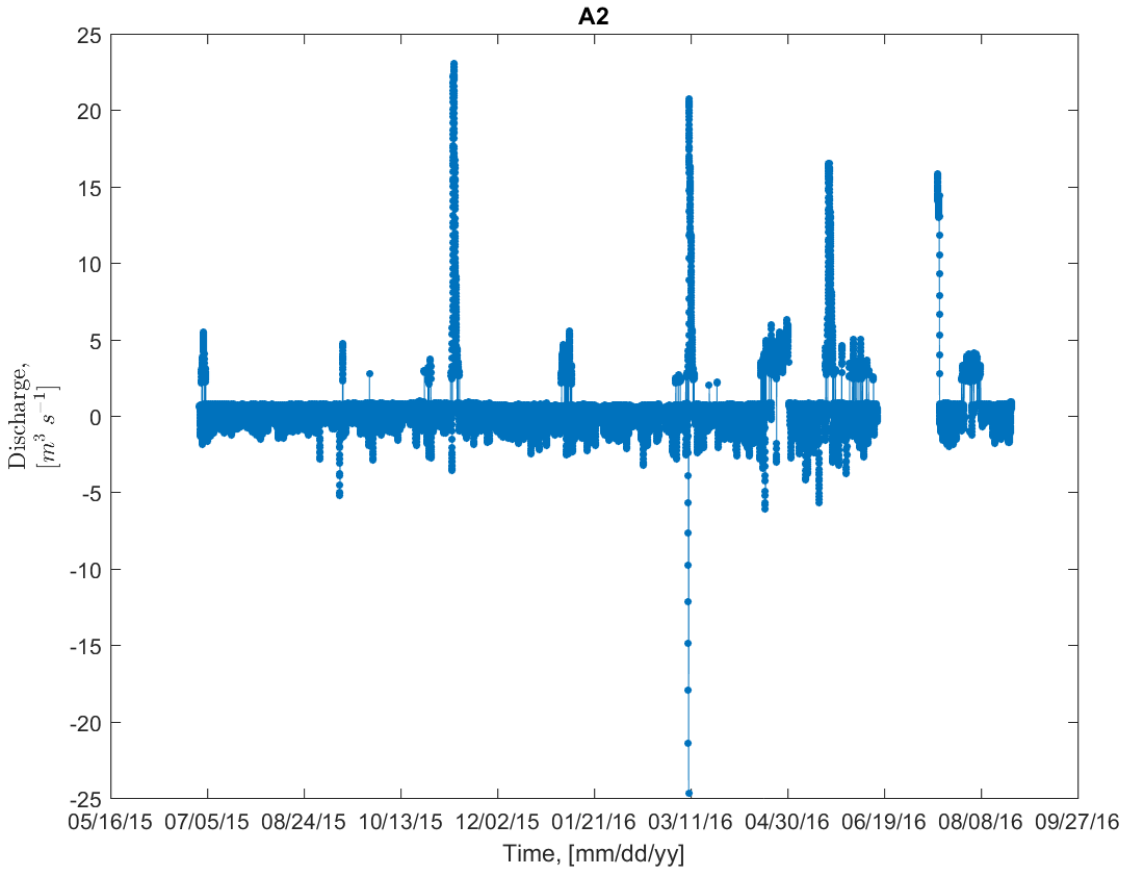

Figure K.2: The calculated discharge time series for M-A site: A2.

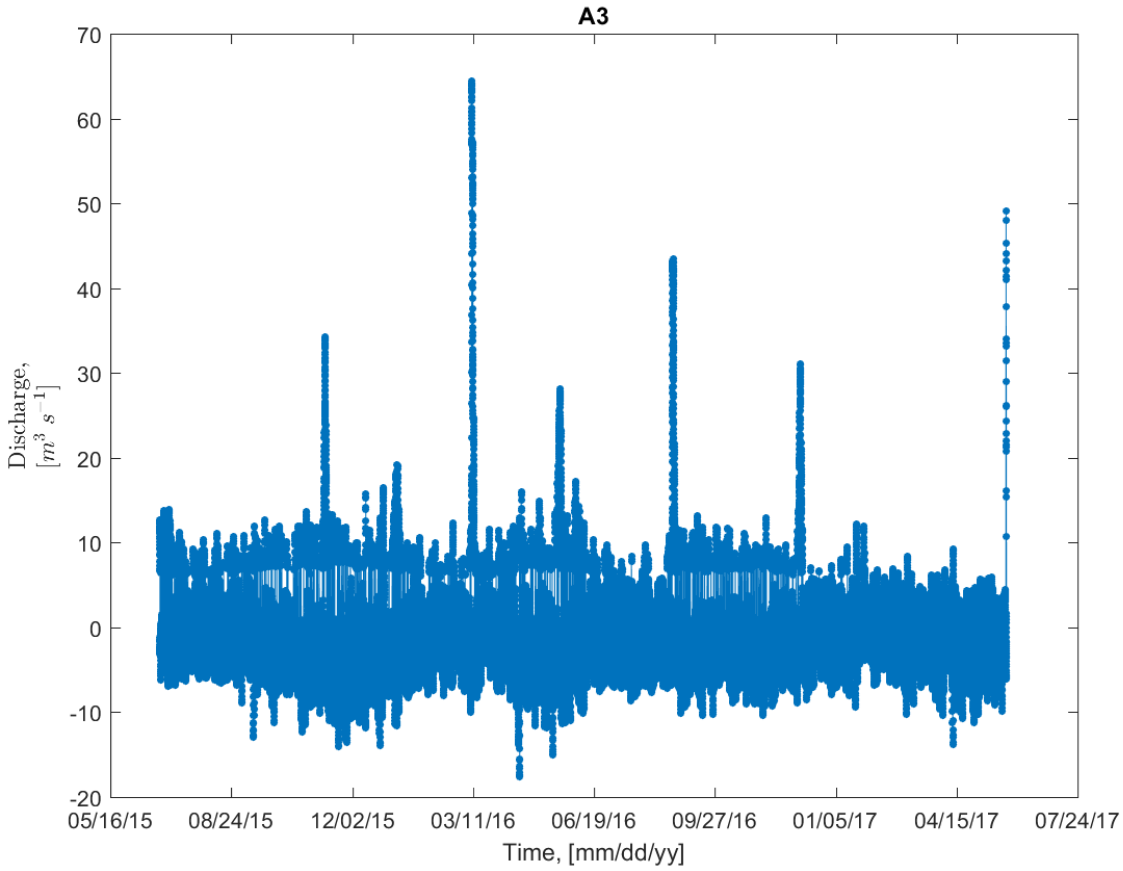

Figure K.3: The calculated discharge time series for M-A site: A3.

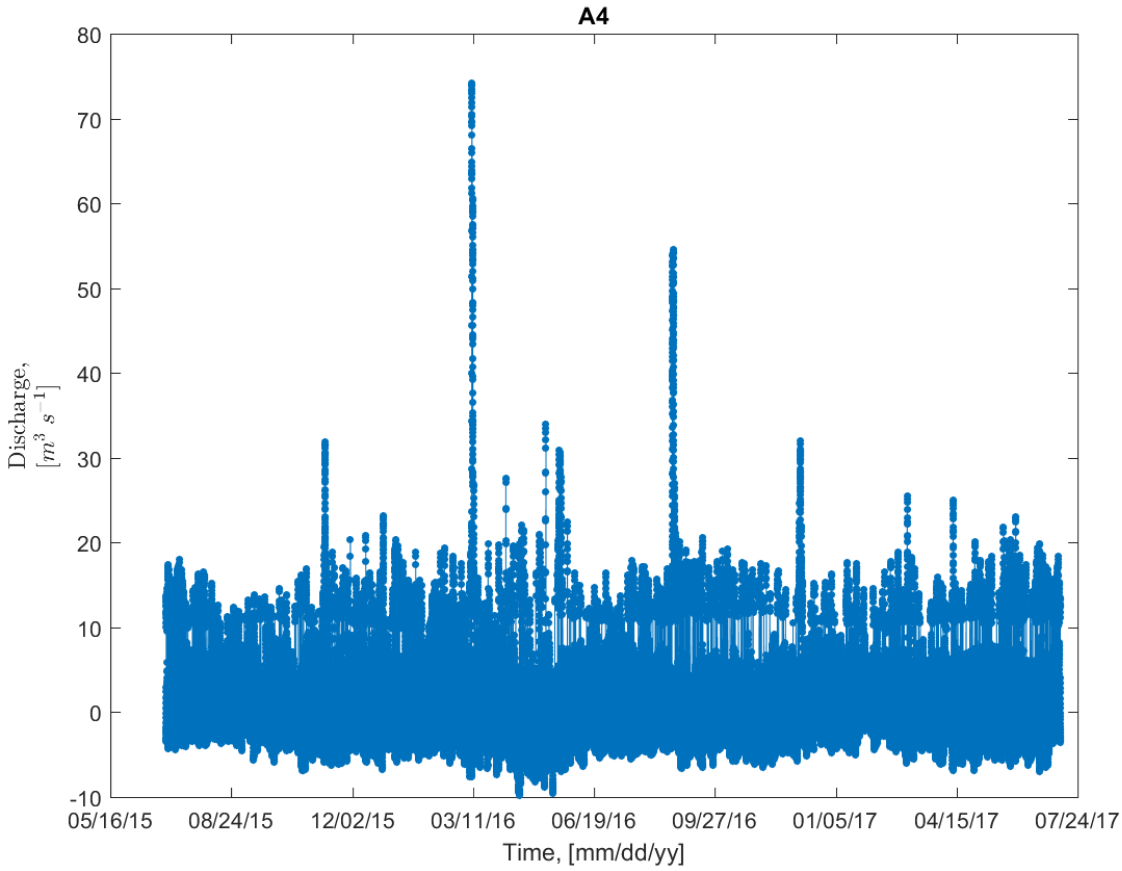

Figure K.4: The calculated discharge time series for M-A site: A4.

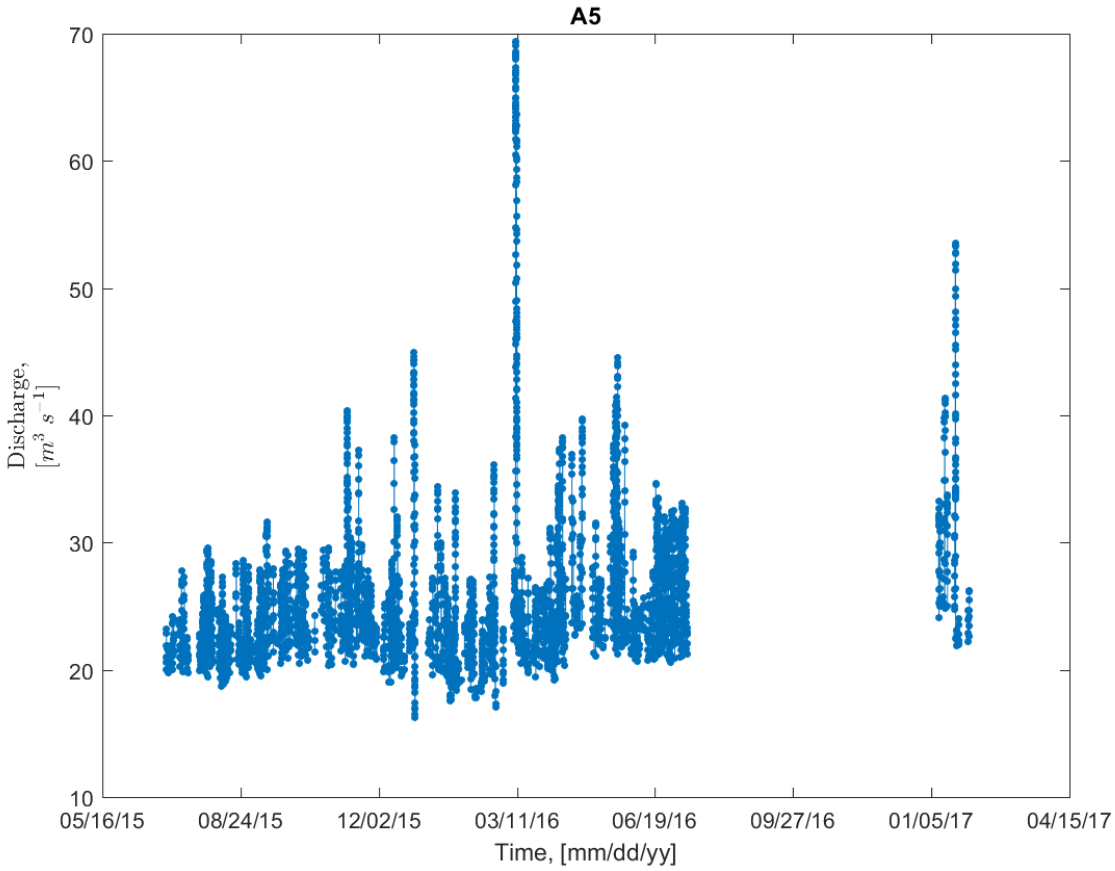

Figure K.5: The calculated discharge time series for M-A site: A5. There are no baseflow discharge conditions calculated for this site, because no ADP transects were completed at this site due to safety concerns. All that is presented are predicted storm discharges.

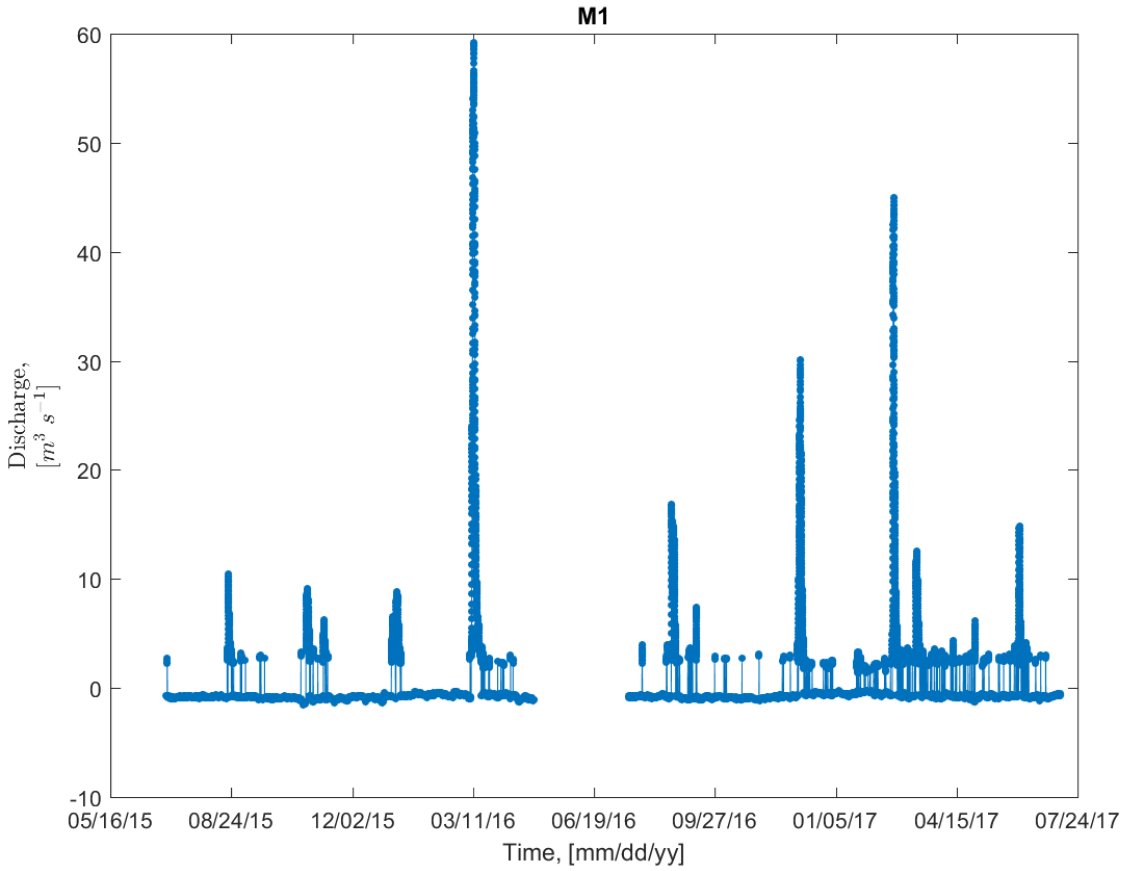

Figure K.6: The calculated discharge time series for M-A site: M1.

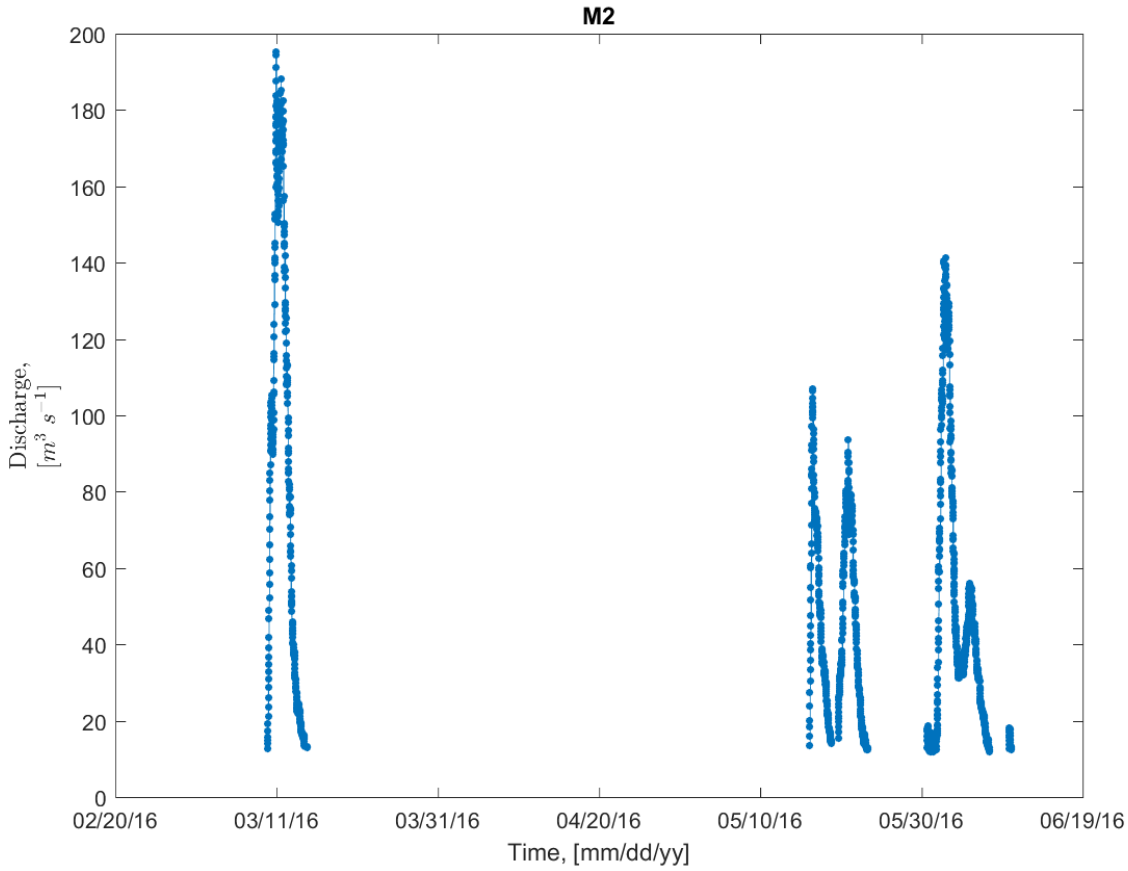

Figure K.7: The calculated discharge time series for M-A site: M2. Baseflow discharge was not calculated for this sites due to multiple sensor malfunctions and insufficient ADP transects. The discharges presented are only predictions of storm discharge.

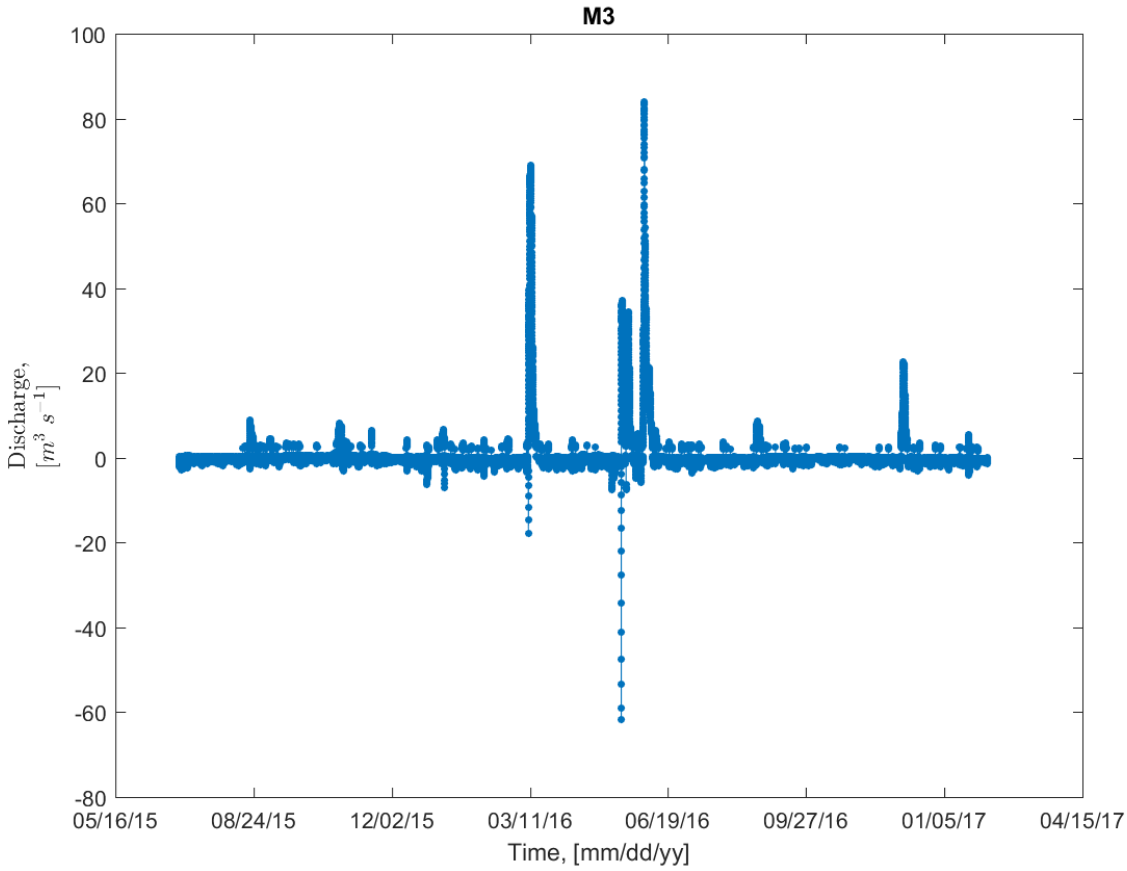

Figure K.8: The calculated discharge time series for M-A site: M3. The spike in upstream discharge near 16 May 2016 is related to the rising limb of storm dramatically altering the dS conditions before shifting the cross-sectional velocity towards storm conditions. This meant that the simplistic method for discerning storm v. baseflow periods calculated discharge with the baseflow equation (eq. 4.3) and coefficients producing a negative (i.e., upstream) discharge associated with sharp rise in stage (i.e., large magnitude positive dS).

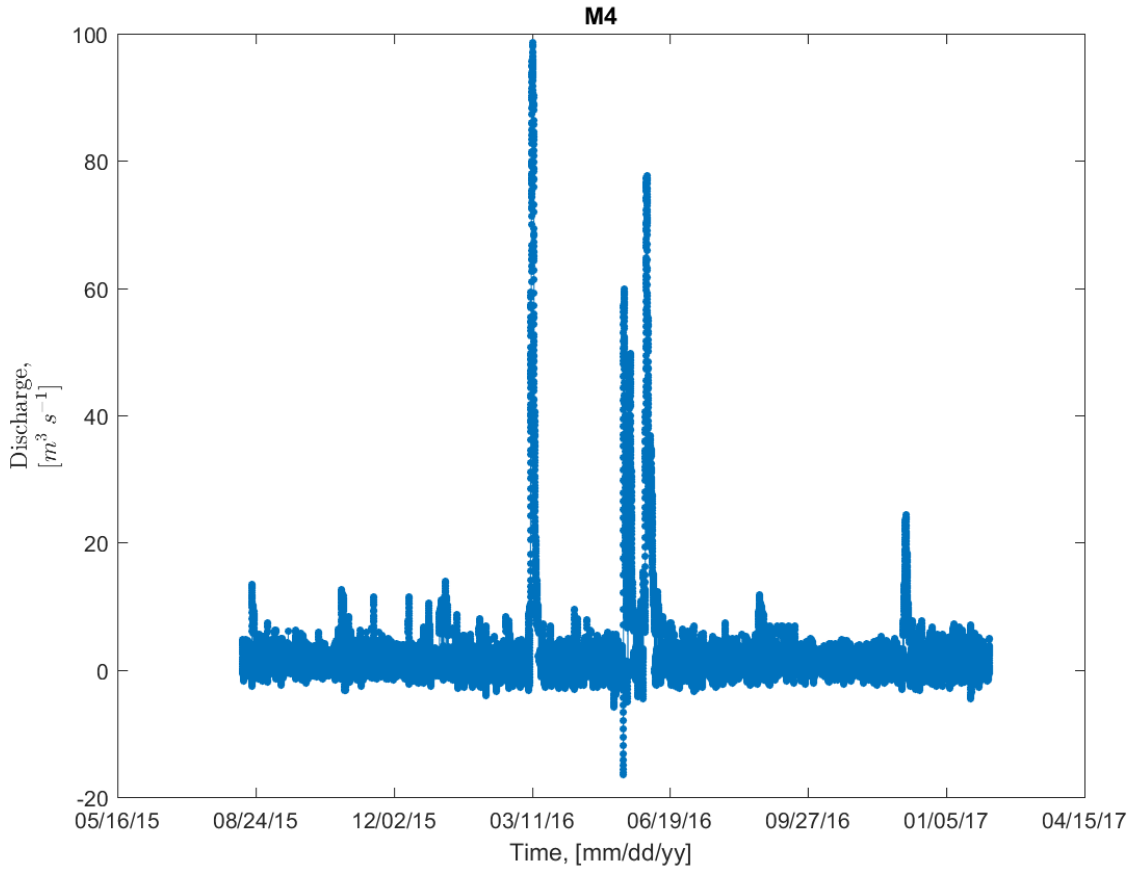

Figure K.9: The calculated discharge time series for M-A site: M4.

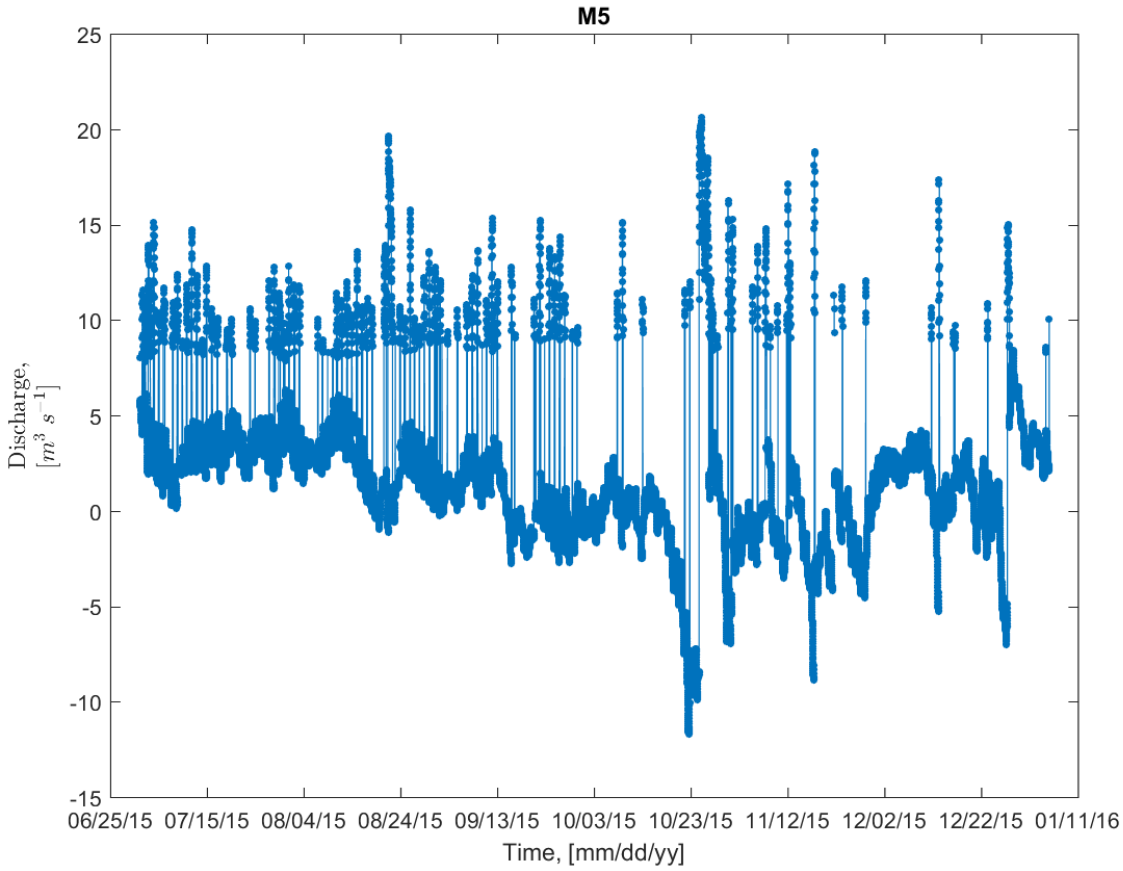

Figure K.10: The calculated discharge time series for M-A site: M5. Unfortunately, throughout much of the study period, the TCM for this site was malfunctioning. Thus, this is a very incomplete record of discharge, one that may not have any actual storm periods.

Bibliography

Adebisi, A. A. (1981). The physico-chemical hydrology of a tropical seasonal river-upper Ogun river. *Hydrobiologia*, *79*(2), 157–165. Retrieved from http://link.springer.com/article/10.1007/BF00006123

Alexander, D., & Fairbridge, R. W. (Eds.). (1999). *Encyclopedia of environmental science*. Dordrecht ; Boston: Kluwer Academic Publishers.

Allan, J. D., & Goulden, C. E. (1980). Some aspects of reproductive variation among freshwater zooplankton. *Evolution and Ecology of Zooplankton Communities. University Press of New England*, 388–410.

Andersen, D. C., & Shafroth, P. B. (2010). Beaver dams, hydrological thresholds, and controlled floods as a management tool in a desert riverine ecosystem, Bill Williams River, Arizona. *Ecohydrology*, *3*(3), 325–338. https://doi.org/10.1002/eco.113

Aretxabaleta, A. L. *et al.* Near-bottom circulation and dispersion of sediment containing Alexandrium fundyense cysts in the Gulf of Maine during 2010–2011. *Deep Sea Research Part II: Topical Studies in Oceanography* **103,** 96–111 (2014).

Arndt, S., Vanderborght, J.-P., & Regnier, P. (2007). Diatom growth response to physical forcing in a macrotidal estuary: Coupling hydrodynamics, sediment transport, and biogeochemistry. *Journal of Geophysical Research: Oceans*, *112*(C5), C05045. https://doi.org/10.1029/2006JC003581

Arndt, Sandra, Lacroix, G., Gypens, N., Regnier, P., & Lancelot, C. (2011). Nutrient dynamics and phytoplankton development along an estuary–coastal zone continuum: A model study. *Journal of Marine Systems*, *84*(3), 49–66. https://doi.org/10.1016/j.jmarsys.2010.08.005

Baranyi, C., Hein, T., Holarek, C., Keckeis, S., & Schiemer, F. (2002). Zooplankton biomass and community structure in a Danube River floodplain system: effects of hydrology. *Freshwater Biology*, *47*(3), 473–482. Retrieved from http://onlinelibrary.wiley.com/doi/10.1046/j.1365-2427.2002.00822.x/full

Basu, B. K., & Pick, F. R. (1996). Factors regulating phytoplankton and zooplankton biomass in temperate rivers. *Limnology and Oceanography*, *41*(7), 1572–1577. https://doi.org/10.4319/lo.1996.41.7.1572

Benenati, E. P., Shannon, J. P., Blinn, W., Wilson, K. P., & Hueftle, S. J. (2000). Reservoir-River Linkages: Lake Powell and the Colorado River, Arizona. *Journal of the North American Benthological Society*, *19*(4), 742. https://doi.org/10.2307/1468131

Benke, A. C., Chaubey, I., Ward, G. M., & Dunn, E. L. (2000). Flood pulse dynamics of an unregulated river floodplain in the southeastern US coastal plain. *Ecology*, *81*(10), 2730–2741. Retrieved from http://www.esajournals.org/doi/abs/10.1890/0012-9658(2000)081%5B2730:FPDOAU%5D2.0.CO%3B2

Bianchi, T., Pennock, J., and Twilley, R. *Biogeochemistry of Gulf of Mexico estuaries*. (John Wiley, 1999).

Bianchin, M., Smith, L., & Beckie, R. (2010). Quantifying hyporheic exchange in a tidal river using temperature time series. *Water Resources Research*, *46*(7), W07507. https://doi.org/10.1029/2009WR008365

Błędzki, L. A., & Ellison, A. M. (2001). Effects of water retention time on zooplankton of shallow rheolimnic reservoirs. *Internationale Vereinigung Fur Theoretische Und Angewandte Limnologie Verhandlungen*, *27*(5), 2865–2869. Retrieved from http://home.mtholyoke.edu/~lbledzki/Les_Publications/BE2000efects.PDF

Brock, D. A. Nitrogen Budget for Low and High Freshwater Inflows, Nueces Estuary, Texas. *Estuaries* **24,** 509–521 (2001).

Bruesewitz, D. A., Gardner, W. S., Mooney, R. F., Pollard, L., & Buskey, E. J. (2013). Estuarine ecosystem function response to flood and drought in a shallow, semiarid estuary: Nitrogen cycling and ecosystem metabolism. *Limnol. Oceanogr*, *58*(6), 2293–2309.

Buffagni, A., Armanini, D. G., & Stefania, E. (2009). Does the lentic-lotic character of rivers affect invertebrate metrics used in the assessment of ecological quality? *Journal of Limnology*, *68*(1), 92–105. Retrieved from http://www.jlimnol.it/index.php/jlimnol/article/view/161

Cole, J. J., Caraco, N. F., & Peierls, B. L. (1992). Can Phytoplankton Maintain a Positive Carbon Balance in a Turbid, Freshwater, Tidal Estuary? *Limnology and Oceanography*, *37*(8), 1608–1617. https://doi.org/10.2307/2838056

Collins, M., R. Knutti, J. Arblaster, J.-L. Dufresne, T. Fichefet, P. Friedlingstein, X. Gao, W.J. Gutowski, T. Johns, G. Krinner, M. Shongwe, C. Tebaldi, A.J. Weaver and M. Wehner, (2013): Long-term Climate Change: Projections, Commitments and Irreversibility. In: *Climate Change 2013: The Physical Science Basis. Contribution of Working Group I to the Fifth Assessment Report of the Intergovernmental Panel on Climate Change* [Stocker, T.F., D. Qin, G.-K. Plattner, M. Tignor, S.K. Allen, J. Boschung, A. Nauels, Y. Xia, V. Bex and P.M. Midgley (eds.)]. Cambridge University Press, Cambridge, United Kingdom and New York, NY, USA.

Church, J.A., P.U. Clark, A. Cazenave, J.M. Gregory, S. Jevrejeva, A. Levermann, M.A. Merrifield, G.A. Milne, R.S. Nerem, P.D. Nunn, A.J. Payne, W.T. Pfeffer, D. Stammer and A.S. Unnikrishnan, (2013): Sea Level Change. In: *Climate Change 2013: The Physical Science Basis. Contribution of Working Group I to the Fifth Assessment Report of the Intergovernmental Panel on Climate Change* [Stocker, T.F., D. Qin, G.-K. Plattner, M. Tignor, S.K. Allen, J. Boschung, A. Nauels, Y. Xia, V. Bex and P.M. Midgley (eds.)]. Cambridge University Press, Cambridge, United Kingdom and New York, NY, USA.

Day, R. H., Williams, T. M., & Swarzenski, C. M. (2007). Hydrology of Tidal Freshwater Forested Wetlands of the Southeastern United States. In *Ecology of Tidal Freshwater Forested Wetlands of the Southeastern United States* (pp. 29–63). Springer Netherlands.

Destouni, G., Hannerz, F., Prieto, C., Jarsjö, J., & Shibuo, Y. (2008). Small unmonitored near-coastal catchment areas yielding large mass loading to the sea. *Global Biogeochemical Cycles*, *22*(4), n/a-n/a. https://doi.org/10.1029/2008GB003287

Dickman, M. (1969). Some Effects of Lake Renewal on Phytoplankton Productivity and Species Composition. *Limnology and Oceanography*, *14*(5), 660–666. Retrieved from http://www.jstor.org/stable/2834058

Dingman, S. L. (2008). *Physical hydrology* (2nd ed. / reissue). Long Grove, IL: Waveland Press Inc.

Dottori, F., Martina, M. L. V., & Todini, E. (2009). A dynamic rating curve approach to indirect discharge measurement. Hydrology and Earth System Sciences, 13(6), 847. Retrieved from http://search.proquest.com/openview/854ef6955be6af7e35a010c574f673b0/1?pq-origsite=gscholar&cbl=105724

Doyle, T. W., O'Neil, C. P., Melder, M. P. V., From, A. S., & Palta, M. M. (2007). Tidal Freshwater Swamps of the Southeastern United States: Effects of Land Use, Hurricanes, Sea-level Rise, and Climate Change. In *Ecology of Tidal Freshwater Forested Wetlands of the Southeastern United States* (pp. 1–28). Springer Netherlands. Retrieved from http://link.springer.com/chapter/10.1007/978-1-4020-5095-4_1

Dyer, K. R. *Estuaries: a physical introduction*. (John Wiley, 1997).

Elser, J. J., Bracken, M. E. S., Cleland, E. E., Gruner, D. S., Harpole, W. S., Hillebrand, H., … Smith, J. E. (2007). Global analysis of nitrogen and phosphorus limitation of primary producers in freshwater, marine and terrestrial ecosystems. *Ecology Letters*, *10*(12), 1135–1142. https://doi.org/10.1111/j.1461-0248.2007.01113.x

Ensign, S. H., Doyle, M. W., & Piehler, M. F. (2013). The effect of tide on the hydrology and morphology of a freshwater river: TIDAL RIVER HYDROLOGY AND MORPHOLOGY. *Earth Surface Processes and Landforms*, *38*(6), 655–660. https://doi.org/10.1002/esp.3392

Evans, A., Madden, K., & Morehead Palmer, S. (2012). *The Ecology and Sociology of the Mission-Aransas Estuary: an estuarine and watershed profile*. Port Aransas, TX: Mission-Aransas National Estuarine Research Reserve. Retrieved from http://www.missionaransas.org/pdf/Mission-Aransas_NERR_Site_Profile_11062012_web.pdf

Findlay, S., Pace, M., & Lints, D. (1991). Variability and transport of suspended sediment, particulate and dissolved organic carbon in the tidal freshwater Hudson River. *Biogeochemistry*, *12*(3), 149–169. https://doi.org/10.1007/BF00002605

Fulbright, T. E., Diamond, D. D., Rappole, J., & Norwine, J. (1990). The coastal sand plain of southern Texas. *Rangelands*, 337–340. Retrieved from http://www.jstor.org/stable/4000522

Ganju, N. K., Schoellhamer, D. H., Warner, J. C., Barad, M. F., & Schladow, S. G. (2004). Tidal oscillation of sediment between a river and a bay: a conceptual model. *Estuarine, Coastal and Shelf Science*, *60*(1), 81–90. https://doi.org/10.1016/j.ecss.2003.11.020

Hein, T., Baranyi, C., Steel, A., & Schiemer, F. (2003). The importance of autochthonous particulate organic matter in large floodplain rivers: evidence of restoring hydrological connectivity. In *EGS-AGU-EUG Joint Assembly* (Vol. 1, p. 621). Retrieved from http://adsabs.harvard.edu/abs/2003EAEJA.....621H

Heinesch, B. (2006, July). *Coordinate Rotation*. Oral Presentation presented at the Summer school “eddy-covariance flux measurements,” Namur, Belgium. Retrieved from http://hdl.handle.net/2268/60780

Heniche, M., Secretan, Y., Boudreau, P., & Leclerc, M. (2000). A two-dimensional finite element drying-wetting shallow water model for rivers and estuaries. *Advances in Water Resources*, *23*(4), 359–372. Retrieved from http://www.sciencedirect.com/science/article/pii/S0309170899000317

Hittle, C., Patino, E., & Zucker, M. (2004). Hydrologic Characteristics of Estuarine River Systems within Everglades National Park. *US Department of the Interior US Geological Survey*, (2004–3129). Retrieved from https://pubs.usgs.gov/fs/2004/3129/

Hoffsten, P.-O., & Malmqvist, B. (2000). The macroinvertebrate fauna and hydrogeology of springs in central Sweden. *Hydrobiologia*, *436*(1–3), 91–104. Retrieved from http://link.springer.com/article/10.1023/A:1026550207764

Huhta, C. (2002). Handheld Acoustic Doppler Velocimeter (ADV) for Water Velocity Surveys. *Hydraulic Measurements and Experimental Methods*. https://doi.org/10.1061/40655(2002)30

Humphries, P., Keckeis, H., & Finlayson, B. (2014). The River Wave Concept: Integrating River Ecosystem Models. *BioScience*, *64*(10), 870–882. https://doi.org/10.1093/biosci/biu130

Intergovernmental Panel on Climate Change (IPCC) (2013), Climate change 2013: The physical science basis, in *Contribution of Working Group I to the Fifth Assessment Report of the Intergovernmental Panel on Climate Change*, edited by T. F. Stocker, 1535 pp., Cambridge Univ. Press, Cambridge, U. K.

Johnson, S. L. (2009). *A general method for modeling coastal water pollutant loadings* (Ph.D.). The University of Texas at Austin, United States -- Texas. Retrieved from http://search.proquest.com/docview/856598483/abstract?accountid=7118

Jones, A. E., Hodges, B. R., McClelland, J. W., Hardison, A. K., & Moffett, K. B. (2017). Residence-time-based classification of surface water systems. *Water Resources Research*. https://doi.org/10.1002/2016WR019928

Kennedy, E. J. (1984). *Discharge Ratings at Gauging Stations* (U.S. Geological Survey Techniques of Water-Resources Investigations No. Book 3, Chap. A10) (p. 59). Washington, D.C., USA: United States Geological Survey. Retrieved from https://pubs.usgs.gov/twri/twri3-a10/pdf/TWRI_3-A10.pdf

Knights, D., Sawyer, A. H., Barnes, R. T., Musial, C. T., & Bray, S. (2017). Tidal controls on riverbed denitrification along a tidal freshwater zone: Tides on Riverbed Denitrification. *Water Resources Research*, *53*(1), 799–816. https://doi.org/10.1002/2016WR019405

Krawczyk, A. C. de D. B., Baldan, L. T., Aranha, J. M. R., Menezes, M. S. de, & Almeida, C. V. (2013). The invertebrate's community in adjacent Alto Iguaçu's anthropic lakes of different environmental factors. *Biota Neotropica*, *13*(1), 47–60.

Levesque, V. A. (2004). *Water Flow and Nutrient Flux from Five Estuarine Rivers along the Southwest Coast of the Everglades National Park, Florida, 1997-2001* (Scientific Investigations Report No. 2004–5142). Reston, VA: US Department of the Interior US Geological Survey.

Levesque, V. A., & Oberg, K. A. (2012). *Computing Discharge Usin the Index Velocity Method* (Techniques and Methods No. 3-A23) (p. 148). Reston, Virginia: U.S. Geological Survey. Retrieved from http://pubs.usgs.gov/tm/3a23/

Lovley, D. R., & Phillips, E. J. P. (1986a). Availability of Ferric Iron for Microbial Reduction in Bottom Sediments of the Freshwater Tidal Potomac River. *Applied and Environmental Microbiology*, *52*(4), 751–757. Retrieved from http://aem.asm.org/content/52/4/751

Lovley, D. R., & Phillips, E. J. P. (1986b). Organic Matter Mineralization with Reduction of Ferric Iron in Anaerobic Sediments. *Applied and Environmental Microbiology*, *51*(4), 683–689.

Maio, C. V. *et al.* Sediment dynamics and hydrographic conditions during storm passage, Waquoit Bay, Massachusetts. *Marine Geology* **381,** 67–86 (2016).

Manzoni, S., & Porporato, A. (2011). Common hydrologic and biogeochemical controls along the soil-stream continuum. *Hydrological Processes*, *25*(8), 1355–1360. https://doi.org/10.1002/hyp.7938

Moftakhari, H. R., Jay, D. A., Talke, S. A., Kukulka, T., & Bromirski, P. D. (2013). A novel approach to flow estimation in tidal rivers. *Water Resources Research*, *49*(8), 4817–4832. https://doi.org/10.1002/wrcr.20363

Monsen, N. E., Cloern, J. E., Lucas, L. V., & Monismith, S. G. (2002). A comment on the use of flushing time, residence time, and age as transport time scales. *Limnology and Oceanography*, *47*(5), 1545–1553. Retrieved from http://onlinelibrary.wiley.com/doi/10.4319/lo.2002.47.5.1545/full

Mooney, R. F., & McClelland, J. W. (2012). Watershed Export Events and Ecosystem Responses in the Mission–Aransas National Estuarine Research Reserve, South Texas. *Estuaries and Coasts*, *35*(6), 1468–1485. https://doi.org/10.1007/s12237-012-9537-4

National Estuarine Research Reserve (NERR) (2015). Tunnell, J., Buskey, E. J. & Peterson, T. (Eds.) *Freshwater Inflows: Determining Flow Regimes in the Face of Land Use Change, Climate Change, and Other Unknowns*. 47 (National Estuarine Research Reserve, 2015).

National Oceanic and Atmospheric Administration (NOAA) (2017a). Climate Prediction Center - Monitoring & Data: ENSO Impacts on the U.S. - Previous Events. *National Weather Service - Climate Prediction Center* (2015). Available at: http://www.cpc.ncep.noaa.gov/products/analysis_monitoring/ensostuff/ensoyears.shtml. (Accessed: 19th July 2017)

National Oceanic and Atmospheric Administration (NOAA) (2017b). El Niño Southern Oscillation (ENSO). *Earth System Research Laboratory: Physical Sciences Division* (2017). Available at: https://www.esrl.noaa.gov/psd/enso/enso_101.html. (Accessed: 19th July 2017)

National Oceanic and Atmospheric Administration (NOAA) Tides & Currents (2017c), Station Selection—NOAA Tides & Currents NOAA Tides & Currents—Station Selection, National Oceanic and Atmospheric Administration, Washington, D. C. [Available at https://tidesandcurrents.noaa.gov/stations.html?type5Water1Levels#Texas, accessed 19th July 2017.]

Neumann, B., Vafeidis, A. T., Zimmermann, J., & Nicholls, R. J. (2015). Future Coastal Population Growth and Exposure to Sea-Level Rise and Coastal Flooding - A Global Assessment. *PLOS ONE*, *10*(3), e0118571. https://doi.org/10.1371/journal.pone.0118571

NOAA Tides & Currents (2015), Station Selection—NOAA Tides & Currents NOAA Tides & Currents—Station Selection, National Oceanic and Atmospheric Administration, Washington, D. C.
[Available at https://tidesandcurrents.noaa.gov/stations.html?type5Water1Levels#Texas, accessed Oct. 2015.]

Odum, W. E. (1988). Comparative Ecology of Tidal Freshwater and Salt Marshes. *Annual Review of Ecology and Systematics*, *19*, 147–176. https://doi.org/10.2307/2097151

Pace, M. L., Findlay, S. E., & Lints, D. (1992). Zooplankton in advective environments: the Hudson River community and a comparative analysis. *Canadian Journal of Fisheries and Aquatic Sciences*, *49*(5), 1060–1069. Retrieved from http://www.nrcresearchpress.com/doi/abs/10.1139/f92-117

Palmer, T. A., Montagna, P. A., Pollack, J. B., Kalke, R. D., & DeYoe, H. R. (2011). The role of freshwater inflow in lagoons, rivers, and bays. *Hydrobiologia*, *667*(1), 49–67. https://doi.org/10.1007/s10750-011-0637-0

Pellett, S., Bigley, D. V., & Grimes, D. J. (1983). Distribution of Pseudomonas aeruginosa in a riverine ecosystem. *Applied and Environmental Microbiology*, *45*(1), 328–332. Retrieved from http://aem.asm.org/content/45/1/328.short

Pollack, J., Kim, H.-C., Morgan, E., & Montagna, P. (2011). Role of Flood Disturbance in Natural Oyster (Crassostrea virginica) Population Maintenance in an Estuary in

South Texas, USA. *Estuaries and Coasts*, *34*(1), 187–197. https://doi.org/10.1007/s12237-010-9338-6

Rasmussen, J. B., Godbout, L., & Schallenberg, M. (1989). The humic content of lake water and its relationship to watershed and lake morphometry. *Limnology and Oceanography*, *34*(7), 1336–1343. Retrieved from http://onlinelibrary.wiley.com/doi/10.4319/lo.1989.34.7.1336/full

Rennella, A. M., & Quirós, R. (2006). The Effects of Hydrology on Plankton Biomass in Shallow Lakes of the Pampa Plain. *Hydrobiologia*, *556*(1), 181–191. https://doi.org/10.1007/s10750-005-0318-y

Ropelewski, C. F., & Halpert, M. S. (1986). North American Precipitation and Temperature Patterns Associated with the El Niño/Southern Oscillation (ENSO). *Monthly Weather Review*, *114*(12), 2352–2362. https://doi.org/10.1175/1520-0493(1986)114<2352:NAPATP>2.0.CO;2

Ruhl, C. A., & Simpson, M. R. (2005). *Computation of Discharge Usin the Indexd-Velocity Method in Tidally Affected Areas* (Scientific Investigations Report No. 2005–5004) (p. 31). Reston, Virginia: U.S. Geological Survey.

Russell, M. J., Montagna, P. A. & Kalke, R. D. The effect of freshwater inflow on net ecosystem metabolism in Lavaca Bay, Texas. *Estuarine, Coastal and Shelf Science* **68,** 231–244 (2006).

Rzóska, J. (1978). *On the nature of rivers: with case stories of Nile, Zaire, and Amazon: essay*. The Hague ; Boston: Dr. W. Junk.

Saunders, D. L., & Kalff, J. (2001). Nitrogen retention in wetlands, lakes and rivers. *Hydrobiologia*, *443*(1–3), 205–212. Retrieved from http://link.springer.com/article/10.1023/A:1017506914063

Savenije, H. H. G. (2005). *Salinity and tides in alluvial estuaries* (1st ed). Amsterdam ; Boston: Elsevier.

Scavia, D., Field, J. C., Boesch, D. F., Buddemeier, R. W., Burkett, V., Cayan, D. R., Fogarty, M., Harwell, M. A., Howarth, R. W., Mason, C., Reed D. J., Royer, T.C., Sallenger, A. H., and Titus, J. G. (2002). Climate Change Impacts on U. S. Coastal and Marine Ecosystems. *Estuaries*, *25*(2), 149–164. Retrieved from http://www.jstor.org/stable/1353306

Seitzinger, S. P., Mayorga, E., Bouwman, A. F., Kroeze, C., Beusen, A. H. W., Billen, G., … Harrison, J. A. (2010). Global river nutrient export: A scenario analysis of past

and future trends: GLOBAL RIVER EXPORT SCENARIOS. *Global Biogeochemical Cycles*, *24*(4), n/a-n/a. https://doi.org/10.1029/2009GB003587

Sheldon, J. E., & Alber, M. (2002). A comparison of residence time calculations using simple compartment models of the Altamaha River estuary, Georgia. *Estuaries*, *25*(6), 1304–1317. https://doi.org/10.1007/BF02692226

Shen, J., & Haas, L. (2004). Calculating age and residence time in the tidal York River using three-dimensional model experiments. *Estuarine, Coastal and Shelf Science*, *61*(3), 449–461. https://doi.org/10.1016/j.ecss.2004.06.010

Sheremet, V. (2013, February). *Building Observing System Deployed on Lobster Traps along the Northeast Atlantic Shelf*. Presented at the Fishermen & Scientist Research Society: 20th Annual Conference, Truro, Nova Scotia. Retrieved from http://www.fsrs.ns.ca/docs/Building%20Observing%20Systems%20Vitalii%20SharemetManning_PubRelease.pdf

Sheremet, V., Manning, J., & Pelletier, E. (2009). *Environmental monitors on lobster traps (eMOLT) Phase VI: Bottom Currents* (Annual Report). Northeast Fisheries Science Center. Retrieved from http://www.northeastconsortium.net/pdfs/awards_2007/Sheremet%2007/Sheremet%2007%20Final%20Report.pdf

Simmons, D. B. D., and D. Wallschlager (2005), A critical review of the biogeochemistry and ecotoxicology of selenium in lotic and lentic environments, *Environ. Toxicol. Chem.*, 24(6), 1331−1343.

Smoot, G. F., & Novak, C. E. (1969). *Measurement of discharge by the moving-boat method* (USGS Numbered Series No. 03-A11). U.S. Govt. Print. Off.,. Retrieved from http://www.comm-tec.com/Library/technical_papers/USGS/twri_3-A11_a.pdf

Soballe, D. M., & Kimmel, B. L. (1987). A Large-Scale Comparison of Factors Influencing Phytoplankton Abundance in Rivers, Lakes, and Impoundments. *Ecology*, *68*(6), 1943. https://doi.org/10.2307/1939885

SonTek. (2007). *RiverSurveyor System Manual* (System Manual) (p. 189). San Diego, CA: SonTek/YSI Inc. Retrieved from http://www.sontek.com

Stanley, E. H., Short, R. A., Harrison, J. W., Hall, R., & Wiedenfeld, R. C. (1990). Variation in nutrient limitation of lotic and lentic algal communities in a Texas (USA) river. *Hydrobiologia*, *206*(1), 61–71. Retrieved from http://link.springer.com/article/10.1007/BF00018970

Sullivan, S. M. (2013), Surveying amazon river tributaries for tug and barge navigation, Sea Surveyor, Inc., Benicia, Calif. [Available at http://www.seasurveyor.com/wp-content/uploads/2013/01/Surveying-Amazon-River-Tributaries-for-Tug-and-Barge-Navigation.pdf, accessed Oct. 2016.]

Svendsen, L. M., & Kronvang, B. (1993). Retention of nitrogen and phosphorus in a Danish lowland river system: implications for the export from the watershed. *Hydrobiologia*, *251*, 123–135. Retrieved from http://link.springer.com/chapter/10.1007/978-94-011-1602-2_15

Teledyne. (2015). *StreamPro ADCP Guide* (ADCP Guide No. 95B–6003–00) (p. 101). Poway, CA: Teledyne RD Instruments. Retrieved from http://www.rdinstruments.com

Texas Coastal Ocean Observation Network (TCOON) (2015), CBI, Texas A&M University Corpus Christi, Corpus Christi, Tex. [Available at http://www.cbi.tamucc.edu/TCOON/, accessed Nov. 2015.]

Texas Commission on Environmental Quality (TCEQ) (2015), Surface Water Quality Viewer TCEQ Surface Water Quality Viewer, Texas Commission on Environmental Quality, Austin, Tex. [Available at https://gisweb.tceq.texas.gov/segments/default.htm, accessed Oct. 2015.]

Thorp, J. H., Thoms, M. C., & Delong, M. D. (2006). The riverine ecosystem synthesis: biocomplexity in river networks across space and time. *River Research and Applications*, *22*(2), 123–147. https://doi.org/10.1002/rra.901

Tockner, K., Malard, F., & Ward, J. V. (2000). An extension of the flood pulse concept. *Hydrological Processes*, *14*(16–17), 2861–2883. https://doi.org/10.1002/1099-1085(200011/12)14:16/17<2861::AID-HYP124>3.0.CO;2-F

Trigg, M. A., Wilson, M. D., Bates, P. D., Horritt, M. S., Alsdorf, D. E., Forsberg, B. R., & Vega, M. C. (2009). Amazon flood wave hydraulics. *Journal of Hydrology*, *374*(1–2), 92–105. https://doi.org/10.1016/j.jhydrol.2009.06.004

United States Geological Survey (USGS) (2015), USGS Current Water Data for Texas, USGS NWIS United States Geological Survey, Reston, Va. [Available at http://waterdata.usgs.gov/tx/nwis/rt, accessed Oct. 2015.]

United States Geological Survey (USGS) (2017a), USGS Current Conditions for USGS 08189700 Aransas Rv nr Skidmore, TX, USGS NWIS United States Geological Survey, Reston, Va. [Available at https://waterdata.usgs.gov/tx/nwis/uv/?site_no=08189700, accessed May 2017]

United States geological Survey (USGS) (2017b), USGS Current Conditions for USGS 08211200 Nueces Rv at Bluntzer, TX, USGS NWIS United States Geological Survey, Reston, Va. [Available at https://waterdata.usgs.gov/tx/nwis/uv/?site_no=08211200, accessed May 2017]

Vannote, R. L., Minshall, G. W., Cummins, K. W., Sedell, J. R., & Cushing, C. E. (1980). The River Continuum Concept. *Canadian Journal of Fisheries and Aquatic Sciences*, *37*(1), 130–137. https://doi.org/10.1139/f80-017

Vegas-Vilarrúbia, T., & Herrera, R. (1993). Seasonal alternation of lentic/lotic conditions in the Mapire system, a tropical floodplain lake in Venezuela. *Hydrobiologia*, *262*(1), 43–55.

Ward, G. H. (1997). Process and Trends of Circulation Within the Corpus Christi Bay National Estuary Program Study Area. *Corpus Christi Bay National Estuary Program*, *CCBNEP-21*.

Ward, J. V., Tockner, K., Arscott, D. B., & Claret, C. (2002). Riverine landscape diversity. *Freshwater Biology*, *47*(4), 517–539. https://doi.org/10.1046/j.1365-2427.2002.00893.x

Wang, C.-F., Hsu, M.-H., & Kuo, A. Y. (2004). Residence time of the Danshuei River estuary, Taiwan. *Estuarine, Coastal and Shelf Science*, *60*(3), 381–393. https://doi.org/10.1016/j.ecss.2004.01.013

Wilczak, J. M., Oncley, S. P., & Stage, S. A. (2001). Sonic anemometer tilt correction algorithms. *Boundary-Layer Meteorology*, *99*(1), 127–150. Retrieved from http://www.springerlink.com/index/p32123684246g213.pdf

Wolter, K., Dole, R. M., & Smith, C. A. (1999). Short-term climate extremes over the continental United States and ENSO. Part I: Seasonal temperatures. *Journal of Climate; Boston*, *12*(11), 3255–3272. Retrieved from https://search-proquest-com.ezproxy.lib.utexas.edu/docview/222898488?pq-origsite=summon

Yankovsky, A. E., Torres, R., Torres-Garcia, L. M., & Jeon, K. (2012). Interaction of Tidal and Fluvial Processes in the Transition Zone of the Santee River, SC, USA. *Estuaries and Coasts*, *35*(6), 1500–1509. https://doi.org/10.1007/s12237-012-9535-6

Yuan, R., Kang, M.-S., Park, S.-B., & Hong, J.-K. (2007). The Effect of Coordinate Rotation on the Eddy Covariance Flux Estimation in a Hilly KoFlux Forest Catchment. *Korean Journal of Agricultural and Forest Meteorology*, *9*(2), 100–108. https://doi.org/10.5532/KJAFM.2007.9.2.100